Site U1352[1]

Expedition 317 Scientists[2]

Chapter contents

[1] Expedition 317 Scientists, 2011. Site U1352. *In* Fulthorpe, C.S., Hoyanagi, K., Blum, P., and the Expedition 317 Scientists, *Proc. IODP,* 317: Tokyo (Integrated Ocean Drilling Program Management International, Inc.). doi:10.2204/iodp.proc.317.104.2011
[2] Expedition 317 Scientists' addresses.

Background and objectives

Hole U1352A

Position: 44°56.2440′S, 172°1.3615′E
Start hole: 1145 h, 30 November 2009
End hole: 1530 h, 30 November 2009
Time on hole (d): 0.16
Seafloor (drill pipe measurement from rig floor, m DRF): 354.8 (APC mudline)
Distance between rig floor and sea level (m): 11.0
Water depth (drill pipe measurement from sea level, m): 343.8
Total depth (drill pipe measurement from rig floor, m DRF): 397.0
Total penetration (m DSF): 42.2
Total length of cored section (m): 42.2
Total core recovered (m): 43.92
Core recovery (%): 104
Total number of cores: 5

Hole U1352B

Position: 44°56.2558′S, 172°1.3630′E
Start hole: 1530 h, 30 November 2009
End hole: 1615 h, 5 December 2009
Time on hole (d): 5.03
Seafloor (drill pipe measurement from rig floor, m DRF): 354.6
Distance between rig floor and sea level (m): 11.0
Water depth (drill pipe measurement from sea level, m): 343.6
Total depth (drill pipe measurement from rig floor, m DRF): 1185.5
Total penetration (m DSF): 830.9
Total length of cored section (m): 830.9
Total core recovered (m): 613.87
Core recovery (%): 74
Total number of cores: 94

Hole U1352C

Position: 44°56.2662′S, 172°1.3630′E
Start hole: 2015 h, 5 December 2009
End hole: 2200 h, 20 December 2009
Time on hole (d): 15.07

doi:10.2204/iodp.proc.317.104.2011

Seafloor (drill pipe measurement from rig floor, m DRF): 354.5 (tagging seafloor)
Distance between rig floor and sea level (m): 11.0
Water depth (drill pipe measurement from sea level, m): 343.5
Total depth (drill pipe measurement from rig floor, m DRF): 2282.0
Total penetration (m DSF): 1927.5
Total length of cored section (m): 1296.4
Total core recovered (m): 655.02
Core recovery (%): 51
Total number of cores: 146

Hole U1352D

Position: 44°56.2326′S, 172°1.3611′E
Start hole: 0615 h, 21 December 2009
End hole: 2100 h, 21 December 2009
Time on hole (d): 0.61
Seafloor (drill pipe measurement from rig floor, m DRF): 345.2 (APC mudline)
Distance between rig floor and sea level (m): 11.0
Water depth (drill pipe measurement from sea level, m): 344.2
Total depth (drill pipe measurement from rig floor, m DRF): 472.2
Total penetration (m DSF): 127.0
Total length of cored section (m): 127.0
Total core recovered (m): 130.84
Core recovery (%): 103
Total number of cores: 14

Integrated Ocean Drilling Program (IODP) Site U1352 (proposed Site CB-04B) is located on the upper slope (344 m water depth) within the Canterbury Bight and is the most basinward site of the Canterbury Basin drilling transect. This location was chosen as a primary site in response to an Environmental Protection and Safety Panel (EPSP) request (December 2005) to avoid the high seismic amplitudes observed at 1.6–1.7 s two-way traveltime at Site CB-04A. Site U1352 is located downdip from Site CB-04A on dip seismic Profile EW00-01-60 (Figs. **F1, F2**). Because of the move from Site CB-04A, there is no crossing strike profile at Site U1352.

Site U1352 penetrates seismic sequence boundaries U6–U19 where sediments are finer grained and pelagic microfossils are more abundant than at shelf sites. This provides good age control for sequences drilled on the shelf.

An additional target, requiring deep penetration, was the Marshall Paraconformity, which has been dated at its onshore type section using strontium isotopes as representing a hiatus of ~3.4 m.y. (32.4–29 Ma) (Fulthorpe et al., 1996). The paraconformity probably records intensified current erosion or nondeposition at all water depths that accompanied the development of ocean circulation following the opening of the seaway south of Tasmania (Carter, 1985; Fulthorpe et al., 1996; Carter et al., 2004). Seismic interpretation supports a current-related origin by indicating that the paraconformity forms the base of the interval of sediment drift deposition. Indeed, immediately post–Marshall Paraconformity sedimentation involves sediment drift deposition in shallow (Ward and Lewis, 1975), intermediate (Fulthorpe and Carter, 1991; Lu et al., 2003), and deep water settings (Shipboard Scientific Party, 1999a; Carter et al., 2004). Drilling during Ocean Drilling Program (ODP) Leg 181 indicates that the paraconformity developed in deep (bathyal) water ~1–2 m.y. earlier than in shallow water (McGonigal and Di Stefano, 2002). Dating the paraconformity in the offshore Canterbury Basin at Site U1352 provides a further test of this hypothesis.

Because of time constraints, drilling into one of the large elongate sediment drifts of the Canterbury Basin, specifically drift D11 (Lu et al., 2003; Lu and Fulthorpe, 2004), became a secondary objective. Therefore, sites that were originally proposed for drilling into drift D11 (proposed Sites CB-05B to CB-05E) became contingency sites to be drilled only if drilling at shelf sites was not possible. Nevertheless, insights into sediment drift deposition and paleoceanography are expected from drilling at Site U1352. The largest mounded elongate drifts lie within the northeastern part of the shelf-slope sediment prism. Drift geometries become gradually less pronounced along strike toward the southwest, and mounded drifts are absent at Site U1352 (Lu and Fulthorpe, 2004). However, the generation of mounded drifts requires specific conditions that are not well understood; a slope contour current alone is insufficient, as indicated by the fact that such drifts are not forming under the present current regime. Current reworking of sediments is evident at Site U1352, and currents may have left a paleoceanographic record of glacial–interglacial cycles, as at ODP Site 1119 (Carter et al., 2004), without producing distinctive geometries.

The principal objectives at Site U1352 were

1. To sample slope sediments basinward of clinoform breaks of progradational seismic sequence boundaries, particularly U6–U9, U11, and U13–U19 (late Miocene to Pleistocene) to provide sequence boundary ages;
2. To penetrate the Marshall Paraconformity and the top of the underlying Amuri Limestone (late Eocene at total depth); and
3. To provide insights into the role of contour current deposition in a location where prominent sediment drift geometries are absent.

Operations

Transit to Site U1352

After a 3 h, 8 nmi move from Site U1351 in dynamic positioning (DP) mode, the R/V *JOIDES Resolution* was positioned at Site U1352 at 0500 h (all times are ship local time, Universal Time Coordinated [UTC] + 13 h) on 30 November 2009. The position reference was a combination of Global Positioning System (GPS) and an acoustic beacon on the seafloor, weighted heavily toward the acoustic beacon (80%). A positioning beacon (FSI BAP-547W, SN 1025, 14.0 kHz, 200 dB) was deployed at 0455 h on 30 November.

Site U1352 overview

Four holes were drilled at this site (Table T1). Hole U1352A was cored with the advanced piston corer (APC) system to 42.2 m drilling depth below seafloor (DSF) with the objective of providing whole-round samples for microbiology, chemistry, and geotechnical studies. Hole U1352B was cored with the APC/extended core barrel (XCB) coring system to XCB refusal at 830.9 m DSF. Hole U1352C was drilled and cored with the rotary core barrel (RCB) system to the target, record depth of 1927.5 m DSF. Hole U1352D was cored with the APC system to 127 m DSF while we waited for the weather to improve before transiting to the next site.

Logging was attempted with partial success in Holes U1352B and U1352C. The third-generation advanced piston corer temperature tool (APCT-3) was deployed five times with good results. Overall recovery for Site U1352 was 102% with the APC, 59% with the XCB, and 51% with the RCB. The total cored interval for Site U1352 was 2296.5 m, and total recovery was 1444.1 m (63%).

Rig floor operations commenced at 0500 h on 30 November when the vessel shifted to DP control and ended at 2100 h on 21 December when the vessel was secured for transit.

Hole U1352A

The bottom-hole assembly (BHA) was made up with an APC/XCB bit, and coring in Hole U1352A began at 1145 h on 30 November. The mudline was established at 354.8 m drilling depth below rig floor (DRF) (343.8 meters below sea level [mbsl]). APC coring continued through Core 317-U1352A-5H (42.2 m DSF), using nonmagnetic coring assemblies. Core orientation was measured on all cores, and a temperature measurement was taken with Core 317-U1352A-4H. Contamination testing was done on all cores with perfluoromethylcyclohexane (PFT) and microspheres. A total of 43.92 m of core was recovered from Hole U1352A (104%). The drill string was pulled back to the seafloor, and the bit cleared the seabed at 1530 h on 30 November, officially ending operations in Hole U1352A.

Hole U1352B

The vessel was offset 20 m south of Hole U1352A, and Hole U1352B was piston cored to Core 317-U1352B-36H at 297.0 m DSF, with a total recovery of 298.85 m (101%). Core orientation was measured with the Flexit tool on the first 17 cores before the tool was pulled because of more severe piston coring conditions. The XCB coring system was deployed for Cores 317-U1352B-37X through 94X (297.0–830.9 m DSF). Recovery with the XCB system was very good to ~500 m DSF. Below that depth, a steadily increasing number of cores had poor recovery. A total of 533.9 m was cored, and 315.02 m was recovered (59%). Toward the bottom of the hole, the XCB cutting shoe overheated and the formation caused excessive torque. The risk of damaging the core barrel was too high to continue with the XCB system. A 50 bbl high-viscosity mud sweep was pumped to clean the hole.

The drill string was tripped back to 80 m DSF, and the triple combination (triple combo) logging tool string was rigged up and run into the hole (RIH). The first logging run failed to pass 487 m wireline log depth below seafloor (WSF) because the hole evidently had collapsed during logging preparations. Two passes were successfully recorded. The caliper readings indicated that the borehole was too large to allow an adequate clamp for the Versatile Seismic Imager (VSI) tool to obtain reliable data, so the vertical seismic profile (VSP) plan was canceled. The Formation MicroScanner (FMS)-sonic tool string was subsequently deployed, and it also encountered a borehole obstruction, this time somewhat higher in the hole. FMS-sonic logs were recorded from 442 m WSF. After the logging tools were rigged down, a 12 bbl cement plug was pumped at 154.4 m DSF. The drill string was tripped back to the surface and cleared the rotary table at 1615 h on 5 December, ending operations in Hole U1352B.

PFT and microspheres were deployed every ~50 m throughout Hole U1352B for microbiological contamination testing. Temperature measurements with the APCT-3 tool were taken with Cores 317-U1352B-6H, 10H, 15H, and 20H. All temperature measurements had good decay curves. The cored interval in

Hole U1352B was 830.9 m, and total recovery was 613.87 m (74%).

Hole U1352C

The ship was offset 20 m south of Hole U1352B, and operations in Hole U1352C began with the makeup of a new BHA for the RCB system, which was fitted with a mechanical bit release to facilitate logging after coring was completed. Drilling in Hole U1352C began at 2015 h with a center bit installed. At ~300 m DSF, the center bit was recovered, inspected, and reinstalled. The hole was then advanced to 574.7 m DSF, at which point the center bit was pulled and an RCB was dropped. The hole was cored with the RCB system from 574.7 to 603.6 m DSF (Cores 317-U1352C-2R through 4R), and 12.79 m of core (44%) was recovered. The center bit was reinstalled, and drilling continued to 660.0 m DSF. The center bit was again pulled, and rotary coring resumed for Cores 317-U1352C-6R through 41R (660.0–1009.9 m DSF), with 20 bbl high-viscosity mud sweeps every 50 m of coring to clean the cuttings from the hole. At 1900 h on 8 December, a 50 bbl sweep was pumped and a wiper trip of the drill string was made from 1007 to ~200 m DSF and back. Coring resumed ~8 h later for Cores 317-U1352C-42R through 118R (1009.9–1661.5 m DSF), with sections of good and poor recovery. The deplugger was run, and coring intervals were reduced to 5 m several times in attempts to improve core recovery. On 15 December at 2030 h, a 50 bbl sweep was pumped and a wiper trip of the drill string was made from 1662 to ~1000 m DSF and back; coring resumed ~7 h later. The interval for regular 20 bbl hole cleaning mud sweeps was decreased to 40 m.

On 17 December, it became evident that the scientific target for the hole, the Marshall Paraconformity, was deeper than anticipated. Permission was requested and received to exceed the original EPSP limit of 1913 m DSF by up to 250 m (to 2163 m DSF). The Marshall Paraconformity was recovered in Core 317-U1352C-140R (1851–1861 m DSF) on 18 December. Coring continued to Core 317-U1352C-148R (1927.5 m DSF) in order to provide sufficient depth to log across the Marshall Paraconformity. The last core from Hole U1352C was received on deck at 1740 h on 19 December.

Starting at 796 m DSF, PFT and microspheres were deployed at ~50 m intervals throughout Hole U1352C for microbiological contamination testing.

The penetration depth of 1928 m for Hole U1352C established a new single-bit, single-expedition record for the *JOIDES Resolution* and made Hole U1352C the deepest sediment hole ever drilled by IODP or its predecessor programs. The cored interval in Hole U1352C was 1296.4 m, with 655.02 m of core recovered (51%).

The hole was swept clean with a 50 bbl sweep of high-viscosity mud, the RCB coring bit was released, and the drill string was tripped out to ~900 m DSF. The top drive was picked back up, and 400 bbl of high-viscosity logging mud was displaced into Hole U1352C. The top drive was set back, and an attempt was made to continue the trip out of the hole. After one stand, excessive drag required the top drive to be reinstalled, and the trip out of the hole continued with rotation until the end of the string reached 545 m DRF. The top drive was then set back and the drill string was pulled back to 439 m DRF. The upper guide horn was removed, and the vibration-isolated television (VIT) camera was deployed to observe and document the cone of cuttings at the seafloor during logging. The drill string was set to a logging depth of 458 m DRF. The logging string was rigged up to run a modified version of the triple combo tool string. The first logging run indicated that the hole had collapsed, and the tool string was unable to pass 207.5 m WSF. The tool string was pulled back to the surface and rigged down. The drill string was tripped back to the surface, clearing the rotary table at 2200 h on 20 December, ending Hole U1352C.

Hole U1352D

When operations in Hole U1352C concluded, the winds and swells were too high to begin operations at the next site, which was in extremely shallow (<100 m) water. We anticipated a weather delay of ~24 h and decided to core Hole U1352D. An APC/XCB assembly was made up, and piston coring in Hole U1352D began at 0615 h on 21 December and continued through Core 317-U1352D-14H (0–127.0 m DSF). Core recovery totaled 130.84 m (103%).

Nonmagnetic coring assemblies were used, and core orientation was measured on all cores.

The drill string was pulled back to the rotary table, the BHA was racked back, and the rig floor was secured for transit at 2100 h on 21 December, ending Hole U1352D and Site U1352.

Lithostratigraphy

Four holes were drilled at Site U1352, reaching a total depth of 1927 m core depth below seafloor (CSF-A; unless otherwise noted, all depths in this section are reported in m CSF-A) and spanning the Holocene to late Eocene. APC drilling was used in Holes U1352A and U1352B to 297 m and in Hole U1352D for the entire cored interval. XCB drilling was used

in Hole U1352B to 822 m (total depth), and RCB drilling was used in Hole U1352C.

The succession was divided into three lithologic units (Table T2; Figs. F3, F4). Recovery was variable, ranging from an average maximum of 103% in Subunit IA (Holes U1352A, U1352B, and U1352D) to 38% in Subunit IIA (15% in Hole U1352B and 43% in Hole U1352C). Subunit IB had an average recovery of 97%, whereas recovery for Subunit IC averaged 45% (15% in Hole U1352C and 60% in Hole U1352B). The remaining units occur only in Hole U1352C, where Subunit IIB averaged 53% recovery, Subunit IIC averaged 67%, and Unit III averaged 54%.

Unit I spans the Holocene to middle Pliocene and contains predominantly mud-rich sediment consisting of calcareous sandy mud; interbedded sand, mud, and clay; massive sand; mottled sandy mud; homogeneous mud; shelly mud; and marl.

Although the boundary between Units I and II was placed at 710 m, the lithologic transition between Units I and II is gradual, reflecting a progressive change in water depth to deeper slope depositional environments. Unit II spans the middle Pliocene through early Miocene and contains hemipelagic to pelagic sediment consisting of calcareous sandy mud, sandy marls, chalk, sandy marlstone, and sandy limestone, with minor amounts of calcareous mudstone and sandstone. Unit II contains a gradual progression from uncemented calcareous sandy mud and marl to lithified marlstone and limestone. Notably, this unit generally lacks clay-sized material, except in discrete mudstone beds present in the lower half of the unit. Glauconitic laminae and layers also occur in the lowermost part of this unit. Packages of recumbent and isoclinal folds, tilted beds, contorted strata, and fluid escape features are present within the middle portion of Unit II.

A hiatus representing ~12 m.y. occurs at the base of Unit II at 1853 m, where there is an abrupt change to lithologic Unit III, which is composed of hemipelagic to pelagic foraminifer-bearing nannofossil limestone of early Oligocene to late Eocene age. Except for minor abundances of quartz and clay minerals, Unit III lacks siliciclastic components. This unit is correlative with the onshore Amuri Limestone.

Site U1352 represents a late Eocene to early Oligocene and nearly complete Neogene continental slope sedimentary record dominated by pelagic to hemipelagic sedimentation with minor traction and gravity-flow sediments. The gradual downhole transition in lithofacies from more siliciclastic rich Pleistocene to Holocene muddy facies into pelagic limestones and glauconitic marls and marlstones appears to reflect the transition seen on seismic profiles from an upper-slope location on a clinoformal margin with a sharp shelf-slope break in the Pleistocene to Holocene toward a toe-of-slope to basin-floor position on a more ramplike margin in the Miocene (Lu and Fulthorpe, 2004).

Like those at other Expedition 317 sites, the lithologic units defined at Site U1352 exhibit gradual changes downhole, making definition of unit boundaries difficult. Lithologic units (Table T2) were defined primarily by their lithologies and, importantly, by the repetitive assemblages of facies that occur in each unit. The boundaries between units and subunits were chosen based on these criteria and not, in general, on correlation to any other data set (such as whole-round physical property measurements or downhole logs). However, in intervals of relatively poor recovery, such data sets were used in conjunction with lithologic logs and percentages to determine the locations or depth ranges of unit boundaries. Note that downhole logs exist only for the uppermost 487 m of Hole U1352B and for the uppermost 207 m of Hole U1352C because of hole cave-in below these depths (see **"Downhole logging"**).

Description of lithologic units

Unit I

Intervals: Cores 317-U1352A-1H through 5H; 317-U1352B-1H through 81X; and 317-U1352C-2R to Section 11R-1, 92 cm
Depths: Hole U1352A: 0–43.11 m (total depth); Hole U1352B: 0–710.78 m; and Hole U1352C: 574.7–709.32 m
Age: Holocene to mid-Pliocene

Unit I is divided into subunits according to the occurrence of two sandy lithologies. The first subunit boundary (IA/IB) is placed at 98 m, below which sharp-based, thin gray sand beds are absent. The second subunit boundary (IB/IC) is placed at 447 m to mark the first downhole occurrence of thick gray-green calcareous muddy sand beds, which become sandy marls with >30% carbonate content toward the base of the unit.

Subunit IA

Intervals: Cores 317-U1352A-1H through 5H and 317-U1352B-1H to Section 11H-4, 23 cm
Depths: Hole U1352A: 0–43.11 m (total depth) and Hole U1352B: 0–98.41 m
Age: Holocene to Pleistocene

Subunit IA is dominated by homogeneous mottled and interbedded mud facies that generally contain a few percent of very fine sand, often with thin clay-

rich intervals (Figs. F5, F6). Sand beds occur either as thin, very fine to fine, dark gray, sharp-based beds on a scale of a few centimeters or as thin to thick, sharp-based, shelly, greenish very fine to fine muddy sand or sandy mud (Fig. F7). The mud is gray and sometimes mottled or color banded and has either abundant shells (including *Tawera*, *Chlamys patagonica delicatula*, and other bivalve, gastropod, barnacle plate, bryozoa, and worm tube fragments) or is devoid of shells (especially in intervals of interbedded mud, sand, and clay). The alternation between shelly and nonshelly mud beds occurs on a scale of 10–40 m. Deformation occurs in the uppermost 20 m of Subunit IA, including normal faulting (interval 317-U1352A-2H-2, 0–50 cm) and folding (intervals 2H-4, 99–130 cm, and 317-U1352B-2H-3, 10–57 cm) (Fig. F8). The ichnofabric index ranges from 1 to 5 but is typically moderate to complete (3–5) in the mud intervals. The thin gray sand beds are generally not bioturbated, although sand-filled burrows sometimes extend a few centimeters below their sharp basal contacts (e.g., Section 317-U1352B-5H-3, 102 cm).

Subtle changes occur within this subunit. At the top of Hole U1352A and in Cores 317-U1352B-1H through 7H there is a marked alternation between green calcareous muddy sand or sandy mud facies and thicker beds composed of gray clay-rich mud beds alternating with sharp-based, thin dark gray sand beds with sand-filled burrows below (Fig. F9). The boundaries of these beds are very distinct, although they are often deformed by drilling (Fig. F8). Below Core 317-U1352B-7H the boundaries of the clay, mud, and thin sand beds are no longer distinct, but individual beds can still be identified. The lack of distinct bedding contacts is presumably the result of increased bioturbation. Below Section 317-U1352B-11H-3, green sand beds are less common, and the thin gray sand beds that occur frequently within the interbedded mud and clay above are absent. Section 317-U1352B-11H-3 also marks a change in magnetic susceptibility logs, with an apparent baseline shift from higher to lower values across the Subunit IA/IB boundary.

Mineralogy from smear slides in Subunit IA shows that the dominant detrital components are quartz, feldspar, rock fragments, mica (dominated by muscovite; see **"Site U1352 smear slides"** in "Core descriptions"), ferromagnesian minerals (e.g., hornblende), and dense minerals (e.g., epidote and zircon). The authigenic fraction is dominated by pyrite in the upper part of the succession and by microcrystalline carbonate in the lower part of the succession and in cemented zones. The percentage of carbonate components is generally characterized by a wide range of values in Subunit IA, with especially high values in smear slides taken from localized yellow patches within the muddy units (partly cemented burrow fills). The carbonate content of smear slides appears to decrease downhole from the mudline and then increase toward the base of Subunit IA (Fig. F10). Rock fragments observed in this subunit represent a range of lithologies, including grains of siltstone, sandstone, and foliated metamorphic rocks (phyllite and schist), as well as indeterminate rock fragments. Biogenic components are composed dominantly of foraminifers, nannofossils, and undifferentiated or highly altered, abraded, or fragmented bioclasts.

A thin section of a burrowed lithified concretion in interval 317-U1352B-2H-2, 32–34 cm, contains subequal amounts of quartz, feldspar, sedimentary to metasedimentary rock fragments, and mica grains locally suspended in a micritic to clay-rich matrix. The shallow depth of this concretion (10 m) suggests a very early precipitation of authigenic carbonate, perhaps in association with methanogenesis.

X-ray diffraction (XRD) analyses of samples selected from the dominant lithologies show that in Subunit IA peak intensities of quartz and total clay are relatively high, whereas calcite is largely zero (Fig. F11; see also XRD in **"Supplementary material"**). In this subunit, the micas (muscovite/biotite) and chlorite have relatively low, constant peak intensities with depth relative to their intensities in the rest of the hole. Plagioclase is variable and is not correlated with quartz, as it is at Site U1351, and hornblende is relatively low. Siderite is present in trace amounts, but no appreciable pyrite or dolomite was observed.

Subunit IB

Interval: Sections 317-U1352B-11H-4, 23 cm, to 53X-1, 18 cm
Depth: 98.41–446.88 m
Age: Pleistocene

Subunit IB is dominated by gray to greenish gray and dark greenish gray mud containing rare to locally abundant shells; these shells become less abundant and occur as broken fragments with depth. Decimeter-thick, greenish gray, calcareous very fine to fine sand, sandy mud, and muddy sand are intercalated with the mud, the latter typically forming fining-upward packages. Shells are also commonly associated with the basal boundaries of green calcareous muddy sand beds. These sharp basal surfaces of greenish gray calcareous sandy mud or muddy sand beds are often clustered, occurring as frequently as three times in one core (e.g., Cores 317-U1352B-16H, 23H, and 28H), separated by thicker uninterrupted gray mud beds. Burrows often extend ~50 cm below the base of the graded sand beds. Shells include bivalves

(including *Chlamys patagonica delicatula*), gastropods, echinoid spines, serpulid tubes, coral (*Flabellum*), and foraminifers. The alternating lithologies change below a sharp-based green sandy marl in Section 317-U1352B-37X-2, becoming dominated by color-banded mud with only very thin green sandy layers. The green sandy layers at the base of each fining-upward succession become increasingly calcareous throughout Subunit IB. Below Core 317-U1352B-35H, very dark greenish gray, poorly sorted very fine to medium sandy marls first appear. These become more frequent with depth, as indicated by smear slide data. Calcareous nodules occur throughout this subunit and are relatively common below 350 m. The ichnofabric index ranges from no bioturbation to heavy bioturbation (1–4), and identifiable traces include *Thalassinoides*.

Smear slide analysis of Subunit IB reveals components similar to those found in Subunit IA, although with higher carbonate percentages (Fig. **F10**). The highest carbonate values occur close to the base of Subunit IB, between 380 and 440 m. Smear slide data through Subunit IB document an increase in siliceous biogenic components (diatoms, siliceous sponge spicules, and other minor siliceous debris) in tandem with increasing carbonate content (Fig. **F10**) to a depth approaching 300 m. Below 300 m, siliceous components are less common, although they are present throughout the remainder of Subunit IB. Below ~205 m, micrite is a common component in smear slides. Below 350 m, concretions or nodules are relatively common; notably, this depth also coincides with the start of an increasing trend in calcium concentration in interstitial water analysis (see **"Geochemistry and microbiology"**).

Thin sections of lithified intervals in Subunit IB have variable lithologies (see **"Site U1352 thin sections"** in "Core descriptions"). The most numerous stratigraphic examples are concretions similar in texture to those found near the top of Subunit IA (intervals 317-U1352B-16H-4, 130–134 cm; 17H-4, 69–72 cm; and 21H-1, 0–2 cm; Fig. **F12A**). These concretions contain bioturbated, micritized marlstone (muddy limestone) with sparse, angular silt- to sand-sized terrigenous components, organic debris, and bioclasts (including echinoderm fragments); degraded and micritized foraminifers; and molds of dissolved mollusks. Localized concentrations of pyrite were found within burrows and moldic pores. Lower in Subunit IA, the lithified intervals are more variable and lithification appears to be related to a combination of compaction and cementation rather than micrite formation within the matrix. Some samples are foraminiferal limestones (e.g., Sample 317-U1352B-35H-2, 40–41 cm [294.7 m]) having textures that vary between grain (foraminifer) and matrix supported (e.g., Sample 42X-5, 5–7 cm [347 m]; Fig. **F12C**). Textural variations in the latter sample are related to bioturbation, and platy fossil fragments show no preferred orientation. This sample also contains evidence of significant compaction. Additionally, glauconite is more prevalent, occurring as a pale green fill in foraminifer tests, as well as in darker green discrete lobate pellets, alteration products of biotite, and likely some epigenetic glauconite in the matrix. The lowermost thin section in the subunit is of a matrix-rich, burrowed marlstone containing a mixture of diagenetic and compactional features.

The interval from 280 to 300 m contains some unusual lithologies in the cores, including a >3 m thick bed of shelly sand that was partly liquefied during the coring process (Sections 317-U1352B-32H-5 through 33H-1) and a sandy marl bed (Sections 36H-2 through 37X-2). In addition to high values of carbonate content, estimates from smear slide and XRD data reveal marked fluctuations in mica, quartz and feldspar, glauconite, and clay between 250 and 300 m (Figs. **F10, F11**). As at Site U1351, the relative intensity of the calcite peak correlates with the total calcium carbonate concentration determined by coulometry, indicating that calcite is the dominant carbonate mineral. However, minor amounts of Mg calcite and aragonite based on peak heights were also observed, always co-occurring with calcite (e.g., Sample 317-U1352B-32H-CC, 53–55 cm).

XRD data show a distinct mineralogical transition within Subunit IB (Fig. **F11**). Quartz content determined from XRD analysis is significantly lower ($p = 0.05$ for this and other t-tests and correlations) below the Subunit IA/IB boundary, which is matched by a decrease in sand content, as seen in smear slides. Additionally, quartz content decreases significantly within Subunit IB below ~250 m; this trend is also observed in smear slides. Plagioclase remains fairly constant within this subunit, but, in contrast to Subunit IA, a significant correlation ($N = 40$) exists between quartz and plagioclase. Total clays remain relatively high with no apparent depth trends, as also seen in smear slides, but mica and hornblende increase significantly below the Subunit IA/IB boundary, with the increase in mica supported by smear slide observations. Calcite peak intensity also significantly increases below the Subunit IA/IB boundary, supported by both coulometry and smear slide observations. Pyrite and siderite peak intensities are highest in Subunit IB, especially below 250 m. Dolomite was infrequently observed, with peak highs close to detection limits.

Subunit IC

Intervals: Section 317-U1352B-53X-1, 18 cm, through Core 81X and Core 317-U1352C-2R to Section 11R-1, 92 cm
Depths: Hole U1352B: 446.88–710.78 m and Hole U1352C: 574.7–709.32 m
Age: Pleistocene to mid-Pliocene

The top of this subunit was placed at the top of a 6.5 m thick bed of sandy marl, marking the top of an interval of ~40 m where this lithology is dominant. Below this, core recovery in Hole U1352B dropped dramatically, with the recovered intervals containing homogeneous mud (largely lacking in shells), calcareous sandy mud and sandy marl, and sandy marlstone. Many of these sandy mud and sandy marl beds fine upward. Recovery from Hole U1352C (starting at 574.7 m) was also poor; however, the cores from this hole contain largely lithified intervals, generally of very fine sandy marlstone (with scattered small shells, including foraminifers). Bioturbation is particularly evident in the sandy marlstones (ichnofabric index of 1–4, where sediments without recognizable depositional structures were recorded as 1). Poor recovery in Hole U1352B may be caused by the intermittent presence of lithified layers composed of thick sandy marlstone between layers of unlithified sandy marl and homogeneous mud.

The quartz, feldspar, and mica mineralogy in Subunit IC, as estimated from smear slides, is similar to that of Subunits IA and IB, with higher and more variable average carbonate concentrations and therefore lower percentages of other minerals (Fig. **F10**). The presence of shells in the muddy sediments and sedimentary rocks below ~575 m is extremely rare. All mineral percentage estimates are highly variable throughout Subunit IC, which distinguishes this subunit somewhat from Subunits IA and IB and Unit II. This high variability is also reflected in XRD data (Fig. **F11**). Glauconite is more common toward the top of Subunit IC and decreases in concentration downhole. The proportion of siliceous bioclasts increases toward the base of the subunit before dropping markedly in the unit below.

Seven thin sections were prepared from Subunit IC. One thin section (Sample 317-U1352B-72X-CC, 27–29 cm) contains micritic limestone/marlstone and is compositionally and texturally very similar to concretions observed at the top of the hole in Subunit IA, which is likely attributable to downhole contamination. Three other thin sections show slightly different microfacies from those described in Subunit IB: Samples 317-U1352B-54X-4, 4–6 cm (~459 m); 65X-1, 14–17 cm (~563 m); and 317-U1352C-4R-5, 52–54 cm (~600 m). In general, these microfacies are finer grained and better sorted and have a smaller, better sorted population of bioclasts. The sand fraction is mainly quartz, feldspar, mica, chlorite, and dense minerals. These samples have variable amounts of calcareous matrix and no distinct lamination, and they are somewhat homogenized by bioturbation, with rare large (centimeter scale) discrete burrows.

The low core recovery in Subunit IC hampered a detailed analysis of depth trends in XRD mineralogy (Fig. **F11**). In general, this subunit can be characterized as having no clear trends with depth in the minerals discussed above, although there is a notable increase in the variance of all these minerals. Quartz, total clays, and micas co-vary and appear to be inversely related to calcite content. Interestingly, quartz and plagioclase are not well correlated, as was also the case in Subunit IB. Calcite has the highest peak intensities of Unit I within this interval, which is also supported by both coulometry and smear slide observations. Pyrite and siderite peak intensities are highly variable, and dolomite was not observed.

Unit I/II boundary

As at other Expedition 317 sites, the Unit I/II boundary is transitional. All of Subunit IC represents a transition between Unit I and Unit II lithologies, marked by increasing percentages of carbonate and decreasing amounts of clay (Fig. **F11**), although the noncalcareous homogeneous mud common in Subunits IA and IB occurs as deep as Core 317-U1352B-74X. The Unit I/II boundary was placed at the bottom of Core 317-U1352B-81X (and at the base of Section 317-U1352C-11R-1) at the base of calcareous muddy sand where (1) an abrupt change of baseline occurs in magnetic susceptibility and gamma ray whole-round measurements (see **"Physical properties"**), (2) the chemistry of interstitial water analyses shows a local peak (see **"Geochemistry and microbiology"**), and (3) the analysis of XRD mineralogy data shows a major shift in composition from clay-dominated to carbonate-dominated lithologies. When total clays are normalized to calcite to account for carbonate-dilution effects, clay content decreases notably downhole beginning at 709 m (Fig. **F13**). Similar increases in magnetic susceptibility and natural gamma ray data were observed at the same depth (see **"Physical properties"**). Below this depth, sediments are carbonate dominated and clay content only occasionally increases.

Unit II

Intervals: Cores 317-U1352B-81X through 94X and Sections 317-U1352C-11R-1, 92 cm, to 140R-2, 47 cm
Depths: Hole U1352B: 710.78–822.13 m (total depth) and Hole U1352C: 709.32–1852.63 m
Age: middle Pliocene to early Miocene

Unit II is dominated by homogeneous calcareous sandy mud or sandy marl (uncemented intervals) and sandy marlstone (cemented intervals) throughout Holes U1352B and U1352C. Subtle differences in Hole U1352C allow for unit subdivision based on the presence of dark muddy intervals (noncalcareous), current-generated structures, and laminated sandstone beds in Subunit IIB, as opposed to the more thorough degree of bioturbation present in Subunit IIA and the presence of glauconite-rich beds in Subunit IIC (Fig. **F14**).

Subunit IIA

Intervals: Cores 317-U1352B-81X through 94X and Sections 317-U1352C-11R-1, 92 cm, to 61R-1, 30 cm
Depths: Hole U1352B: 710.78–822.13 m (total depth) and Hole U1352C: 709.32–1189.30 m
Age: middle Pliocene to early Pliocene

Subunit IIA is dominated by dark greenish gray to greenish gray homogeneous sandy marlstone along with the less lithified sandy marl recovered in Hole U1352B. Subordinate lithologies such as calcareous very fine sandy mud, muddy sand, mud, and mudstone were recovered from both holes. The partially to fully lithified sandy marl and sandy marlstone were heavily bioturbated, and *Chondrites, Helminthopsis, Terebellina, Scolicia, Planolites, Zoophycos,* and *Thalassinoides* ichnogenera were identified in the lithified layers. The ichnofabric index for Hole U1352B cores is generally 1 (partly because drilling overprint obscured the ichnofabric), but in Hole U1352C it ranges between 1 and 5 (typically 3–4). Distinct bedding planes are not visible; however, in some intervals the overprinting of shallow and deeper trace fossils (e.g., *Thalassinoides* over *Chondrites*) suggests erosion or other changes at the sediment/water interface (Fig. **F15**). Shells are extremely rare or are absent in the lower part of Subunit IIA and include fragments of bivalves, brachiopods, and foraminifers. Small ovoid crystalline calcareous fragments or "blebs" first occur in Core 317-U1352C-38R. Calcareous concretions occur sporadically throughout the subunit.

Although variable, carbonate content is more uniform in Subunit IIA than it is in overlying units, and estimated percentages from smear slide observations range generally between 10% and 40% (Fig. **F10**). Rare outliers, estimated from smear slide observations at >70% (chalk or limestone) carbonate, occur in discrete, paler (light greenish gray) intervals (note that coulometry analyses are not generally available from these minor lithologies). The percentage of carbonate components appears to increase downhole in the uppermost 200 m of Unit II, and values below 900 m seem to fall largely between 30% and 60% carbonate based on smear slide estimations (15%–50% based on coulometry data; Fig. **F10**). Mica percentages from smear slide and XRD data appear in general to be higher than values in Unit I, whereas clay concentrations are lower. Both glauconite and siliceous bioclastic material become extremely rare with depth. The percentage of ferromagnesian minerals is generally very low throughout Subunit IIA.

Subtly different facies, such as paler greenish gray layers, begin to appear at ~1026 m (Core 317-U1352C-44R) and become more common with depth. These paler intervals, also bioturbated, are generally more cemented and occasionally contain >70% carbonate (estimated from smear slide observation), placing them in the chalk or limestone classification (Fig. **F15**). The dominant lithotype continues to be dark greenish gray very fine to fine sandy marlstone, but the pale layers give the rock a color-banded appearance in some places (e.g., Core 317-U1352C-44R). In addition to these paler layers, sandy laminae, sand lenses, and wavy or ripple laminae are occasionally present in the cores, increasing in frequency downhole.

Thin sections from Subunit IIA contain distinctly microburrowed marlstone facies. Although the overall composition is marlstone to sandy marlstone, lighter trace-fossil fills and laminae observed in cores were seen in thin section to be arkosic, micaceous, and bioclastic siltstone to fine sandstone that is variably cemented by carbonate or that contains calcareous matrix. Darker burrow fills are mainly calcareous marlstone, a combination of carbonate (nannofossils and/or micrite) and clay with traces of organic matter. Minor terrigenous components include phyllite lithic fragments, glauconite, and dense mineral grains. A few samples contain higher percentages of siliceous debris, including diatoms and sponge spicules, the latter locally concentrated in burrows (e.g., Sample 317-U1352C-11R-2, 21–23 cm). Some samples contain a higher proportion of clay and organic-rich matrix (e.g., Sample 317-U1352C-40R-3, 2–3 cm). Diagenesis is limited to carbonate cementation and pyrite formation as both pore-filling cement and grain replacement, as well as replacement of opaline sponge spicules by birefringent chert/quartz.

Based on XRD analysis, the mineralogy of Subunit IIA is similar to that of Subunit IC, with relatively

moderate to high amounts of quartz, micas, and plagioclase feldspars relative to the remainder of the succession (Fig. F11). These mineral groups have no overall trend with depth but do have pronounced variability with depth in this subunit. Total clays are highest near the top of the subunit and decrease from 660 to ~800 m within Hole U1352B. Hornblende is relatively low and variable. Calcite is lowest near the top of the subunit and increases slightly from 660 to 800 m, below which it has no trend with depth but reveals the same pattern of variability shown by silicate minerals, with the relative amount of silicates inversely proportional to the amount of calcite (significant at p = 0.05). The micas (muscovite/biotite) and chlorite are highly positively correlated (R = 0.92), and quartz and the micas are positively correlated, with a stronger correlation between quartz and chlorite (R = 0.4). Plagioclase and quartz abundances do not correlate in Subunit IIA, as was also the case in Subunit IC. XRD mineralogy and smear slide observations agree well, with both showing fluctuating trends in micas and sand, a relative decrease in clays, and an increase in carbonate content near the top of the subunit.

Subunit IIB

Interval: Sections 317-U1352C-61R-1, 30 cm, to 123R-1, 142 cm

Depth: 1189.30–1693.92 m

Age: early Pliocene to late early Miocene

Darker gray and brown lithologies appear in the succession below 1170 m (Fig. F15). Sandy marlstone is the dominant lithology, along with subordinate dark gray, centimeter-thick, bioturbated very fine sandy mudstone beds and centimeter-thick, horizontally laminated fine sandstone. Based on smear slide observations, the latter lithologies are calcareous to noncalcareous but are uniformly less calcareous than the sandy marlstone. The Subunit IIA/IIB boundary was placed at the base of an irregular surface that separates lighter (above) from darker (below) very fine sandy marlstone. Below this boundary, distinct dark brown mudstone beds are more common and are associated with more frequent sandstone beds, wavy laminations, ripples, and sand lenses. Ferromagnesian minerals disappear from smear slides below Core 317-U1352C-62R (1204 m) and are below detection in XRD analyses from approximately Core 317-U1352C-59R (1170 m) and below.

Subhorizontal wavy laminae marked by millimeter-thick, brownish very fine sandy mudstone are increasingly more frequent downcore, becoming prominent from Core 317-U1352C-70R downhole. Below Core 317-U1352C-110R, these laminae are frequently intercalated with lighter gray sandy marlstone, which sometimes gives the rock a dark–light pin-striped appearance (Fig. F15F–F15G). Millimeter-diameter white calcareous blebs were observed throughout the marlstone. Light blue-gray sand-filled burrows are common within the marlstone, particularly in the lower portion of the subunit. Bioturbation is abundant throughout Subunit IIB, ranging between 1 and 5 (mostly 3–4) on the ichnofabric index, and includes traces of *Zoophycos, Planolites, Chondrites, Thalassinoides, Paleophycus, Helminthopsis, Terebellina, Scolicia,* and *Teichichnus*.

The Pliocene/Miocene boundary occurs within Core 317-U1352C-73R, probably either at the top or the base of a distinctive paler calcareous unit, the sharp top of which occurs at Section 73R-2, 33 cm (1276.83 m), and the sharp and bioturbated base of which occurs at 73R-4, 20 cm (1279.7 m) (see **"Biostratigraphy"**).

In Sections 317-U1352C-88R-1 through 88R-4 (1371–1376 m), 94R-CC through 95R-1 (1437–1439.5 m), and 105R-2 through 106R-5 (1528–1541 m), variable stratification attitudes, folding, shells, and a greater proportion of carbonaceous material mark several distinct stratigraphic intervals containing mass-transport complexes (slumps) that often include internal planar surfaces that divide areas with different deformation characteristics or bedding angles (Fig. F16).

The common occurrence of dark brown muddy layers stops in Core 317-U1352C-90R (1392 m), although these layers continue to occur sporadically downhole, and a notable change in mineralogy occurs at ~1400 m, as indicated by XRD analyses (Fig. F11). These changes may be associated with a hiatus observed in Core 317-U1352C-91R that is possibly associated with a highly carbonate rich layer at 1409.12 m (Section 91R-7, 73 cm), where the faunal age changes (between Sections 90R-CC and 91R-CC) from latest Miocene to early late Miocene (upper Kapitean to lower Tongaporutuan, ~5.30–11.01 Ma; see **"Biostratigraphy"**).

Carbonaceous material is rare near the top of Unit II, appears more frequently below 1400 m in association with the slumped material mentioned above, and appears again in greater concentration in dark brownish gray layers in Cores 317-U1352C-110R and 111R (1575–1590 m). Glauconite is a common constituent below Core 317-U1352C-105R, where a graded bed has a glauconitic basal layer.

A banded appearance becomes evident in Core 317-U1352C-113R (1603 m) and below. Distinctly wavy, darker gray layers (laminae to thin beds) alternate with greenish gray very fine sandy marlstone layers (Fig. F15). The darker layers are commonly finer and have the appearance of incipient stylolites (although

little dissolution appears to have occurred across these surfaces). This banding increases in intensity with depth, and glauconite begins to appear at low concentrations in the marlstones in Core 317-U1352C-117R.

The major minerals of Subunit IIB, as indicated by XRD analyses, are similar to those of Subunit IIA, with the exception of hornblende, which was not observed apart from trace amounts in two samples, and quartz, which decreases significantly in this unit, especially below 1400 m (Fig. **F11**). Micas (and chlorite) and plagioclase gradually decrease from the top of the subunit to 1400 m and then increase notably to a maximum for this subunit at ~1550 m, below which they decline throughout the remainder of the subunit. Total clays are also higher within this subunit, especially in the uppermost part. Below 1580 m, clays were not detected by XRD. As in Subunit IIA, micas and chlorite are positively correlated and total clays and calcite are inversely correlated; however, there is no correlation between total clays and micas, micas and quartz, or quartz and plagioclase.

Thin section observations show that Subunit IIB contrasts with the overlying subunit in having more matrix in its upper part and mainly a sandy marlstone lithology and some marlstone lithologies. No other difference in the types or ratios of components between Subunits IIA and IIB were observed. Siliceous sponge spicules, organic debris (plant matter), and phosphatic debris (fish remains and fecal pellets?) are also present. In the upper part of Subunit IIB, the matrix is a mixture of nannofossils and clay that changes to micrite and clay below Section 317-U1352C-78R-1 (1314 m). Most samples are bioturbated, but original laminations composed of alternating matrix-rich and well-sorted matrix-poor laminae are locally preserved. The latter are slightly coarser and are carbonate cemented locally by poikilotopic calcite crystals (Sample 317-U1352C-90R-1, 0–3 cm). Sand and silt grains are generally angular.

Differential compaction is evident between more competent cemented zones (usually better sorted burrow fills) and less competent muddy zones. Longer mica flakes are bent and fractured across more competent grains. Evidence for pressure solution is more pronounced within and below Sample 317-U1352C-95R-6, 39–42 cm (1447 m), where glauconite and phosphatic and organic debris are more common. In particular, compaction (fracturing and interpenetration) and truncation (press-solved boundaries) of foraminifers were observed. Dark seams visible in the core were shown to be created by aligned and compacted platy organic matter, which organic geochemical analyses indicate to be of terrestrial origin (see **"Geochemistry and microbiology"**). The irregular and stylolitic appearance of the seams is a result of differential compaction around more competent grains, as well as some apparent pressure solution. Note that the more calcareous samples below this interval (e.g., Cores 317-U1352C-114R, 116R, and 118R) show evidence for pressure solution only where minor organic matter is present.

Opaline siliceous sponge spicules are variably preserved and locally replaced by silica (chert) and microcrystalline calcite. In some samples (e.g., Cores 317-U1352C-70R and 89R), all three phases, original opal, and secondary chert or carbonate are present. Carbonate cement is present throughout as intraparticle filling of foraminifer chambers and as interparticle filling in better sorted grainstone/siltstone/sandstone laminae and burrow fills. Zeolites were observed as pore-filling cement in foraminifer chambers in thin sections from Cores 317-U1352C-112R and 113R. Zeolite crystals are locally encased by later carbonate cement, indicating that they were an earlier diagenetic process.

Subunit IIC

Interval: Sections 317-U1352C-123R-1, 142 cm, to 140R-2, 47 cm
Depth: 1693.9–1852.6 m
Age: early Miocene

Subunit IIC is characterized by thin, intercalated glauconitic sandstone interspersed with sandy marlstone and sandy limestone and, less frequently, with mudstone lithotypes (Fig. **F17**). Sandstone first occurs as a minor lithology in Core 317-U1352C-115R, and highly glauconitic sandstone first occurs in Core 123R (top of the subunit). Thereafter, these glauconitic layers become common, and the background sandy marlstone also becomes glauconitic.

The marlstone consists of greenish gray, well-sorted very fine to fine sandy marlstone. A glauconitic, bioturbated section at 317-U1352C-125R-5, 134 cm (1714.34 m), was estimated by smear slide analysis to contain >70% carbonate, making this interval glauconitic sandy limestone. The sandy marlstone in Core 317-U1352C-126R changes to greenish gray, well-sorted very fine to fine sandy limestone (i.e., >70% carbonate) by Core 132R and remains limestone to the base of the subunit. Stylolites are more common with depth and are marked by millimeter-thick muddy layers. A subordinate lithology consists of dark greenish gray very fine sandy calcareous mudstone. Bioturbation ranges between an ichnofabric index of 1 and 5 and includes *Zoophycos* and *Rosselia* forms.

Glauconitic sandstones become more common with depth to the base of the subunit. They consist of moderately to well-sorted, very fine to fine (mostly very fine), planar- to ripple-laminated calcareous glauconitic sandstone. Ripple sets are <2 cm thick, and the units themselves are typically <10 cm thick, although one thicker unit (44 cm) occurs in Core 317-U1352C-135R. In the same core, the glauconitic sandstones include both bedding-parallel (i.e., in situ beds) and glauconitic sandstones that truncate bedding and burrows (i.e., sedimentary dikes and sills; Fig. **F17**). The latter units generally appear to be subhorizontal but also occur at a high angle to stratification. They also bifurcate around centimeter-thick sandy limestone units. In both types of glauconitic sandstone, planar lamination is common. In the glauconitic sandstones that cut primary stratification, two colors of sandstone occur: light blue-gray and dark greenish gray. These layers also contain small clasts of the surrounding limestone. Beginning in Core 317-U1352C-139R, pyrite nodules as large as 1 cm in diameter occur.

Thin sections (see **"Site U1352 thin sections"** in "Core descriptions") from this subunit are mainly glauconitic calcareous sandstone and glauconitic sandy marlstone at the top of the subunit, transitioning to foraminifer micritic limestone at the base of the subunit. Glauconite occurs as pellets, altered bioclasts, and altered mica grains. Phosphatic fish remains and fecal pellets are locally present in minor amounts. The matrix is a mix of micrite with an indeterminate amount of admixed clay minerals, and the proportion of matrix changes within a sample because of the presence of darker laminae and burrow fills. At the top of the subunit, the darker laminae are arguably depositional features enriched in organic matter and clay minerals. Downsection, these pass to striking dark bands that crosscut the limestone fabric and are composed of glauconitic calcareous sandstone to sandy marlstone. Some of these crosscutting laminae fork, and others taper and pass laterally into stylolites.

Authigenic phases are mainly carbonate (as intraparticle and interparticle cement) and pyrite. Diagenesis includes patchy silicification, and low-birefringence sulfate(?) cement is present in Samples 317-U1352C-135R-5, 38–41 cm, and 137R-2, 58–60 cm (Fig. **F12E, F12F**).

Evidence for compaction includes grain fracturing, interpenetration, deformation of micrite-filled burrow margins, pressure solution, development of dark seams, and stylolites. The darker intervals (laminae/burrow fills) are associated with organic matter, which appears to enhance pressure solution, creating darker seams and leading to the formation of stylolites. The amount of organic matter essentially declines downhole throughout the subunit, and below Section 317-U1352C-137R-2 there is less compaction or pressure solution and little evidence for stylolitization of the limestone lithologies.

The mineralogy of Subunit IIC from XRD analyses is substantially different from that of other portions of this unit. All silicates decrease significantly, and carbonate increases between Subunits IIB and IIC. As in Subunit IIB, there is no detectable total clay content, with the exception of Sample 317-U1352C-136R-3, 127–129 cm (1816.86 m), which also contains elevated quartz and mica (Fig. **F11**). Also similar to Subunit IIB, micas and chlorite are positively correlated, but no correlation exists between total clays and calcite, total clays and micas, micas and quartz, or quartz and plagioclase.

Unit II/III boundary

The boundary between Units II and III is an abrupt lithologic change from glauconitic sandy limestones and marlstones in Unit II to clean foraminiferal limestone in Unit III. The boundary coincides with the Marshall Paraconformity, which represents some 12 m.y. of missing time at this locality (see **"Biostratigraphy"**). The unconformity occurs as a zone of rubble (apparently mostly blocks of the underlying limestone) in interval 317-U1352C-140R-2, 44–48 cm.

Unit III

Interval: Section 317-U1352C-140R-2, 47 cm, through Core 148R
Depth: 1852.6–1924.3 m (total depth)
Age: early Oligocene to late Eocene

Lithologic Unit III consists of white, cemented, fine-grained slightly sandy or silty (a few percent) limestone. This unit was recovered largely in pieces as long as 10 cm. Bioturbation is common throughout and includes abundant *Zoophycos* burrows, together with *Chondrites* and *Planolites*. Ichnofabric index values range between 1 and 5. Stylolites are very common and are better developed than in Subunit IIC. Medium gray siliceous nodules as large as 5 cm in diameter occur sporadically throughout the unit. Color differences include slightly darker intervals and burrow fills as well as a purple coloration that is associated with burrows or appears as circular or curved features. Pyrite nodules in Unit III are associated with burrow fills or stylolites. Below Core 317-U1352C-147R, well-laminated, light greenish gray very fine sandy marlstones occur in beds as thick as 3 cm and may contain pyrite specks or fragments. These marlstone beds appear to occur more frequently downhole.

Smear slide and thin section observations show that the limestone matrix is recrystallized with preserved fabric, suggesting that the original composition was a foraminifer-bearing nannofossil ooze, with a few percent (generally silt sized) grains of quartz and feldspar. Of the seven thin sections prepared from Unit III, six are composed of foraminifer micritic limestone. The stylolites are marked by concentrations of mainly opaque minerals (including pyrite; Figs. **F12, F18**), but they also contain clay, silt-sized quartz, and organic matter and are oriented at several different angles in the cores, commonly crosscutting each other. They have variable amplitudes, although they are better developed at the top of the section, where they exhibit higher amplitudes, thicker clay seams, and distinct crosscutting relationships. In contrast, the amplitude becomes very low in the muddy limestone below the Oligocene–Eocene unconformity (Cores 317-U1352C-147R and 148R). One stylolite in Sample 317-U1352C-146R-3, 21–24 cm, appears to have had a later dilational phase with intra-stylolite precipitation of microcrystalline carbonate and sulfate(?). The same sample contains a partly silicified bioclast, and some chert nodules and patches are present. In this section (Sample 317-U1352C-145R-1, 36–37 cm) the siliceous rocks appear to be silicified equivalents of the limestone, having been replaced by microquartz/chalcedony (chert) and opal-CT (porcellanite).

The mineralogy of Unit III from XRD analyses is notably different from that of the overlying units at this site and is dominated by carbonate minerals (calcite) with only a minor amount of quartz below 1900 m.

Downhole trends in sediment composition and mineralogy

The composition and mineralogy of Site U1352 is generally comparable to the other Expedition 317 sites. However, because of more complete core recovery, deeper penetration, and the subsequent collection of older strata, several distinct downhole changes in the concentration and relative proportions of components and mineralogy can be recognized between the three lithologic units. Primarily, carbonate concentrations increase and clay content decreases with depth in the hole.

Unit I is a clay-rich unit, composed primarily of quartz, clay, feldspar, rock fragments, mica, hornblende, rare dense minerals, carbonate, and siliceous bioclasts. Quartz and feldspar content is relatively invariant within Unit I, with somewhat higher plagioclase peak intensities within Subunit IC. A distinct feature of Unit I is the co-varying changes between total clay content, total micas, chlorite, and ferromagnesian minerals. Subunits IA and IB have relatively high total clay and ferromagnesian content, with increasing mica and chlorite peak intensities with depth. Subunit IC has distinctly lower ferromagnesian and total clay peak intensities and higher mica and chlorite peak intensities. Glauconite is relatively low throughout Unit I but becomes relatively more prevalent between 250 and 500 m, occurring as fossil infills, often within cemented layers or concretions. Dolomite and siderite were occasionally observed, but peak intensities are close to the limit of detection (see XRD in **"Supplementary material"**).

Overall, the depth trends in calcite peak intensity follow smear slide and bulk $CaCO_3$ concentrations. Within Unit I, calcite concentrations are lowest in Subunit IA, although there are local patches of high authigenic microcrystalline carbonate concentrations, abundant large shells and shell fragments, and concretions that occur as shallow as 10 m, indicating early precipitation of authigenic carbonate. Micrite becomes increasingly common below 205 m, and concretions or nodules (marlstones to fossiliferous muddy limestones) become common below 350 m, corresponding to an increasing calcium concentration in interstitial water analysis. Subunit IC, below 450 m, has a higher carbonate concentration, which is due to both high volumes of calcareous microfossils and also higher concentrations of authigenic carbonates. In contrast with the other three sites, Site U1352 has high proportions of siliceous biogenic components, with relatively elevated concentrations at ~300 and ~575 m, below which siliceous fragments become abruptly less common.

The Unit I/II boundary at 710 m coincides with a downhole shift from clay-dominated to carbonate-dominated lithologies, which corresponds to changes in magnetic susceptibility and gamma ray measurements and interstitial water chemistry. Below this point, the sediments are significantly dominated by carbonate components ($p = 0.05$, $N = 74$), and Unit II is subdivided largely according to the presence or absence of other noncalcareous lithologies. Total clay from XRD is significantly lower in Unit II relative to Unit I ($p = 0.05$, $N = 74$). Carbonate concentrations increase gradually downhole through Unit II, whereas hornblende and siliceous bioclasts become rare and clay concentrations also decrease. Below ~800 m, depth trends become less obvious, but the mineralogy remains highly variable. An increase in carbonaceous material at ~1375, 1439, and 1535 m corresponds to lithologies interpreted as mass-transport deposits. A decrease in quartz peak intensities coinciding with an increase in mica and plagioclase occurs at 1400 m, associated with a de-

crease in the number of dark muddy layers occurring downhole. These changes may be associated with an unconformity that is possibly associated with a carbonate-rich layer at 1409 m, representing ~5 m.y. of Miocene time missing. Below this point, previously rare carbonaceous material becomes more common and glauconite content begins to increase below 1550 m, whereas mica and plagioclase decrease from this point and clays were not detected below 1580 m. Pressure solution is evident in samples below 1440 m and is often associated with minor concentrations of organic matter. Some replacement of siliceous bioclasts by secondary chert or carbonate occurs, and carbonate cement is common, especially in better sorted sandy layers and burrow fills.

A notable change in composition and mineralogy occurs below 1700 m and the transition into Subunit IIC, where the concentration of silicate minerals decreases significantly and carbonate content increases. Clay content was not detectable, except for a few isolated intervals that also contain elevated quartz and mica in rare muddy layers. The content of glauconite increases downhole, although much of this is associated with discrete layers that are interpreted as intrusions from below.

Unit III comprises recrystallized limestone, probably originally a foraminifer-bearing nannofossil ooze, with a few percent of generally silt-sized grains of quartz and feldspar. Total clay, total micas, chlorite, and ferromagnesian minerals were not observed in Unit III. Below 1900 m, pyrite is associated with thin-bedded very fine sandy marlstones, which increase in frequency downhole. Stylolites are well developed in the upper part of this unit and decrease in frequency and amplitude downhole.

Correlation with wireline logs

Only a short interval of downhole wireline logging data could be obtained from Hole U1352B because of a blockage at ~500 m within Subunit IC, presumably from hole cave-in. The caliper tool indicated that the hole above this point was very wide (washed out) (see **"Downhole logging"**), but a few narrow sections provided points at which caving material could accumulate. In Hole U1352C, the triple combo tool string was blocked at ~200 m. However, enough downhole logging data were acquired to allow some correlation to Unit I lithology (Fig. **F19**). In addition to the limited downhole logging data, good core recovery over most of the drilled interval at Site U1352 makes it possible to compare lithologic trends to other physical property data (e.g., magnetic susceptibility) acquired from whole-round measurements. Note that the mineralogy of the sediments (feldspar and mica in the sand fraction and quartz in the clay fraction) reduced the ability of gamma ray logging data to unambiguously resolve sand-to-mud transitions (see **"Lithostratigraphy"** in the "Site U1351" chapter for further discussion). Also, the hole was enlarged, so gamma ray logs should be used with caution (see **"Downhole logging"**).

In Subunit IA, the lithology alternates between an interbedded sand/clay/mud lithology and calcareous, often shelly, green muddy sands. The green sandy beds correlate with low values of magnetic susceptibility measured on the recovered cores and also with low values on the downhole gamma ray log. Mud beds or interbedded lithologies have relatively high magnetic susceptibility and gamma ray values. A particularly high peak in magnetic susceptibility occurs between 58 and 61 m (Cores 317-U1352B-6H through 7H).

In Subunit IB, the succession alternates between homogeneous mud intercalated with green sand. The green sand beds are again calcareous and rich in shells. As in Subunit IA, the sand beds in Subunit IB have low magnetic susceptibility and gamma ray values; however, some low values in the downhole gamma ray data (e.g., 255–265 m) do not apparently correlate with lithologic beds and may relate to mineralogical differences within the mud beds or with conditions in the hole.

The lithology of Subunit IC is characterized by more frequent and more highly calcareous beds of green sand and gray or green mud. The sand beds contain shell fragments, biogenic clasts, and calcareous concretions. The low magnetic susceptibility and gamma ray values correspond to calcareous sand beds, as above; however, a relatively high value of magnetic susceptibility between 630 and 668 m does not correspond to any observed lithologic change in the cores, although it does correspond to a peak in clay and mica concentrations, observed in XRD analyses, as well as a minimum in calcite concentrations (Fig. **F11**; also see **"Physical properties"**).

No downhole logging data are available for Units II and III. Physical property measurements done on the cores, including magnetic susceptibility and natural gamma radiation (NGR), show trends associated with lithologic changes within Units II and III (see **"Physical properties"**). Magnetic susceptibility shows another peak at the Unit I/II boundary at ~710 m and then decreases gradually until ~810 m, where there is an abrupt upward baseline shift in the readings and an increase in variability of the measurements, although there is no obvious change in lithology. Below 900 m, variability in magnetic susceptibility and NGR decreases, concurrent with an increase in recovery that is possibly related to increasing carbonate content or cementation. Peaks in

magnetic susceptibility and NGR occur at 1200 m (near the Subunit IIA/IIB boundary) and 1440 m, and another upward baseline shift occurs between 1450 and 1500 m (poor core recovery over this interval means the exact location of this shift is unknown). The peaks correspond to lost recovery intervals and to peaks in clay and mica concentrations in XRD measurements and quartz and feldspar contents in smear slide data, possibly indicating that these layers are less cemented, more terrigenous rich layers.

Below 1500 m, NGR and magnetic susceptibility trends decrease steeply, probably related to the rapidly increasing carbonate content of the sediments in the lower part of Subunits IIB and IIC. The Marshall Paraconformity at the Unit II/III boundary shows up as a dramatic downward shift and decrease in variability of both magnetic susceptibility and NGR as a result of the homogeneous and almost purely calcareous nature of the sediments below the boundary.

P-wave velocity measured on the cores shows a relatively stable average value downhole to 1500 m (within Subunit IIB), where the measured velocity increases to ~1700 m (at the base of Subunit IIB), and then remains stable until ~1770 m before increasing until ~1820 m (just above the Unit II/III boundary; see **"Physical properties"**). A slight downward trend may be present in the bottommost 50 m of core, possibly related to the increasing clay content in the Eocene limestone at the base of the hole. It appears from these trends that velocity is directly related to the carbonate cement content of the sediments, which increases downhole to the Oligocene–Eocene unconformity within Unit III.

Description of lithologic surfaces and associated sediment facies

Sedimentary package description

A major objective of Expedition 317 was to understand how eustasy, climate, and tectonics influence sedimentation in the Canterbury Basin, with a particular emphasis on assessing how these large-scale forcing mechanisms interacted to create stratal packages and the surfaces that bound them, as resolved in seismic reflection profiles (Lu and Fulthorpe, 2004). To this end, we developed a very generalized classification of the different types of lithologic contacts and their associated deposits to aid in core-seismic integration and possible correlation with onshore strata of equivalent age. The classification scheme used here reflects the general changes in lithology of the different lithologic units and applies to all drilled sites. In Unit I at Site U1352, the uppermost 50 m of strata (Subunit IA) contains both centimeter-scale and meter-scale interbedding that reflects lithologic changes, whereas the lower 50–450 m (Subunit IB) generally contains sharp contacts that separate different lithologies and that are associated with discrete, thicker (1–6 m) beds. Poor recovery within the lower part (450–710 m; Subunit IC) hampered evaluation of the presence of surfaces and their associated sediments within that interval. From 710 to 1852 m in Unit II, the sediment is characterized by calcareous cemented lithologies that contain large-scale (6 m thick) and small-scale (5–30 cm thick) sedimentary packages bounded by sharp basal surfaces. Discrete contacts and their associated lithologies are recognized by changes in grain size, texture, color, bioturbation, and carbonate content.

Based on these large-scale trends and the characteristics of the sediments, distinct contacts and facies associations were defined as sedimentary packages, which may potentially vary acoustic impedance and therefore be resolvable in seismic reflection data. These classifications are greatly simplified for the expedition report, and postcruise analyses will permit better definition of sedimentary packages and improve their correlation to seismic data. Broadly, contacts and facies associations were classified based on grain size (muddy sand, sandy mud, sandy marl, marl, or clay), bed thickness, the nature of the basal and upper contacts, and the amalgamation of thinner (centimeter thick) beds with discrete contacts that form meter-thick or thicker packages (Figs. **F20, F21**).

Type A contacts and facies associations are characterized by a sharp contact that commonly separates thick lithologies above and below. The lithology above the contact can be as thick as 6 m (Fig. **F20**). Specific examples include thick, dark greenish gray calcareous fine to medium muddy sand or sandy mud in sharp contact with underlying greenish gray mud. The basal contacts of the overlying greenish gray sandy lithology are sharp and lightly to heavily bioturbated, whereas their upper contacts tend to be gradational. When their lower contacts are heavily bioturbated, discrete burrows can be tracked 100 cm beneath the contact. Shells and shell fragments are present in the greenish gray muddy sand and sandy mud deposits within the uppermost 150 m of Holes U1352A and U1352B. These become rare in Hole U1352B from 150 to 250 m and are generally absent from the deeper lithologies, except in a bed near 372 m where they are abundant. When shells and shell fragments are present, they are as long as 3 cm and are abundant within the greenish gray sands immediately above the basal contact. Shells and shell fragments can be present below the basal contact in the

greenish gray mud, but the position of these shells is most likely the result of burrowing disturbance because they seem to be closely associated with greenish sand-filled burrows. Mass wasting deposits (as thick as 15 m) found in Unit II from ~1370 to 1550 m are a second example of Type A contacts and deposits. These deposits have a sharp upper and lower contact, soft-sediment deformation features, and medium to coarse sand layers, with generally lower bulk density than the adjacent strata (e.g., Sections 317-U1352C-94R-6 through 94R-7 and Cores 105R and 106R; Fig. **F16**).

Type B contacts and facies associations represent amalgamation packages of thinly bedded but distinctly contrasting lithologies (e.g., sand, mud, and clay interbedding and sandstone–marlstone and marlstone–limestone alternations). These contrasting lithologies also form meter-thick packages (Fig. **F20**). The individual beds are thin (1–5 cm), have decimeter-scale spacing, and commonly have sharp basal contacts. When sand is present, it is normally graded. Because of the sharp contrasts in lithology and the thickness of these packages, these types of deposits may be resolvable in seismic reflection profiles.

Type C contacts and facies associations are always sharp and separate contrasting lithologies, for example sand and mud or sandstone and marlstone. Because of this sharp contact in lithology, these surfaces have the potential to create reflections in seismic profiles. However, the thickness of any beds associated with these contacts could not be clearly delineated on board ship (e.g., muddy sand layers fining upward into sandy mud), and additional shore-based analyses are required to establish the relative importance of each in terms of its potential to generate a seismic reflection (Fig. **F20**).

Table **T3** lists the occurrence of each of the three types of contacts and their associated sediments at Site U1352. Type A contacts and associated facies are more common in Unit I than they are in Unit II. Type B contacts and facies associations are more common in the uppermost 50 m of Unit I and throughout Unit II, where they consist of more heavily cemented mudstone and marlstone, marlstone and sandstone, and marlstone and limestone beds within homogeneous sandy marlstone. Within Unit I, Type B contacts and facies associations are packages of interbedded sand and mud or mud and clay (e.g., 26, 34, and 98 m) or several decimeter-thick muddy sand beds that are closely spaced (e.g., 148, 159, 331, and 338 m). Type C contacts and facies associations are found throughout Holes U1352B and U1352C and represent a range of lithologic contacts. Within Unit I, these sedimentary packages tend to comprise fining-upward muddy sand that sharply overlies mud; within Unit II, they comprise beds with distinctly different carbonate contents and/or degrees of cementation. An additional example is the Unit II/III boundary between sandy limestones and limestone.

Description of significant surfaces

Because of time restrictions on board ship, surfaces were only examined close to the predicted depths of seismic sequence boundaries; therefore, the lithologic surfaces identified here are implicitly linked to the predicted occurrences of sequence boundaries identified on the seismic (Lu and Fulthorpe, 2004). A similar approach was used on board ship during ODP Legs 150 and 174A, the objectives of which were also to study sea level changes. Postcruise study will attempt to clarify the exact relationship of all lithologic surfaces and facies associations to sea level changes and seismic stratigraphy. The numbering system used in the site chapters, tables, and summary diagrams comprises a hole-specific prefix and a surface designation (e.g., U1352A-S1) that links each surface to a seismic sequence boundary; therefore, these lithologic surfaces and associated sediments are thought to be correlative between sites across the transect.

The following section contains a brief description of each surface identified at Site U1352, as summarized in Table **T4.** In contrast to the situation at Site U1351, the identification of significant surfaces at this site was complicated by the common presence of more than one lithologic package per core near the predicted depths of seismic sequence boundaries (Lu and Fulthorpe, 2004). In these situations, the significant surface has generally been assigned to the lithologic package that was thicker and best preserved, but the other surfaces identified nearby are also mentioned.

Surfaces U1352B-S1 and U1352D-S1

A Type A contact and its associated facies, designated U1352B-S1, is tentatively placed at Section 317-U1352B-7H-6, 96 cm (64.20 m) (Table **T4**). A second sharp, angular dipping contact is present above (62.50 m). This surface is similar to that at 64.20 m, but the former is less burrowed, contains fewer shells and shell fragments, and has thinner beds that grade upward into greenish mud. Note also that from 75 to 93 m there are several intervals of muddy sand beds 25, 86, and 88 cm thick in Cores 317-U1352B-9H,

10H, and 11H, respectively. A lithologic surface of similar character, U1352D-S1, was observed at Section 317-U1352D-8H-3, 88 cm (64.38 m).

Surface U1352B-S2

A Type B contact and its associated facies, designated U1352B-S2, is tentatively placed at Section 317-U1352B-16H-5, 5 cm (147.22 m) (Table T4). The sediments associated with this contact contain a 5 cm thick cemented layer at Section 317-U1352B-16H-4, 128 cm (146.96 m). A second Type B contact is present at 146 m. The overlying sedimentary package is 30 cm thinner than the sedimentary package beneath, and the contacts above and below are gradational into gray mud. Surface U1352B-S2 is therefore tentatively positioned in the sharp contact of the thickest sand bed at 147.22 m.

Surface U1352B-S3

Surface U1352B-S3 is tentatively positioned at a sharp contact at Section 317-U1352B-23H-1, 130 cm (200.00 m). A second sharp contact is present at Section 317-U1352B-23H-6, 80 cm (207.00 m). Note that muddy sand beds 4–27 cm thick are present in most sections of Cores 317-U1352B-24H and 25H.

Surface U1352B-S4

Surface U1352B-S4 is tentatively placed at Section 317-U1352B-28H-4, 7 cm (250.20 m) and is defined by a sharp contact that separates gray mud below from sandy mud above. This Type A contact and facies associations is thin (<1 m) relative to other packages. Two other intervals of sandy mud were also observed between 246 and 249 m. It should also be noted that sand beds as thick as 88 cm are present in Sections 317-U1352B-27H-4 through 27H-7, indicating that these sandy intervals extend several meters below the selected contact.

Surfaces U1352B-S5 and U1352B-S5.1

Two potential Type B surfaces and their associated sediments are designated as surfaces U1352B-S5 (Section 317-U1352B-51X-1, 131 cm [428.81 m]) and U1352B-S5.1 (Section 53X-5, 30 cm [453.00 m]). The latter is associated with an unusually thick (6.5 m) bed of very fine sandy calcareous mud.

Surface U1352B-S6

Lithologically, the depth interval from 475.5 to 484.2 m is very unusual. From the base up, it contains a 15 cm thick bed of very fine sandy mud that fines upward. The basal contact at 484.2 m that separates the sand above from the mud beneath is heavily bioturbated for 15 cm below the contact. A second sand bed (4.15 m thick) is present from 478.10 to 482.20 m. This muddy very fine sand is calcareous and terminates in a sharp basal contact at 482.2 m. Heavy bioturbation is present for 45 cm beneath the contact. Surface U1352B-S6 is positioned at the base of the thickest sand associated with the sharp contact at Section 317-U1352B-56X-5, 70 cm (482.20 m).

Surface U1352C-S9

Surface U1352C-S9 is located within a more calcareous interval within the marlstones defined as chalk. This interval contains a sandy chalk bed from 990.25 to 990.56 m and several 2–5 cm thick chalk-rich intervals between 1026 and 1034 m. The sandy chalk bed has a sharp, scoured contact at Section 317-U1352C-40R-3, 5 cm (990.56 m), that separates it from marlstones above and chalky marlstones beneath. This contact is designated as surface U1352C-S9.

Surface U1352C-S10

A series of Type B contacts with silty sand beds with planar bedding, ripple laminations, shell fragments, and rip-up clasts are present between 1112.50 and 1113.00 m. The contact at Section 317-U1352C-53R-1, 90 cm (1113.00 m), is designated as surface U1352C-S10.

Surface U1352C-S11

An unusually thick (3 m), very calcareous deposit with sharp basal and upper contacts is present between 1276.50 and 1279.80 m (Fig. F22). This deposit is present within Sections 317-U1352C-73R-2 and 73R-4, where the Pliocene/Miocene boundary was identified. Surface U1352C-S11 was placed at the base of the deposit at 1279.8 m.

Surface U1352C-S12

A succession of Type A/B facies deposits found from 1400 to 1438 m documents an increase in laminations and other current structures, such as planar beds and ripples, as well as an increase in grain size and sand beds interpreted as stronger current activity (Fig. F15). Additionally, slump deposits are present between 1371 and 1438 m (Fig. F16). The base of a slump deposit (Section 317-U1352C-94R-7, 60 cm [1938.20 m]) was selected as surface U1352C-S12.

Surface U1352C-S13

One of the most notable surfaces, U1352C-S13, is linked to the Marshall Paraconformity (Fig. F18). This surface is present at Section 317-U1352C-140R-2, 48 cm (1852.64 m), and is marked by a limestone

gravel bed that separates glauconitic silty limestone above from limestone beneath. The gravel bed is composed of ~5–10 cm long subrounded limestone fragments having weathered surfaces.

Discussion and interpretation

Interpretation of Unit I

Subunit IA

Seismic reflection profiles indicate a series of downlapping reflectors in this interval, as described by Browne and Naish (2003), who interpreted these as a series of lowstand delta front deposits. The lithologies and sedimentary structures of Subunit IA are consistent with this interpretation. We interpret the sharp-based, dark gray sand to be a product of sediment gravity flows fed by such deltas (gravity flow in this context implies downslope mass transport, not a specific type of transport). The slumped and faulted intervals observed in the uppermost 20 m of both Holes U1352A and U1352B may be related to high rates of sediment supply in delta or pro-delta settings.

Subunit IA is characterized by dark gray muds as well as sharp-based, gray and greenish sand beds. The greenish sand beds are calcareous, and in part siliceous, with abundant to common macrofossils often concentrated into layers. This, together with the sharp-based and fining-upward character of the beds, suggests deposition from gravity flows. The background mud observed in the cores throughout this subunit probably formed through hemipelagic deposition in slope settings or areas removed from major point sources of sediment input from either westerly or southerly source areas.

The gray sand beds in this subunit have compositions consistent with derivation from low-grade zeolite and prehnite-pumpellyite graywacke rocks (Torlesse Terrane) of the Canterbury region. This subunit differs from other units, which appear to have a predominantly schist-derived provenance. For example, XRD data indicate that chlorite is low throughout Subunit IA but increases markedly at 100 m, which is consistent with a change from a dominantly Torlesse provenance in Subunit IA to an increased Otago Schist provenance in Subunit IB (Fig. **F11**). Grains within the subunit are both well rounded and angular—a bimodal transport history suggesting that the well-rounded grains may be recycled or were rounded in a high-energy beach setting and mixed with less rounded, fluvially transported sediment before being transported offshore.

Subunit IA, characterized by an overall high siliciclastic content, corresponds to the past ~0.25 m.y. (see **"Biostratigraphy"**), a time period of pronounced glaciation in the Southern Alps (Suggate, 1990). The relatively high concentration of quartz and feldspars within clay-rich intervals might be a glacial rock-flour signature (Heiden and Holmes, 1998; Peuraniemi et al., 1997), and the input of Torlesse-derived material implies that glaciers that originated from the Southern Alps were a dominant sediment source for this subunit.

Subunit IB

The interbedded greenish sands that occur in dark gray muds are typically sharp based and fine upward and are interpreted as sediment gravity flows. Similar sands were interpreted as contourites in Subunit IIB at Site 1119, but because we lack evidence of coarsening- and then fining-upward trends, we prefer to suggest that these sand beds represent either downslope mass transport from shallower areas rich in carbonate or are winnowed condensed intervals. For example, one such sand interval found in Sections 317-U1352B-32X-5 through 32X-CC contains abundant shells that likely represent a sediment gravity flow originating from a shallow-marine setting. XRD analyses show that total clays are lowest and calcite is highest in the calcareous, olive-green muddy sands, which may indicate that these units formed during periods of minimal hemipelagic sediment input or during periods of enhanced traction transport and erosion that winnowed out the clay component. Lastly, the noted decrease in quartz and mica content at ~250 m corresponds to ~0.8 Ma (see **"Biostratigraphy"**), which is during the mid-Pleistocene climatic transition from high- to low-amplitude eustatic sea level change (Clark et al., 2006).

Similarly, we suggest that the homogeneous mud, which has a relatively high total clay concentration, represents mostly hemipelagic deposition in upper slope settings based on micropaleontological evidence for an upper slope depth of deposition (see **"Biostratigraphy"**).

Subunit IC

Coulometry and smear slide data indicate higher carbonate content in Subunit IC than in the overlying Subunit IB interval. The fine-grained sediments are interpreted to be hemipelagic sediments deposited with a large amount of pelagic carbonate components. Small to moderate proportions of terrigenous sand (10%–35%) may have been derived from downslope mixing or along-slope sand supply, but the better sorting and fine-grained nature of the sand fraction, including a high percentage of bioclasts, suggest considerable transport. Occasional clay-rich

muddier units indicate episodic increases in terrigenous supply. Micropaleontological evidence (including the presence of reworked microfauna) supports an interpretation of drift sedimentation in a slope setting for this subunit. This interpretation is consistent with the seismic line in a strike perspective between Sites U1352 and 1119 that shows a series of small drifts at this stratigraphic level (seismic Line EW00-01-19).

Interpretation of Unit II

Unit II is distinguished from Unit I in that it is dominantly calcareous and is composed of sandy marlstone with minor components of limestone and sandy mudstone.

Subunit IIA

Subunit IIA is interpreted to have been deposited in a hemipelagic to pelagic setting largely removed from clastic sediment sources, although the very fine to fine sand, mica, and clay were probably derived from upslope terrigenous sources or along-slope sediment supply, as suggested by the variable mineralogy within this subunit. The sandy sediments are interpreted as thin traction deposits, formed during the reworking of some of the sand into planar-laminated and ripple-laminated beds. We interpret the marlstone as largely drift deposits, consistent with the seismic profile between Sites U1352 and 1119 (seismic Line EW00-01-19). The more calcareous lithologies may represent condensed intervals formed during periods when sediment was starved on these drifts. The increased frequency of chalky intervals in the lower part of Subunit IIA may relate to a slower rate of sedimentation at the base of a clinoformal package of sediment.

Subunit IIB

The alternation of light-colored marlstone with darker colored mudstone and sandstone layers indicates an alternation of dominant processes from more quiescent periods of pelagic deposition to periods of increased sediment supply and current activity. The overall downhole decrease of silicate minerals in this subunit is a continuation of the transition to a more carbonate rich (pelagic) environment with less terrigenous sediment input.

This subunit contains numerous types of bedding structures that may have formed from a combination of transport and diagenetic processes. The common thin, brown, wavy lamination that causes the pin-striped appearance of the lower part of the unit could be (1) original burrows, (2) primary ripple lamination, (3) stylolitic laminae, or (4) a combination of the above. These laminae appear to become better defined and more pervasive with depth, and lower in the subunit some of the white calcareous blebs are dissolving about their margins and forming white trails into the laminae. Thin section observations indicate that the brown wavy laminae are composed of organic matter and associated clay-rich material deposited in laminae and reworked in burrows that have undergone pressure solution, in effect a combination of the proposed mechanisms above.

The sharp-based nature of the darker sandstones and mudstones suggests increased current activity and rapid deposition of these beds. It is probable that the mudstone represents increased deposition of continent-derived material (clay, organic material, etc.). The horizontally and ripple-laminated sandstone beds were deposited by traction currents, probably also sourced from continental areas or, less likely, from reworking of the sand component of the marlstones. Smear slides indicate a considerable amount of organic matter (as much as 10%) in the lower portions of the subunit, implying that a landmass was not too distant from the depocenter. Perhaps the mudstone intervals represent periods of lower sea level, when land-derived sediment was prevalent, whereas the marlstone might represent hemipelagic sedimentation during periods of reduced sediment input from the continent, possibly during rising and high sea level. In general, we interpret these sediments to represent largely hemipelagic to pelagic deposition removed from major sources of sediment (except during lowstands), consistent with a sediment-drift setting.

Intervals of soft-sediment deformation recorded in the lower portion of Subunit IIB may reflect instability caused by sediment loading, seismic triggering, and/or topography within the drift deposits or adjacent submarine highs (the “Endeavour High” of Field and Browne, 1989). These slumped intervals have higher quartz, clay, mica, and feldspar contents, supporting the interpretation that these deposits were formed by mass movements originating closer to shore. The association of a graded sandstone-mudstone turbidite at the top of one of these mass flow units suggests that subsequent mass flows were concentrated into bathymetric lows, which formed by the evacuation of the mass-transport complex that preceded it.

A prominent variance in mineralogy occurs within this subunit, as indicated by the interval of higher mica and chlorite content between ~1470 and 1570 m. As opposed to other sections at this site where micas and quartz/clay positively co-vary, the rise in mica content does not correspond to a similar rise in quartz or clay minerals but does increase along with plagioclase. Smear slides and thin sections from

these same intervals reveal the presence of altered basaltic fragments, plagioclase, and zeolites, suggesting that chlorite may be authigenic rather than detrital and may have formed from alteration of mafic volcanic fragments. This depth interval corresponds to ~10–13 Ma (see **"Biostratigraphy"**), when the mafic volcanic fields at Banks and Otago peninsulas formed (McDougall and Coombs, 1973; Coombs et al., 1986; Sewell, 1988; Sewell et al., 1992).

Subunit IIC

The marlstones and limestones in this subunit are predominantly fine grained, suggesting pelagic to hemipelagic deposition in a deepwater setting with only a small terrigenous sediment supply. Micropaleontology suggests deposition in a lower bathyal setting (see **"Biostratigraphy"**). The horizontally laminated nature of the intercalated glauconitic sandstone beds implies some form of traction deposition. In these instances, the sandstone may represent reworking of sediment from areas enriched in glauconite, such as sediment-starved highs. Although this is probably true for some of the observed layers, many of the sandstone layers, especially those in the lower part of the subunit, clearly crosscut primary stratigraphic features and are interpreted as diapiric in nature, both dikes and sills. Examples of this exist in the core where vertical or near-vertical glauconitic sandstone bodies fed into or were fed from subhorizontal glauconitic sandstone. Other core examples show thinner glauconitic sandstones branching from thicker equivalents with a dendritic-type morphology. Some diapiric sandstones show fragments of the surrounding carbonate lithology within them, implying that these fragments were broken off the surrounding walls during emplacement. Accounts of diapiric sandstones at Oamaru (Lewis, 1973) and southern North Island (Browne, 1987) indicate that similar diapiric features occur nearby in similar lithotypes. We suggest that the source of the glauconitic sandstone is the Oligocene Kokoamu Greensand, which should occur stratigraphically below these limestones (but was not recovered in the core) and immediately above the Amuri Limestone (Unit III), based on the nearby exploration well Clipper-1. Sediment loading and/or mild tectonic warping may have caused the upward injection of the glauconitic sand into Subunit IIC (e.g., Jolly and Lonergan, 2002).

Interpretation of Unit III

We interpret Unit III to have accumulated as pelagic foraminifer-bearing nannofossil ooze. The faint purple bands and rings noted in the cores may be related to disseminated fine iron sulfide within the limestone, as described in similar facies recovered from the Ontong Java Plateau during ODP Leg 130 (Lind et al., 1993). These color bands are interpreted as a possible alteration of volcanic ash or other impurities in the limestones. Foraminifer and nannofossil studies reported here (see **"Biostratigraphy"**) suggest a lower bathyal depth between 1000 and 1500 m water depth.

This unit is correlative to the regionally extensive Amuri Limestone, which is widespread throughout South Island and lower North Island, New Zealand. Regional studies suggest that deposition may occur in either shelf (van der Lingen et al., 1978) or bathyal (Edwards et al., 1979) settings. Seismic reflection profiles suggest that Site U1352 was situated slightly seaward of the shelf during the early Oligocene but that the margin was a broad ramp at that time with no clear shelf/slope break. This is consistent with the interpretation made by Field and Browne (1989) that the Amuri Limestone was deposited in an outer shelf to slope paleoenvironment.

Interpretation of lithologic surfaces and associated sediment facies

Hole U1352B

The identified lithologic surfaces and their associated sedimentary packages (Types A, B, and C) are in some instances near the predicted depths of seismic sequence boundaries (Lu and Fulthorpe, 2004), allowing a tentative correlation of lithology to seismically defined surfaces (Figs. **F22, F23;** Table **T4;** see also Table **T4** in the "Site U1351" chapter). The sharp and often heavily burrowed basal contacts of some of these packages suggest that erosion and/or sediment bypass are associated with the formation of the discontinuity. The lithologic surfaces from Site U1352 differ from those of Site U1351 in that they are composed of several Type A sedimentary packages per core (~9 m intervals) instead of just one event, as was observed at Site U1351. Multiple sedimentary packages can potentially provide a stronger impedance contrast and stronger seismic reflections on the seismic lines. This should be further investigated during postcruise study.

Surface U1352B-S1 is tentatively correlated to seismic sequence boundary U19, which is predicted at 68 m. Of the two depositional events present, surface U1352B-S1 is correlated to the thicker sand bed at 64.16 m and to U19. Surface U1352A-S1 has a similar age range as U1352B-S1 and was identified in interval 317-U1352A-3H-1, 0–70 cm.

Surface U1352B-S2 is a Type B contact and associated facies and is tentatively placed at 147.3 m and correlated with U18, which has a predicted depth of 142

m. Surface U1351B-S2 has a similar age range as U1352B-S2 and was identified in Holes U1351A and U1351B at 27.75 and 31.00 m, respectively (see Table **T4** in the "Site U1351" chapter).

Surface U1352B-S3 is tentatively positioned at a sharp contact at 200 m. The Type A contact and associated facies designated U1352B-S3 correlates to U17, predicted at a depth of 195 m. Surface U1352B-S3 has a similar age range as U1351B-S3 (see Table **T4** in the "Site U1351" chapter).

Surface U1352B-S4 is tentatively placed at 250.20 m and correlated with U16, which has a predicted depth of 249 m. Again, as in previous surfaces, the lithology indicates three depositional events associated with this interval. Surface U1352B-S4 has the same age range as U1351B-S4 (see Table **T4** in the "Site U1351" chapter).

Surface U1352B-S5 at 428.81 m is correlated to U15, which has a predicted depth of 428 m. Surface U1351B-S5 is also tentatively correlated to U15.

Surface U1352B-S5.1 at 453.20 m is tentatively correlated to U14, which has a predicted depth of 448 m. A lithologic surface correlative to U14 was not found at Site U1351, probably because of a recovery gap between 97 and 113 m over the predicted depth of U14 at Site U1351 (103 m).

Surface U1352B-S6 is tentatively positioned at the base of the thickest of two sand beds associated with a sharp contact at 482.20 m. This surface is correlated with U13, which has a predicted depth of 500 m. The sediments from 485.10 to 504.40 m are composed of gray homogeneous mud and had good recovery, except for intervals of cementation between 489 and 492 m. The series of sand beds associated with this contact provides evidence of sediment transport. Surface U1352B-S6 has a similar age range as U1351B-S6, where sand beds and evidence of sediment reworking also make the placement of the Pleistocene/Pliocene boundary in that core questionable (see Table **T4** in the "Site U1351" chapter).

U12 and U10 were not found at Site U1352. A Type A contact and facies association, U1351B-S7, is present in Core 317-U1352B-81X at 710.65 m. This lithologic surface and its facies association is tentatively correlated to a seismic surface that could potentially be the continuation of U12. U12 could not be traced from Site U1351 to U1352, so at this point this interpretation is based on the lithology only and not on a seismic surface.

U11 has a predicted depth of 769 m, but a corresponding lithologic surface was not located near this depth. U10 is absent. The Type A surface U1351B-S7 is present in Section 317-U1351B-22X-1 (171.4 m) and tentatively correlated with U12.

Hole U1352C

Several cores in this hole have distinctive lithologies that could be identified as Type A or Type B surfaces. These surfaces, although rare, are important and have been tentatively linked to U9 and U8 (U1352C-S9 [990.60 m] and U1352C-S10 [1113.00 m], respectively). Sediments from 1113 m to the base of the hole at 1924 m include notable events associated with hiatuses and mass flows, also classified as Type A and Type B contacts and facies associations. These events have been tentatively linked to U7 and U6 and to the Marshall Paraconformity. These surfaces and associated sediments are named U1352C-S9 to U1352C-S13. Sediments that could be interpreted as representing U5 and U4 were not recovered at Site U1352.

Surface U1352C-S9 is tentatively linked to U9, which occurs at a predicted depth of 970 m, based on increased calcareous content and a sandy chalk bed. Because of its high calcareous content, the deposit associated with this lithologic surface may represent late high-stand episodes of condensation. This lithologic surface was not directly identified at Site U1351 because sediments near the predicted depth of U9 (312 m) were not recovered.

Surface U1352C-S10 and its associated facies is a Type B lithologic contact positioned at 1113 m and tentatively correlated to U8, which occurs at a predicted depth of 1136 m. The depth at which U8 is predicted at Site U1351 (394 m) was not recovered because of recovery gaps between 394 and 400 m. U1352C-S10 cannot be correlated to the shelf Site U1351.

Surface U1352C-S11 is a Type A contact and facies association. As a result of its sediment composition, sharp boundaries, and age, the base of this deposit is tentatively correlated to U7, which occurs at a predicted depth of 1251 m. The predicted depth interval for U7 at Site U1351 is 614 m; however, this surface was not identified at Site U1351 because of poor recovery from 611 to 620 m.

Surface U1352C-S12 was chosen at the base of a slump deposit at 1438 m. This lithologic surface closely corresponds in depth with U6, which occurs at a predicted depth of 1428 m. The corresponding U6 interval at Site U1351, at the predicted depth of 895 m, was not recovered.

Based on age and lithologic relations, U1352C-S13 is correlated to the Marshall Paraconformity (observed at 1852.6 m), which correlates to the predicted depth of seismic reflector "Green" at 1824 m. A gravel bed marks this lithologic surface, which suggests that the gravels were derived from the limestone beneath and were reworked prior to deposition of the overlying

sediment. It is likely that these reworked limestone blocks were derived from the weathered top surfaces of the underlying chalky limestone and that a layer of unconsolidated glauconitic sand between the rubbly surface of the underlying limestone and the coherent glauconitic limestone above exists in the subsurface but was not recovered by coring. This interpretation is based on the exposures onshore of a similar (though shorter duration) unconformity (e.g., Fulthorpe et al., 1996). The unconsolidated glauconitic sediments or rubbly top surface of the limestone would provide a strong impedance contrast, leading to the strong seismic signal of the Marshall Paraconformity sequence bounding unconformity. U1352C-S13 correlates with a hiatus between the upper Miocene (18–19 Ma) and upper Oligocene (30–32 Ma), and its recovery was a very important goal of the expedition. There are no major lithologic features at 1647 m, the originally predicted depth for the Marshall Paraconformity.

Biostratigraphy

Core catcher samples from Holes U1352A–U1352D were examined for calcareous nannofossils, diatoms, planktonic and benthic foraminifers, and bolboformids to develop a preliminary biostratigraphic framework for the cored succession (Fig. **F24;** Table **T5**). Calcareous nannofossils and planktonic foraminifers provided the primary means of age control at Site U1352, but marine diatoms, bolboformids, and benthic foraminifers also contributed to dating. Benthic foraminifers were used to determine paleowater depths and interpret depositional environments. All depths in this section are reported in m CSF-A.

Integrated microfossil records from Site U1352 reveal a 1924 m thick sedimentary succession spanning the Holocene to Eocene. Although not identified biostratigraphically, the base of the Holocene was tentatively assigned in Hole U1352B at 1.2 m, the level at which shell-rich greenish gray marly sands with a sharp base overlie gray muds. The base of the Pleistocene was loosely constrained between Samples 317-U1352B-57X-CC and 61X-CC (491.74–525.34 m). The base of the Pliocene was constrained with planktonic foraminiferal evidence between Samples 317-U1352C-72R-CC and 73R-CC (1266.38–1283.95 m). The base of the Miocene was picked using calcareous nannofossil evidence between Samples 317-U1352C-139R-CC and 140R-CC (1848.49–1852.71 m), and the base of the Oligocene was placed between Samples 317-U1352C-146R-CC and 147R-CC (1903.29–1916.63 m). Calcareous nannofossil and planktonic foraminiferal dating indicate a late Eocene age of 35.2–36.0 Ma at the bottom of the hole (Sample 317-U1352C-148R-CC [1924.26 m]).

At least five biostratigraphically defined hiatuses were recognized. The first hiatus occurs between the Pliocene and Pleistocene (Samples 317-U1352B-57X-CC and 61X-CC [491.74–504.14 m]), where most, if not all, of the late Pliocene is missing. An intra-late Miocene unconformity was recognized between the New Zealand upper Kapitean and lower Tongaporutuan Stages (Samples 317-U1352C-90R-CC and 91R-CC [1394.62–1409.66 m]), where at least 5 m.y. is missing. Another hiatus was identified between the middle and late Miocene (Samples 317-U1352C-101R-CC and 102R-CC [1486.78–1496.50 m]), with at least 1.3 m.y. missing. A substantial unconformity, identified as the Marshall Paraconformity, was constrained between Samples 317-U1352C-139R-CC and 140R-CC (1848.49–1852.71 m), where the lower Miocene unconformably overlies the lower Oligocene. At least 12 m.y. is missing at this level. A hiatus was also recognized between the early Oligocene and late Eocene (Samples 317-U1352C-146R-CC and 147R-CC [1903.29–1916.63 m]), where at least 2.3 m.y. is missing.

Calcareous nannofossils

All core catcher samples from Holes U1352A–U1352D contained calcareous nannofossils, with the exception of Sample 317-U1352B-71X-CC (614.56 m). Abundances ranged from barren to very abundant, and preservation was generally good in the Pleistocene–Miocene and moderate to poor in the Oligocene and Eocene (Table **T6**). Nannofossil datums used for age determination at this site are summarized in Table **T5.**

Holocene–Pleistocene

All sediment samples from Hole U1352A were zoned in NN21 (0–0.29 Ma). Core catcher samples from Holes U1352A (317-U1352A-1H-CC through 5H-CC [4.21–43.06 m]) and U1352D (317-U1352D-1H-CC through 14H-CC [3.55–127.61 m]) contained rare *Emiliania huxleyi,* likely placing them below the acme of this species in Subzone NN21a (0.08–0.29 Ma).

Hole U1352B contained a thick Pleistocene section from Samples 317-U1352B-1H-CC through 61X-CC (7.93–525.34 m). Samples 317-U1352B-1H-CC through 12H-CC (7.93–112.82 m) were zoned in NN21a. Sediments recovered from Samples 317-U1352B-13H-CC through 17H-CC (121.1–155.99 m) were zoned in NN20 (0.29–0.44 Ma).

The highest occurrence (HO) of *Pseudoemiliania lacunosa* (top of Zone NN19) was recognized between Samples 317-U1352B-17H-CC and 18H-CC (155.99–164.18 m). Within the *P. lacunosa* and small *Gephyrocapsa* subzones of NN19 (Gartner, 1977), several nannofossil bioevents were observed:

- The highest common occurrence (HCO) of *Reticulofenestra asanoi* between Samples 317-U1352B-29H-CC and 30H-CC (257.09–266.92 m; 0.91 Ma),
- The lowest common occurrence (LCO) of *R. asanoi* between Samples 317-U1352B-34H-CC and 35H-CC (292.54–295.24 m; 1.14 Ma),
- The HO of *Gephyrocapsa* >6.5 µm between Samples 317-U1352B-42X-CC and 43X-CC (348.59–360.08 m; 1.24 Ma), and
- The HO of *Gephyrocapsa* >5.5 µm between Samples 317-U1352B-43X-CC and 44X-CC (360.08–369.84 m; 1.26 Ma).

The top of the *Helicosphaera sellii* NN19 Subzone was tentatively picked between Samples 317-U1352B-46X-CC and 47X-CC (388.95–398.56 m; 1.34 Ma). The lowest occurrence (LO) of *Gephyrocapsa* >5.5 µm was observed within this subzone between Samples 317-U1352B-49X-CC and 50X-CC (412.30–427.34 m; 1.56 Ma).

The primary marker for the *Calcidiscus macintyrei* NN19 Subzone (*C. macintyrei* >11 µm) was not observed; however, secondary markers (LO of *Gephyrocapsa* >4 µm between Samples 317-U1352B-54X-CC and 55X-CC [463.67–469.84 m; 1.69 Ma] and LO of *Gephyrocapsa caribbeanica* between Samples 317-U1352B-55X-CC and 56X-CC [469.84–484.83 m; 1.73 Ma]) support the presence of this subzone.

The Pliocene/Pleistocene boundary was constrained between Samples 317-U1352B-57X-CC and 61X-CC (491.74–525.34 m) using nannofossil and foraminiferal markers that approximate the boundary. Below this boundary, *Reticulofenestra ampla* was observed in Sample 317-U1352B-62X-CC (542.58 m). The HO of this species is dated at 2.78 Ma (Kameo and Bralower, 2000), which suggests a hiatus spanning the late Pliocene.

Pliocene

Nannofossil biostratigraphy was problematic for Samples 317-U1352B-60X-CC through 94X-CC (514.61–821.74 m [total depth]) and 317-U1352C-2R-CC through 93R-CC (576.47–1419.06 m) because almost all standard zonal markers were absent. The *Reticulofenestra* lineage, however, was abundant in this cored succession, making it useful as a secondary proxy for age constraint. The HO of *Reticulofenestra pseudoumbilicus* was observed between Samples 317-U1352C-29R-CC and 30R-CC (884.91–894.37 m; 3.7 Ma), defining the base of the middle Pliocene. The base of the Pliocene was picked between Samples 317-U1352C-72R-CC and 73R-CC (1266.38–1283.95 m; 5.33 Ma) with planktonic foraminiferal evidence.

Miocene

Standard Miocene nannofossil zonal markers based on warm-water taxa were sparse at Site U1352, except in the early Miocene, where they were more common. Planktonic foraminifers and bolboformids show evidence of a major intra-late Miocene hiatus between Samples 317-U1352C-90R-CC and 91R-CC (1394.62–1409.66 m), where at least 5 m.y. is missing. The HO of *Coccolithus miopelagicus* (11.02 Ma) was observed between Samples 317-U1352C-94R-CC and 95R-CC (1438.43–1446.91 m). The first in situ discoaster was noted in Sample 103R-CC (1515.94 m). Below this level, discoasters (common in low- to mid-latitudes) occurred sporadically and were dominated primarily by *Discoaster deflandrei*; however, zonal marker species for the late Miocene were still absent.

The HO of *Calcidiscus premacintyrei* was observed between Samples 317-U1352C-101R-CC and 102R-CC (1486.78–1496.50 m), implying a late middle Miocene age (12.45 Ma). In addition, a marked increase in six-rayed discoasters was observed in Samples 317-U1352C-119R-CC and 120R-CC (1670.41–1669.36 m). Some of these were confidently identified as *Discoaster deflandrei*, but others were too overgrown to be distinguished at the species level. The interval between these samples was tentatively considered as the acme event of *D. deflandrei* (15.80 Ma), even though the position of this event is uncertain because of caved-in local sediments found between the two samples.

The lower Miocene HO of *Sphenolithus heteromorphus* was picked between Samples 317-U1352C-114R-CC and 115R-CC (1622.61–1632.61 m). Below Core 317-U1352C-115R, *S. heteromorphus* was consistently seen in core catcher samples down to Sample 317-U1352C-129R-CC (1749.66 m). The LCO of this species, dated at 17.71 Ma, was therefore placed between Samples 129R-CC and 130R-CC (1749.66–1760.69 m).

Sphenolithus belemnos (HO = 17.95 Ma) occurred in extreme paucity in cored sediments; however, the HCO of this species was questionably picked between Samples 317-U1352C-132R-CC and 133R-CC (1777.59–1789.60 m), and it is certainly common by Sample 135R-CC (1810.40 m). The LO of this species was questionably picked between Samples 317-U1352C-137R-CC and 138R-CC (1829.75–1841.54 m; 19.03 Ma).

A major hiatus, identified as the Marshall Paraconformity, occurred between Samples 317-U1352C-139R-CC and 140R-CC (1848.49–1852.71 m). This hiatus separates the early Miocene (18–19 Ma) from the early Oligocene (30.1–32.0 Ma), with ~12 m.y. missing based on nannofossil and foraminiferal biostratigraphy.

Oligocene

Nannofossil abundance was generally low in Oligocene sediments, and preservation was generally poor. Samples 317-U1352C-140R-CC through 143R-CC (1852.71–1878.85 m) were constrained between 30.0 and 32.0 Ma (early Oligocene) based on the presence of *Dictyococcites scrippsae, Dictyococcites stavensis, Reticulofenestra filewiczii*, and *Chiasmolithus altus*.

The HO of *Reticulofenestra umbilicus* (32.0 Ma) was identified between Samples 317-U1352C-143R-CC and 144R-CC (1878.85–1885.85 m). The HO of *Isthmolithus recurvus* was observed between Samples 317-U1352R-145R-CC and 146R-CC (1893.50–1903.29 m; 32.5 Ma).

A hiatus spanning at least 2.3 m.y. was recognized with calcareous nannofossil evidence between the early Oligocene and late Eocene (Samples 317-U1352C-146R-CC and 147R-CC [1903.29–1916.63 m]). Sediments above the hiatus were dated at 32.5–32.9 Ma, and those below were dated at 35.2–36.6 Ma.

Eocene

Calcareous nannofossil abundances were generally low in the Eocene, and preservation was better than in the Oligocene. Samples 317-U1352C-147R-CC and 148R-CC (1916.63–1924.26 m [total depth]) contained the late Eocene species *Reticulofenestra reticulata, Isthmolithus recurvus,* and *Chiasmolithus oamaruensis,* which constrains the age of the bottom of the hole between 35.2 and 36.6 Ma.

Planktonic foraminifers and bolboformids

Planktonic foraminiferal and bolboformid biostratigraphy at Site U1352, on the upper slope, was based on the examination of core catcher samples from Holes U1352A–U1352D (Tables **T7, T8, T9, T10, T11, T12, T13, T14**). The absolute ages assigned to biostratigraphic datums follow the references listed in Table **T3** in the "Methods" chapter. The percentage of planktonic foraminifers in the cored Holocene–Eocene succession generally increased from ~70% in the upper part of the succession to ~95% in the lower part (Fig. **F25**). Preservation was variable but was generally good in the Pleistocene, moderate in the Pliocene, poor in the Miocene and Oligocene, and moderate to poor in the Eocene. Bolboformids only occurred in the late middle Miocene to early late Miocene.

Holocene

Although not identified biostratigraphically, the base of the Holocene was tentatively correlated with a distinct lithologic boundary at Section 317-U1352B-1H-1, 120 cm (1.20 m). Mudline samples from Sections 317-U1352A-1H-1, 0 cm (0.00 m), and 317-U1352D-1H-1, 0 cm (0.00 m), contained temperate assemblages and were dominated by the eutrophic species *Globigerina bulloides* s.l. They also contained abundant *Globoconella inflata* and *Turborotalita quinqueloba* and common *Truncorotalia truncatulinoides* (sinistral), *Neogloboquadrina incompta,* and *Orbulina universa*.

Pleistocene

The abundance of planktonic foraminifers varied throughout the Pleistocene sections of Holes U1352A, U1352B, and U1352D, but planktonic forms increased on average from 66% of the total foraminiferal assemblage in the upper part of the section to 74% in the lower part. This is consistent with deposition under suboceanic conditions on the upper slope. Preservation was generally good, and planktonic assemblages were dominated by small, thin- to thick-walled specimens. Larger thick-walled forms were found in some samples, especially in greenish gray sandy marls, where temperate species were more common.

The Pleistocene succession included several useful planktonic foraminiferal bioevents, although primary age control was provided by calcareous nannofossils. *Hirsutella hirsuta* (0–0.34 Ma) was found in Samples 317-U1352B-19H-CC (173.71 m) and 317-U1352D-14H-CC (130.26 m). *Truncorotalia truncatulinoides* (0–1.1 Ma) was present in most samples in the upper part of the succession (Samples 317-U1352A-1H-CC through 4H-CC [4.21–33.43 m], 317-U1352B-1H-CC through 19H-CC [7.93–173.71 m], and 317-U1352D-1H-CC through 14H-CC [3.55–127.61 m]). The HO of *Globoconella puncticuloides* was recognized as a very well defined event in Sample 317-U1352B-22H-CC (198.87 m), ~20 m below the LO of the Haweran marker species *Hirsutella hirsuta*. It occurred persistently below this level down to the early Pliocene. The HO of *Gc. puncticuloides* was dated at 1.5 Ma at ODP Site 1123 (Cooper, 2004), but in Hole U1352B calcareous nannofossil and diatom dating suggests it occurs between 0.44 and 0.70 Ma. This suggests the disappearance of this species occurred ~1 m.y. later in the cold waters of the Canterbury Basin than in the warmer subtropical water surrounding Site 1123. *Globoconella* cf. *puncticuloides,* a dis-

tinctly inflated form with a flattened dorsal surface, occurred in most samples with *Gc. puncticuloides* between Samples 317-U1352B-24H-CC and 94X (217.96–821.74 m) and 317-U1352C-7R-CC and 43R-CC (671.20–1019.69 m). This distinctive form has a pustulate ultrastructure similar to *Truncorotalia crassaformis,* but it is distinguished from the latter species by its low-arched rather than slitlike aperture.

The abundance of the subantarctic species *Neogloboquadrina pachyderma* was highly variable in the Pleistocene succession. This cold-water species was common and sometimes dominant in gray mud lithologies and was often associated with high numbers of *Gc. puncticuloides*. Interbedded greenish gray sandy marls contained lower abundances of *Nq. pachyderma,* and the temperate species *Neogloboquadrina incompta* and the eutrophic species *Globigerina bulloides* s.l. and *Turborotalita quinqueloba* were generally more common. Subtropical species were absent except for rare occurrences of *Globigerinella aequilateralis* in Samples 317-U1352D-7H-CC (60.32 m) and 317-U1352B-50X-CC (427.34 m) and a single specimen of *Globigerinoides* cf. *ruber* in Sample 317-U1352B-21H-CC (189.06 m).

Pliocene

Tentative biostratigraphic evidence indicates that the late Pliocene is missing at Site U1352 (see discussion below).

Planktonic foraminifers were abundant and moderately well preserved in the middle Pliocene section in Samples 317-U1352B-61X-CC through 94X-CC (525.34–821.74 m) and 317-U1352C-2R-CC through 29R-CC (576.47–884.91 m) and moderate to poorly preserved in the early Pliocene section in Samples 317-U1352C-30R-CC through 72R-CC (894.37–1266.38 m). The abundance of planktonic foraminifers varied, but on average abundances increased down through the Pliocene from ~74% at the top of the section to 85% at the base. Such abundances are consistent with deposition under suboceanic conditions on the upper to middle slope.

Pliocene planktonic assemblages were dominated by *Globigerina bulloides* and other small species of *Globigerina*. *Globoconella inflata, Gc. puncticuloides, Gc.* cf. *puncticulata, Gc. puncticulata* s.s. (below Sample 317-U1352C-56R-CC [1147.41 m]), *Neogloboquadrina pachyderma, Nq. incompta, Turborotalita quinqueloba,* and related forms were common to abundant in some samples. *Orbulina universa, Truncorotalia crassaformis,* and *Tr. crassaconica* also occurred sporadically with rare *Globigerinita glutinata, Globoconella* cf. *pliozea,* and *Zeaglobigerina woodi*.

Biostratigraphically useful middle Pliocene events include the LO of *Truncorotalia crassula* between Samples 317-U1352B-60X-CC and 61X-CC (514.61–525.34 m; 2.40 Ma) and the poorly constrained HO of *Truncorotalia crassaconica*? between Samples 317-U1352B-60X-CC and 61X-CC (514.61–525.34 m; >3.09 Ma). The juxtaposition of these events suggests the presence of a hiatus at this level with at least 0.7 m.y. missing. The HO of calcareous nannofossil *Reticulofenestra ampla* (2.78 Ma) between Samples 317-U1352B-61X-CC and 62X-CC (525.34–542.58 m) and the HO of planktonic foraminifer *Zeaglobigerina woodi* (>2.7 Ma) between Samples 317-U1352B-67X-CC and 68X-CC (573.33–583.56 m) support the presence of a hiatus, but it is uncertain whether the upper Pliocene is represented in part or is completely missing.

Early Pliocene bioevents include the HO of *Globoconella subconomiozea* between Samples 317-U1352C-26R-CC and 27R-CC (855.29–864.94 m; 3.35 Ma), the LO of *Gc. inflata* s.s. and the HO of *Gc. puncticulata* s.s. between Samples 317-U1352C-56R-CC and 57R-CC (1147.41–1155.03 m; 4.3 Ma), and the HO of *Gc. pliozea* between Samples 317-U1352C-61R-CC and 62R-CC (1197.57–1206.27 m; 4.49 Ma). The LO of *Gc. puncticulata* s.s. (5.30 Ma) and the HO of *Globoconella sphericomiozea* s.s. (5.30 Ma), which serve as proxies for the Miocene/Pliocene boundary, were reliably identified between Samples 317-U1352C-72R-CC and 73R-CC (1266.38–1283.95 m).

Miocene

Planktonic foraminifers in Hole U1352C were abundant and moderately to poorly preserved in the late Miocene (Samples 317-U1352C-73R-CC through 101R-CC [1283.95–1486.78 m]), abundant to common and poorly preserved in the middle Miocene (Samples 317-U1352C-102R-CC through 121R-CC [1496.50–1678.60 m]), and common to few and poorly preserved in the early Miocene (Samples 317-U1352C-122R-CC through 139R-CC [1690.44–1848.49 m]). Foraminiferal tests were often recrystallized and infilled with sparry calcite, and some also exhibited microcrystalline overgrowths (Fig. **F26**). Planktonic foraminiferal abundances generally increased down through the Miocene succession of Hole U1352C from 85% of the total foraminiferal assemblage at the top of the section to 94% at the base. Such abundances are consistent with deposition on the lower slope and base of slope under suboceanic and oceanic conditions.

Planktonic assemblages in the Miocene succession were characterized by abundant *Globigerina,* including *Gg. bulloides*. *Zeaglobigerina woodi* and *Turborotalita quinqueloba* and related forms were also present along with rare *Globigerinopsis obesa* and *Globigerinita glutinata*. Globoconellids, including *Gc. sphericomiozea*

(upper Kapitean; uppermost Miocene), *Gc. miotumida* (Tongaporutuan to upper Waiauan; upper Miocene), *Gc. miozea* (Lillburnian to Altonian; middle to upper lower Miocene), *Gc. zealandica* (middle Altonian; middle lower Miocene), and *Gc. praescitula* (early Altonian; lower Miocene), were present in respective parts of the Miocene section, but abundances varied. *Neogloboquadrina pachyderma* and *Nq. incompta* were present in the late Miocene, *Paragloborotalia mayeri* s.l. was abundant in the early late Miocene, *Orbulina universa* occurred sporadically down into the middle Miocene, and *Orbulina suturalis* was present in the early middle Miocene. Subtropical species were absent, except for single specimens of *Globigerinoides trilobus* in the middle Miocene (Sample 317-U1352C-105R-CC [1534.20 m]) and lower Miocene (Sample 317-U1352C-128R-CC [1743.51 m]).

The uppermost Miocene (upper Kapitean) species *Gc. sphericomiozea* s.s. (5.30–5.60 Ma) was common from Samples 317-U1352C-73R-CC to 90R-CC (1283.95–1394.62 m). Its presence immediately above the HOs of *Globoconella miotumida* (7.07 Ma), *Bolboforma metzmacheri* s.s. (8.85 Ma), and *Bolboforma subfragoris* s.l. (10.58 Ma) suggests a hiatus in the late Miocene section between Samples 317-U1352C-90R-CC and 91R-CC (1394.63–1409.66 m) with at least 3.25 m.y. missing. The concurrence of these two bolboformid species is also somewhat enigmatic because they have range zones that are separated in time, which suggests there may be another shorter hiatus between Samples 317-U1352C-91R-CC and 93R-CC (1409.66–1419.06 m).

The HCO of *Paragloborotalia mayeri* s.l. (10.97 Ma) occurred between Samples 317-U1352C-95R-CC and 96R-CC (1446.91–1448.00 m) and the LO of *Bolboforma subfragoris* s.l. (11.64 Ma) occurred between Samples 317-U1352C-101R-CC and 102R-CC (1486.78–1496.50 m). The HO of *Globoconella conica* (12.98 Ma) was noted immediately below the LO of *B. subfragoris* s.l., which suggests a hiatus between Samples 317-U1352C-101R-CC and 102R-CC (1486.78–1496.50 m). *Bolboforma* cf. *reticulata*, a bolboformid that has never before been recognized in New Zealand, occurred at the same level as the HO of *Gc. conica* and was not recorded in any other sample. Sample 317-U1352C-103R-CC (1515.94 m) is also significant in that it contained the HO of *Gc. miozea*, the LO of *Orbulina universa* (13.63 Ma), and *B.* cf. *robusta*, one sample above the HO of *Or. suturalis* in Sample 104R-CC (1525.67 m). The close stratigraphic spacing of these bioevents between Samples 317-U1352C-103R-CC and 104R-CC (1515.94–1525.67 m) suggests that the section is condensed or that parts of the section are missing.

The LO of *Globoconella miozea* (16.7 Ma), a bioevent that marks the base of the upper Altonian, was identified between Samples 317-U1352C-125R-CC and 126R-CC (1714.42–1725.45 m; 16.7 Ma). Other bioevents include the poorly constrained HO of *Globoconella praescitula* (16.7 Ma) between Samples 317-U1352C-123R-CC and 124R-CC (1697.39–1707.63 m), the HO of *Gc. zealandica* (16.7 Ma) between Samples 317-U1352C-125R-CC and 126R-CC (1714.42–1725.45 m), the HO of *Gc. incognita* (18.3 Ma) between Samples 317-U1352C-131R-CC and 132R-CC (1769.18–1777.59 m), and the poorly constrained HO of *Zeaglobigerina connecta* (18.5 Ma) between Samples 317-U1352C-135R-CC and 136R-CC (1810.4–1819.56 m). The early Miocene marker species *Catapsydrax dissimilis* was also tentatively identified in Samples 317-U1352C-133R-CC (1789.6 m) and 135R-CC (1810.40 m). The range of this species is reported by Cooper (2004) to extend to the top of the lower Miocene Otaian Stage (18.7 Ma), but its HO in Hole U1352C appeared to be slightly younger. This is consistent with unpublished data from ODP Site 1171 (50°S) on the South Tasman Rise, where *Cs. dissimilis* occurs in conjunction with the early Miocene (lower Altonian) species *Gc. praescitula* (M.P. Crundwell, pers. comm., 2009).

Oligocene

The top of the Oligocene was identified using calcareous nannofossil evidence between Samples 317-U1352C-139R-CC and 140R-CC (1848.49–1852.71 m). This coincides with a significant change in planktonic foraminiferal assemblages at the same level. The HO of the early Oligocene (lower Whaingaroan) marker species *Subbotina angiporoides* was identified between Samples 317-U1352C-140R-CC and 141R-CC (1852.71–1862.57 m). These biostratigraphic events suggest the presence of a major hiatus (Marshall Paraconformity) between Samples 317-U1352C-139R-CC and 140R-CC (1848.49–1852.71 m), where at least 12 m.y. is missing.

Foraminiferal assemblages in the Oligocene (Samples 317-U1352C-140R-CC through 146R-CC [1852.71–1903.29 m]) are characterized by low abundances and poor preservation, which is attributed to the cemented nature of the Oligocene limestone. Planktonic foraminifers in the Oligocene composed >95% of the total foraminiferal assemblage, except in Sample 317-U1352C-144R-CC (1885.85 m). Such abundances are consistent with basin-floor deposition under open oceanic conditions. Planktonic assemblages include *Zeaglobigerina euapertura, Subbotina angiporoides, Globorotaloides suteri,* and *Zg. brevis*?

Eocene

The top of the Eocene is marked by the HO of the late Eocene (Runangan) marker species *Globigerinapsis index* (34.4–36.0 Ma) between Samples 317-U1352C-146R-CC and 147R-CC (1903.29–1916.63 m). The HO of this species coincides with a change in lithology to less cemented chalky limestone and more common, better preserved foraminiferal assemblages. Calcareous nannofossil dating (Table T5) suggests the presence of a hiatus between the early Oligocene and the late Eocene with at least 2.3 m.y. missing.

Eocene planktonic foraminiferal assemblages are characterized by abundant *Globigerinapsis index,* along with *Subbotina minima, Tenuitella gemma*?, and *Turborotalita ciperoensis*. Planktonic foraminifers and calcareous nannofossils indicate a late Eocene age of 35.2–36.0 Ma at the bottom of the hole.

Benthic foraminifers

Benthic foraminifers from 242 core catcher samples from Holes U1352A–U1352D were examined (Table T15). Benthic foraminifer abundances varied throughout the cored section, ranging from rare to dominant. Preservation was generally good in the Pleistocene, poor to moderate in the Pliocene and Miocene, and poor in the Oligocene and Eocene. Eleven benthic foraminiferal bioevents were identified at Site U1352 (Table T5). The calibration of benthic bioevents, in general, was poorly constrained, but these bioevents provided useful age control where planktonic foraminifers and calcareous nannofossils were poorly represented.

Holocene–Pleistocene

The HO of *Proxifrons advena* (~0.4 Ma; Table T5) was identified between Samples 317-U1352B-14H-CC and 15H-CC (130.26–141.17 m). The HO of *Bolivinita pliozea* (0.6 Ma) was identified between Samples 317-U1352B-16H-CC and 17H-CC (150.74–155.99 m). The latest Pleistocene–Holocene (Haweran) restricted species, *Loxostomum karrerianum* (0–0.34 Ma), was recognized in Samples 317-U1352D-1H-CC (3.55 m) and 8H-CC (70.00 m) and 317-U1352B-20H-CC (180.38 m). These ages are generally consistent with those from calcareous nannofossils and planktonic foraminifers.

Pliocene

The HO of *Haeuslerella morgani* (3.62–5.30 Ma) was identified between Samples 317-U1352B-64X-CC and 65X-CC (557.28–562.35 m). The HO of the deep middle bathyal species *Hopkinsina mioindex* (3.62 Ma) was recognized between Samples 317-U1352C-64R-CC and 65R-CC (1217.80–1222.21 m). The stratigraphic suppression of this species relative to planktonic events suggests that the disappearance of *H. mioindex* in Hole U1352B might have been controlled by water depth.

Miocene

The LO of *Uvigerina pliozea* (5.30 Ma) was observed between Samples 317-U1352C-84R-CC and 85R-CC (1342.48–1352.39 m), ~50 m above the Miocene/Pliocene boundary, located between Samples 317-U1352C-72R-CC and 73R-CC (1266.38–1283.95 m; 5.33 Ma) using planktonic foraminiferal evidence. Other useful benthic foraminifer bioevents include a single record of *Loxostomum truncatum* (8.95–12.76 Ma) in Sample 317-U1352C-94R-CC (1438.43 m), the LO of *Notorotalia taranakia* (11.01 Ma) between Samples 317-U1352C-95R-CC and 96R-CC (1446.91–1448.00 m), occurrences of *Notorotalia wilsoni* (11.01 Ma) in Samples 317-U1352C-95R-CC and 96R-CC (1446.91–1448.00 m), and the LO of *H. morgani* (~11.01 Ma) between Samples 317-U1352C-95R-CC and 96R-CC (1446.91–1448.00 m). The LO of *H. mioindex* (15.10 Ma) was tentatively recognized between Samples 317-U1352C-104R-CC and 105R-CC (1525.67–1534.20 m). These events generally agree with other microfossil dating.

Oligocene–Eocene

Sample 317-U1352C-147R-CC (1916.63 m) contained the late Eocene to early Oligocene species *Cibicidoides parki*.

Paleowater depths

Paleowater depths were estimated by the analysis of benthic foraminiferal assemblages from Holes U1352A–U1352D (Table T15; Fig. F27). Terminology used for paleowater depth estimates is given in Figure F7 in the "Methods" chapter.

Holocene–middle Pliocene sediments were dominated by inner to outer shelf benthic foraminiferal taxa, although the rare but persistent presence of bathyal marker species suggests the shelfal taxa composing the bulk of the benthic assemblage were transported downslope. Paleodepths generally increased downhole to lower bathyal depths in the lower part of the cored succession. Middle to deep bathyal taxa occurred in lower Pliocene and older sediments, which is consistent with a general downhole increase in the abundance of planktonic foraminifers through the progradational foreset sequence into the bottom sets and basin-floor facies. It also coincides with the change from suboceanic to open oceanic conditions.

Estimates of paleowater depths, based on the general composition of benthic foraminiferal assemblages, ranged from outer shelf to upper bathyal during the middle–late Pleistocene. The estimated upper depth limits are shallower than seismic data interpretation at this site suggests, which is consistent with the bulk of the assemblage being reworked downslope. The subtidal to inner shelf species *Elphidium charlottense* and *Notorotalia aucklandica* were abundant in upper Pleistocene Samples 317-U1352A-1H-CC through 5H-CC (4.21–43.06 m) and 317-U1352D-1H-CC through 10H-CC (3.55–88.92 m). These species occurred consistently with the outer shelf to uppermost bathyal species *Globocassidulina canalisutulata* (Eade, 1967) down to Sample 317-U1352D-14H-CC (127.61 m). In Samples 317-U1352B-1H-CC through 31H-CC (7.93–272.44 m), outer shelf species *G. canalisutulata* and *Nonionella flemingi* were dominant and the upper bathyal indicator *Trifarina angulosa* was abundant, particularly between Samples 317-U1352B-22H-CC and 28H-CC (198.87–250.70 m).

In the lower Pleistocene to upper middle Pliocene section between Samples 317-U1352B-32H-CC and 65X-CC (280.84–562.35 m), the outer shelf species *Nonionella flemingi* and *Notorotalia profunda* were dominant. Uvigerinids that characterize deeper water, including *Uvigerina peregrina* and *Trifarina angulosa,* were present throughout most of this section and indicate deposition in upper bathyal water depths. The middle to lower bathyal species *Bulimina exilis* (van Morkhoven et al., 1986) was also present sporadically between Samples 317-U1352B-38X-CC and 48X-CC (310.85–408.18 m), suggesting even deeper bathyal water depths in this interval.

In the lower Pliocene section between Samples 317-U1352B-66X-CC and 94X-CC (572.40–821.74 m) and 317-U1352C-2R-CC and 65R-CC (576.47–1222.21 m), the outer shelf species *Notorotalia profunda* was abundant and was associated with upper bathyal uvigerinids, including *Uvigerina peregrina, Astrononion* spp., and *Bolivinita pliozea. Notorotalia taranakia* was also abundant in this same interval; however, the ecological preferences of this species are not fully understood. *Melonis pompilioides* (an extant deep lower bathyal species) occurred sporadically between Samples 317-U1352C-2R-CC and 65R-CC (576.47–1222.21 m), becoming more common in the lowermost Pliocene between Samples 317-U1352C-56R-CC and 64R-CC (1147.41–1217.80 m). Paleodepth markers that are considered to be in situ suggest that paleowater depths increased downhole from outer shelf–uppermost bathyal depths in the uppermost part of the lower Pliocene section to lower bathyal depths in the lowermost part of the lower Pliocene section.

Assemblages in the lowermost Pliocene to uppermost Miocene section, between Samples 317-U1352C-65R-CC and 88R-CC (1222.21–1379.88 m), are characterized by a decrease in shelfal species and a reciprocal increase in upper bathyal marker species, including *Cibicidoides neoperforatus* and *Uvigerina* spp.

The upper Miocene to upper middle Miocene section between Samples 317-U1352C-89R-CC and 104R-CC (1386.04–1525.67 m) was dominated by benthic taxa indicative of middle bathyal water depths, including *Karreriella bradyi* and *Sigmoilopsis schlumbergeri,* and occasional specimens of the deep middle bathyal species *Hopkinsina mioindex*.

In the middle Miocene section between Samples 317-U1352C-105R-CC and 112R-CC (1534.20–1597.08 m), benthic foraminifers were poorly preserved and too sparse for reliable estimates of paleodepths based on benthic assemblages. Deep middle to deep lower bathyal water depths are inferred, however, based on the presence of *Cibicidoides robertsonianus* and *Melonis dorreeni,* which is morphologically similar to the extant deep lower bathyal species *M. pompilioides*. Benthic foraminifers were very sparse to absent in samples from the middle Miocene to Eocene (Samples 317-U1352C-113R-CC through 148R-CC; 1611.72–1924.26 m).

Diatoms

Samples 317-U1352A-1H-CC through 5H-CC (4.21–43.06 m) were barren of diatoms (Table **T16**).

Core catcher samples from Hole U1352B were examined for diatoms (Table **T16**). In the majority of the 50 samples containing diatoms, abundances were low, and preservation was moderate to poor. Several robust diatom species with thickly silicified valves (e.g., *Paralia sulcata, Thalassionema nitzschoides,* and *Chaetoceros* resting spores) were better preserved than delicate forms with weakly silicified valves.

The HO of marker species *Fragilariopsis fossilis* (0.70 Ma) was identified in Sample 317-U1352B-23H-CC (208.46 m), although this species occurred only sporadically below this level and the reliability of its HO is uncertain. A single record of *Actinocyclus karstenii* (HO 1.73 Ma) was also identified in Sample 317-U1352B-55X-CC (469.84 m). The distribution of these species is consistent with calcareous nannofossil dating.

Most diatom assemblages in Hole U1352B contained marine resting spores of the genus *Chaetoceros,*

which is indicative of high productivity in nearshore upwelling regions and coastal areas. Also included was a mixture of coastal, brackish, and freshwater species, which suggests marine deposition with an influence from coastal upwelling and some river input.

Core catcher samples from Hole U1352C were examined for diatoms, and their distribution is reported in Table **T15.** Diatoms were only found in six middle Pliocene samples from this hole, between Samples 317-U1352C-7R-CC and 12R-CC (671.20–719.46 m). Preservation was moderate to poor. *Cyclotella,* a genus diagnostic of brackish and freshwater, occurred in greater abundances than other taxa in these samples. Other diatoms included coastal and brackish water species. The diatom assemblage shows evidence of some river and/or estuarine input.

All core catcher samples from Samples 317-U1352D-1H-CC through 14H-CC were examined for diatoms (3.55–127.61 m) (Table **T15**). Diatoms were found in 7 of the 14 samples examined and were relatively rare. The assemblages and preservation were similar to those of samples from the equivalent section in Hole U1352B. The presence of a single record of *Hemidiscus karstenii* (HO 0.30 Ma) in Sample 317-U1352D-12H-CC (108.55 m) is consistent with calcareous nannofossil dating.

Macrofossils

Macrofossils were examined in cored sediments from all Site U1352 holes. Provisional identification, age, and habitat preference are provided in Table **T17.**

Paleomagnetism

Paleomagnetic analyses at Site U1352 included routine measurement and partial demagnetization of natural remanent magnetization (NRM) of archive section halves and some discrete samples from the working halves of cores. Rock magnetic experiments were also performed on these discrete samples. All depths in this section are reported in m CSF-A.

Section-half measurements

NRM was measured on all archive section halves from Holes U1352A–U1352D unless the core material was too heavily disturbed by the drilling process. A single demagnetization step at peak fields of 20 mT was applied to all measured sections. The NRM intensities of the sediments typically range from 10^{-4} to 10^{-2} A/m and tend to decrease with depth. The short records from Holes U1352A and U1352D are comparable to and entirely overlapped by the record from Hole U1352B (Figs. **F28, F29, F30**) and are therefore not shown. The deepest record from Site U1352 was from Hole U1352C, which overlaps the record from Hole U1352B for ~200 m (Fig. **F31**).

Hole U1352B

Hole U1352B was cored to 246.2 m using the APC system with both nonmagnetic core barrels (Cores 317-U1352B-1H through 27H [246.2 m]) and magnetic core barrels (Cores 317-U1352B-28H through 36H [246.2–297.0 m]). The remainder of the hole was cored using the XCB system. Distinct changes in magnetic behavior were observed where coring systems were changed (Fig. **F28**). In the nonmagnetic APC cores, NRM inclinations are usually steeply positive (~70°) with occasional intervals of shallow or negative inclination. After demagnetization at 20 mT, inclinations are steep and negative (approximately –60°). Declination varies between cores but is consistent, both before and after demagnetization, within individual cores.

Declination variability between cores suggests that this signal was not strongly overprinted by the drilling process (Richter et al., 2007). The first 18 APC cores (317-U1352B-1H through 18H [0–165.7 m]) were oriented using the Flexit tool, which records the orientation of the APC core barrel. Data from this tool were used to orient the cores with respect to true north (Fig. **F30**). Orienting core barrels brings the declination of NRM after 20 mT alternating-field (AF) demagnetization into good agreement between cores. The mean orientation is a declination of 27.7° and an inclination of –60.1°.

APC cores were recovered using magnetic core barrels between 246.2 and 297.0 m (Cores 317-U1352B-28H through 36H). This depth interval shows an increase in NRM intensity from ~2 × 10^{-3} to ~9 × 10^{-3} A/m and a slight increase in susceptibility. Declinations are consistently grouped around north during this interval, which comprises nine cores. Inclinations are fairly steeply positive throughout (~60°). Remanence does not change after AF demagnetization and is interpreted to reflect a drilling overprint that was not removed.

The XCB system was used to core from 297 m to the total depth of Hole U1352B (Cores 317-U1352B-37X through 94X [830.9 m]). Intensity varies throughout this interval. Declinations cluster close to north both before and after AF demagnetization at 20 mT, suggesting unsuccessful removal of the drilling overprint. Inclinations are typically fairly steeply positive (~55°) but do vary, with some cores showing shallower or negative inclinations.

Hole U1352C

Hole U1352C was cored with the RCB system from 575 m to a total depth of 1928 m (Fig. F31). Both recovery and intensity are low downcore to ~900 m, and a low signal to noise ratio is apparent downcore to ~1200 m. Below this interval, NRM has a consistently steep positive inclination (~70°) and a northward declination before and after demagnetization. This indicates a drilling overprint that was not removed. Intensity peaks at 1×10^{-2} A/m at ~1700 m and drops significantly between 1850 and 1870 m from ~1×10^{-3} A/m above to 1×10^{-4} A/m below. At this point, data again show a wide spread as the noise level of the SRM was approached. Demagnetization at 20 mT removed up to 80% of the intensity of samples from Hole U1352C.

The boundaries between low-intensity intervals, noisy intervals, and higher intensity intervals with tightly grouped orientations correlate to lithologic unit and subunit Boundaries IIA/IIB (1189 m) and IIC/III (1852.64 m; Marshall Paraconformity), as described in "Lithostratigraphy."

Discrete measurements

Pairs of cubes were extracted from the working half of each core for shipboard analyses. Ten of these pairs were selected to characterize the sediments in Hole U1352B. Seven samples from lithologic Subunit IIC, which was found only in Hole U1352C, were also demagnetized with alternating fields.

NRM demagnetization

Seventeen samples were AF demagnetized up to 80 mT. The signal to noise ratio is poor, but drilling overprints persist to ~30 mT. Some samples (e.g., 70.33 m; Fig. F32A) show a characteristic component that demagnetizes toward the origin. Others (e.g., 255.00 m; Fig. F32C) appear to acquire a gyro-remanent magnetization (GRM) after 40 mT.

Ten samples were thermally demagnetized at 30°–40° intervals up to 460°C (Fig. F32B, F32D). Susceptibility was measured after each heating step to monitor any chemical alteration resulting in new magnetic minerals (Fig. F32G). All samples increase in susceptibility by 460°C, and four samples (at 70.32, 105.84, 230.99, and 255.03 m) show a slight (5%–10%) decrease in susceptibility between 310° and 430°C. The drilling overprint is removed by ~150°–200°C, and a characteristic component can be resolved before thermal alteration occurs.

Demagnetization of discrete samples confirmed that a subvertical overprint persists in the samples beyond the 20 mT demagnetization step applied to section-half samples. This overprint was removed in most cases by further demagnetization. Magnetic mineralogy is not fully constrained, but the acquisition of a GRM in some samples at 40 mT and the thermal alteration above 310°C suggest the presence of some iron sulfides in the sediment.

IRM acquisition and demagnetization

An isothermal remanent magnetization (IRM) was imparted to 10 samples from Hole U1352B in a stepwise manner up to 1 T (Fig. F33A) followed by backfield acquisition, which revealed fairly uniform behavior. All samples appear to saturate between 400 and 600 mT with coercivities of remanence between 40 and 75 mT.

The same 10 samples then had a 1 T IRM imparted and were stepwise AF demagnetized up to 80 mT (Fig. F33B–F33C). A clear grouping of significantly higher saturation remanence is evident in four samples (at 70.33, 202.58, 221.68, and 326.96 m) (Fig. F32B). This group also shows a softer magnetization and loses a higher proportion of this magnetization at 80 mT peak fields (Fig. F32C). The presence of these two behaviors upon AF demagnetization of IRM may suggest the presence of two low-coercivity mineralogies and/or grain-size fractions. Median destructive fields are between 40 and 50 mT for all samples.

Magnetostratigraphy

A pervasive drilling overprint prevented magnetostratigraphic interpretation of much of Site U1352. Biostratigraphic evidence suggests that the Brunhes/Matuyama boundary lies between Samples 317-U1352B-24H-CC and 30H-CC (217.9–266.9 m), constrained between the presence of *Fragilariopsis fossilis* (diatom; HO = 0.70 Ma) and the HCO of *Reticulofenestra asanoi* (nannofossil; 0.91 Ma) in these two samples, respectively. Some noisy intervals were encountered within this range, where inclinations are not clearly negative (normal). From Core 317-U1352B-28H (246.2 m) downward, magnetic core barrels were used, and characteristic magnetizations could not be isolated. Therefore, it was not possible to identify the Brunhes/Matuyama boundary, despite a promising trend toward positive inclinations throughout Core 317-U1352B-27H.

No further magnetostratigraphic constraints could be given at this site because of the pervasive drilling overprint. This overprint may eventually be removed by the full demagnetization of working-half cube samples onshore.

Physical properties

Gamma ray attenuation (GRA) densitometer bulk density, magnetic susceptibility (loop sensor; MSL), NGR, and *P*-wave velocity measured with the *P*-wave logger (PWL) were measured on whole-round core sections from Holes U1352A–U1352C. Additionally, magnetic susceptibility (point sensor; MSP) and spectrophotometry and colorimetry were measured on section halves from the same holes. Whole-round measurements on XCB and RCB cores were degraded in quality because of drilling disturbance associated with coring and the slightly smaller diameters of XCB and RCB cores relative to the core liner. Discrete *P*-wave velocity (measured using the *P*-wave caliper [PWC] and *P*-wave bayonets [PWB]) and moisture and density (MAD) were measured on section halves from Holes U1352B and U1352C. Sediment strength was determined only on section halves from Hole U1352B. Unless otherwise noted, all depths in this section are reported in m CSF-A.

Gamma ray attenuation bulk density

GRA bulk density was measured with the densitometer at 5 cm intervals (measurement time = 5 s). Below 1361.4 m, the sampling resolution was increased to 2.5 cm (Section 317-U1352C-87R-1). The raw data range from –0.42 to 2.467 g/cm^3 in Hole U1352B and from –0.417 to 2.606 in Hole U1352C (Fig. **F34**). Low values are assumed to represent cracks in the cores, gas, and/or incomplete filling of the cores with sediment. Thus, only bulk density values >1.4 g/cm^3 were compared with MAD-derived bulk density and downhole GRA density estimates (Figs. **F35, F36**). GRA bulk density records from Holes U1352B and U1352C show the same long-term trends even where XCB cores from Hole U1352B overlap RCB cores from Hole U1325C.

A comparison of GRA densitometer and MAD data from samples in Hole U1352B (Fig. **F35**) yields results similar to those from Hole U1351B. That is, GRA data tend to be lower than, but roughly parallel to, MAD bulk density estimates. Lower bulk density estimates mainly reflect incomplete filling of the core liner as well as cracks in the core caused by gas expansion. These features do not affect MAD results. In general, higher GRA bulk density values are consistent with MAD estimates, and both methods reveal a trend toward higher bulk densities with depth. The increase and broadening of bulk density estimates across the lithologic Subunit IB/IC boundary (Fig. **F35A–F35B**) may reflect the sampling of increasingly calcite-cemented soft sediments.

In Hole U1352C, both MAD and GRA bulk density estimates generally increase with depth (Fig. **F36**). As the sediments become increasingly cemented, filled core liners become increasingly rare. In a few locations, GRA estimates reach those obtained by MAD analyses. The two trends of MAD data between 550 and 1200 m (Fig. **F36A–F36B**) are a result of cementation, with the higher MAD bulk densities reflecting more highly indurated strata (see **"Moisture and density"**). GRA data in this region (lithologic Subunit IIA; see **"Lithostratigraphy"**) include measurements of both denser cemented sediments and less dense uncemented sediments. Lower GRA values (Fig. **F36B**) suggest that parts of the core liner were not filled. Below 1200 m (lithologic Subunit IIB), unlithified strata are rare and GRA results are consistently lower than MAD results by ~0.2 g/cm^3 (Fig. **F36A, F36C**), which can be attributed to the ~10% smaller diameter of the RCB cores relative to the APC core diameter used for calibration.

A comparison of bulk density generated by the different laboratory methods and expanded to include downhole logging results in Hole U1352B is shown in Figure **F35.** For this comparison, only results from 100 to 500 m are considered because downhole density logs were acquired only in this interval. Very low densities measured by the downhole tool are spurious and may reflect hole enlargement generated by drilling (see **"Downhole logging"**). Beginning at ~280 m, density log values that exceed MAD values may be the result of the downhole tool sensing the more indurated beds not sampled via APC and XCB coring.

Magnetic susceptibility

Magnetic susceptibility (MSL and MSP) was measured at 5 cm intervals (measurement time = 2 s). Because of the excellent core quality and time-consuming RCB coring at greater depths, the sampling resolution for MSL data was increased to 2.5 cm below 1361.4 m (starting with Section 317-U1352C-87R-1) in order to provide a more detailed magnetic susceptibility record of the lowermost cores from Hole U1352C.

Raw MSL values are 3.7–39.0 instrument units for Hole U1352A, 0–97.2 instrument units for Hole U1352B, and 0–28.1 instrument units for Hole U1352C. The data were filtered using a Gaussian low-pass filter (30 passes; Fig. **F34**). The overall less noisy loop sensor data, lower amplitudes, and a shift to lower values in Hole U1352C compared to Hole U1352B may have resulted from the mainly cemented sediment and the smaller diameter of RCB cores relative to the core liner.

Magnetic susceptibility was measured at 5 cm intervals on the Section Half Multisensor Logger (SHMSL) using the MSP (Fig. **F34**). These measurements were

made on all sections unless drilling disruption or surface disruption precluded the collection of meaningful results. MSP measurements made on section halves from Holes U1352A and U1352B are noisier than MSL data; however, the key trends are still resolvable after 30-pass Gaussian filtering of the data, and these trends correlate well with MSL data. The noise level in the MSP data increases markedly at ~520 m in Hole U1352B. A faulty MS2F sensor was suspected to cause this deterioration in data quality, and the unit was replaced at Core 317-U1352C-4R. The replacement MS2F sensor measured slightly higher instrument unit values than the older unit, and data quality improved using this new sensor.

In general, higher magnetic susceptibility values from both instruments correspond to darker sediments, and lower values correspond to lighter sediments (see **"Spectrophotometry and colorimetry"** and Fig. **F37**). In the uppermost 275 m, both MSP and MSL data display a cyclicity, with peaks and lows (Fig. **F34**) that are broadly similar to the magnetic susceptibility record from Site 1119 (Shipboard Scientific Party, 1999b) for the last glacial cycle. For example, three peaks between 50 and 70 m in Hole U1352B (Fig. **F38**) correlate with similar peaks from Holes 1119B and 1119C (between 36 and 46 m) that were interpreted as representing marine isotope Stage (MIS) 5 (Shipboard Scientific Party, 1999b). Between 555 and 630 m, magnetic susceptibility, NGR, and GRA density show a conspicuous negative peak followed by a corresponding positive peak between 630 and 655 m (Fig. **F34**). Below ~1500 m, magnetic susceptibility and NGR signals decrease overall, whereas color reflectance increases, likely reflecting increasing carbonate content (see **"Spectrophotometry and colorimetry"**).

Below the Marshall Paraconformity at ~1852.6 m (see **"Lithostratigraphy"**), magnetic susceptibility measured with both the MSP and MSL becomes negative, indicating the predominance of diamagnetic limestone.

Natural gamma radiation

NGR was measured on all core sections at 10 cm intervals down to 1333 m (Section 317-U1352C-82X-1). The values measured range from near zero to >60 counts per second (cps), with higher values associated with muddy lithologies and lower values associated with sands (Fig. **F34**).

A sustained downhole decrease in NGR from ~55 to ~40 cps occurs between the seafloor and ~1400 m, consistent with decreasing radiogenic terrigenous material and increasing carbonate content. This decrease is punctuated by a major NGR perturbation (with matching displacements in the magnetic susceptibility records) between 555 and 655 m, which comprises a negative excursion to <20 cps, followed by a positive excursion to >50 cps. No obvious lithologic explanation exists for this feature.

A further rapid decrease in NGR to ~15 cps occurs just above the Marshall Paraconformity. Below the unconformity, in the Amuri Limestone facies, NGR reaches its lowest levels of 3–5 cps, indicating very low terrigenous content.

A marked NGR cyclicity is apparent in the uppermost 275 m (Fig. **F38**), similar to that observed at nearby Site 1119. Postcruise analysis will likely permit the development of a timescale for this interval by comparing it with the Site 1119 age model, which Carter and Gammon (2004) constructed using an inverted NGR record that apparently forms a close New Zealand proxy for global MIS stages to at least 2.4 Ma. Assigning a provisional age of 127 ka to the inferred MIS 5e peak at ~63 m at Site U1352 gives an average sedimentation rate of ~50 cm/k.y. for the last glacial–interglacial cycle, compared with 37 cm/k.y. at Site U1351 and 20 cm/k.y. at Site 1119 over the same interval.

P-wave velocities

P-wave velocity measurements were recorded with different coverage on sections from Holes U1352A, U1352B, and U1352C using the PWL, PWC, and PWB (Figs. **F39, F40**). The differences in coverage depend on core condition. Poor results were caused by signal attenuation and sediment cracking resulting from high gas content in APC and XCB cores and sediment disturbance related to XCB coring. PWL measurements on whole-round sections from Holes U1352A and U1352B at 4 cm intervals yielded poor results below ~20.0 and 14.0 m, respectively (Fig. **F39A–F39B**). PWB *P*-wave velocities were measured only on the uppermost 20 m (*y*-axis) and 10 m (*z*-axis) of core, respectively, from Hole U1352B (Fig. **F39C**). Excellent PWC results were obtained from mainly cemented sediments in RCB cores (Fig. **F40A**). PWC measurements were conducted on the uppermost 20 m of core from Hole U1352B (Fig. **F39C**) and continuously on nearly every section half from Hole U1352C (Fig. **F40A**).

P-wave velocities (PWL, PWB, and PWC) from Holes U1352A and U1352B range from ~1400 to ~1800 m/s, whereas *P*-wave velocities (PWC) from Hole U1352C range from ~1600 to ~5900 m/s. The significantly higher velocities in XCB cores are probably caused by good conductive contact with the mainly cemented material. All velocity measurements from Holes U1352A and U1352B show an abrupt change

from lower to higher values between 1.5 and 2 m. A similar change was observed in the uppermost ~2.0 m of Hole U1351B. Scattered values in the lowermost part of the PWL curves are attributed to decreased core quality (Fig. F39). Whole-round and discrete *P*-wave velocity measurements from Hole U1352B are positively correlated. PWC and PWB velocity measurements abruptly decrease between 12 and 14 m, approximately the same depth at which the PWL measurements terminate. At greater depth, PWC values from Hole U1352C are inversely correlated with porosity (Fig. F40C), showing a slight increase below 1255 m (average = ~2500–3500 m/s) and a large increase between 1500 and 1670 m (average = ~3500–4000 m/s) (Fig. F40B). Between 1670 and ~1795 m, velocity is continuously high (average = ~3900 m/s). Below ~1795 m, *P*-wave velocity increases again to ~5900 m/s. A slight increase in *P*-wave velocity was observed below the Marshall Paraconformity at ~1852.6 m (see "Lithostratigraphy"). The unexpectedly high velocities below 1255 m require a revision of the present traveltime/depth interpretation of seismic records in this area.

Spectrophotometry and colorimetry

Spectrophotometric measurements and associated colorimetric calculations were made on section halves at 5 cm intervals at the same positions used for MSP measurements. Color data were recorded as L*, a*, and b* variations. L* values are relatively constant in Holes U1352A and U1352B. Where Holes U1352B and U1352C overlap between 600 and 800 m, L* values are slightly but noticeably lower in Hole U1352C (Fig. F37). A clear increase in L* values occurs at ~1576 m. This increase can be attributed to a transition to paler, more carbonate-rich lithologies over this interval (see "Lithostratigraphy").

Notably, the degree of scatter in L* data also increases from Hole U1352B to Hole U1352C, and a further, more pronounced increase in scatter occurs downhole in Hole U1352C below ~1600 m. This change in L* between Holes U1352B and U1352C is due to the change from homogeneous, unlithified sediment in Hole U1352B to the more heterogeneous, lithified rock that characterizes Hole U1352C. The additional increase in L* variance downhole in Hole U1352C at ~1600 m is partly due to an increase in reflectivity difference (i.e., contrast) between the dominant pale marlstone and carbonate lithologies and the minor interbedded dark lithologies (e.g., glauconitic muddy sandstone layers; see "Lithostratigraphy"). Furthermore, the change to lithified rock in Hole U1352C is also accompanied by an increase in the occurrence of fractures within the split sections. Spectrophotometer measurements of these fractures resulted in anomalously low L* values.

The a* and b* values are less scattered than L* values, and trends are discernible (Fig. F37). b* values in Holes U1352B and U1352C increase over the uppermost ~1000 m before falling slightly downhole to the bottom of Hole U1352C. Several more abrupt changes also occur, and these are readily discernible in the filtered b* data. The position of abrupt changes in b* values matches the position of similarly abrupt shifts in a*. However, a* values do not show the same long-term trends as b*, and, as demonstrated at Site U1351, the a* record is not as variable as the b* record. In general, a* is negatively correlated with b*, and changes in these two parameters reflect changes from grayer (low b* and high a*) to more greenish lithologies (high b* and low a*).

a* and b* values for Hole U1352A do not correlate well with those for Hole U1352B between ~18 and ~54 m (i.e., the bottom of Hole U1352A). This difference may reflect a problem with instrument calibration in Hole U1352A for this depth interval because the minimum and maximum values of b* and a* in Hole U1352A are anomalous compared to values from the rest of the site. In addition, as observed in L* data, a* and b* data from Holes U1352B and U1352C where the two holes overlap have different absolute values. In particular, b* values at the top of Hole U1352C (i.e., between ~574 and 670 m) are anomalously high compared to b* values from the same depth interval in Hole U1352B (Fig. F37). As inferred for L* data, these differences reflect the fact that different coring techniques preferentially recover different lithologies that may have different color characteristics.

Moisture and density

Throughout Holes U1352B and U1352C, MAD measurements were made on approximately one sample per core for low-recovery cores and on 3–5 samples per core for complete cores with 6–8 sections. Samples were coordinated with thermal conductivity measurements, discrete *P*-wave (PWC) measurements, chemical analyses, and smear slide samples. Whenever possible, both soft-sediment samples and indurated sediment samples were taken (using syringe or minicorer, respectively). When soft sediments were sampled, the standard Method C analysis was employed. When the minicorer was used and the sample formed a measurable cylinder, the Method D calculation was used in addition to the Method C calculation (see "Physical properties" in the "Methods" chapter).

The first three cemented samples were tested to evaluate the need to soak samples in seawater for 24 h

before obtaining reliable wet sample measurements. These test samples were weighed immediately, soaked in seawater for 24 h, and then weighed again. In all cases, sample weight after soaking was greater than that before soaking. However, the difference was never >0.55% of sample weight. Because this is well below other measurement errors, subsequent rock samples were not soaked in seawater for 24 h before their wet mass was determined.

MAD porosity results were calculated using Methods C and D (Fig. **F41**) with a correlation coefficient of 0.98. Method D, in which wet volume is measured and wet mass is calculated, is best used when pore water may have been lost during sampling, because it tends to slightly overestimate porosity (Fig. **F41A**). Although occasional chips caused cylinder volume to be overestimated, more often the top and base or sides of the cylinder were not parallel. In either case, the calipers tend to measure the largest diameter or height, resulting in a tendency to overestimate wet volume.

The porosity trend for sediments that were hard enough to be sampled with the minicorer is readily distinguished from that of sediments that were soft enough to be sampled using the syringe method (Figs. **F41B, F42**) between ~600–1750 m. Indurated sediments within that interval have a relatively constant porosity downhole, whereas the softer sediments follow a decreasing porosity trend downcore until their trend merges with that of the indurated samples at ~1750 m.

Overall, density and porosity trends are clear in Holes U1352B and U1352C (Fig. **F42**), and the data are consistent over the interval from 575 to 821 m where the two holes overlap. A few semi-indurated samples from Hole U1352B show cementation beginning at ~500 m, whereas softer sediments tend to more gradually decrease in porosity and void ratio and increase in bulk density. Grain density slightly decreases with depth and shows no relationship with cementation, which supports the interpretation that the lithologic makeup of these rocks is consistent throughout.

Downhole logging of Hole U1352B was successful between ~100 and 500 m (Fig. **F43**). An overall decrease in porosity with depth is overshadowed by very large excursions that are indicated by downhole logging tools and missing from MAD porosity estimates. Despite a relatively wide hole near the top, porosity values derived from density logs are consistent with those obtained by MAD analyses, whereas neutron porosity log values follow similar, though consistently higher, trends (Fig. **F43B**). Slight offsets between MAD results and downhole log measurements may be related to differences in depth measurement between CSF-A and wireline log matched depth below seafloor (WMSF). Deeper in the hole (Fig. **F43C**), very high downhole log porosity values (70%–100%) occur where the hole diameter is ≥20 inches, suggesting that the sediments surrounding the hole may have been washed out at that level, generating unrealistically high porosities. In general, where this is not the case, porosities from downhole logging are near or in some cases lower than those obtained from MAD analyses. Again, this could reflect the presence of indurated horizons that were not sampled by the XCB system, despite the apparent near-100% recovery at these depths. The very high porosity excursion seen between ~240 and 300 m in the downhole logs (Fig. **F43A**) is likely a result of drilling disturbance in the surrounding sediments.

Sediment strength

Sediment strength measurements were conducted on working section halves from Hole U1352B using automated vane shear (AVS) and fall cone penetrometer (FCP) testing systems (Fig. **F44**). A comparison of both measurement methods is shown in the crossplot in Figure **F44D.** Shear strength indicates that sediments range from very soft (0–20 kN/m^2) to very stiff (150–300 kN/m^2). Vane shear and fall cone shear strength correlate well in very soft and soft sediments, but AVS values are about three times lower in firm to very stiff sediments (standard deviation = 24.5 kN/m^2) than FCP values (standard deviation = 81.8 kN/m^2). These findings suggest that the applicability of vane shear in firm to very stiff sediments is limited and that sediment strength from vane shear tests is underestimated. Overall, vane shear and fall cone strength data from Hole U1352B are positively correlated (Fig. **F44**). Between 0 and ~295 m, shear strength increases continuously, indicating a change from very soft to firm sediments. The increase and range of values seen in vane shear tests in the uppermost ~170 m of Hole U1352B are comparable to those from Hole 1119B (Fig. **F44C**). A pronounced cyclicity like that seen in holes at Site U1351 was not observed. The generally lower sediment strength below ~295 m in cores from Hole U1352B coincides with the change from APC to XCB drilling at 297 m.

Below ~295 m, sediment cracking resulting from high gas content and sediment disturbance associated with XCB coring often prevented optimal insertion of the vane blade. Repeated downcore increases in sediment strength were also observed within longer cores of uniform lithology by both AVS and FCP tests. These downhole increases were interpreted as an effect of secondary sediment compaction caused

by drilling stress. Similar drilling effects were observed in magnetic susceptibility data. We caution, therefore, that interpretation of sediment strength using raw data from XCB cores from Hole U1352B requires careful analysis of both the drilling technique used and also of the in situ sedimentology.

Geochemistry and microbiology

Organic geochemistry

Shipboard organic geochemical studies of cores from Site U1352 included monitoring hydrocarbon gases, carbonate carbon, total organic carbon (TOC), total sulfur (TS), and total nitrogen (TN) and characterizing organic matter by pyrolysis assay. The procedures used in these studies are summarized in **"Geochemistry and microbiology"** in the "Methods" chapter. All depths in this section are reported in CSF-A.

Volatile gases

All cores recovered in sufficient quantity at Site U1352 were monitored for gaseous hydrocarbons using the headspace (HS) gas technique, and, where possible, core gas voids were analyzed using the vacuum syringe (VAC) technique (Tables **T18, T19, T20;** Figs. **F45, F46**).

Hole U1352A was sampled at relatively high frequency (every other section or at ~1.5–3.5 m intervals) with the headspace gas technique to estimate the depth of the sulfate–methane transition (SMT) and the dissolved methane versus depth gradient. Sediment gas was below detection levels in the uppermost five samples collected (1.5–8.7 m), with the first trace appearance of methane (~3 µM) occurring at 11.7 m. Comparison with dissolved sulfate measurements (see **"Inorganic geochemistry"**) indicates that the SMT is between 15.2 and 16.6 m.

Headspace methane contents in Hole U1352A are shown in Table **T18** as dissolved methane in sediment pore space (millimolar) and headspace gas (parts per million by volume). At shallow depths beneath the sulfate reduction zone, methane concentrations are initially greater than saturation at surface conditions (~2 mM), having apparently maintained some degree of supersaturation during core retrieval and sampling. Estimated methane concentrations in sediment pore space were not calculated for Holes U1352B and U1352C because of obvious gas loss prior to sampling.

Detectable ethane is present in all cores from 18.2 m and below. The composition of the gas, as expressed by the C_1/C_2 ratio (Fig. **F45C**), shows the expected gradual increase in relative ethane content with increasing depth and temperature. The C_1/C_2 values of the core void gases (Fig. **F45C**) generally parallel those of headspace gas but are offset to higher values because of greater retention of C_1 during core retrieval and sampling. The ratio of C_1/C_2 in headspace gas decreases by three orders of magnitude (from >10,000 to 60) over the total depth interval (1927 m). The decrease in C_1/C_2 is due to a gradual increase in ethane content (Fig. **F45A**); below ~650 m, this decrease is also due to a decrease in methane and total gas content associated with a decrease in core porosity and fluid content. However, C_1/C_2 reaches very low values (<10) from 1385 to 1393 m, with headspace methane contents of <50 ppmv. This depth also corresponds to a major discontinuity identified between 1394 and 1410 m, with an apparent hiatus of >5 m.y. (see **"Lithostratigraphy"** and **"Biostratigraphy"**). In addition, the deepest interstitial water sample (collected at 1385 m) contains 3 mM of sulfate, somewhat more than is usually observed for cores contaminated with seawater. The very low methane and C_1/C_2 values of these cores must represent either an interval in which all methane was lost or an interval in which sulfate was never depleted and methane was never generated. In a few cores below this depth, gas returns to normal, with methane contents of 3,000–22,000 ppmv and most C_1/C_2 ratios of 35–75 from 1512 to 1922 m. There is no evidence for migrated thermogenic hydrocarbons in the gas profiles.

Some headspace and all core void gas samples were analyzed for the presence of C_{4+} hydrocarbons (Tables **T19, T20;** Fig. **F46**). Headspace samples were analyzed mainly below 650 m, when the character of the cores made core void gas samples less frequent. Butanes, pentanes, and occasionally hexanes are present in most of the samples analyzed but are generally at low levels (1–100 ppmv) (Fig. **F46A–F46C**). C_4–C_6 hydrocarbons become more abundant with increasing burial depth (excluding the ~1300–1450 m interval that spans the hiatus), probably because of the same low-temperature thermogenic alteration of the indigenous organic matter that produces increased ethane and propane. A distinct preference for branched C_4 and C_5 isomers is present in shallow headspace samples, and this tendency diminishes somewhat with increasing depth to ~1750 m (Fig. **F46F**). The C_4 hydrocarbons in the deeper parts of the core have subequal amounts of normal and branched isomers (e.g., below 1700 m), but C_5 hydrocarbons continue to be dominated by *i*-C_5, and only the branched C_6 hydrocarbons and no *n*-C_6 could be detected in this depth range (Table **T19;** Fig. **F46F**). A predominance of branched alkanes was also

observed in some core void gas samples from Site U1351 (at 811 and 961 m) and may be a result of organic matter being derived mainly from land plants. Core void gas samples have less of an iso-predominance (60%–80%) than headspace gases from similar depth intervals and have no depth trend.

The plot of the ratio of *n*-butane to the sum of *n*-butane and *i*-butane ($n\text{-}C_4/[n\text{-}C_4 + i\text{-}C_4]$) follows a wormlike trend with increasing depth. This trend has remarkable detail that may be related to lithostratigraphy and more precisely to formation porosity and permeability. Below 1400 m, where gas content is very low, this ratio first increases and then decreases below 1500 m from a high of ~60% $n\text{-}C_4$ to ~15% at 1600 m (Fig. **F46F**). With increasing depth, this ratio increases again to ~45% at 1700 m, below which it remains roughly constant. The $n\text{-}C_5/(n\text{-}C_5 + i\text{-}C_5)$ ratio shows a similar but less distinct trend, with a low between 1600 and 1700 m (0%–9%) and a high of ~20% $n\text{-}C_5$ in the deepest sample. Explanations for these trends remain uncertain, but they most likely reflect the mixing of thermogenic equilibrium mixtures of *normal*- and *iso*-isomers (e.g., below 1800 m) with variably retained original hydrocarbons dominated by *iso*-isomers. Gases below 1650 m that are richer in C_4 and C_5 hydrocarbons (Fig. **F46A–F46B**) form a cluster at the lowest part of the $n\text{-}C_4/(n\text{-}C_4 + i\text{-}C_4)$ ratio trend, implying that original hydrocarbons were retained in this zone and were not substantially diluted by more recently generated thermogenic gases. In contrast, the zone immediately underlying the discontinuity mentioned previously (below ~1450 m) is strongly depleted in original hydrocarbons, and gases in these sediments are diluted by small amounts of more recently generated thermogenic gas.

Table **T20** and Figure **F46D** show ethene ($C_{2=}$) contents measured in some void gas samples. Ethene was also detected in some headspace gases (Table **T18**). Ethene is common in near-surface sediments, where it is thought to be a product of biological activity (Claypool and Kvenvolden, 1983). However, short-chain unsaturated hydrocarbons are unstable under the reducing conditions of deeper sediments, so the presence of ethene and other alkenes in some of the deeper (250–690 m; especially 422–467 m) cores is somewhat unusual. Especially noteworthy is the composition of the gas sample from Section 317-U1352B-55X-1 (467 m), in which the amounts of some of the alkenes are greater than the saturated homologs (Fig. **F47**). Ethene and propene were quantified, but the peaks attributed to butenes and pentenes could be only tentatively identified. These samples are from depth intervals where XCB cores that jammed in the core catcher gave off a strong odor (422–467 m) and from the interval just above, where cores became continually jammed in the core barrel, requiring a switch from XCB to RCB coring. Alkenes observed in some void gas and headspace gas samples, especially the high quantities at 467 m, may be the product of high-temperature alteration of organic matter due to frictional heating during drilling, similar to that observed in previous ODP cores from Site 682 (Shipboard Scientific Party, 1988).

CO_2 concentrations in headspace and void gas samples are given in Tables **T19** and **T20** and illustrated in Figure **F46E**. Atmospheric air contains 387 ppm CO_2, but the majority of measured values exceed this significantly; furthermore, some samples contain less CO_2 than is found in air. Values obtained from core void gas samples show no clear difference from those of headspace samples. Therefore, these values likely reflect the true composition of CO_2 in the subsurface, which was formed by a mixture of microbial, diagenetic, and early thermogenic processes.

Carbon and elemental analyses

Inorganic carbon (IC), total carbon (TC), total organic carbon by difference (TOC_{DIFF}), TN, and TS were analyzed in 323 samples from 0 to 1924 m at Site U1352 (Table **T21**; Fig. **F48**). Carbonate fluctuates between 0.14 and 96 wt%, with lower averages of ~5 wt% in the uppermost 500 m and scattered high-carbonate (>20 wt%) samples throughout the cored sediments below ~600–700 m (Fig. **F48A**). The deepest samples (1700–1927 m) are characterized by very high carbonate contents (up to 96 wt%). Four samples (317-U1352C-129R-2, 104 cm; 130R-4, 103 cm; 131R-2, 96 cm; and 147R-6, 71 cm; Table **T21**) are carbonate-calcareous mudstone/marlstone pairs from closely interbedded strata. TC values cluster at ~0.5–1 wt%, with frequent scatter as high as 9 wt% in the uppermost 700 m. Below this depth, average values increase slightly and fluctuate between 1 and 7 wt% from 700 to 1600 m before finally reaching 12 wt% in the deepest part of the hole below 1600 m (Fig. **F48B**).

TOC_{DIFF} fluctuates between 0.1 and 1.5 wt% but is mostly <0.5 wt% and averages 0.4% (Fig. **F48C**). TOC_{DIFF} is systematically lower than the organic carbon determination given by the source rock analyzer (TOC_{SRA}) (Fig. **F48D**). A cross-plot of TC from the elemental analyzer and TOC_{SRA} plus IC from the coulometer shows a good correlation and indicates that the elemental analyzer gives consistently lower values by 0.3–0.5 wt% (Fig. **F49**), similar to Site U1351.

TN and TS contents are scattered in the range of 0.02–0.07 wt% for TN and 0–0.5 wt% for TS in the

uppermost 500 m. They slightly decrease downhole to averages of ~0.01–0.02 wt% and 0.02 wt% for TN and TS, respectively (Fig. F50C–F50D). No TS content was analyzed below 1526 m because of an onboard shortage of elemental analyzer reactors, which had to be replaced every 100 samples because the vanadium pentoxide catalyst used for sulfur determination deteriorated the activated copper package in the reactor. TOC_{DIFF}/TN ratios generally range from 5 to 50 and tend to increase with depth to ~1600 m before slightly decreasing near the bottom of the hole. Occasional values as high as 304 were observed, reflecting very low TN contents, mostly in carbonates (Fig. F50A). TOC_{DIFF}/TS ratios are mostly low, ranging from 0.1 to 10, with scattered individual samples as high as 80 (Fig. F50B). TOC_{DIFF}/TN and TOC_{DIFF}/TS ratios are much higher at Site U1352 than at Site U1351.

Organic matter pyrolysis

Most of the samples used for carbon-nitrogen-sulfur analysis were also characterized by source rock analyzer (SRA) pyrolysis (Table T22; Figs. F51, F52). S_1 and S_2 slightly increase with depth from 0 to 400 m, with ranges of ~0.0–0.3 and 0.1–1.4 mg/g, respectively. Values range widely at these shallow depths, especially for S_1. Below 600 m, values cluster more tightly near 0.04 mg/g for S_1 and 0.1–0.5 mg/g for S_2 (Fig. F51A–F51B), and average values decrease slightly downhole. S_2 values at 1500–1600 m are occasionally as high as 2.4 mg/g, representing sediment layers with higher organic carbon contents. S_3 has no trend and a range of 0.1–0.9 mg/g, with occasional values as high as 1.2 mg/g (Fig. F51C). Pyrolysis carbon necessarily mirrors S_1 and S_2 (Fig. F51D).

The hydrogen index (HI) generally ranges from 10 to 100 mg/g C, and values increase with depth, reaching a maximum at ~1000 m before decreasing slightly toward the bottom of the hole. Values as high as 133 mg/g C were observed at ~1500–1600 m (Fig. F52A). The oxygen index is scattered between 10 and 100 mg/g C, and values slightly decrease with depth (Fig. F52B). T_{max} values (Fig. F52C) range from ~370° to 440°C, with more scatter in the uppermost 500 m of the sediment column. Values increase downhole from ~400°C at the seafloor (with much scatter) to 430°C at the bottom of the hole. The cloud of data in the uppermost 500 m tightens into a more consistent trend in deeper sediments. The production index decreases in the uppermost 700 m from an average of 30% at the seafloor to ~10% at ~1000 m and then stays constant to ~1500 m (Fig. F52D). Below 1500 m, the production index increases significantly in some samples to 20%–30%.

A modified van Krevelen diagram (Fig. F53) indicates that organic matter is of slightly better quality at Site U1352 than at Site U1351, with most samples clustering near the Type III line. The highest HI (133 mg/g C) was found in a thin Miocene calcareous mudstone from 1575 m that was interbedded with carbonates.

Preliminary interpretation of organic matter

Variations in organic matter composition are subtle and largely correlate with lithologic Units I (0–710 m) and II (710–1853 m). Unit I is interbedded mud and sand with scattered high carbonate intervals, Unit II is a marlstone with mud and sand, and Unit III is nannofossil-rich limestone. In Unit I, samples with high carbonate contents tend to have higher organic carbon contents and higher S_1 and S_2 pyrolysis yields, whereas background mud/sand sediments have relatively low organic carbon contents (TOC_{DIFF} = 0.4–0.5 wt%). Unit II marls generally have low organic carbon contents (TOC_{DIFF} = 0.5–0.6 wt%), and organic carbon does not correlate with carbonate content except at the bottom of the unit below 1700 m, where an inverse correlation is apparent (Fig. F48A, F48C). Unit III limestones contain the highest amounts of carbonate and the lowest TN at Site U1352 (Figs. F48A, F50C). Unit I probably contains organic matter that is less altered diagenetically and that volatilizes more readily during pyrolysis. Organic matter in Units II and III is more diagenetically stabilized as protokerogen, as shown in the lower part of Unit II by the elimination of some scatter in the pyrolysis response, especially in S_3 and T_{max} (Figs. F51C, F52C). T_{max} values, especially those below ~1200 m, have less scatter and are shifted to higher temperatures, consistent with the progressive elimination of the more reactive protokerogen components of organic matter (Fig. F52C).

SRA data from Site U1352 can be compared to existing source rock quality and thermal maturity data from the Canterbury Basin (Newman et al., 2000; Sykes and Funnel, 2002; Sykes, 2004; Sykes and Johansen, 2009). Source rock quality at Site U1352 is rather low, with most HI values <100 mg/g (Fig. F52A), so the organic matter is largely interpreted to be land plant or degraded marine in origin. This contrasts with deeper Pukeiwitahi Formation coals (late Campanian–early Maastrichtian) in offshore petroleum exploration wells that have considerably higher HI values (Endeavour-1: 2094–2353 m, mean HI = 210; Galleon-1: 2822–2885 m, mean HI = 250) (Sykes, 2004). It is possible that the reported HI values at Site U1352 are underestimates because it was demonstrated that the TOC_{SRA} values from the SRA

are high relative to TOC_{DIFF} calculated by the difference method (see **"Geochemistry and microbiology"** in the "Methods" chapter).

The thermal maturity gradient defined by T_{max} variation at Site U1352 ranges from ~380° to 400°C in the shallowest samples to an average of ~430°C at ~1900 m (Fig. **F52C**). This trend is quite steep and suggests a rather high geothermal gradient. The deepest values are within the early oil-generative window, according to published T_{max} data that show that the onset of oil generation in the Canterbury Basin occurs at T_{max} = 425°C (0.65% vitrinite reflectance; coal band rank S_r = 10) (Sykes and Funnel, 2002; Sykes and Johansen, 2009). Note that this conclusion is inconsistent with the interpreted bottom-hole temperature of ~60°C at Site U1352 that was calculated using a variable heat flow determined by thermal conductivity (see **"Heat flow"**). However, the geochemical results are more consistent with a bottom-hole temperature of ~100°C that is achieved if a constant geothermal gradient is assumed. Supporting evidence for an early oil-generative window thermal maturity at the base of Site U1352 is that the production index increases above 20% below 1700 m (Fig. **F52D**), showing greater free hydrocarbons that are perhaps generated by thermal processes. However, similar T_{max} values are generally only reached deeper in the Canterbury Basin (>2100–2800 m in Endeavour-1 and Galleon-1; Sykes, 2004; Sykes and Johansen, 2009). One possible explanation is the known loss of section at erosional unconformities at Site U1352 (see **"Lithostratigraphy"**). A second possible explanation is that heat flow at Site U1352 is high because of a deeper igneous intrusion, although there is no evidence on seismic profiles at Site U1352 for igneous intrusions at depths that we believe could have had a thermal effect in the drilled hole. Newman et al. (2000) have shown evidence for anomalously high thermal maturities in the Canterbury Basin at Clipper-1 below 4000 m, which is inferred to have been the result of a thermal intrusion at depth.

SRA data obtained on board ship, especially HI and T_{max}, will need to be confirmed and calibrated using a second instrument before initial interpretations about source rock quality and thermal maturity at Site U1352 can be confirmed. These analyses are scheduled for early postcruise research.

Inorganic geochemistry

Interstitial water

A total of 112 interstitial water samples (Tables **T23, T24, T25**) were collected and analyzed at Site U1352. Thirty-one samples were taken from Hole U1352A, which was dedicated mainly to whole-round sampling for geochemistry and microbiology. Three samples were taken from Core 317-U1352B-6H, two samples were taken from each of Cores 7H through 10H, and one sample was taken per core (where recovery was sufficient) to Core 35H (294 m). Samples were taken from approximately every other core for Cores 317-U1352B-37X through 90X (783 m). Cores 317-U1352C-2R, 3R, 6R, 11R, 14R, and 18R were spot sampled from 576 to 780 m, and every second or third core was sampled to Core 40R (989 m). From Cores 317-U1352C-45R through 58R (1034–1164 m), sampling was irregular and some whole-round samples as long as 30 cm failed to yield any water for analysis. Thereafter, only a few interstitial water samples were selected, based on appearance and apparent degree of cementation. The amount of interstitial water extracted from whole-round samples decreases with depth from ~2 to 5 mL/cm in the uppermost 700 m to <1 mL/cm below 900 m (Table **T23;** Fig. **F54**). The deepest whole-round sample successfully sampled for interstitial water was from 1386 m and yielded 0.5 mL/cm.

Salinity, chloride, and pH

Salinities in samples near the seafloor are slightly lower than normal seawater at 3.3, rapidly decline to 3.0 at 28 m, and remain relatively constant at 2.9–3.1 in the rest of the section analyzed (to 1400 m) (Fig. **F55B, F55D**). Chloride parallels salinity measurements, with the shallowest samples having slightly lower concentrations than seawater (540 mM) and most other samples having relatively constant but scattered chloride concentrations of 520–550 mM (Fig. **F55A, F55C**). The isolated deepest sample has a chloride concentration of 453 mM. Measured pH values seem to vary with the dominant diagenetic process—decreasing during sulfate reduction, increasing during methanogenesis, and decreasing again, possibly because of authigenic carbonate precipitation (Fig. **F56C**).

Alkalinity, sulfate, ammonium, phosphate, and dissolved silica

Alkalinity increases relatively slowly from 2.8 mM at the seafloor to 9 mM at 10.1 m and then increases rapidly to a maximum of 24.2 mM at 16.6 m (Fig. **F57A, F57C**). Alkalinity then decreases to ~15 mM at 100 m and remains relatively constant to ~400 m. From 400 to 600 m, alkalinity declines steadily to ~2.3 and then remains in the range of 1.4–3.0 mM to the base of sampling. The sulfate decline is almost exactly the inverse of the alkalinity increase, with sulfate declining slowly over the 0–10 m interval and rapidly from 10 to 24 m (Fig. **F57B, F57D**). Below

this depth, sulfate remains essentially at zero, except in cores contaminated with small amounts of the seawater used as a drilling fluid.

Ammonium is zero to ~7 m and then increases gradually to a shallow maximum of ~2.3 mM between 40 and 50 m (Fig. F58C). After decreasing to 1.3 mM between 50 and 80 m, ammonium increases again to a maximum of ~7 mM at 470 m before decreasing steadily to ~2 mM in the deepest samples analyzed at 1000 m. Phosphate is low at 1–4 µM from the seafloor to 8.5 m. It then increases rapidly and spikes at 92 µM at 14.8 m (Fig. F58A). After dropping back to 41 µM at 16.6 m, phosphate varies within a range of 23–59 µM to 55 m before dropping to ~7 µM at 60 m and declining steadily to essentially zero by 400 m.

Dissolved silica is present at 272 µM at 1.1 m, increases to 645 µM at 27.5 m, remains relatively constant at a range of 380–660 µM to 200 m, and then increases to a maximum of 1066 µM at 480 m (Fig. F58B). Silica declines to 215 µM at 653 m and then increases again to 831 µM at 699 m before dropping back to 258 µM in the deepest samples analyzed at 765 m.

Calcium, magnesium, and strontium

Calcium and magnesium both decrease during sulfate reduction and then continue to decrease to minimum values (1.4 mM for Ca^{2+} and 7 mM for Mg^{2+}) from 300 to 400 m (Fig. F56D–F56E). Below 400 m, both major cations increase to ~20–23 mM at ~600 m, below which magnesium remains relatively constant to ~1200 m. Calcium continues to increase to just above 30 mM in the deepest samples at >1100 m. The ratio of magnesium to calcium increases from 5 to >9 in surface sediments as deep as 18 m. It then decreases to ~1.6 at 500 m before slowly declining to 0.5 at 1386 m (Fig. F56F). Strontium is initially at seawater values of ~0.1 mM and then increases slightly to 0.3 mM at 400 m before quickly increasing downhole to 2 mM at ~800 m. Strontium then decreases to ~1.7 mM at maximum depth (1386 m) (Fig. F56A). The Sr/Ca ratio increases steadily from 0.01 to a maximum of 0.15 at 480 m and then decreases again to 0.06 in the deepest sample (Fig. F56B).

Sodium, potassium, lithium, barium, silicon, boron, iron, and manganese

Sodium increases from near-seawater values of 466 mM to 515 mM at 286 m, decreases to ~440 mM at 600 m, drops to ~410 mM at 1184 m, and then decreases to 348 mM at 1386 m (Fig. F59C). Potassium decreases during sulfate reduction and then increases during the initial stages of methanogenesis, reaching a maximum of 11 mM at 144 m. Potassium then declines to ~6 mM at 550 m, declines further to ~3 mM at 600 m, spikes back up to 5.7 mM at 709 m, and finally declines to ~2 mM in the deepest samples below 900 m (Fig. F59B).

Lithium increases steadily from 25 µM at the sediment/water interface to ~50 µM at 450 m. Lithium then increases more rapidly to a maximum of 166 µM at 700 m before declining to ~100 µM at 800–900 m (Fig. F59A). Below 900 m, lithium increases again to ~130 µM between 1000 and 1200 m before dropping to 76 µM in the deepest sample. Barium increases from ~2 to ~7 µM at the base of the SMT before gradually increasing to 19 µM at 500 m (Fig. F59D). The profile becomes more scattered below 500 m, with concentrations ranging from 7 to 30 µM. A pronounced barium maximum of 84 µM is evident at 1091 m.

Silicon has no obvious trend in the uppermost 300 m of sediment, and values are scattered between 300 and 600 µM (Fig. F58D). Below 300 m, silicon increases to a maximum of ~900 µM at 524 m, drops significantly to ~300 µM at 600 m, increases again to 1013 µM at 700 m, and finally averages ~400 µM below 800 m.

The boron profile shows a remarkable increase from seawater values of ~0.4 mM to a maximum of 5.4 mM at 1113 m before a slight decrease in the subsequent samples and a sharp drop to 1.5 mM in the deepest sample (Fig. F60A).

Manganese ranges from 3 to 9 µM, with a maximum value of 13 µM between 0 and 50 m. Below this depth, manganese declines to 2–4 µM at 100–300 m and then increases downhole to average values of 5–15 µM (Fig. F60C). Iron shows a similar trend, increasing rapidly from ~10 µM to a maximum of 34 µM at 26 m, decreasing again to 4 µM at ~300 m, and finally increasing to 20–36 µM between 500 and 1386 m (Fig. F60B).

Preliminary interpretation of diagenesis

Interstitial water geochemistry in the uppermost 20 m at Site U1352 is dominated by the two main microbially mediated diagenetic processes, sulfate reduction and methanogenesis (Fig. F61). A zone of very gradual sulfate depletion and alkalinity increase occurs in the 0–8.5 m depth interval and represents either very slow organic matter oxidation or a zone of intense bioturbation. The very low phosphate and the absence of ammonium in this interval are more consistent with bioturbation or other physical mixing of seawater than with organic matter oxidation. From 8.5 to 16.6 m, sulfate declines rapidly from 25.1 to 0 mM, whereas alkalinity (dominantly bicar-

bonate ions) increases to a maximum of 24.2 mM. Over this same 8.5–16.6 m depth interval, calcium and magnesium decline by a combined 15 mM, presumably because of authigenic carbonate precipitation. The amount of carbon oxidized during sulfate reduction is equivalent to the alkalinity increase plus the major cation decrease, or ~38 mM, which is 1.5 times the amount of sulfate removed (Fig. F62). This ratio of carbon oxidized to sulfate removed implies that half of the sulfate reduction at Site U1352 is the result of organic matter oxidation and the other half is the result of methane oxidation. At this 1.5 proportion of carbon added to sulfate removed, two-thirds of the carbon added would be from the oxidation of organic matter and one-third would be from the oxidation of methane (see equations in Fig. F62). These interpretations based on interstitial water chemistry could be confirmed by postcruise analysis of stable carbon isotope ratios of dissolved inorganic carbon and diagenetic carbonates. The moderate amount of phosphate in the sulfate reduction zone, especially in the sample at 14.8 m (92 µM), is consistent with some oxidation of marine organic matter because methane oxidation would generate no phosphate.

After an initial drop of 2 mM beneath the sulfate reduction zone, alkalinity remains relatively constant to ~50 m, indicating that organic matter oxidation is replenishing bicarbonate as rapidly as it is removed by methane generation and carbonate precipitation. Below 50 m, alkalinity drops in stages to ~14 mM over the 100–350 m depth interval and then drops steadily to ~3–5 mM at 500–600 m, below which it ranges from 1.4 to 3.0 mM in the rest of the sampled interval. This gradual decline in alkalinity probably represents the final stages of biological activity resulting in the oxidation of organic matter and the reduction of dissolved CO_2 to produce methane. The alkalinity decrease and the major calcium increase occur over the same interval (350–600 m), which also corresponds to a decline in the degree of preservation of calcareous microfossils (see **"Biostratigraphy"**).

Calcium at Site U1352 generally increases to 400 m and then reaches a steady state at ~800 m. This is common for pore fluids from carbonate-dominated sections with little influence from diffusive flux below (McDuff and Gieskes, 1976) and is consistent with high carbonate throughout the cored sediments below ~600–700 m (Fig. F48A). Below 400 m, strontium and magnesium also have profiles similar to that of calcium. Upward diffusive flow from carbonate-dominated sections may cause the abrupt gradual increases in divalent cation concentrations from 400 to 800 m. Strontium reaches values as high as >20 times seawater. The dissolution of Sr-rich aragonite in the sediments is one way of explaining the increasing flux of strontium to pore fluids.

Particles of barite are one of the main carriers of barium in sediments (Dehairs et al., 1980). Barium initially shows a clear rise below the depth of the SMT. The removal of SO_4^{2-} increases the solubility of barite, and dissolved Ba^{2+} concentrations increase from 2 to 9 µM (Fig. F59D). The scattered profiles of silica and silicon below 400 m are possibly associated with the scatter of barium concentrations and may reflect diagenetic dissolution/transition and/or changes in paleoproductivity (Paytan et al., 1996).

Boron steadily increases in the deepest samples, where values are as high as 13 times that of seawater (Fig. F60A). The maximum boron value of 5.4 mM is very similar to that at Site U1351, although at Site U1351 the highest value occurs much shallower (at 300 m). The boron increase is possibly related to the diagenetic opal-A/opal-CT transition and microbial degradation of organic matter.

Biogenic opal is assumed to be a major source of lithium in sediments. The rapid increase and decrease of lithium concentrations from 450 to 800 m (Fig. F59A) is within a zone of highly variable silica and silicon concentrations (Fig. F58B, F58D). A fraction of lithium enrichment also may be associated with lithium in sediments and clay minerals. Lithium is easily removed from clay interlayer exchange sites because of its high hydration energy, which may account for the observed steady increase.

Microbiology

The principal shipboard microbiological objectives at Site U1352 included testing samples for contamination using PFT and a particulate tracer and starting enrichment cultures for different types of metabolisms.

Sample collection

At this site, 107 whole-round samples were collected for microbiological investigations (51 for microbial characterization, 51 for intact polar lipid analysis, and 5 for incubation tests).

Contamination tracer tests

Contamination tests were continuously conducted using water-soluble tracers (PFT) or bacteria-sized particles (fluorescent microspheres) in order to confirm the suitability of sediment samples for microbiological research. The chemical and particle tracer techniques used are described in **"Geochemistry and microbiology"** in the "Methods" chapter.

Water-soluble tracer

At Site U1352, PFT was continuously delivered at its maximum solubility (2 mg/mL in seawater) into cores from which microbiology whole-round samples were taken. To maximize the detection of seawater contamination from drilling, 5 cm^3 sediment samples were taken. No results could be achieved because of analytical problems. In particular, gas chromatograph traces had small peaks (other than PFT) of similar retention time to that of PFT, even after cleaning or changing the column. Consequently, we decided to preserve the samples for onshore analysis by injecting 2 mL of an autoclaved 3% NaCl solution into the vials containing the sediment. The samples were then immediately frozen upside-down at –80°C until they could be shipped on dry ice.

Particulate tracer

Fluorescent microspheres were used as a particulate tracer on all cores from which whole-round samples were subsequently taken. A 1 cm^3 sample of sediment was diluted 10× by a 3% NaCl/3% formalin solution for microsphere detection. Microspheres were detected in 49 of the 51 outer sediment samples (Table **T26**), indicating a heterogeneous distribution of microspheres along the core liner. In the inner part of the core, 40 sediment samples did not contain any microspheres, indicating that no contamination by micron-sized particles took place. In 11 sediment samples (Table **T26**), between 2×10^2 and 2×10^5 microspheres/cm^3 were counted, indicating that potential contamination from drilling fluid may have occurred in the inner part of the core during the drilling process. The bead-delivery method used at this site is the one described by Smith et al. (2000). In samples where microspheres were not detected (Sections 317-U1352A-15H-4 and 317-U1352C-87R-4), prokaryotic molecular diversity was compared to determine if contamination occurred. No difference was found in the deployment of microspheres between APC and XCB coring, but, on average, fewer microspheres were observed at the periphery of the core when RCB coring was used (Fig. **F63**). This can be explained by the fact that beads can potentially become diluted in the drilling fluid. Therefore, we suggest using 40 mL instead of 20 mL microsphere bags for cores retrieved with the XCB or RCB systems.

Total cell counts

Sediment samples of 1 cm^3 were taken from all whole-round samples for microbial characterization and stored at 4°C in a 3% NaCl/3% formalin solution for onshore prokaryotic cell counting.

Cultivations

In Hole U1352C, 11 whole-round samples were collected below the deepest microbiology sample analyzed to date (1626 mbsf; Roussel et al., 2008). These samples are characterized by the presence of lithified layers rich in carbonate (up to 70%; see **"Lithostratigraphy"**) alternating with dark glauconitic layers. When a glauconitic layer was present in the 10 cm long microbial characterization samples, it was sampled separately in order to determine any differences in microbial diversity. Three samples (Sections 317-U1352C-137R-3, 137R-3 [glauconite], and 148R-3) (Table **T26**) were inoculated on several enrichment media, as described in **"Geochemistry and microbiology"** in the "Methods" chapter (see Table **T16** in the "Methods" chapter). All onboard enrichments were incubated near the in situ temperature (70°C) (the temperature at the bottom of the hole was estimated to be 60°C; see **"Heat flow"**) under 5% H_2, 5% CO_2, and 90% N_2 (biogas) headspace.

Heat flow

Geothermal gradient

Temperature measurements were conducted using the APCT-3 during APC coring in Holes U1352A and U1352B and the Sediment Temperature tool during XCB coring in Hole U1352B. Six temperature measurements were taken in total (Fig. **F64;** Table **T27**), and the geothermal gradient was successfully obtained from four of these (Cores 317-U1352B-10H, 15H, 20H, and 38X) within the depth interval of 93.7–313.2 m CSF-A. Unless otherwise noted, all depths in this section are reported in m CSF-A. The other two measurements in Cores 317-U1352A-4H and 317-U1352B-6H were not used because the conductive cooling time after sediment penetration was too short (<300 s) to generate reliable fitting curves (Fig. **F64A**), which could be the result of tool movement caused by ship heave. The fitting line to temperature versus depth data was derived from the four good results (Fig. **F64B**):

$$T(z) = 0.0460 \times z + 8.2325 \qquad (R^2 = 0.9991),$$

where $T(z)$ is in situ temperature at depth z (m CSF-A). The estimated geothermal gradient is therefore 46.0°C/km. Note that this geothermal gradient was established for the depth interval above ~310 m, which consists of soft sediments, and might significantly decrease with depth in accordance with a rapid increase in thermal conductivity, particularly for the interval below 575 m, where rock first occurs (see **"Thermal conductivity,"** below). For reference,

the geothermal gradients at nearby ODP Sites 1120, 1124, and 1125 are 57.4°, 52.1°, and 64.9°C/km, respectively (Carter, McCave, Richter, Carter, et al., 1999). These gradients were established in soft sediments above ~130 m.

Thermal conductivity

Thermal conductivity was measured preferentially in available whole-round core sections from Holes U1352A and U1352B using the full-space needle probe method and in section halves from Hole U1352C using the puck probe method. The puck probe method was employed because the degree of induration of sediments increases with depth in Hole U1352C. Three full-space needle probe measurements were conducted in indurated sediment drilled with the RCB system: two in rather soft sediments in Cores 317-U1352C-6R and 18R and one in rock to compare with puck probe measurements in Core 317-U1352C-76R. Measurement frequency was usually once per section with one measuring cycle at each point for the full-space needle probe method and once per core with five measuring cycles at each point for the puck probe method. This included 32 points in Hole U1352A (0.2–42.1 m), 443 points in Hole U1352B (0.7–821.7 m), and 155 points in Hole U1352C (575.1–1920.6 m) (Table **T28**). The middle of each section was chosen as the measurement point unless a void or crack was observed (see **"Heat flow"** in the "Methods" chapter). Few lithologic variations occur in each section at Site U1352, so this sampling procedure was appropriate. Probes V10701 and V10819 were used, and heating power was kept to ~3 and 2 W for full-space needle probe and puck probe methods, respectively.

Thermal conductivity data were screened when (1) contact between the probe and sediment was poor, (2) thermal conductivity values were close to that of water (0.6 W/[m·K]) because of sediment dilution during coring, and (3) measurements were taken in caved-in layers such as shell hash. In most cases, the first two criteria were controlling parameters for deciding the quality of measurements. Good results were obtained at 13, 214, and 149 points in Holes U1352A, U1352B, and U1352C, respectively, covering depths of 8–42, 1–793, and 575–1921 m, respectively (Table **T28**). The ratio of reliable measurements to total measurements is larger for Hole U1352C, where five measuring cycles were run, than for Holes U1352A and U1352B, where only one measuring cycle was run. Therefore, we recommend increasing the number of measuring cycles at each point from one to at least three, even at the expense of decreasing measuring frequency from once per section to once per core.

Thermal conductivity measurements at Site U1352 range from 0.849 to 3.440 W/(m·K): 0.849–1.696 W/(m·K) (average = 1.305 W/[m·K]) for sediments in Holes U1352A and U1352B in the depth interval of 1–793 m and 1.572–3.440 W/(m·K) (average = 2.360 W/[m·K]) for rocks in Hole U1352C in the depth interval of 575–1921 m (Table **T28**). For reference, the two lowest values in Hole U1352C were measured with the full-space needle probe in sediments in Cores 317-U1352C-6R and 18R. For Core 317-U1352C-76R we compared thermal conductivity measured by the puck probe with that measured by the full-space needle probe within a drilled hole filled with thermal compound. Results were similar (within 0.6%), indicating that the difference between methods is negligible. Thermal conductivity for rocks is ~1.8 times greater than that for sediments. In the uppermost 130 m, thermal conductivity values are higher at Site U1352 than in the same interval at nearby Site 1119 (Shipboard Scientific Party, 1999b). The high conductivities at Site U1352 may be due to high concentrations of quartz (6.5–12.5 W/[m·K]) in fine-grained sediment, including the clay-sized fraction (see **"Lithostratigraphy"**) and/or carbonate cementation (0.5–4.4 W/[m·K]).

Thermal conductivity versus depth data for Holes U1352A and U1352B are consistent (Fig. **F65A**). In the overlapped depth interval between Holes U1352B and U1352C (575–793 m), a gap exists between trends of values that increase with depth. This gap can be explained by sampling bias with respect to the lithologies measured in each hole: soft sediment was preferentially recovered in Holes U1352A and U1352B and hard rock was preferentially recovered in Hole U1352C. Although marlstone first occurs at 575 m (Core 317-U1352C-2H), the rock is still porous and firm at ~900 m, which is manifested in the larger amount of scatter above 900 m compared to below. Three linear trends can be recognized at other depth intervals, including a downhole decrease from 0 to 90 m and increasing trends from 90 to 661 m and 826 to 1921 m. It is unclear why values in the uppermost 90 m interval decrease with depth, because bulk density and porosity are relatively constant in the same interval. However, thermal conductivity, in general, correlates negatively with the porosity profile (see **"Physical properties"**), particularly for hard rock (Fig. **F65B**). A good positive correlation with bulk density obtained from moisture and density, Method C (see **"Physical**

properties" in the "Methods" chapter), is shown in Figure F65C. The linear fits between thermal conductivity and depth for sediments are

$$\lambda_{0–90}(z) = 1.3484–0.0015 \times z \quad (R^2 = 0.0954)$$

and

$$\lambda_{90–661}(z) = 1.1878 + 0.0003 \times z \quad (R^2 = 0.1742),$$

and the linear fit for hard rock is

$$\lambda_{826–1921}(z) = 1.7819 + 0.4101 \times z \quad (R^2 = 0.4101),$$

where z is depth (m CSF-A). Thermal conductivity in the 661–826 m depth interval was calculated using the harmonic mean for cores consisting of alternating sediment–rock layers, based on two regressions, $\lambda_{90–661}(z)$ and $\lambda_{826–1921}(z)$, and the ratio of sediments/rocks in each core because (1) the sediment portion of each core from Hole U1352C steadily decreases below ~661 m (Core 317-U1352C-6R) and almost disappears at 826 m (Core 317-U1352C-23R) and (2) the measured thermal conductivities in Holes U1352B and U1352C represent either sediment or rock among alternating layers of sediment or rock. The resulting linear fit for sediment/rock mixture is

$$\lambda_{661–826}(z) = –1.1457 + 0.004 \times z \quad (R^2 = 0.6376),$$

where z is depth (m CSF-A). In addition to this interval, Cores 317-U1352C-2R, 27R, 53R, and 77R contain alternating layers of sediment and rock, but these were not taken into account in terms of trends.

Bullard plot

Because the thermal conductivity profile in the 94–313 m depth interval, where the geothermal gradient was established, is represented as a linear fit, $\lambda_{90–661}(z)$, thermal resistance for the interval is derived as

$$\Omega_{90–661}(z) = [\ln(1.1878 + 0.0003 \times z) – \ln(1.1878)]/0.0003,$$

where z is depth (m CSF-A).

Following the Bullard approach and assuming conductive heat flow, a linear fit of temperature versus thermal resistance is expected (Fig. F66):

$$T_{90–661}(z) = 7.8814 + 0.0578 \times \Omega(z) \quad (R^2 = 0.9985),$$

where z is depth (m CSF-A).

This yields a heat flow of 57.8 mW/m² for the 94–313 m depth interval, which can be applied to the entire cored depth interval if steady state heat flow is assumed. The resulting heat flow is comparable to the regional heat flow distribution, which decreases from 100–120 mW/m² in the mountainous area to the southwest to <60 mW/m² on the west coast of New Zealand (Reyes, 2007).

Temperature profile

The temperature profile at Site U1352 was predicted using the estimated heat flow of 57.8 mW/m² from the 94–313 m depth interval and estimated thermal conductivity trends under the assumption of steady state (Fig. F67). The temperature profile based on thermal conductivity shows a large inflection at ~575 m because of a rapid increase in thermal conductivity in the lithified material. At the bottom of Hole U1352C (1927 m), the predicted temperature based on this method is ~60°C, which is ~40°C lower than that obtained by assuming a constant geothermal gradient. However, SRA data suggest a higher thermal maturity at the bottom of Hole U1352C than would be consistent with 60°C (see "Geochemistry and microbiology").

Downhole logging

Operations

Two holes were logged at Site U1352. Hole U1352B was logged after reaching refusal with the XCB coring system, and Hole U1352C was logged after coring deep enough to be able to log and fully characterize the Marshall Paraconformity.

Hole U1352B

After an extended period of low core recovery, slow rate of penetration, and hot conditions at the bit, APC/XCB coring operations were terminated, with the last core on deck at ~1900 h on 4 December 2009 (all times are ship local time, UTC + 13 h). Logging operations began by conditioning the hole immediately after the last core was recovered from a total depth of 1185.5 m DRF (831 m DSF). Because of the tool recovery operations in Hole U1351C (see "Downhole logging" in the "Site U1351" chapter), mud supplies on the ship were limited for the remaining sites; however, the drilling process and lithology indicated that this hole could be displaced with seawater rather than logging gel. After the hole was swept, circulated with 50 bbl of high-viscosity mud, and displaced with seawater, the bit was raised to the logging depth of 436.6 m DRF (82 m DSF). Rig up of the triple combo tool string (natural gamma ray, bulk density, electrical resistivity, and porosity) began at 2315 h and was complete at 0025 h on

5 December, and the tool string was RIH at 0045 h. While the tool string was being lowered at a speed of 2500–3000 ft/h, gamma ray and resistivity data were recorded from the seafloor to 842 m wireline log depth below rig floor (WRF), below which it proved impossible to lower the tool string. After multiple unsuccessful attempts to pass the blockage at ~842 m WRF, we decided to log up from this depth, more than 300 m shallower than the total hole depth. A first repeat pass was completed at 0255 h (470 m WRF), and the tool was run back down to 842 m WRF for the full pass, which began at 0305 h at a speed of 900 ft/h. At 0420 h (477 m WRF), the caliper was closed for reentry into the pipe, and the pass was completed at 0500 h when the seafloor was identified by a drop in the gamma ray log at 355.5 m WRF. The tool string was back on deck at 0520 h and rigged down at 0610 h.

Overall, the caliper of the density sonde showed a very irregular borehole, with a hole diameter >20 inches over many intervals. We decided that, even if the quality of FMS images was likely to be poor in some intervals, there was no risk to the tools and the deployment of the FMS-sonic tool string would provide worthwhile velocity and image data. The FMS-sonic tool string was rigged up by 0700 h and RIH at a speed of 2000 ft/h to record sonic velocities on the way down. At 0800 h, a shallower obstruction was met at 795 m WRF and could not be passed. At 0812 h, we decided to begin logging up with both the FMS and sonic tools from the deepest depth reached (797 m WRF) at a speed of 1200 ft/h. The first pass was completed at 0900 h at 480 m WRF, before the top of the tool string reached the bottom of the pipe. The FMS calipers were closed, and the tool was sent down for a second pass. At 0920 h, the same obstruction was reached at 796 m WRF, and the second pass started at a speed of 1500 ft/h. The FMS calipers were closed after the second pass was completed at 1005 h (480 m WRF), before the top of the tool string was pulled into the pipe. Data acquisition was concluded at 1020 h when the sonic log identified the bottom of the drill string. The tool string was back at the surface at 1050 h and was rigged down completely at 1130 h. The initial logging plan included a VSP; however, this was postponed until the next hole because of hole conditions, and the rig floor was cleared to resume drilling operations at 1145 h.

Hole U1352C

The last core was recovered from Hole U1352C at 1740 h on 19 December from a total depth of 1927.5 m DSF. After sweeping the bottom of the hole with 50 bbl of high-viscosity sepiolite/attapulgite mud and circulating two times the annular capacity of the hole with seawater, the RCB bit was dropped at ~2300 h. In order to reserve mud supplies for the remaining sites and in consideration of the stable nature of the formation in the deepest section of the hole, a 450 m interval was targeted between 900 and 450 m DSF to be displaced with logging mud. The pipe was pulled to 900 m DSF, and 400 bbl of logging mud was pumped into the borehole to stabilize this interval, which previous logging and coring operations had shown to be unstable. Shortly thereafter, the drill string indicated significant drag from the formation, which required reconnection of the top drive to restore rotation. The continued upward progress of the pipe was slow between 880 and ~190 m DSF, suggesting a series of ledges rather than a full hole collapse but also indicating that lowering the logging tool could be hazardous. Considering the potential benefits of logging this unique hole, we decided to run the triple combo tool string without radioactive sources.

At 1400 h on 20 December, the pipe was set at a logging depth of ~100 m DSF (354.6 m DRF), and rig-up of the triple combo began at 1520 h. The modified tool string consisted of the Hostile Environment Natural Gamma Ray Sonde (HNGS), the Hostile Environment Litho-Density Sonde (HLDS; without source, for the caliper only), the General Purpose Inclinometry Tool (GPIT), and the Dual Induction Tool (DIT). The tool string was rigged up by 1600 h and RIH at 1620 h at a speed of 4000 ft/h. A downlog was started at 340 m WRF at a speed of 3500 ft/h, and the seafloor and base of pipe were identified at 355 and 457 m WRF, respectively. At 1700 h, cable tension indicated signs of drag from the formation at ~550 m WRF, similar to the shallowest trouble spot identified by the driller as the drill string was pulled out of the hole. After several attempts to pass the obstruction, reaching a maximum depth of 562 m WRF, further downhole progress was deemed hazardous. At 1720 h, the caliper was opened, recording a hole diameter of 6 inches, significantly narrower than the 9⅞ inch bit size, and an uplog was started at a speed of 900 ft/h. The caliper was closed at 490 m WRF before the top of the tool string reached the bottom of the drill string, and the uplog was completed at 1800 h when the gamma ray log identified the seafloor at 355 m WRF. The tool string was at the surface at 1825 h and completely rigged down by 1851 h. The rig floor was cleared to start the hole abandonment protocol at 1904 h.

Data quality

Figures **F68, F69,** and **F70** show a summary of the main logging data recorded in Hole U1352B. These data were converted from original field records to

depth below seafloor and processed to match depths between different logging runs. The resulting depth scale is WMSF (see **"Downhole logging"** in the "Methods" chapter).

The first indicators of the overall quality of the logs are the size and shape of the borehole measured by the calipers. Hole size measured by the HLDS caliper during the triple combo run and by the FMS arms are shown in Figures **F68** and **F69,** respectively. Although both runs indicate an enlarged and irregular hole, the readings of the two orthogonal FMS calipers (Fig. **F69**) suggest that the borehole cross section is not circular and is probably elliptical below ~270 m WSF. One caliper read close to 12 inches over most of the lower half of the logged interval, whereas the other caliper read close to ~14 inches, near the limit of its range. The fact that the curves display variability over most of the hole suggests that both sets of arms made some kind of contact with the formation, possibly with only one pad in some places. The larger HLDS caliper readings above 270 m WMSF indicate that the stronger and narrower single-arm caliper was likely pushing into the formation. Both sets of calipers show that the hole diameter is almost uniformly larger than 16 inches (>46 cm) above 270 m WMSF, suggesting that the tools were not able to make good contact with the formation above this depth. Porosity and density data, in particular, should be used with caution, most clearly between 200 and 270 m WSF, where log data deviate significantly from the same measurements made on cores (see below). Below this depth, the hole is apparently less enlarged, but it remains very irregular, and many anomalously low density readings below this depth are likely indicative of multiple narrow washouts that significantly affect the quality of the density readings.

Logs recorded in Hole U1352C show similar trends to those in Hole U1352B, reflecting the same response to lithology (Fig. **F71**). Lower values in gamma ray and medium resistivity in Hole U1352C can be explained by an extremely enlarged borehole, which is supported by HLDS caliper readings of >19.5 inches throughout the logged interval. Low gamma ray and resistivity above 115 m WMSF and between 185 and 190 m WMSF, in particular, may reflect large borehole washouts.

The quality of the logs can also be assessed by comparing log data with core measurements from the same hole. Figure **F68** shows a comparison of gamma ray and density logs with NGR and GRA bulk density track data and with MAD measurements made on cores recovered from Hole U1352B (see **"Physical properties"**). The gamma ray measurements generally agree well, even in the upper half of the hole, but the density log is seriously affected by hole conditions below ~200 m WMSF, with highly variable and anomalously low readings.

The high coherence in sonic waveforms indicated by distinct red areas in the V_P and V_S tracks in Figure **F69** suggests that, despite the enlarged hole, the Dipole Sonic Imager (DSI) was able to generate strong compressional and flexural waves and should provide reliable compressional and shear velocity values. However, all of the velocity profiles display a high variability that is likely not representative of formation properties and will require additional postcruise processing to be fully characterized. In addition, V_S values above ~150 m WMSF are systematically on the fastest edge of the high-coherence domain, suggesting a processing drift that should also be corrected postcruise.

Porosity and density estimation from the resistivity log

In order to provide a measure of porosity and density from the logs despite the poor hole conditions, we used Archie's (1942) relationship to calculate porosity from the phasor deep induction log (IDPH), which is the log least affected by borehole conditions (Schlumberger, 1989), and combined it with MAD grain density data to derive a more reliable density profile. Archie (1942) established an empirical relationship between porosity (ϕ), formation resistivity (R), and pore water resistivity (R_w) in sandy formations:

$$\phi = (aR_w/R)^{1/m},$$

where m and a are two empirical parameters that are often called cementation and tortuosity (or Archie) coefficients, respectively. The resistivity of seawater (R_w) was calculated as a function of temperature and salinity, as described by Fofonoff (1985). Pore water salinity was assumed to be 30 ppt (or 3%; see **"Geochemistry and microbiology"**), and temperature was assumed to follow a linear gradient of 42°C/km, as established by in situ temperature measurements (see **"Heat flow"**). The most realistic value for the cementation coefficient is a = 1 because this gives a resistivity equal to formation water resistivity when porosity is 100%. A value of m = 1.9 was chosen iteratively to provide the best baseline match with MAD porosity data. Although Archie's relationship was originally defined for sand-rich formations, Jarrard et al. (1989) showed that the effect of clay minerals is moderate, and the relationship is commonly used to estimate porosity in clay-rich formations with poor borehole conditions (Collett, 1998; Jarrard et al., 1989). The resulting porosity log is shown in Figure

F68, where it compares very well with MAD porosity data. Using MAD grain density, we used this resistivity-derived porosity to calculate a new density curve, which is in good agreement with core data and does not display any of the anomalous variability of the original density log.

Logging stratigraphy

The combined analysis of gamma ray, resistivity, density, and velocity logs allows for the identification of logging units defined by characteristic trends. Because of the uniformity of the sediments in the logged interval (see "Lithostratigraphy"), these units are mostly defined by subtle changes in trends and correlations rather than by indications of significant changes in the formation. The downhole logs were used to define two logging units.

Logging Unit 1 (82–250 m WMSF) is characterized by relatively low amplitude variations in gamma ray, resistivity, and acoustic velocities. A distinct increasing-upward trend in gamma ray occurs at 250 m WMSF, and a high gamma ray interval occurs between ~160 and 170 m WMSF, which corresponds to an interval of homogeneous mud with clay beds (Core 317-U1352B-19H). Gamma ray spectroscopy shows a significant uranium contribution to the total radioactivity throughout this unit (Fig. F70). The similarity between the total gamma ray and the potassium and thorium curves suggests that the increase in total gamma ray is related to variations in mineralogy. Gamma ray decreases above 160 m WMSF, which may reflect generally decreasing clay content in this depth interval. The increasing-upward and then decreasing-upward pattern in gamma ray is consistent with gamma ray logs from an equivalent depth at Site 1119 (Shipboard Scientific Party, 1999b). Resistivity decreases gradually with depth, whereas velocity increases with depth. Caliper measurements that were consistently >19.5 inches (the maximum reach of the HLDS caliper) indicate an enlarged borehole.

Logging Unit 2 (250–487 m WMSF) is defined by a change to higher amplitude variations in gamma ray, resistivity, and acoustic velocities. Gamma ray and velocity increase with depth. Sharp peaks in uranium (Fig. F70) are associated with high resistivity values and can be correlated with green calcareous sandy intervals observed in the core recovered in this unit (see "Core-log correlation"). Another distinct feature of this unit is a 15 m thick fining-upward sequence between 435 and 450 m WMSF, characterized by an upward increase in gamma ray that is mirrored by an upward decrease in resistivity. The borehole diameter in this unit is smaller but highly irregular, ranging from 6 to 19.5 inches, which may reflect the presence of more cohesive marls in the formation.

Core-log correlation

Some of the most remarkable features in the logs recorded in Hole U1352B are the sharp peaks in uranium below ~270 m WMSF, all of which are associated with more modest peaks in resistivity and very distinct peaks in velocity, indicating fine indurated layers (Figs. F68, F69, F70). The higher resistivity of these layers, although less pronounced than the changes in velocity or uranium content, is enough to make them appear as bright features in the FMS electrical images, making them easy to correlate with core images. However, some of these peaks coincide with intervals of incomplete recovery (e.g., Cores 317-U1352B-37X, 42X, and 49X), likely because of the hardened, highly resistive layers, and the only means of correlation are missing intervals or traces in the core catcher (e.g., the calcareous nodule in Section 317-U1352B-49X-CC).

Some of these layers are shown in Figure F72. The sections of core that seem to match the high-uranium resistive layers are alternately described as dark greenish gray calcareous sands (Core 317-U1352B-32H), dark greenish gray sandy calcareous mud (Core 317-U1352B-35H), olive calcareous sandy marl (Core 317-U1352B-36H), olive calcareous muddy sand and sandy mud (Core 317-U1352B-37X), or olive sandy mud with calcareous concretions (Core 317-U1352B-42X). These sections of core have in common a calcareous sandy component and the occurrence of nodules or some level of cementation.

Log-seismic correlation

A depth–traveltime relationship can be determined from the sonic logs and used to correlate features in the logs, recorded in the depth domain, to features in the seismic stratigraphy, recorded in the time domain. A synthetic seismogram was constructed for the logged interval in Hole U1352B (82–487 m WSF) using sonic data and the density curve calculated from the resistivity log using Archie's relationship. Several packages of strong seismic reflections were reproduced in the synthetic seismogram shown in Figure F73, particularly below ~250 m WMSF (0.77 s two-way traveltime). In the uppermost 250 m of the borehole, sonic velocity values measured in Hole U1352B are slightly lower than, but in general agreement with, sonic velocities recorded during Leg 181 at Site 1119, located in the slope environment ~35 km from Site U1352 (Fig. F74) (Shipboard Scientific Party, 1999b). Although the general trends in velocity between 250 and 390 m WMSF are consistent, several discrete intervals (e.g., 250–270

and 300–320 m WMSF) have higher velocities at Site 1119. Below 390 m WMSF, sonic velocity at Site 1119 appears significantly higher than that in Hole U1352B. The velocity logs recorded at these two sites are also consistently slower than the velocity model used to determine the depth of the reflectors during the Expedition 317 transect (Fig. **F74;** see **"Traveltime/depth conversion"** in the "Expedition 317 summary" chapter). This velocity model was derived from data recorded in Hole 1119C and in the Clipper-1 well and predicted higher velocity values, which resulted in an offset of ~40 m at the bottom of Hole U1352B between the depths of the reflectors predicted by the velocity model and those predicted by the Hole U1352B synthetic seismogram (Figs. **F73, F74**). Because the velocity measured on core samples recovered from Hole U1352C suggests significantly higher velocity at depth (see **"Physical properties"**), it is possible that the time–depth relationships could have been reconciled at depth if logging of the deep interval in Hole U1352C had been successful.

Stratigraphic correlation

Hole U1352D, located ~20 m from Hole U1352B, was cored as a dedicated APC hole to ~128 m and no whole-round samples were taken. This hole was cored specifically to provide an independent record of Site U1352 that could be correlated with Holes U1352A and U1352B. These three overlapping records provide an opportunity to construct a spliced stratigraphic record against a common core composite depth below seafloor (CCSF) depth scale (see **"Stratigraphic correlation"** in the "Methods" chapter). MSL and NGR data were used to facilitate correlation, and further appraisal of correlations was carried out using color and GRA bulk density records. Because of whole-round sampling of Hole U1352A, coupled with its relatively short length and an analysis of its correlation potential in the software Correlator, the stratigraphic record from this hole was not required for correlation purposes. NGR and MSL data from Holes U1352B and U1352D share a number of key features, allowing correlative ties between the holes to be made (Fig. **F75**). The depths of these correlative features (in CSF-A) often differ between the two holes, requiring depth shifts of individual and/or multiple cores of as much as 7.63 m. Cumulative depth adjustments made to cores from Site U1352 are provided in Table **T29.** Unless they are erroneous, these large adjustments strongly suggest that the stratigraphic record of both holes is characterized by localized differences in the sedimentation records of the two localities. Depth adjustments of this size are much larger than is typical for correlation of pelagic sediments, reflecting the fact that the sedimentation and/or postsedimentation history of the Site U1352 continental slope environment was extremely dynamic. Equally, however, the validity of the composite depth–adjusted records for each hole needs to be treated with caution because of these unusually large depth shifts. Additionally, correlation tie points are generally ambiguous in one way or another, making the correlation fundamentally uncertain. The lack of unambiguous correlation ties between the two holes may stem from a variety of sources, including genuine inconsistencies in the physical properties of contemporaneous strata, inaccuracies/imprecision in NGR and MSL data, and drilling disturbances that affect the fidelity of the data (see **"Stratigraphic correlation"** in the "Methods" chapter).

The spliced record presented in Figure **F75** was constructed using Hole U1352B as the basis of the record because it was deemed to be the most complete. The splicing in of parts of Hole U1352D was performed only over limited intervals as close as possible to correlative ties. For the final spliced record, only four relatively short intervals were spliced in from Hole U1352D to cover either recovery gaps or suspected intervals of relative incompleteness in Hole U1352B.

Correlation between Holes U1352B and U1352D in the uppermost ~90 m was relatively straightforward and required only minimum adjustments of core depths in each hole. Two tie points in the uppermost 10 m suggest that ~4 m of strata may be missing in Hole U1352D between two peaks in the NGR record; the MSL data also support this interpretation. Because the standard shipboard protocol permits depth adjustments only to entire cores, only one point per core can be tied to a point in another core (see **"Stratigraphic correlation"** in the "Methods" section). This means that the depth adjustment of Hole U1352D at the ~7 m tie does not align the prominent low in NGR values at ~11 m in both holes because this feature is in the same core as the tie point (at ~7 m). Between ~64 and ~67 m, the stepwise shift to lower NGR values and the trough in MSL data suggest that Hole U1352B is missing ~2 m of strata relative to Hole U1352D. Edge effects and shell-hash cave-in complicate the records farther downhole, and care was therefore taken that these artifacts were not used to aid in correlation.

A tie at ~102 m was made at the base of a prominent trough in the NGR values of both records, but the known edge effects associated with these measurements on the Whole-Round Multisensor Logger means that this tie also takes into account the overall trend to lower values in the two data sets between ~67 and ~100 m. A smaller depth adjustment was made in Hole U1352B at ~89 m to correlate to a

prominent peak in the NGR data of Hole U1352D (Fig. F75).

Note that the depth shift in Hole U1352D that was needed to create the tie made at ~102 m is potentially erroneous because it is particularly large (~8.3 m) and a good match between the MSL records of the two holes could not be ascertained. In contrast, depth shifts made to both Holes U1352B and U1352D above 70 m resulted in a very good match between the MSL data of both holes (particularly between 50 and 65 m). The lack of correlation between MSL records below ~70 m potentially represents an important caveat to the veracity of the correlations below this depth. The use of additional data such as color and GRA bulk density below ~102 m to aid in correlation between the two holes did not provide any additional support for the ties made using NGR, and the potential correlation of these data sets is similarly equivocal. GRA bulk density measurements within individual APC cores are sometimes inconsistent because of the progressive compaction of sediment downcore and the sensitivity of this physical property to coring disturbance; hence, these data were omitted from the correlation exercise.

An additional tie was made at ~122 m between NGR peaks present in both Holes U1352B and U1352D (Fig. F75). Another peak in both data sets at ~118 m also ties as a consequence of this depth adjustment. A prominent low in the NGR record of Hole U1352D at ~135 m (which is not considered to represent an edge effect) can be spliced into the Hole U1352B record to cover a recovery gap in Hole U1352B based on the correlation of a peak in NGR at ~131 m. As with the depth shift made to create the tie at 102 m, these correlations provide little correlation in the MSL records, and thus these ties should be treated with caution.

Overall, the correlation between Holes U1352B and U1352D emphasizes the difficulty of correlating continental slope sediments within the constraints of the correlation approach used (see **"Stratigraphic correlation"** in the "Methods" chapter) and the fact that both records are potentially stratigraphically incomplete relative to each other.

References

Archie, G.E., 1942. The electrical resistivity log as an aid in determining some reservoir characteristics. *J. Pet. Technol.,* 5:1–8.

Browne, G.H., 1987. In situ and intrusive sandstone in Amuri facies limestone at Te Kaukau Point, southeast Wairarapa, New Zealand. *N. Z. J. Geol. Geophys.,* 30(4):363–374.

Browne, G.H., and Naish, T.R., 2003. Facies development and sequence architecture of a late Quaternary fluvial-marine transition, Canterbury Plains and shelf, New Zealand: implications for forced regressive deposits. *Sediment. Geol.,* 158(1–2):57–86. **doi:10.1016/S0037-0738(02)00258-0**

Carter, R.M., 1985. The mid-Oligocene Marshall Paraconformity, New Zealand: coincidence with global eustatic sea-level fall or rise? *J. Geol.,* 93(3):359–371. **doi:10.1086/628957**

Carter, R.M., and Gammon, P., 2004. New Zealand maritime glaciation: millennial-scale southern climate change since 3.9 Ma. *Science,* 304(5677):1659–1662. **doi:10.1126/science.1093726**

Carter, R.M., McCave, I.N., and Carter, L., 2004. Leg 181 synthesis: fronts, flows, drifts, volcanoes, and the evolution of the southwestern gateway to the Pacific Ocean, eastern New Zealand. *In* Richter, C. (Ed.), *Proc. ODP, Sci. Results,* 181: College Station, TX (Ocean Drilling Program), 1–111. **doi:10.2973/odp.proc.sr.181.210.2004**

Carter, R.M., McCave, I.N., Richter, C., Carter, L., et al., 1999. *Proc. ODP, Init. Repts.,* 181: College Station, TX (Ocean Drilling Program). **doi:10.2973/odp.proc.ir.181.2000**

Clark, P.U., Archer, D., Pollard, D., Blum, J.D., Rial, J.A., Brovkin, V., Mix, A.C., Pisias, N.G., and Roy, M., 2006. The middle Pleistocene transition: characteristics, mechanisms, and implications for long-term changes in atmospheric pCO_2. *Quat. Sci. Rev.,* 25(23–24):3150–3184. **doi:10.1016/j.quascirev.2006.07.008**

Claypool, G.E., and Kvenvolden, K.A., 1983. Methane and other hydrocarbon gases in marine sediment. *Annu. Rev. Earth Planet. Sci.,* 11(1):299–327. **doi:10.1146/annurev.ea.11.050183.001503**

Collett, T.S., 1998. Well log evaluation of gas hydrate saturations. *Trans. SPWLA Annu. Logging Symp.,* 39:MM.

Coombs, D.S., Cas, R.A., Kawachi, Y., Landis, C.A., McDonough, W.F., and Reay, A., 1986. Cenozoic volcanism in north, east, and central Otago. In Smith, I.E.M. (Ed.), Late Cenozoic Volcanism in New Zealand. *Bull.—R. Soc. N. Z.,* 23:278–312.

Cooper, R.A., 2004. *The New Zealand Geological Timescale.* Inst. Geol. Nucl. Sci. Monogr., 22.

Dehairs, F., Chesselet, R., and Jedwab, J., 1980. Discrete suspended particles of barite and the barium cycle in the open ocean. *Earth Planet. Sci. Lett.,* 49(2):528–550. **doi:10.1016/0012-821X(80)90094-1**

Eade, J.V., 1967. New Zealand recent foraminifera of the families Islandiellidae and Cassidulinidae. *N. Z. J. Mar. Freshwater Res.,* 1(4):421–454. **doi:10.1080/00288330.1967.9515217**

Edwards, A.R., Hornibrook, N. de B., Lewis, D.W., Smale, D., and van der Lingen, G.J., 1979. The depositional depth of the Oxford Chalk—Comment. *Newsl. Geol. Soc. N. Z.,* 47:40–43.

Field, B.D., and Browne, G.H., 1989. *New Zealand Geological Survey Basin Studies* (Vol. 2): *Cretaceous and Cenozoic Sedimentary Basins and Geological Evolution of Canterbury*

Region, South Island, New Zealand: Christchurch, New Zealand (DSIR).

Fofonoff, N.P., 1985. Physical properties of seawater: a new salinity scale and equation of state for seawater. *J. Geophys. Res., [Oceans],* 90(C2):3332–3342. **doi:10.1029/JC090iC02p03332**

Fulthorpe, C.S., and Carter, R.M., 1991. Continental-shelf progradation by sediment-drift accretion. *Geol. Soc. Am. Bull.,* 103(2):300–309. **doi:10.1130/0016-7606(1991)103<0300:CSPBSD>2.3.CO;2**

Fulthorpe, C.S., Carter, R.M., Miller, K.G., and Wilson, J., 1996. Marshall paraconformity: a mid-Oligocene record of inception of the Antarctic Circumpolar Current and coeval glacio-eustatic lowstand? *Mar. Pet. Geol.,* 13(1):61–77. **doi:10.1016/0264-8172(95)00033-X**

Gartner, S., 1977. Calcareous nannofossil biostratigraphy and revised zonation of the Pleistocene. *Mar. Micropaleontol.,* 2:1–25. **doi:10.1016/0377-8398(77)90002-0**

Heiden, K.A., and Holmes, M.A., 1998. Grain-size distribution and significance of clay and clay-sized minerals in Eocene to Holocene sediments from Sites 918 and 919 in the Irminger Basin. *In* Saunders, A.D., Larsen, H.C., and Wise, S.W., Jr. (Eds.), *Proc. ODP, Sci. Results,* 152: College Station, TX (Ocean Drilling Program), 39–49. **doi:10.2973/odp.proc.sr.152.248.1998**

Jarrard, R.D., Dadey, K.A., and Busch, W.H., 1989. Velocity and density of sediments of Eirik Ridge, Labrador Sea: control by porosity and mineralogy. *In* Srivastava, S.P., Arthur, M.A., Clement, B., et al., *Proc. ODP, Sci. Results,* 105: College Station, TX (Ocean Drilling Program), 811–835. **doi:10.2973/odp.proc.sr.105.146.1989**

Jolly, R.H., and Lonergan, L., 2002. Mechanisms and controls on the formation of sand intrusions. *J. Geol. Soc. (London, U. K.),* 159(5):605–617. **doi:10.1144/0016-764902-025**

Kameo, K., and Bralower, T.J., 2000. Neogene calcareous nannofossil biostratigraphy of Sites 998, 999, and 1000, Caribbean Sea. *In* Leckie, R.M., Sigurdsson, H., Acton, G.D., and Draper, G. (Eds.), *Proc. ODP, Sci. Results,* 165: College Station, TX (Ocean Drilling Program), 3–17. **doi:10.2973/odp.proc.sr.165.012.2000**

Lewis, D.W., 1973. Polyphase limestone dikes in the Oamaru region, New Zealand. *J. Sediment. Petrol.,* 43(4):1031–1045. **doi:10.1306/74D728E2-2B21-11D7-8648000102C1865D**

Lind, I.L., Janecek, T.R., Krissek, L.A., Prentice, M.L., and Stax, R., 1993. Color bands in Ontong Java Plateau carbonate oozes and chalks. *In* Berger, W.H., Kroenke, L.W., Mayer, L.A., et al., *Proc. ODP, Sci. Results,* 130: College Station, TX (Ocean Drilling Program), 453–470. **doi:10.2973/odp.proc.sr.130.007.1993**

Lu, H., and Fulthorpe, C.S., 2004. Controls on sequence stratigraphy of a middle Miocene–Holocene, current-swept, passive margin: offshore Canterbury Basin, New Zealand. *Geol. Soc. Am. Bull.,* 116(11):1345–1366. **doi:10.1130/B2525401.1**

Lu, H., Fulthorpe, C.S., and Mann, P., 2003. Three-dimensional architecture of shelf-building sediment drifts in the offshore Canterbury Basin, New Zealand. *Mar. Geol.,* 193(1–2):19–47. **doi:10.1016/S0025-3227(02)00612-6**

McDougall, I., and Coombs, D.S., 1973. Potassium-argon ages for the Dunedin volcano and outlying volcanics. *N. Z. J. Geol. Geophys.,* 16(2):179–188.

McDuff, R.E., and Gieskes, J.M., 1976. Calcium and magnesium profiles in DSDP interstitial waters: diffusion or reaction? *Earth Planet. Sci. Lett.,* 33(1):1–10. **doi:10.1016/0012-821X(76)90151-5**

McGonigal, K., and Di Stefano, A., 2002. Calcareous nannofossil biostratigraphy of the Eocene–Oligocene Transition, ODP Sites 1123 and 1124. *In* Richter, C. (Ed.), *Proc. ODP, Sci. Results,* 181: College Station, TX (Ocean Drilling Program), 1–22. **doi:10.2973/odp.proc.sr.181.207.2002**

Newman, J., Eckersley, K.M., Francis, D.A., and Moore, N.A., 2000. Application of vitrinite-inertinite reflectance and fluorescence (VIRF) to maturity assessment in the East Coast and Canterbury Basins of New Zealand. *N. Z. Pet. Conf. Proc.*, 314–333. **http://www.crownminerals.govt.nz/cms/pdf-library/petroleum-conferences-1/2000-conference-proceedings/newman-375-kb-pdf**

Paytan, A., Kastner, M., and Chavez, F.P., 1996. Glacial to interglacial fluctuations in productivity in the equatorial Pacific as indicated by marine barite. *Science,* 274(5291):1355–1357. **doi:10.1126/science.274.5291.1355**

Peuraniemi, V., Aario, R., and Pulkkinen, P., 1997. Mineralogy and geochemistry of the clay fraction of till in northern Finland. *Sediment. Geol.,* 111(1–4)313–327. **doi:10.1016/S0037-0738(97)00023-7**

Reyes, A.G., 2007. Abandoned oil and gas wells: a reconnaissance study of an unconventional geothermal resource. *GNS Sci. Rep.,* 2007/23.

Richter, C., Acton, G., Endris, C., and Radsted, M., 2007. Handbook for shipboard paleomagnetists. *ODP Tech. Note,* 34. **doi:10.2973/odp.tn.34.2007**

Roussel, E.G., Cambon Bonavita, M.-A., Querellou, J., Cragg, B.A., Webster, G., Prieur, D., and Parkes, J.R., 2008. Extending the sub-sea-floor biosphere. *Science*, 320(5879):1046. **doi:10.1126/science.1154545**

Schlumberger, 1989. *Log Interpretation Principles/Applications:* Houston (Schlumberger Educ. Serv.), SMP–7017.

Sewell, R.J., 1988. Late Miocene volcanic stratigraphy of central Banks Peninsula, Canterbury, New Zealand. *N. Z. J. Geol. Geophys.,* 31(1):41–64.

Sewell, R.J., Weaver, S.D., and Reay, M.B., 1992. Geology of Banks Peninsula, 1:100,000. Inst. Geol. Nucl. Sci. Map, 3.

Shipboard Scientific Party, 1988. Site 682. *In* Suess, E., von Huene, R., et al., *Proc. ODP, Init. Repts.,* 112: College Station, TX (Ocean Drilling Program), 363–435. **doi:10.2973/odp.proc.ir.112.113.1988**

Shipboard Scientific Party, 1999a. Leg 181 summary: southwest Pacific paleoceanography. *In* Carter, R.M., McCave, I.N., Richter, C., Carter, L., et al., *Proc. ODP, Init. Repts.,* 181: College Station, TX (Ocean Drilling Program), 1–80. **doi:10.2973/odp.proc.ir.181.101.2000**

Shipboard Scientific Party, 1999b. Site 1119: drift accretion on Canterbury Slope. *In* Carter, R.M., McCave, I.N., Richter, C., Carter, L., et al., *Proc. ODP, Init. Repts.,* 181:

College Station, TX (Ocean Drilling Program), 1–112. doi:10.2973/odp.proc.ir.181.103.2000

Smith, D.C., Spivack, A.J., Fisk, M.R., Haveman, S.A., Staudigel, H., and the Leg 185 Shipboard Scientific Party, 2000. Methods for quantifying potential microbial contamination during deep ocean coring. *ODP Tech. Note,* 28. doi:10.2973/odp.tn.28.2000

Suggate, R.P., 1990. Late Pliocene and Quaternary glaciations of New Zealand. *Quat. Sci. Rev.,* 9(2–3):175–197. doi:10.1016/0277-3791(90)90017-5

Sykes, R., 2004. Peat biomass and early diagenetic controls on the paraffinic oil potential of humic coals, Canterbury Basin, New Zealand. *Pet. Geosci.,* 10(4):283–303. doi:10.1144/1354-079302-568

Sykes, R., and Funnel, R.H., 2002. Petroleum source rock potential and generation history in the offshore Canterbury Basin. *Min. Econ. Dev. N. Z. Pet. Rep.,* PR2707.

Sykes, R., and Johansen, P.E., 2009. Maturation characteristics of the New Zealand coal band, Part 1. Evolution of oil and gas products. *Abstr. Rep. Int. Congr. Org. Geochem.,* 23:571–572.

van der Lingen, G.J., Smale, D., and Lewis, D.W., 1978. Alteration of a pelagic chalk below a paleokarst surface, Oxford, South Island, New Zealand. *Sediment. Geol.,* 21(1):45–66. doi:10.1016/0037-0738(78)90033-7

van Morkhoven, F.P.C.M., Berggren, W.A., and Edwards, A.S., 1986. Cenozoic cosmopolitan deep-water benthic foraminifera. *Bull. Cent. Rech. Explor.—Prod. Elf-Aquitaine,* 11.

Ward, D.M., and Lewis, D.W., 1975. Paleoenvironmental implications of storm-scoured, ichnofossiliferous mid-Tertiary limestones, Waihao District, South Canterbury, New Zealand. *N. Z. J. Geol. Geophys.,* 18(6):881–908.

Publication: 4 January 2011
MS 317-104

Figure F1. Dip Profile EW00-01-60 showing Site U1352 and proposed alternate Site CB-04A. There is no crossing strike profile at this site. Yellow = proposed penetration, red = actual penetration (1927.5 m CSF-A). Authorization to exceed the proposed maximum penetration of 1913 m CSF-A was granted because the Marshall Paraconformity (MP) was deeper than expected. CDP = common depth point.

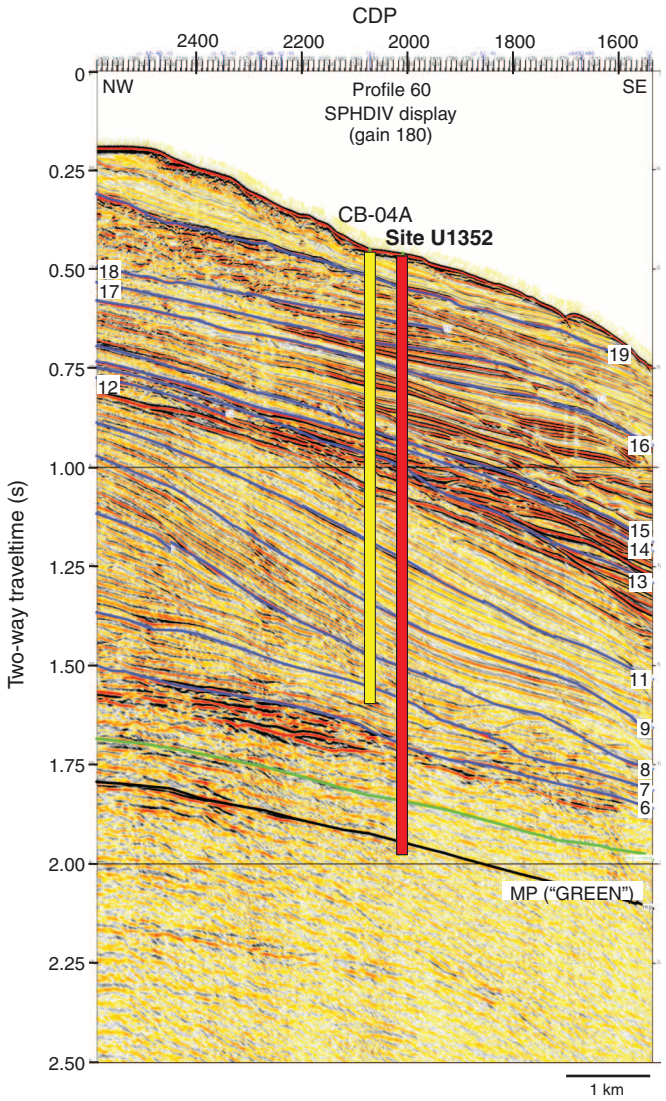

Figure F2. Map of drilled and proposed Expedition 317 sites, together with EW00-01 high-resolution (frequencies up to 300 Hz) MCS grid (thick straight lines), low-resolution CB-82 commercial MCS grid (thin straight lines), exploration wells Clipper and Resolution, and Ocean Drilling Program (ODP) Site 1119. The EW00-01 survey was designed to provide improved vertical resolution (~5 m in the upper 1 s) to enhance our ability to define high-frequency sedimentary sequences. Also shown is the distribution of seismically resolvable sediment drifts D1–D11, along with D8 and D9 subdrifts. Blue curved lines = crests of drift mounds, dashed blue lines = drifts identified on CB-82 profiles. Dip Profiles EW00-01-66, EW00-01-60, EW00-01-01, EW00-01-07a, and CB-82-25 are also labeled.

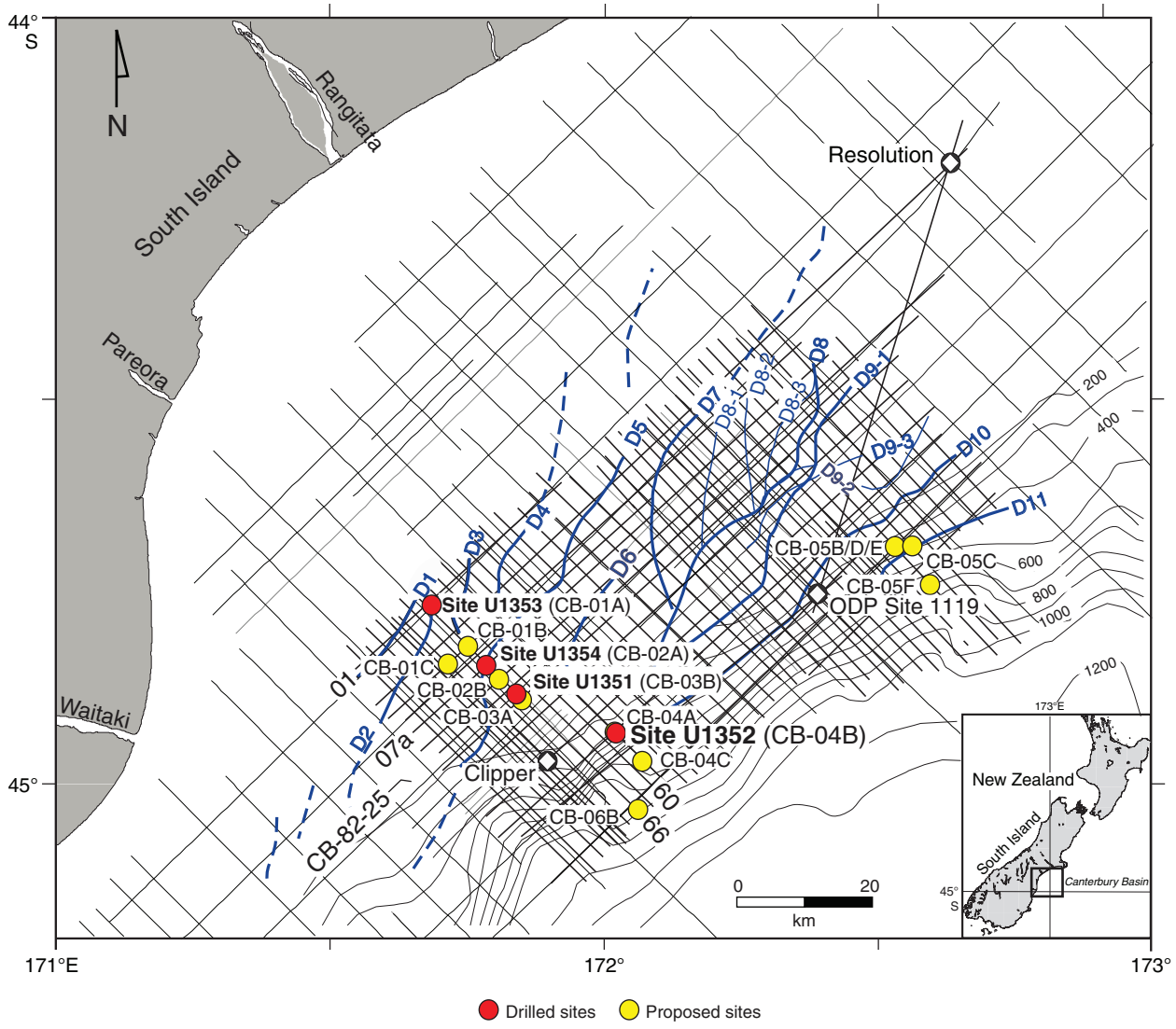

Figure F3. Summary of core recovery, lithology, lithologic units, unit descriptions, physical property data (colorimetry, magnetic susceptibility, and NGR), and gamma ray data from downhole logging, Hole U1352B. Downhole logging data are plotted on the WMSF depth scale. NGR = natural gamma radiation, cps = counts per second.

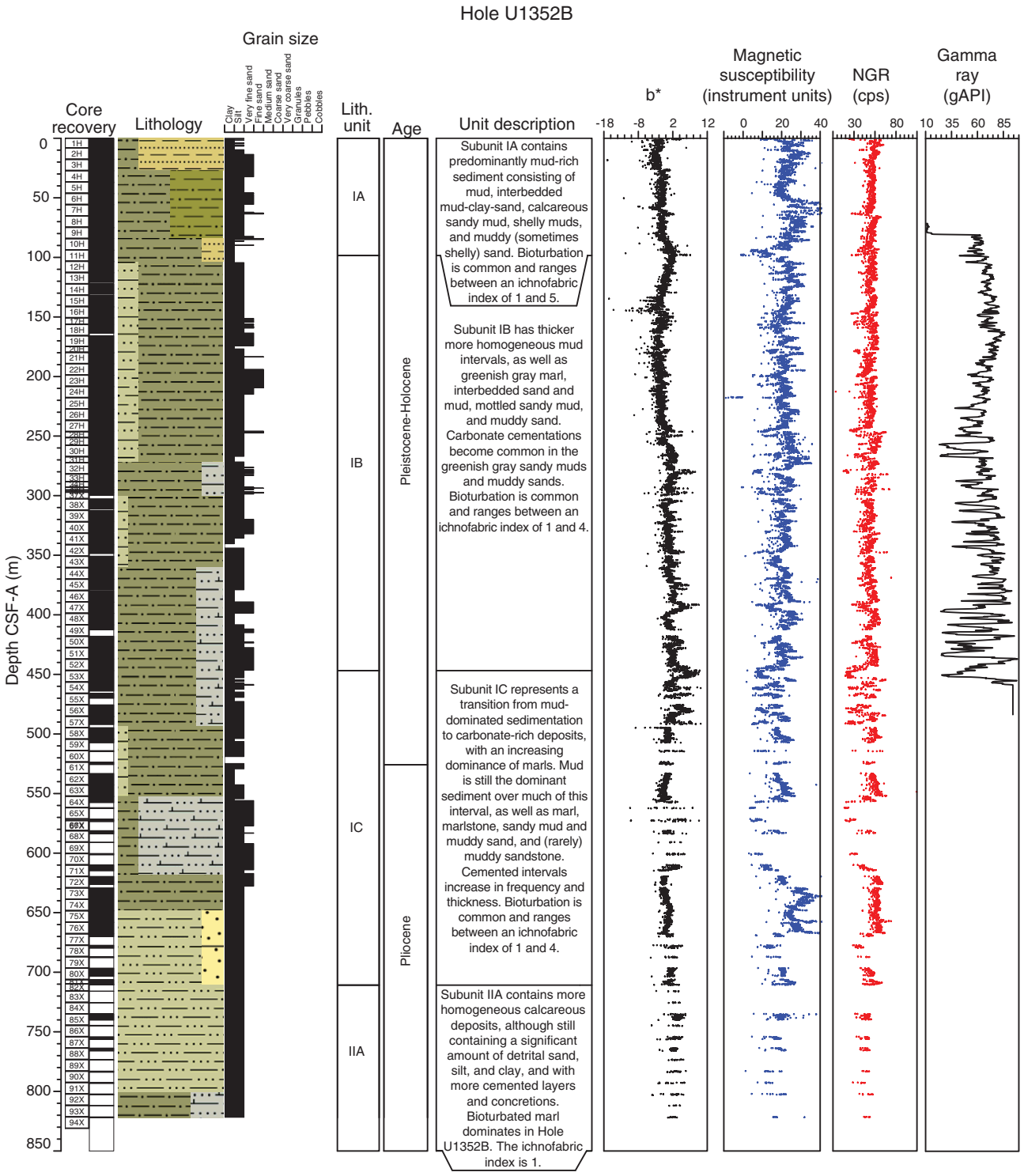

Figure F4. Summary of core recovery, lithology, lithologic units, unit descriptions, physical property data (colorimetry, magnetic susceptibility, and NGR), and gamma ray data from downhole logging, Hole U1352C. Downhole logging data are plotted on the WMSF depth scale. NGR = natural gamma radiation. **A.** 0–1200 m CSF-A. (**Continued on next page.**)

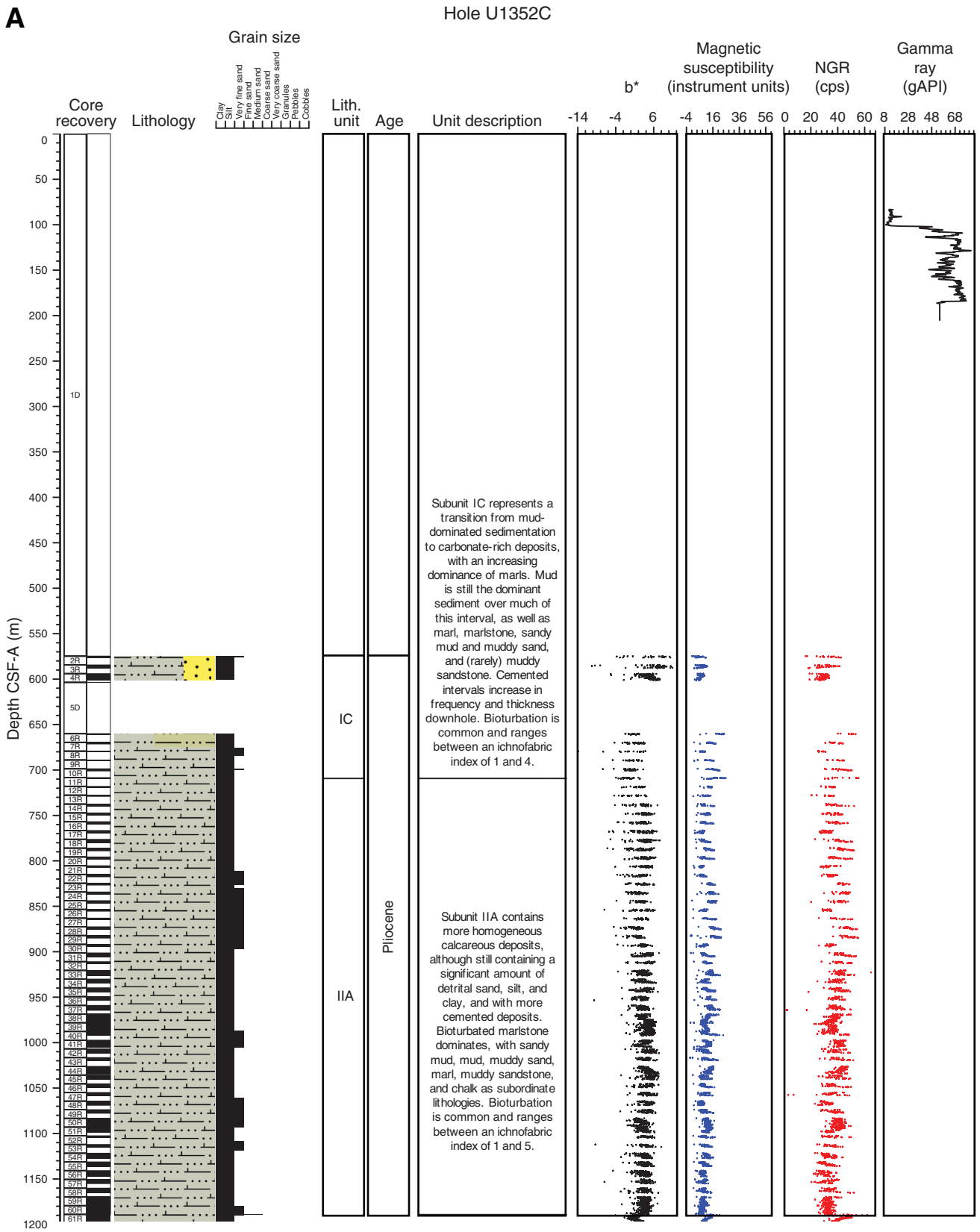

Figure F4 (continued). B. 1200–1930 m CSF-A.

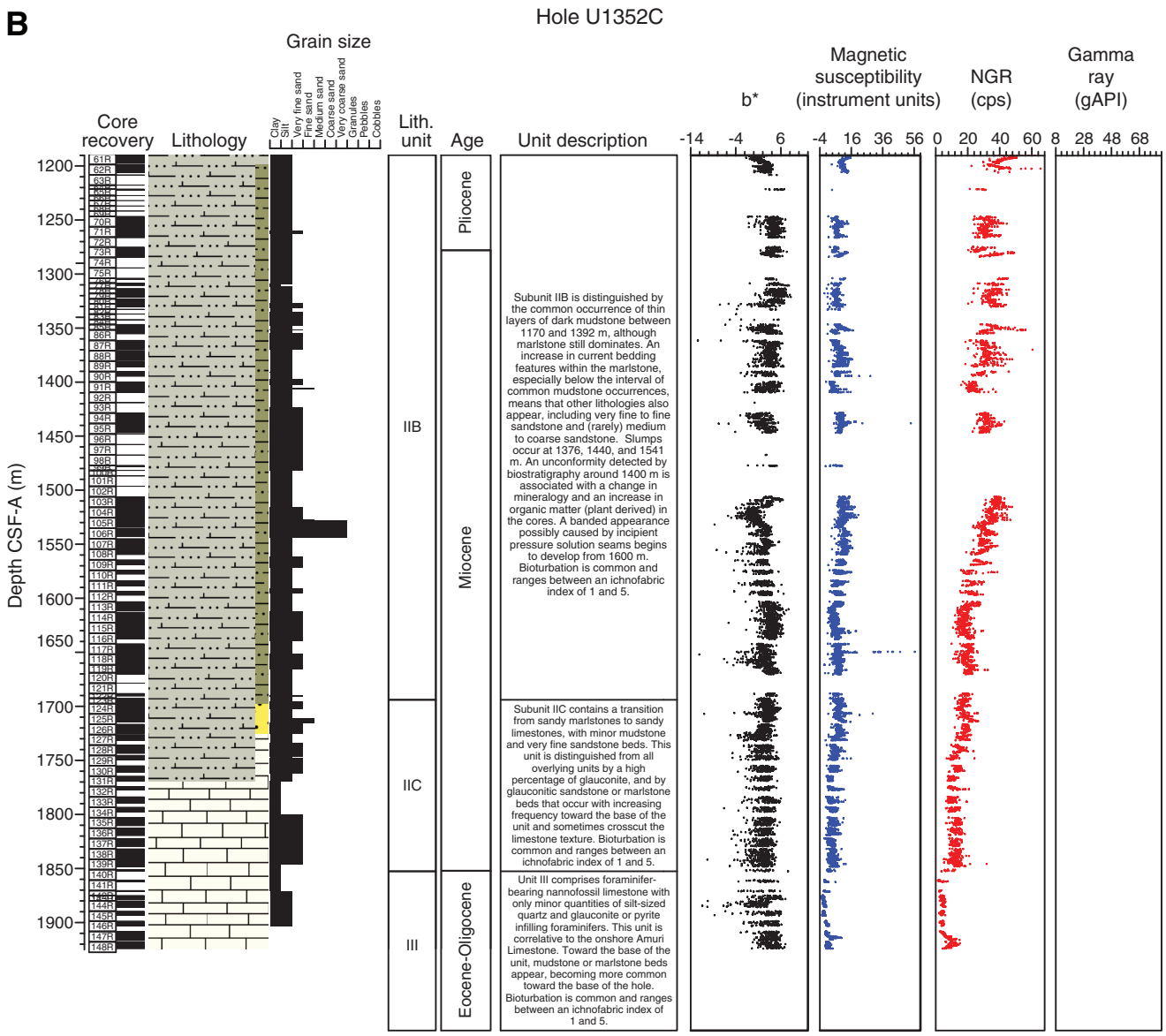

Figure F5. Core recovery and lithology shown as a proportion of the recovered interval (lithology [%] × recovery [%]/100) in Hole U1352B. Depth scale in CSF-A (m) is variable, but for graphical purposes each core is depicted by an equally thick horizontal bar.

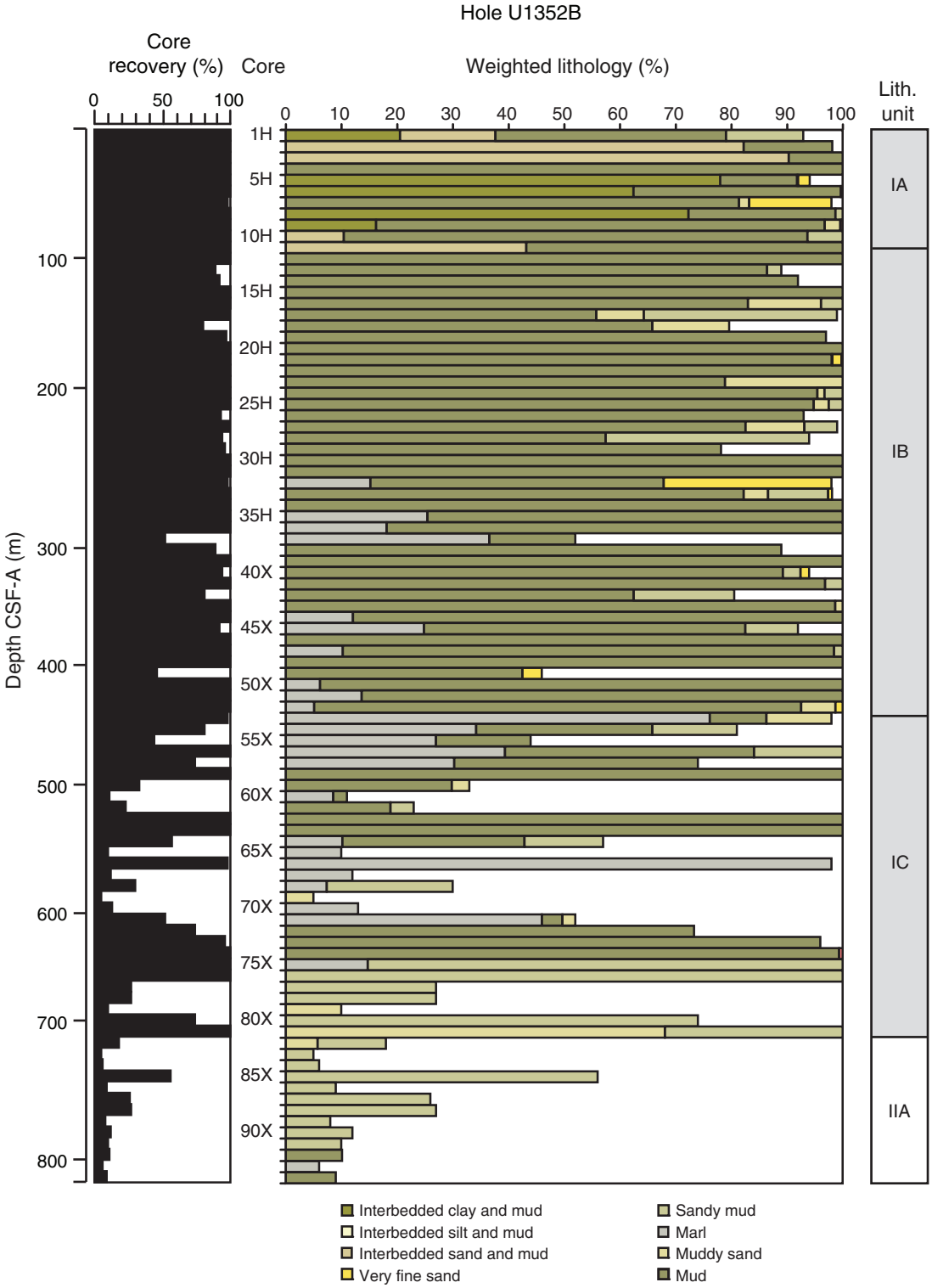

Figure F6. Core photographs of various mud lithofacies from Subunit IA. All pictures have the same vertical scale. **A.** Mud-sand-clay interbedding, dragged down at the edges of the core liner by drilling (interval 317-U1352B-2H-3, 114–134 cm). **B.** Interbedded mud and clay (interval 317-U1352A-1H-2, 91–111 cm). **C.** Mottled massive mud (interval 317-U1352B-7H-1, 1–21 cm). **D.** Homogeneous mud (interval 317-U1352B-9H-6, 5–25 cm).

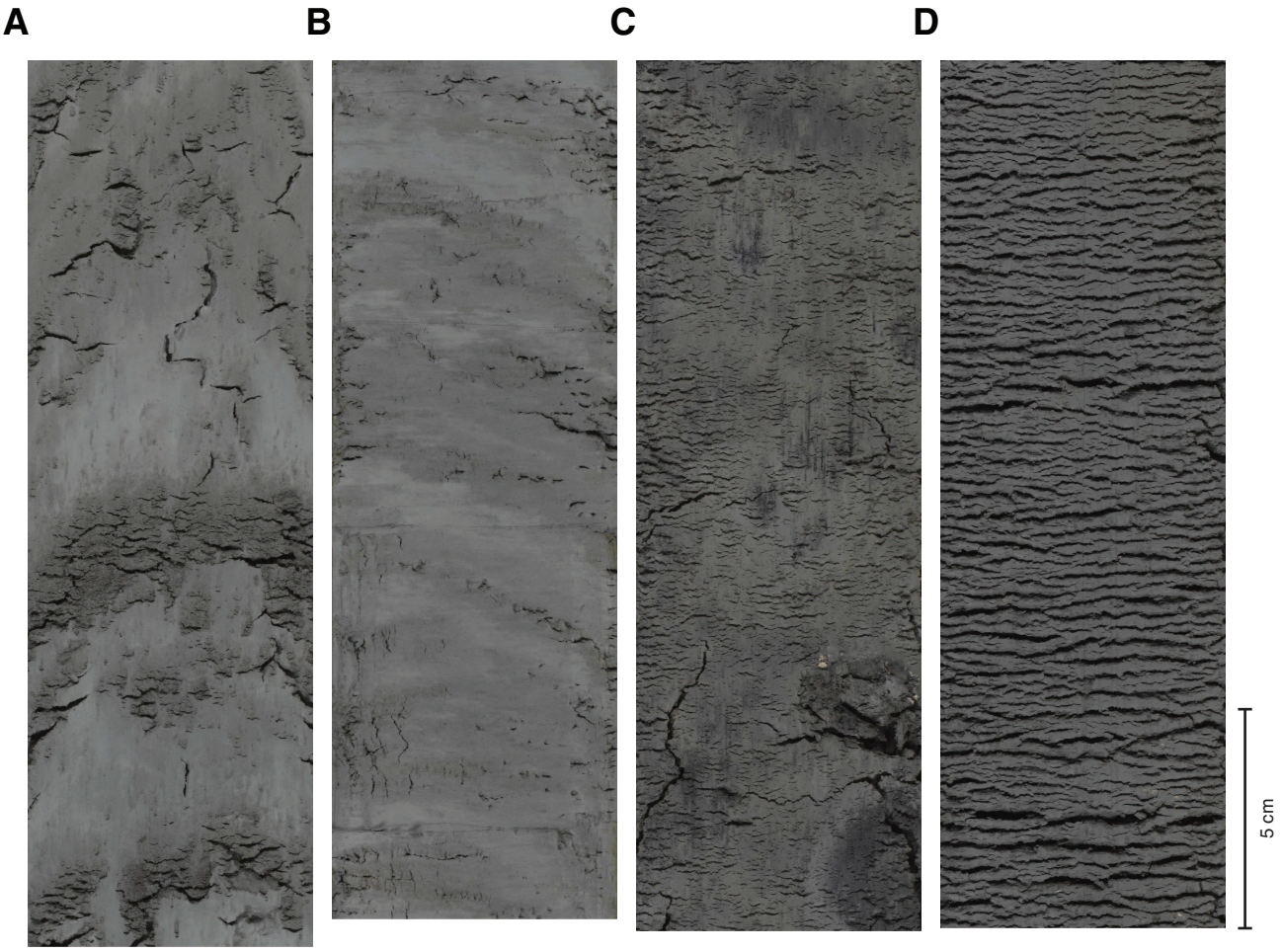

Figure F7. Core photographs of green calcareous sandy beds with sharp to bioturbated bases and concretions in the lower part of Unit I. **A.** Green sandy material in burrows below the contact between gray mud (below) and green muddy sand (above) (interval 317-U1352B-7H-6, 43–125 cm). **B.** Bioturbation of green sandy material into underlying gray mud (interval 317-U1352B-28H-1, 25–65 cm). **C.** Concretions in a green sandy marlstone (interval 317-U1352B-52X-7, 2–17 cm). **D.** Sharp contact between green muddy sandstone and gray mud (interval 317-U1352B-17H-4, 1–21 cm). B, C, and D have the same vertical scale.

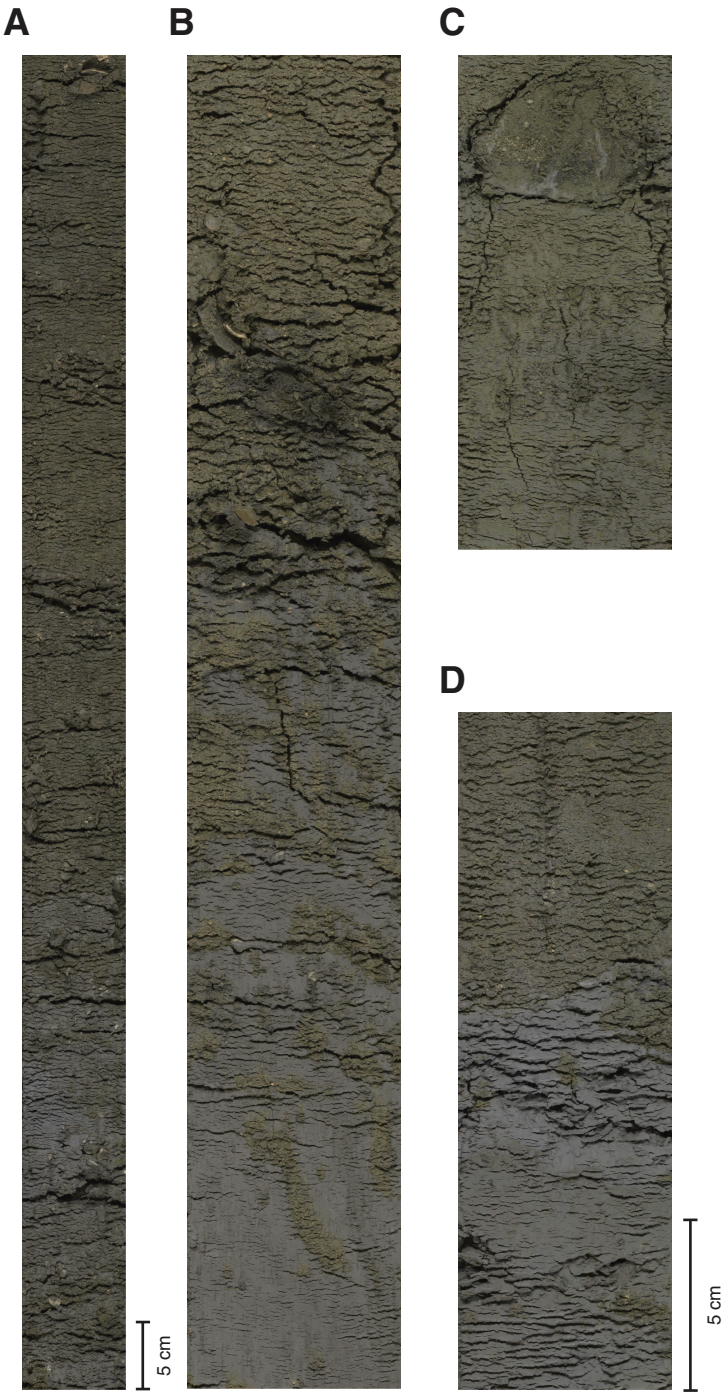

Figure F8. Core photographs of deformation in Subunit IA. All photographs are at the same vertical scale. **A.** Normal fault offsetting layers of mud, clay, and sand (interval 317-U1352A-2H-2, 15–50 cm). **B.** Distortion of clay and mud layers from drilling disturbance (interval 317-U1352A-2H-2, 49–61 cm). **C.** Folding below a thick sand layer (interval 317-U1352A-2H-4, 90–127 cm). **D.** Slump folds in interbedded sand and mud (interval 317-U1352B-2H-3, 20–40 cm).

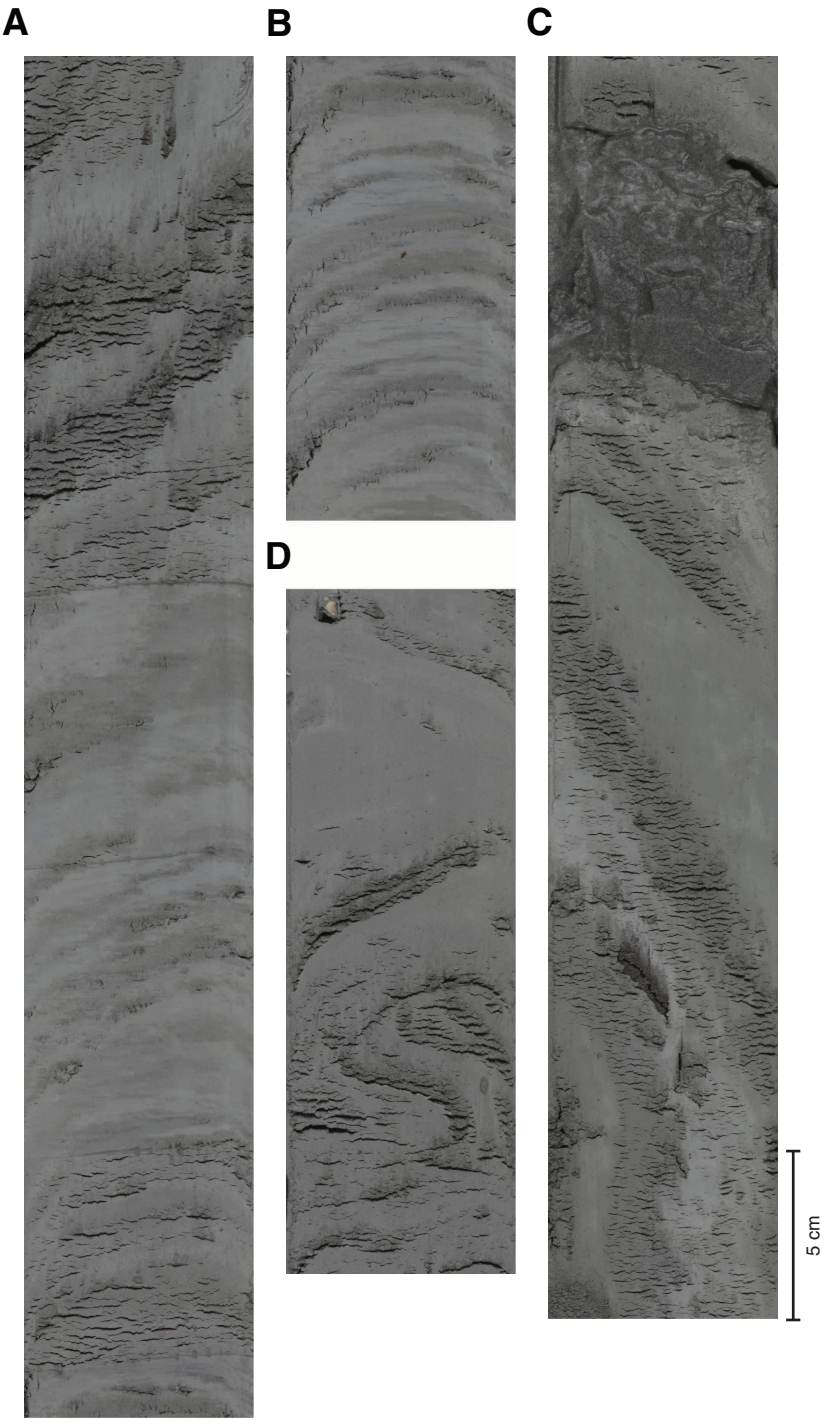

Figure F9. Core photographs of various interbedded lithofacies in Subunit IA. All photographs are at the same vertical scale. **A.** Mud-sand-clay interbedding (interval 317-U1352B-2H-5, 0–25 cm). **B.** Interbedded mud and clay (interval 317-U1352A-2H-5, 20–45 cm). **C.** Thinly interbedded clay-mud and sand-mud (interval 317-U1352B-8H-3, 5–30 cm).

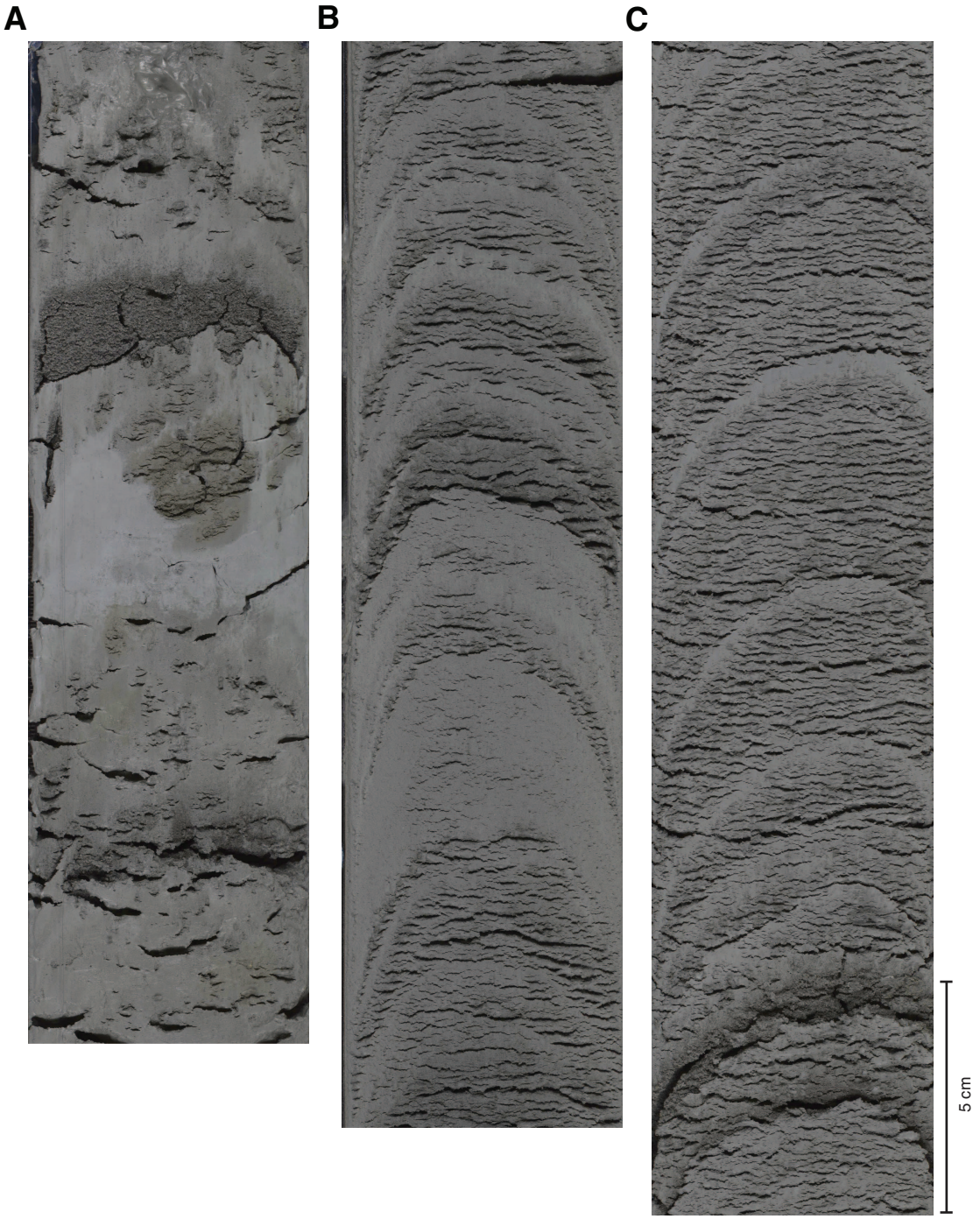

Figure F10. Mineral and textural percentage estimates based on smear slide observations, Site U1352. $CaCO_3$ estimates are plotted against data from coulometry analyses for comparison (see **"Geochemistry and microbiology"**). Clay and sand fractions tend to vary opposite each other, siliceous bioclasts and ferromagnesian minerals both diminish in Unit II, and glauconite increases abruptly in Subunit IIC. Mica refers to undifferentiated micas, biotite, muscovite, and chlorite.

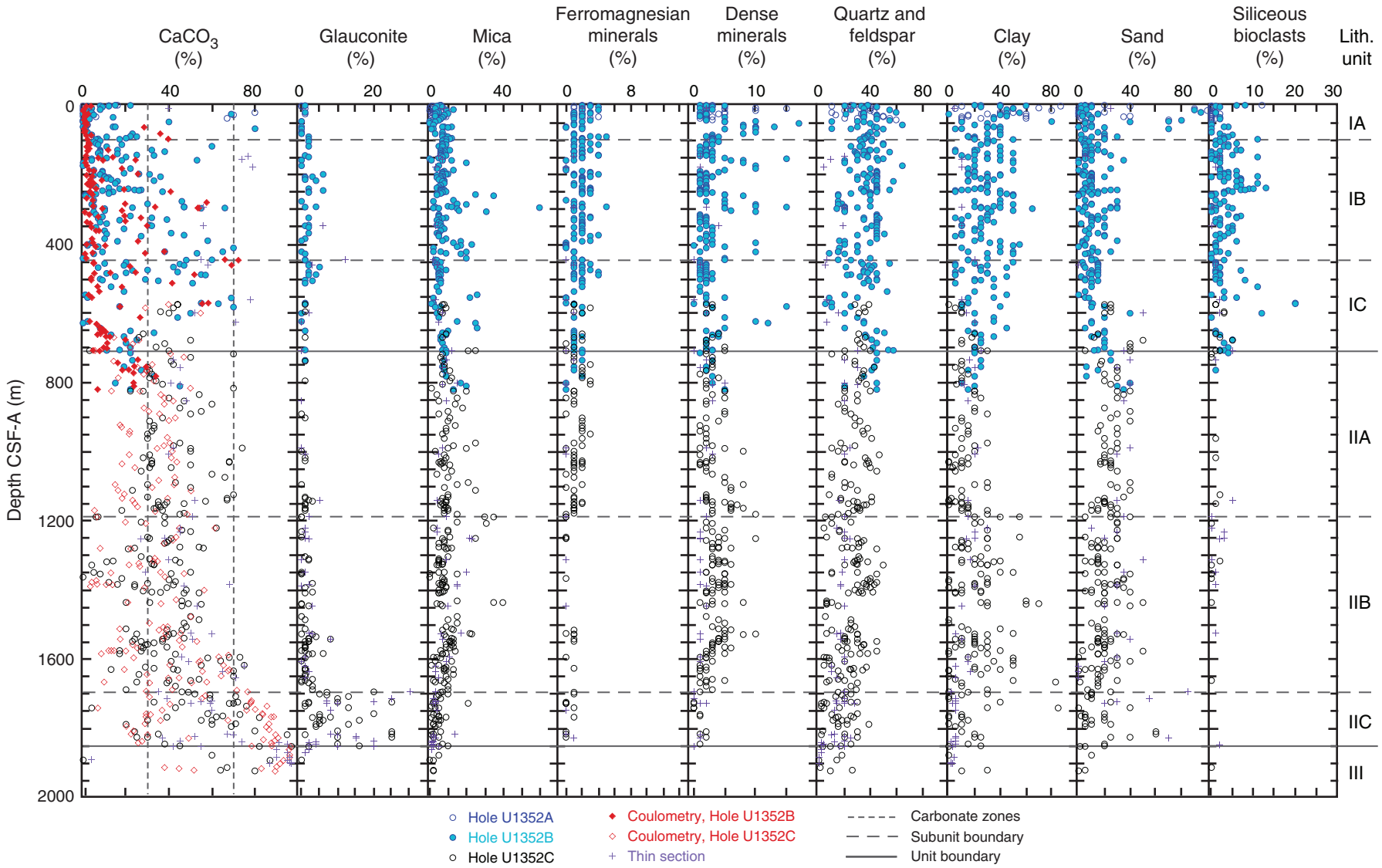

Figure F11. Relative maximum peak intensity in XRD analyses for common minerals, Holes U1352B and U1352C.

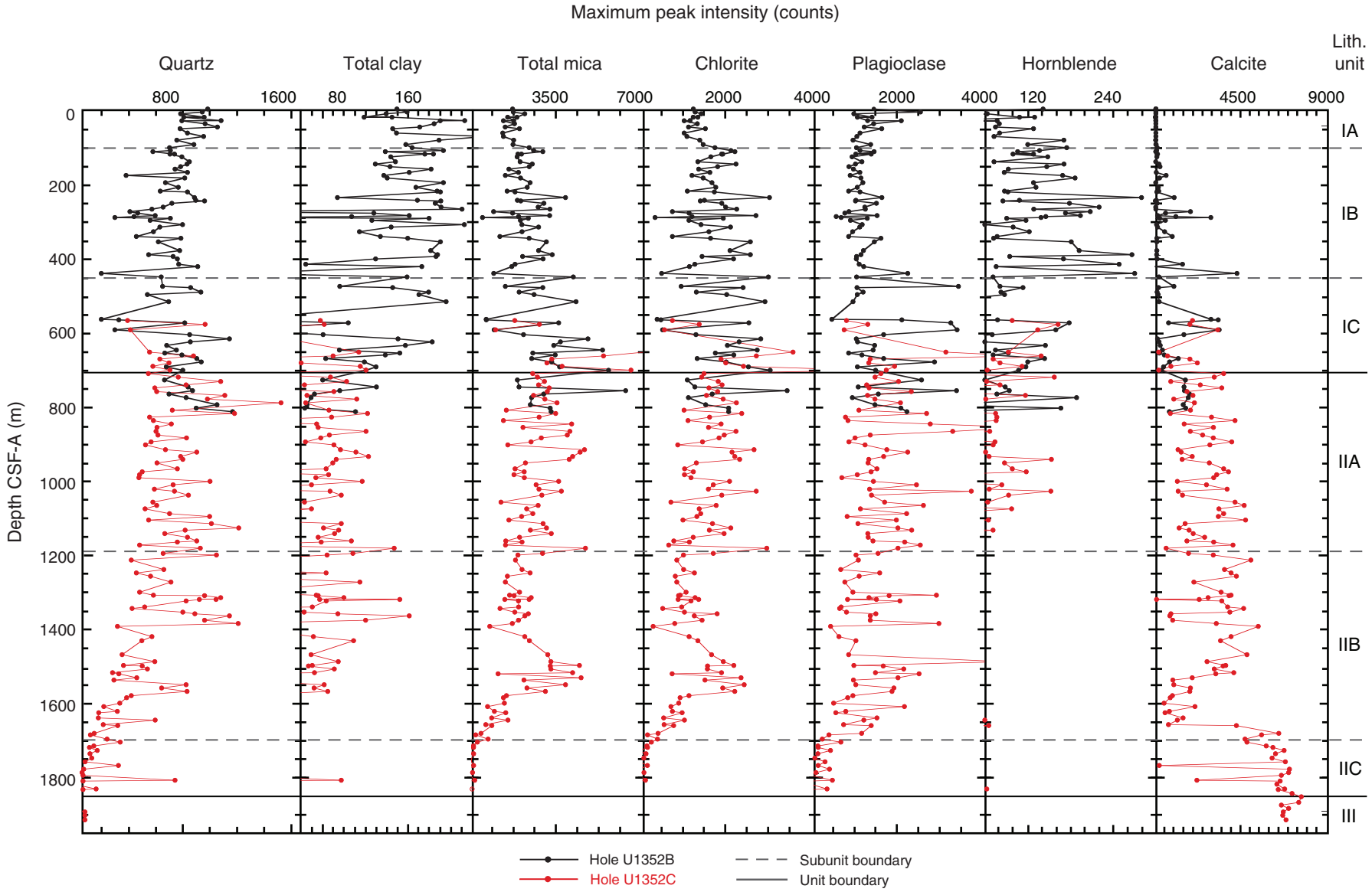

Figure F12. Thin section photomicrographs illustrating changes in lithology and diagenesis in the succession. **A.** Partly dissolved aragonitic gastropod set in a muddy micritic matrix with sparse feldspar and quartz silt (marlstone; Subunit IB); moldic pores occur elsewhere in the slide. Note the authigenic opaque minerals (pyrite?) partly lining shell interior (Sample 317-U1352B-17H-4, 69 cm). **B.** Bioturbated marlstone in Subunit IIA showing the variability of texture/lithology present on a microscopic scale in these mixed (zoned) carbonate/siliciclastic rocks: sandy marlstone (left), marlstone (center), carbonate-cemented sandstone (right) (Sample 317-U1352C-26R-1, 23 cm). **C.** Sandy marlstone in Subunit IB consisting of sand-sized foraminifers and feldspar/quartz grains set in a fine micritic matrix. Reddish brown milliolid foraminifers are less competent than other foraminifer types and show evidence of fracturing, interpenetration, and possibly pressure solution. The more competent foraminifers are locally recrystallized and exhibit fine carbonate overgrowths (far right) and local glauconitic infill (upper left). High residual porosity in this rock is mostly intraparticle within foraminifer tests (Sample 317-U1352B-42X-5, 5 cm). **D.** Section of high-amplitude stylolite passing through pelagic limestone with sparse foraminifers in Unit III. The stylolite is marked by brownish clay, along which the foraminifers are truncated, presumably by pressure solution (Sample 317-U1352B-141R-2, 15 cm). **E, F.** Abrupt high-angle contact between muddy limestone to limestone (transitional) below (within host rock) and glauconitic sandy marlstone above (potential injection material) in Subunit IIC. Limestone color is a function of the foraminifer/nannofossil ratio (higher in light limestone; lower in dark limestone) (Sample 317-U1352C-137R-2, 58 cm).

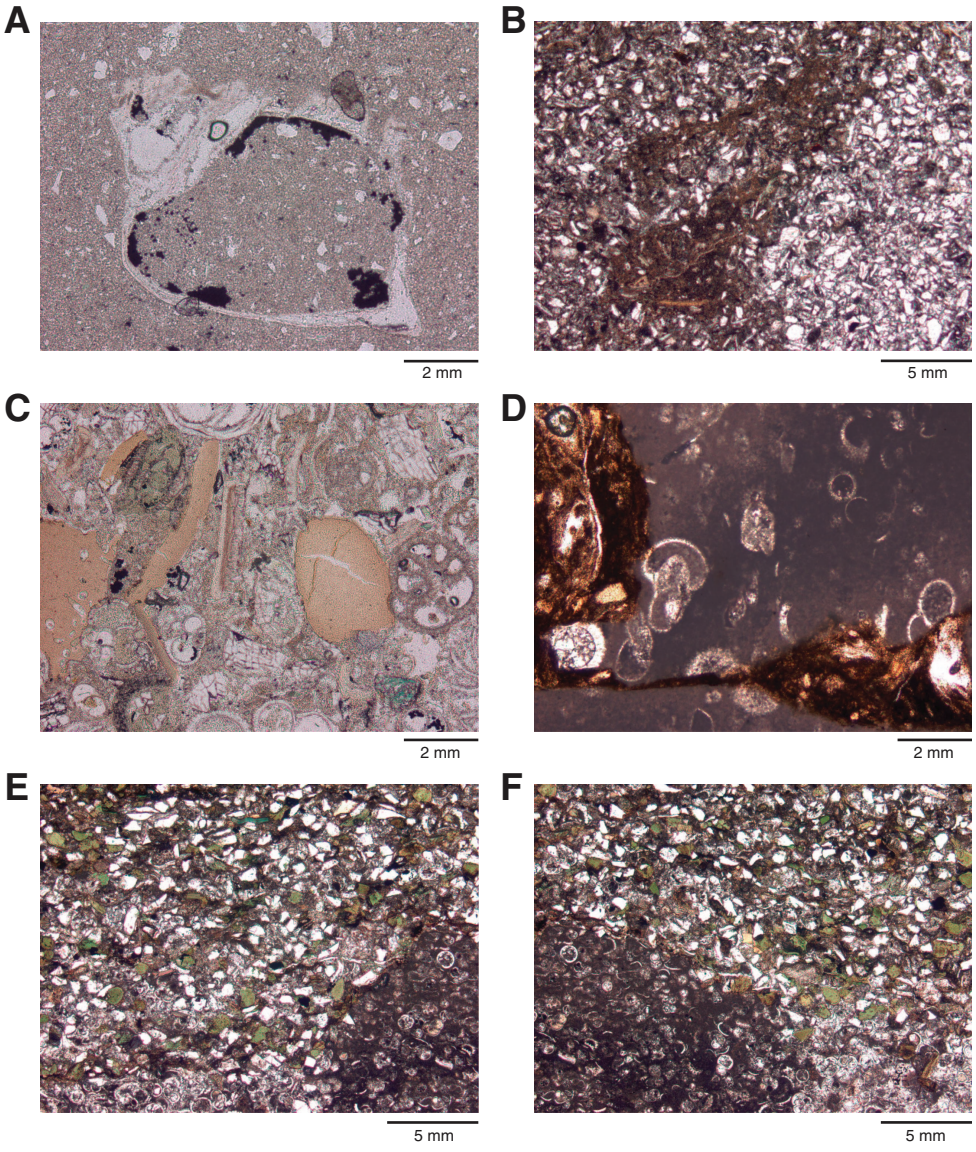

Figure F13. Total clay minerals normalized by calcite content from XRD analyses, Holes U1352B and U1352C.

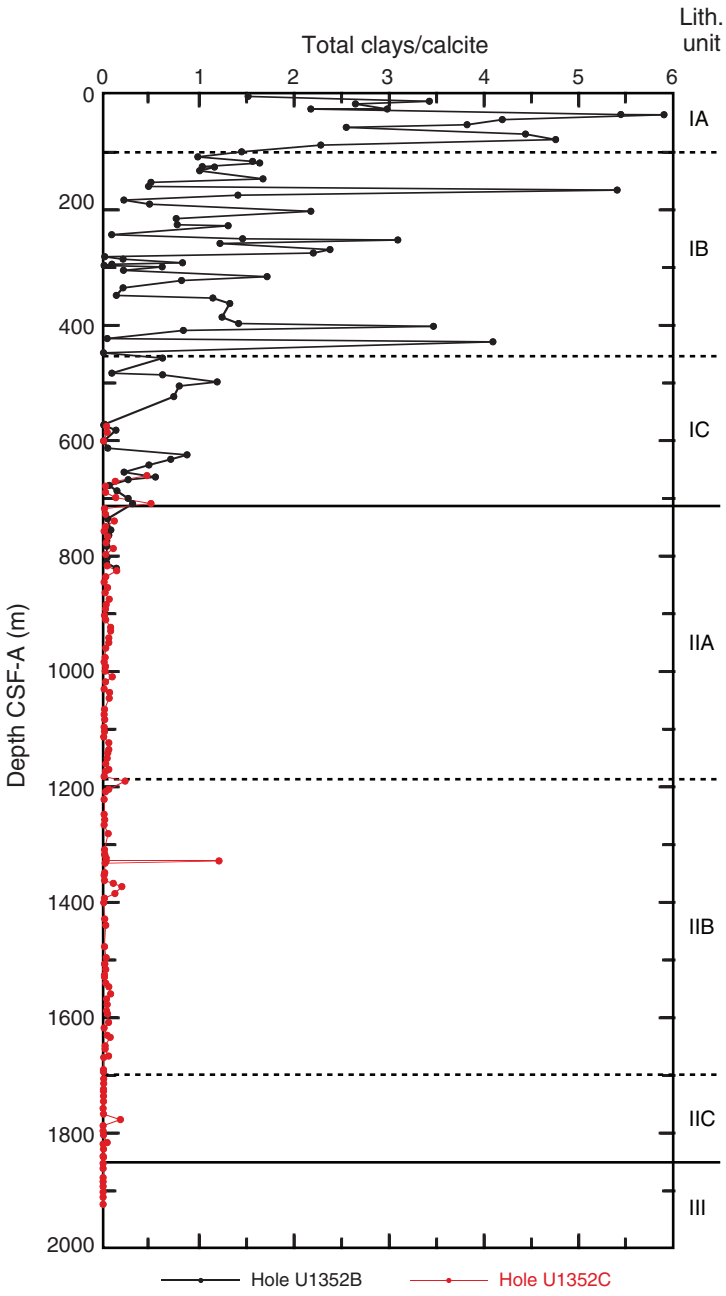

Figure F14. Core recovery and lithology shown as a proportion of the recovered interval (lithology [%] × recovery [%]/100) in Hole U1352C. Depth scale in CSF-A (m) is variable, but for graphical purposes each core is depicted by an equally thick horizontal bar.

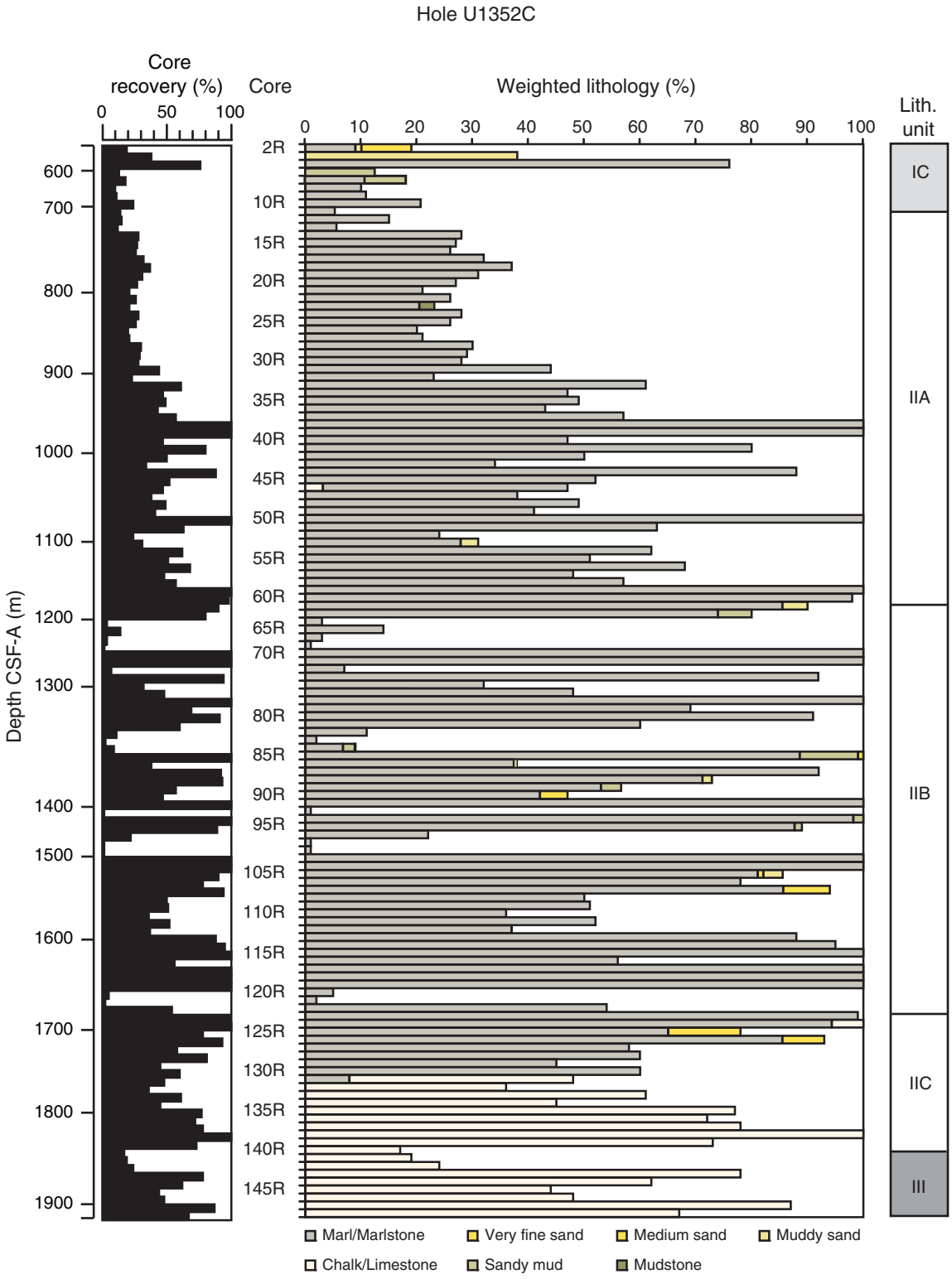

Figure F15. Representative core photographs showing features of sandy marlstones encountered in Unit II. All photographs are at the same vertical scale. **A.** Dark mudstone beds with sharp bases and burrows infilled with dark mud extending into underlying sandy marlstone (interval 317-U1352C-81R-1, 28–66 cm). **B.** Bioturbated sandy marlstone (interval 317-U1352C-42R-2, 1–16 cm). **C.** Large, pale burrows overprinting a small, darker burrow presumably belonging to an earlier episode of burrowing (interval 317-U1352C-59R-3, 31–46 cm). **D.** Lighter colored layer with higher carbonate content (interval 317-U1352C-44R-3, 10–25 cm). **E.** Patches of sand and wavy, discontinuous laminations (interval 317-U1352C-95R-6, 2–17 cm). **F.** Laminated sandy marlstone to calcareous sandstone (interval 317-U1352C-114R-6, 84–98 cm). **G.** Wavy laminations and sand lenses in a sandy marlstone (interval 317-U1352C-114R-7, 15–32 cm).

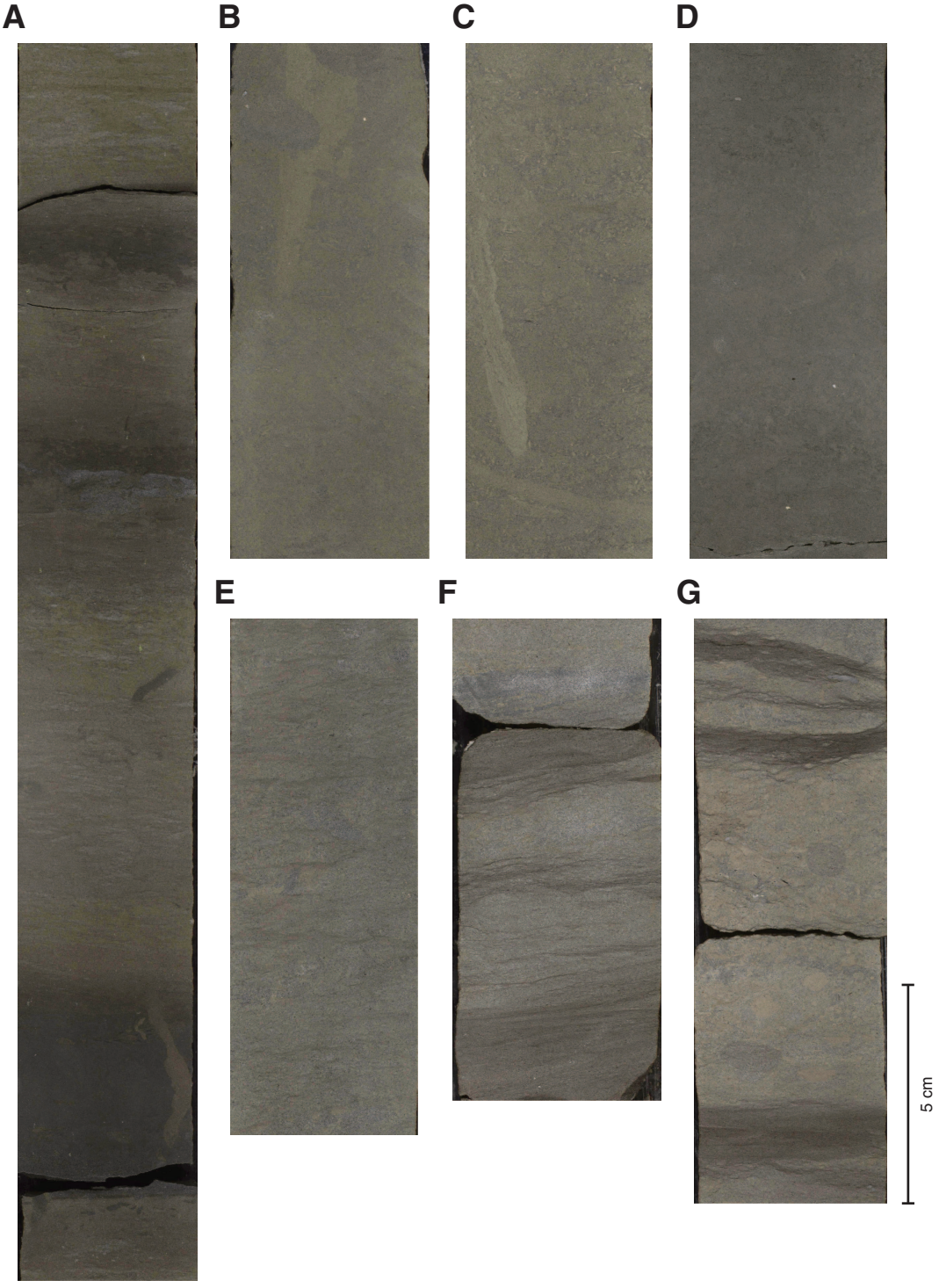

Figure F16. Core photographs, interpretation, and sketches of soft-sediment deformation intervals in Subunit IIB. The base of Section 317-U1352C-94R-7 (1438.2 m) was described as surface U1352C-S12. **A.** Fluidized structures associated with soft-sediment deformation (Core 317-U1352C-94R). Shades of gray indicate color changes in lithology. **B.** Very fine sandy marlstone showing soft-sediment deformation structures: recumbent and isoclinal folding, fluidized structures, and coarse to medium sand (Section 317-U1352C-106R-4). **C.** Poorly sorted sandy marlstone with fine to coarse, angular, lithic clasts near the base of an interval of soft-sediment deformation extending from Sections 317-U1352C-105R-1 to 106R-5 (interval 317-U1352C-106R-4, 49–59 cm).

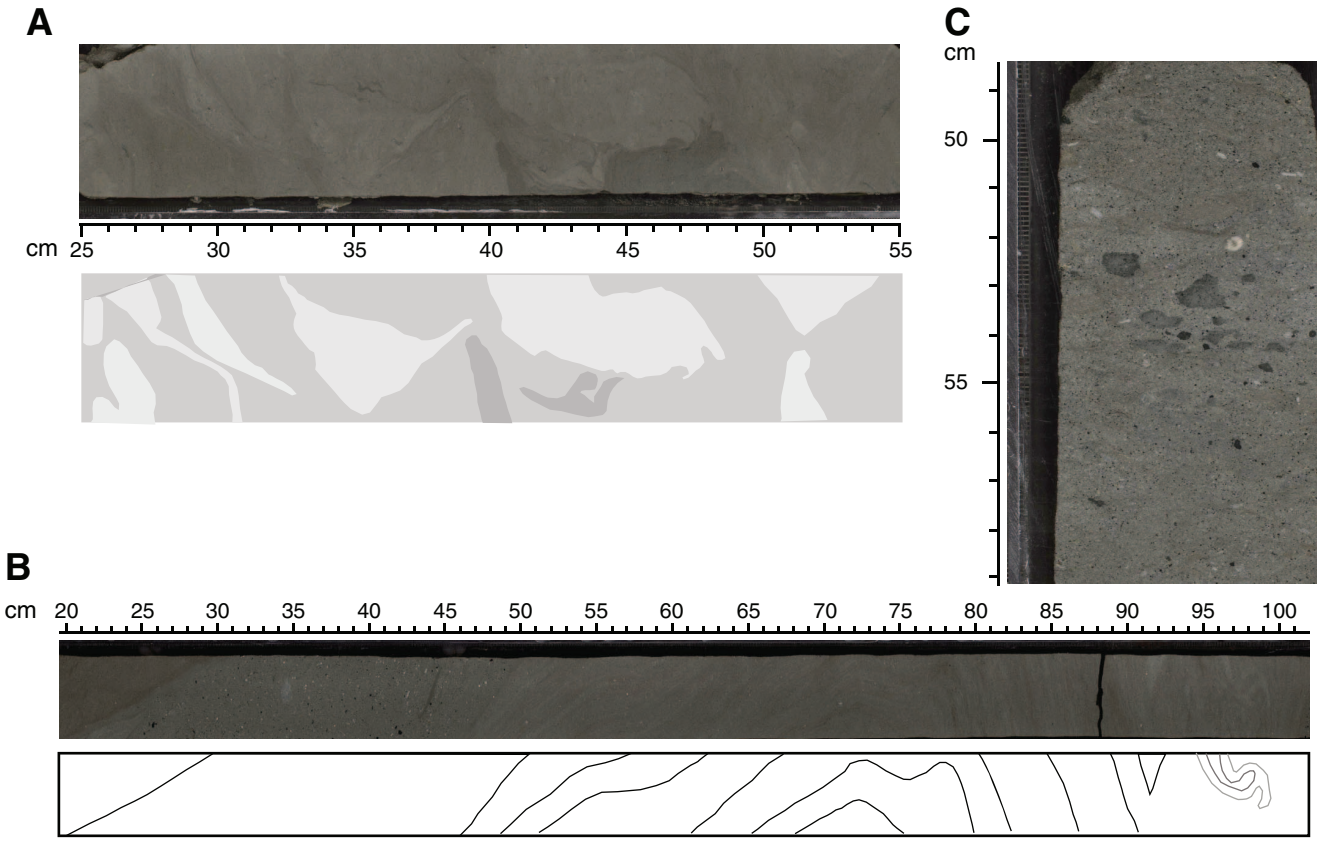

Figure F17. Core photographs showing characteristic features of Subunit IIC. **A.** Characteristic striped pattern of marlstones or limestones and glauconitic sandstone or marlstone layers (interval 317-U1352C-135R-3, 67–128 cm). **B.** Laminated layers of glauconitic sandstone (interval 317-U1352C-135R-3, 66–76 cm). **C.** Intersecting and high-angle layers of glauconitic sandstone (interval 317-U1352C-139R-5, 19–29 cm). **D.** Converging layers of glauconitic sandstone (interval 317-U1352C-135R-2, 62–72 cm). **E.** High-angle layers between blocks of glauconitic limestone (interval 317-U1352C-136R-3, 6–16 cm). **F.** Example of truncation of limestone fabric (burrow) by glauconitic sandstone layer (interval 317-U1352C-134R-1, 71–81 cm). B–F are at the same vertical scale.

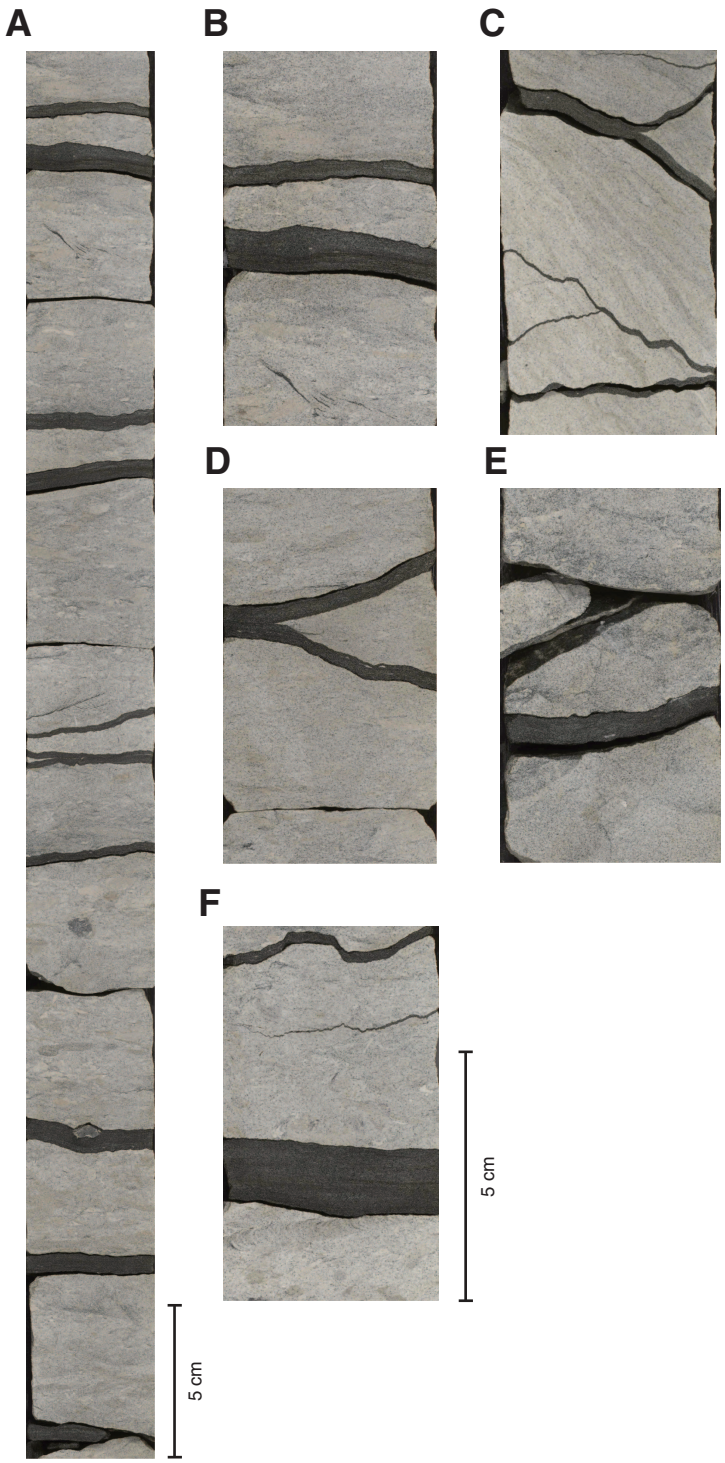

Figure F18. Core photographs of contact between Units II and III. Although only two limestone pieces and some rubble were recovered, it is possible the drilled succession included relatively unconsolidated glauconitic sandstone between the two limestones. **A.** Unconformity (arrow) between glauconitic sandy limestone (Miocene) and white limestone (Oligocene) (interval 317-U1352C-140R-2, 0–55 cm). **B.** Glauconitic limestone above the unconformity, Subunit IIC (interval 317-U1352C-140R-1, 6–26 cm). **C.** Stylolitic white limestone below the unconformity, Unit III (interval 317-U1352C-141R-2, 14–34 cm). **D.** Stylolitic white limestone with purple banding and pyrite concentrated in a stylolite, Unit III (interval 317-U1352C-144R-2, 41–61 cm). **E.** Muddy limestone with layers of marlstone and purple banding, Unit III (interval 317-U1352C-148R-1, 62–68 cm). B–E are at the same vertical scale.

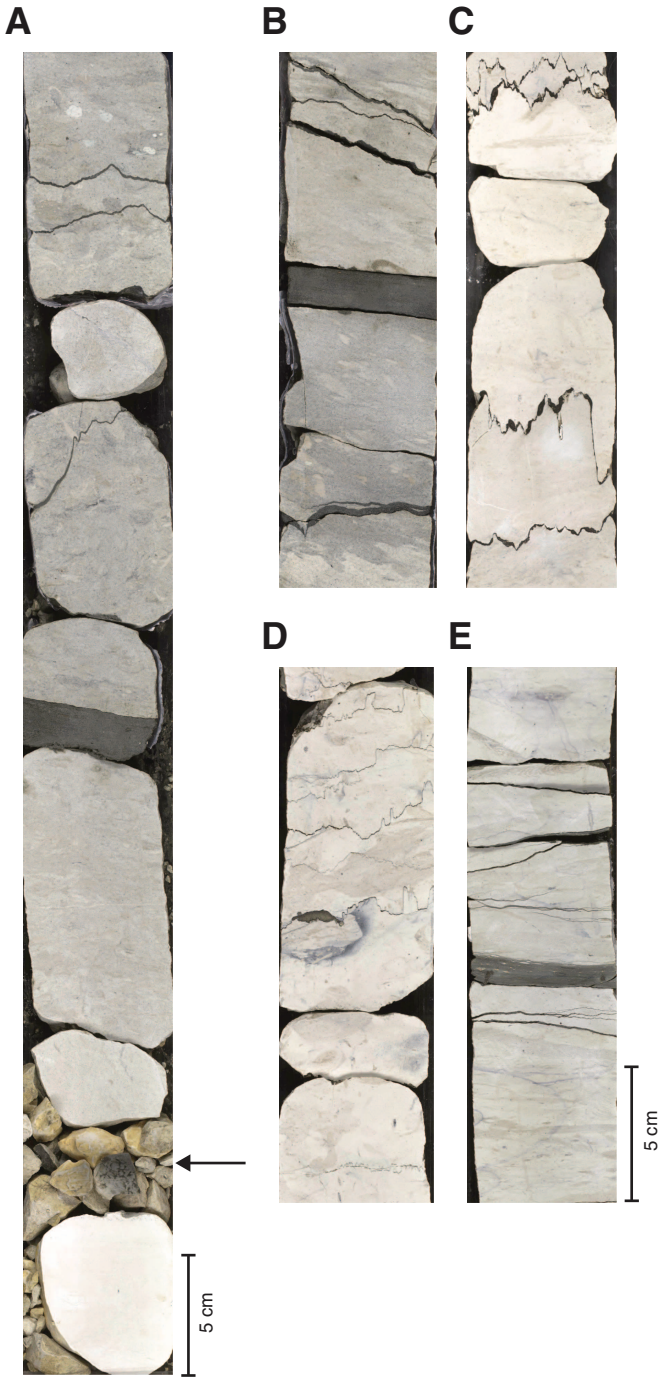

Figure F19. Comparison of downhole gamma ray logs, magnetic susceptibility, lithology, lithologic surfaces identified in core description, and predicted depths of seismic sequence boundaries, Hole U1352B. Downhole logging data are plotted on the WMSF depth scale. **A.** 0–150 m CSF-A. (**Continued on next two pages.**)

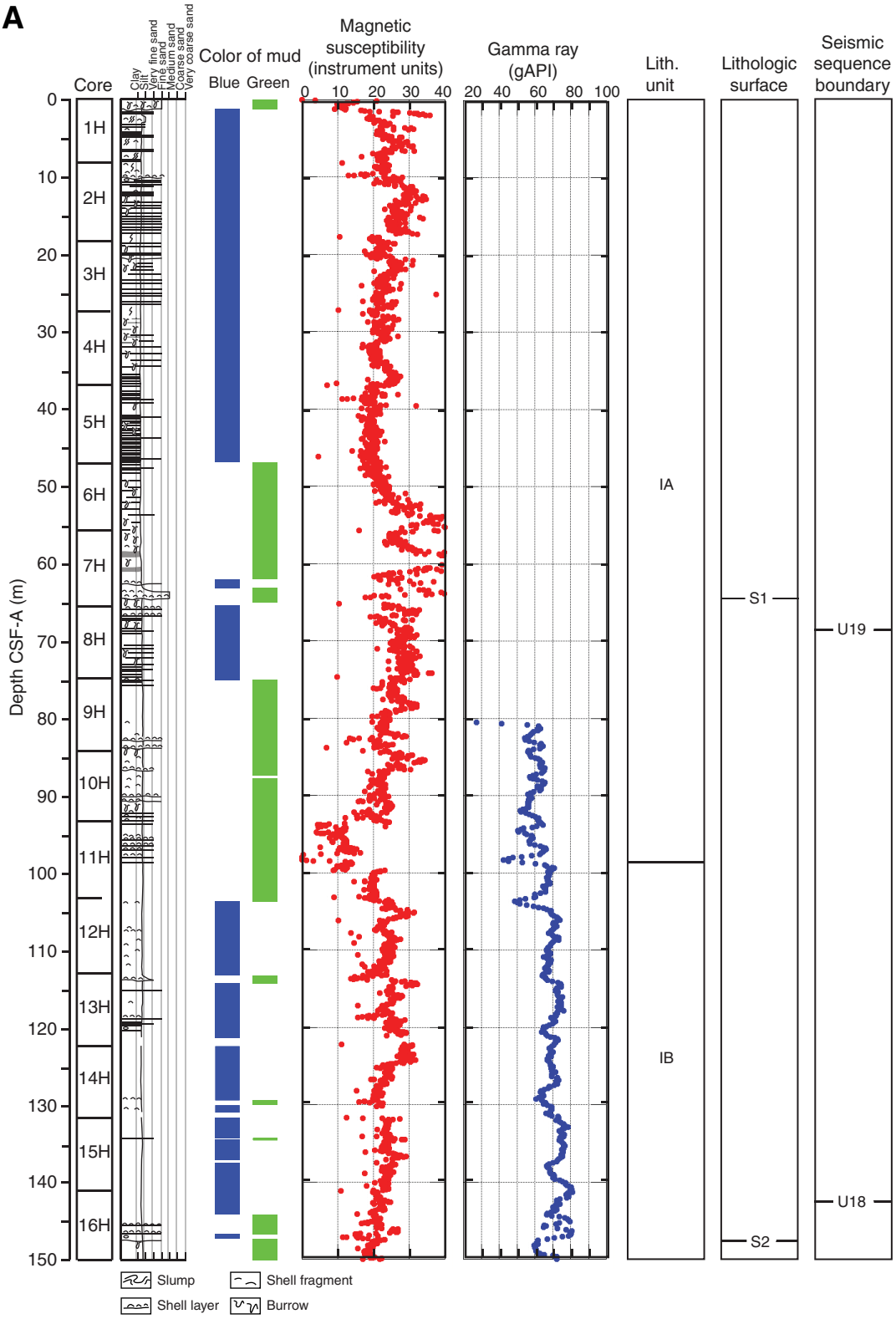

Figure F19 (continued). B. 150–300 m CSF-A. (Continued on next page.)

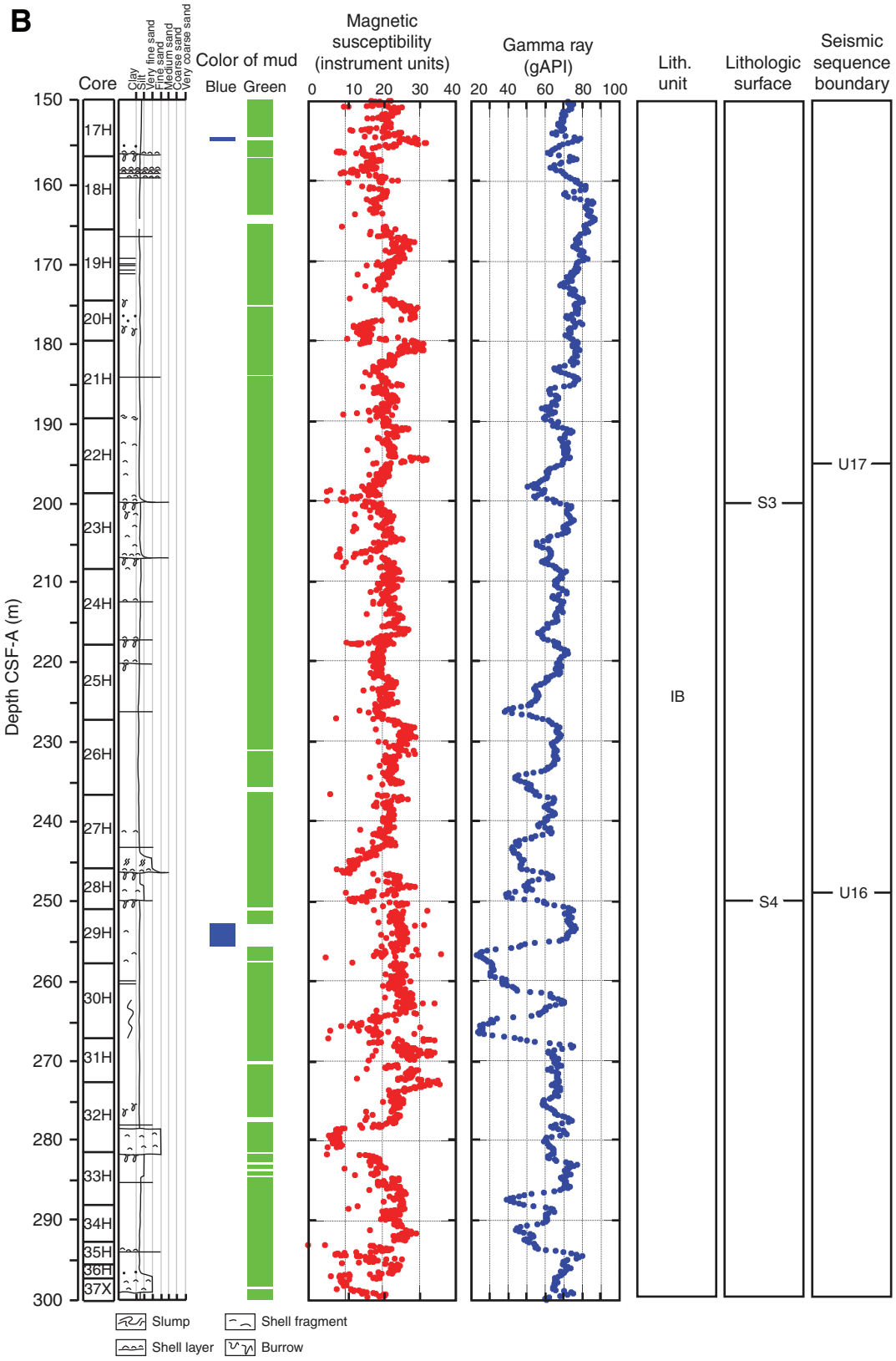

Figure F19 (continued). C. 300–450 m CSF-A.

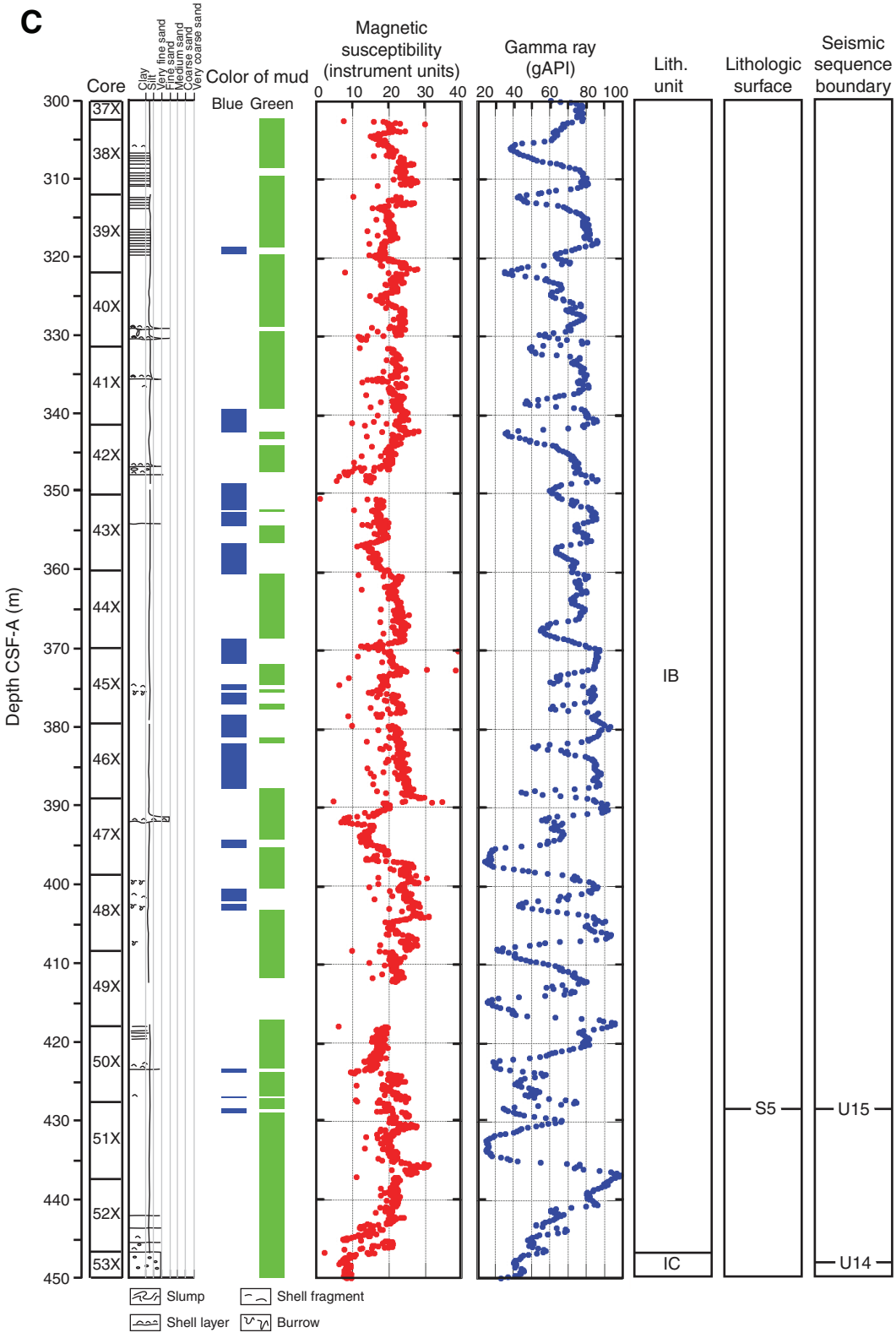

Figure F20. Core photographs and drawings of Type A, B, and C contacts and facies associations. Type A surfaces are characterized by sharp, basal contacts commonly separating two distinct lithologies below >1 m thick deposits. Type B surfaces represent amalgamation packages of >1 m thick thinly bedded (decimeter scale), distinctly contrasting lithologies (e.g., turbidites, interbedded mud and clay, and well-cemented marlstone/chalk) with sharp basal contacts. Type C surfaces are always sharp and separate contrasting lithologies such as sand and mud or marlstone and chalk. However, the total thickness of beds associated with these contacts could not be clearly delineated on board ship. **A.** Surface U1352B-S1 (interval 317-U1352B-7H-6, 76–118 cm). Shells are present, and extensive bioturbation occurs beneath the contact. **B.** Surface U1352B-S3 (interval 317-U1352B-23H-1, 116–148 cm). Heavy bioturbation occurs beneath the contact. **C.** Thinly bedded (1–2 cm thick) sand beds and mud interval (interval 317-U1352B-3H-4, 113–140 cm). **D.** Very fine grained, well-sorted, quartz-rich sand beds (2–5 cm thick) (interval 317-U1352B-2H-6, 17–48 cm). (**Figure shown on next page.**)

Figure F20 (continued). (Caption shown on previous page.)

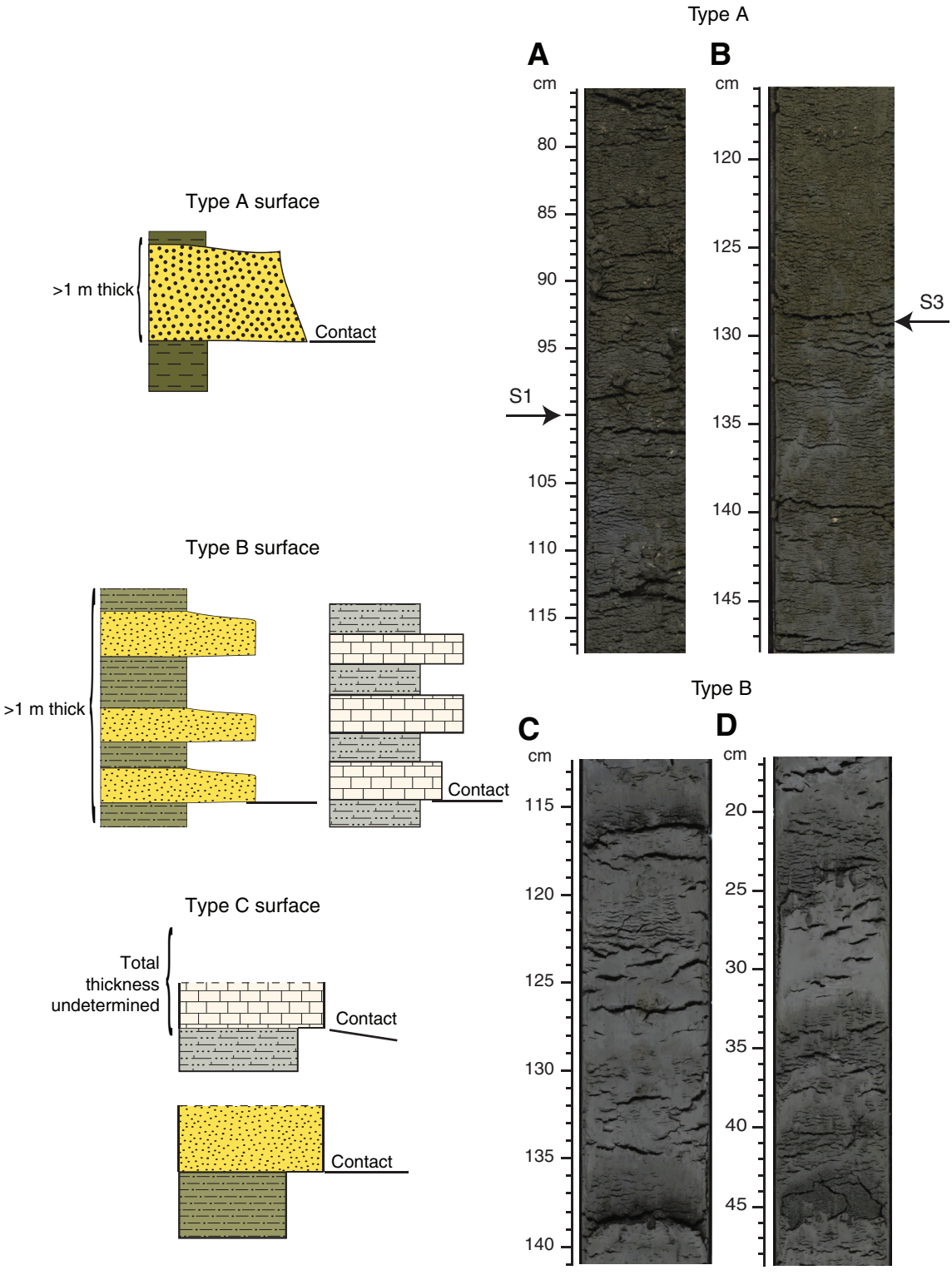

Figure F21. Thicknesses of muddy sand, sandy mud, and clay beds in each core of Hole U1352B. **A.** Sand-mud-clay beds illustrating lithologies associated with Type A. **B.** Interbedded intervals (sand/mud and mud/clay) illustrating lithologies associated with Type B. Red = sand or muddy sand, blue = sandy mud or clay.

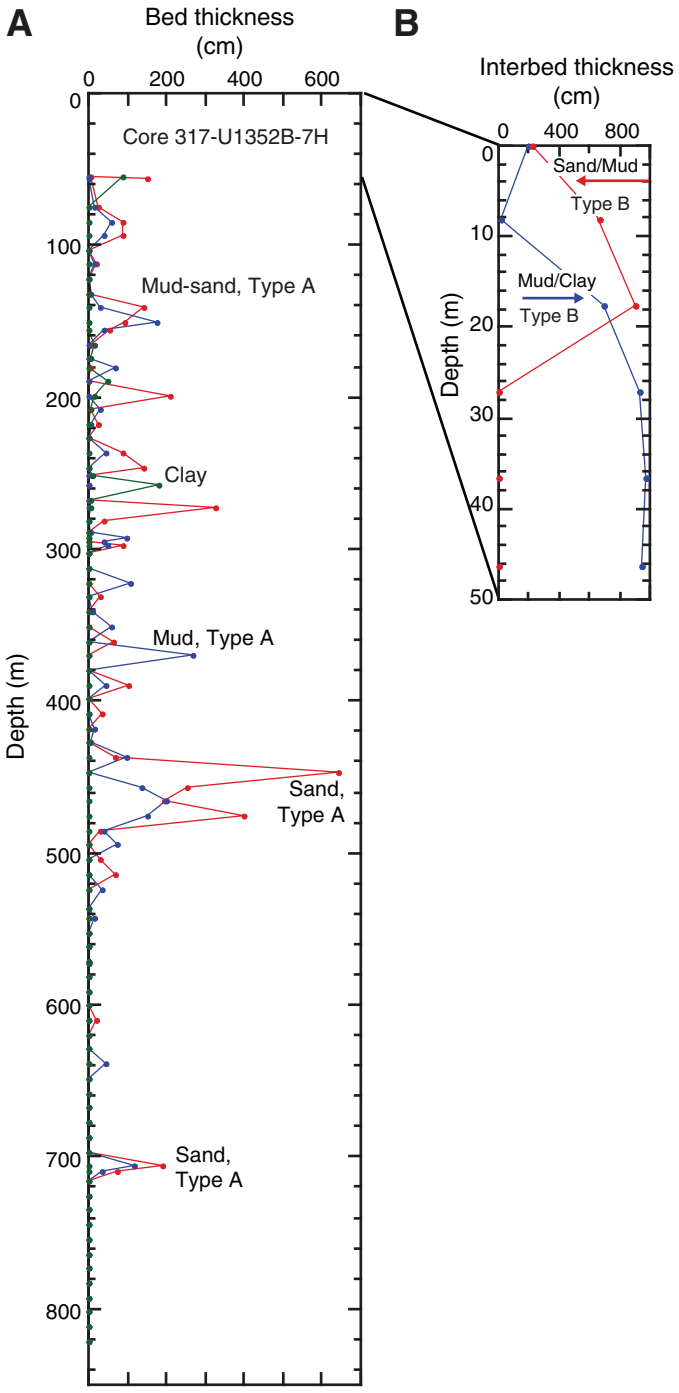

Figure F22. Core photographs of an unusual very calcareous interval likely corresponding to the Pliocene/Miocene boundary. All photographs are at the same vertical scale. **A.** Interval 317-U1352C-73R-2, 18–48 cm (top of calcareous section). **B.** Interval 317-U1352C-73R-3, 53–83 cm. **C.** Interval 317-U1352C-73R-4, 5–35 cm (base of calcareous section, designated as surface U1352C-S11).

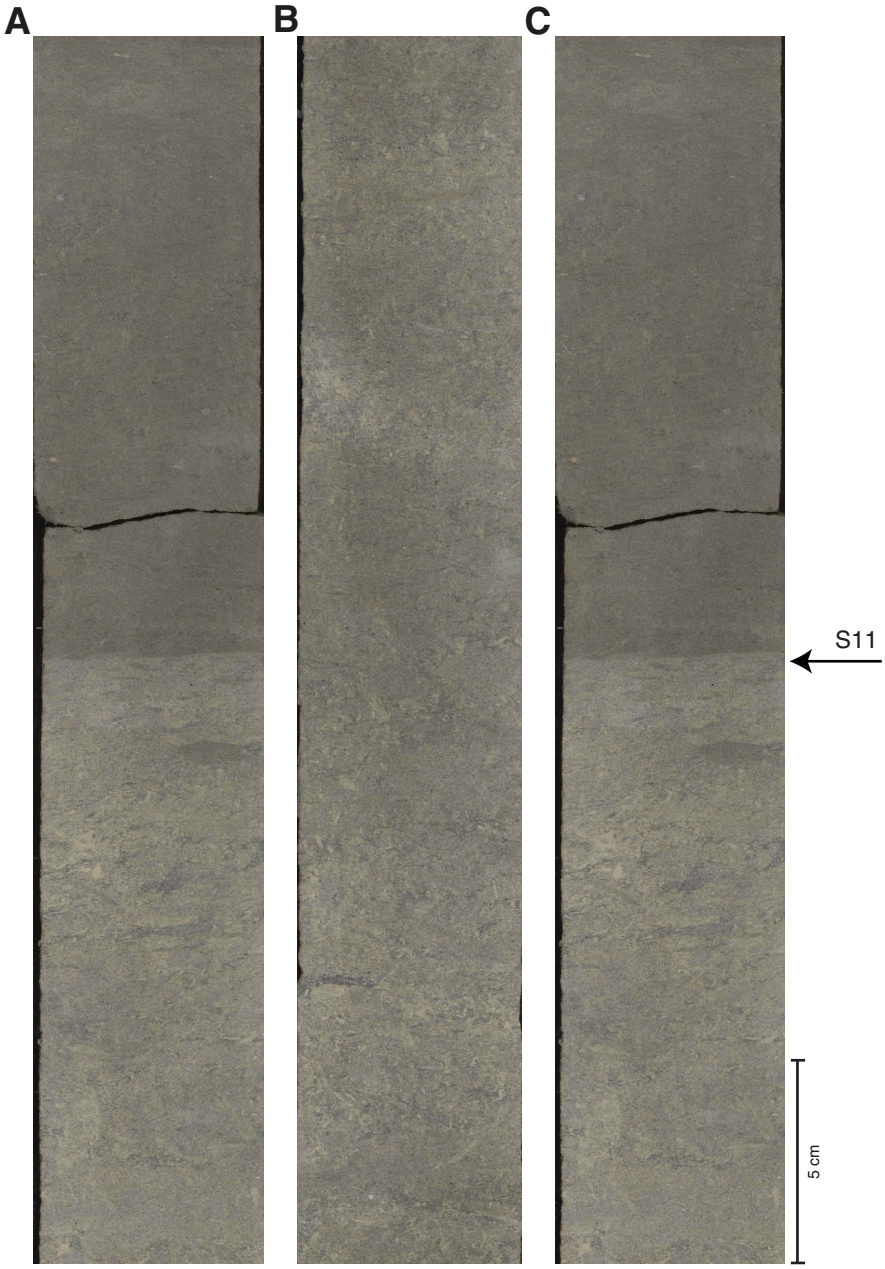

Figure F23. Hole U1352B interpretation of correlation between sand bed thickness, surfaces U1352B-S1 to U1352B-S6, and seismic sequence boundaries U19–U13.

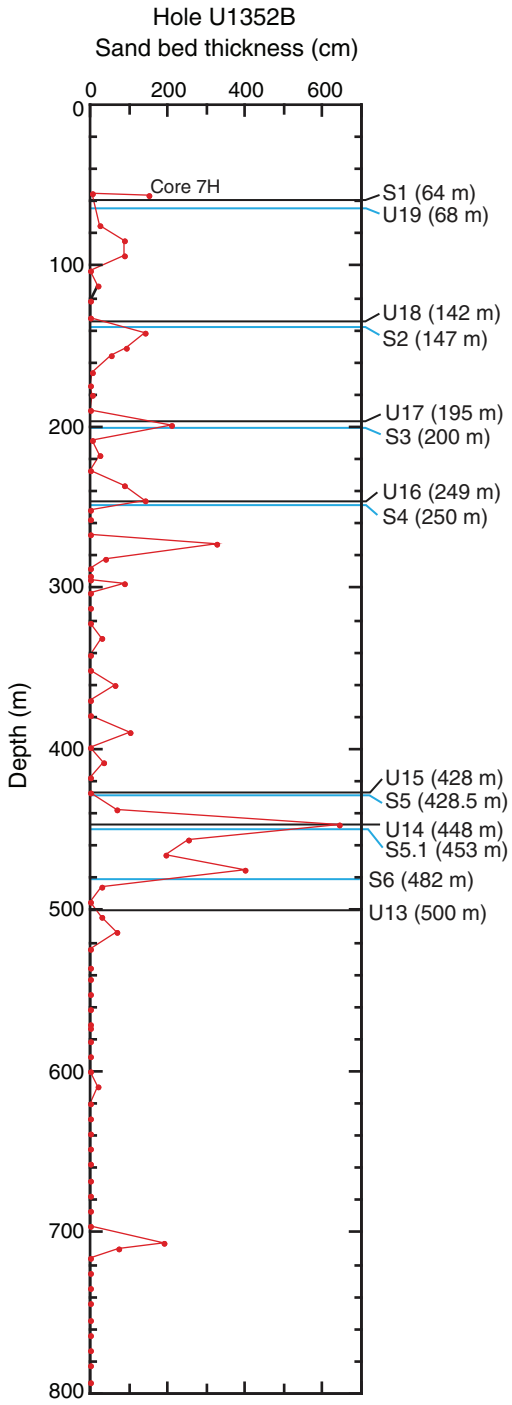

Figure F24. Core recovery, epochs, calcareous nannofossil (NN) zones, and New Zealand (NZ) stage correlation for planktonic foraminifers and bolboformids (PF) and benthic foraminifers (BF), Site U1352. Solid wavy lines = hiatuses between zonal boundaries, dashed wavy lines = hiatuses within biozones, dashed straight line = poorly constrained zonal boundary. See Figure F6 in the "Methods" chapter for NZ stage abbreviations. **A.** 0–1050 m CSF-A. (Continued on next page.)

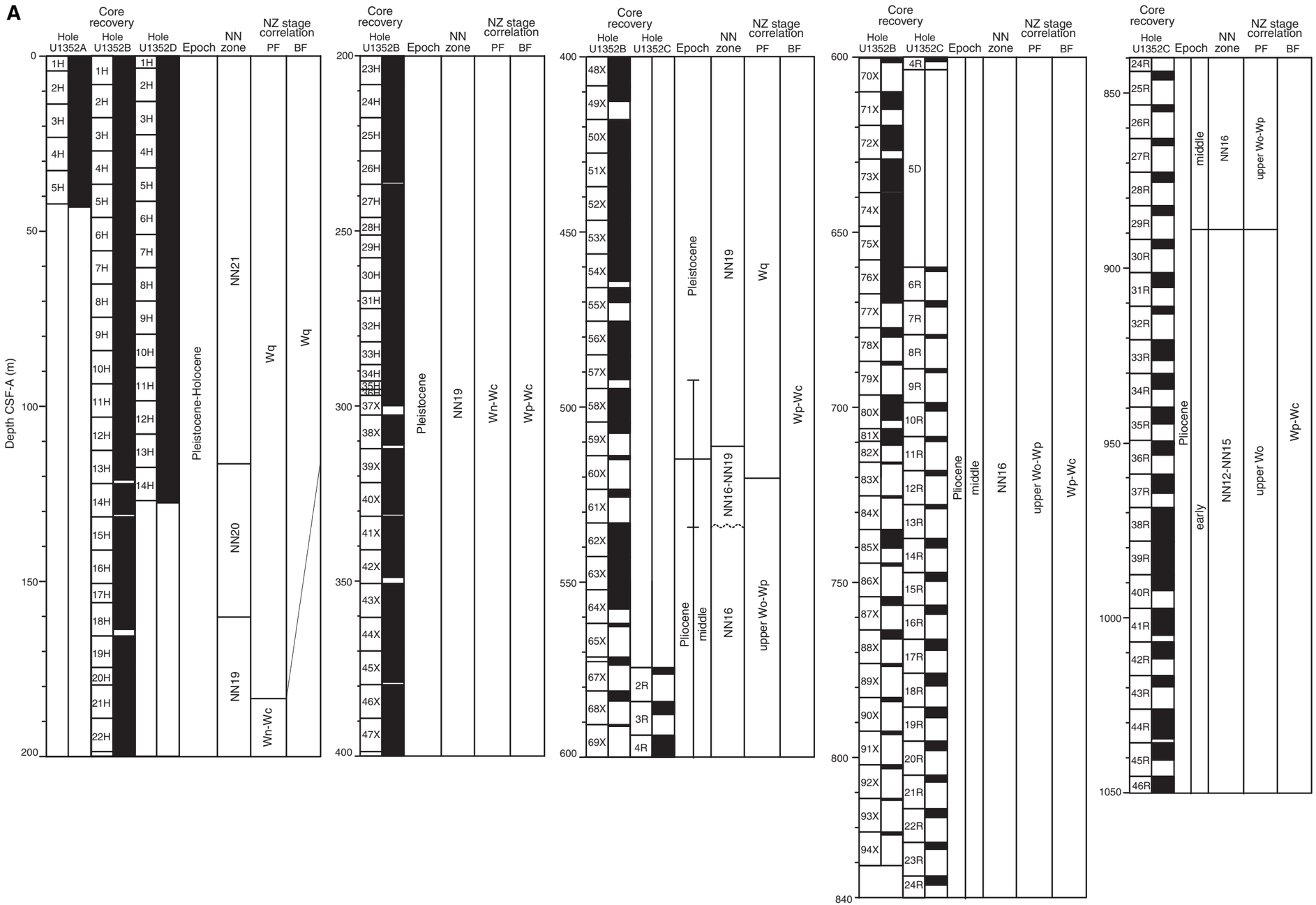

Figure F24 (continued). B. 1050–1930 m CSF-A. The Marshall Paraconformity (at least 12 m.y. missing) is between Samples 317-U1352C-139R-CC and 140R-CC (1848.49–1852.71 m).

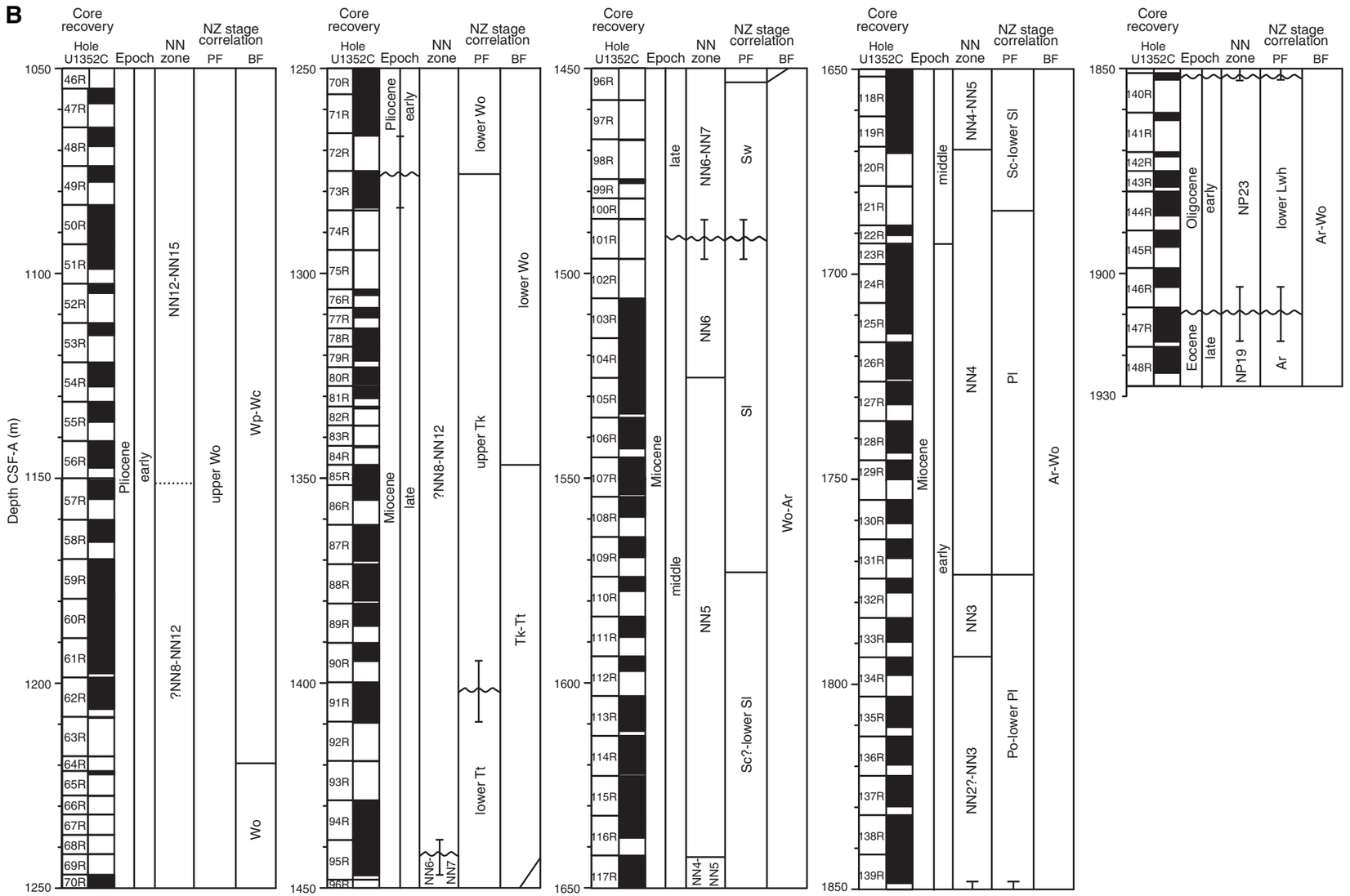

Figure F25. Planktonic foraminiferal abundance relative to total foraminifers and oceanicity, Site U1352.

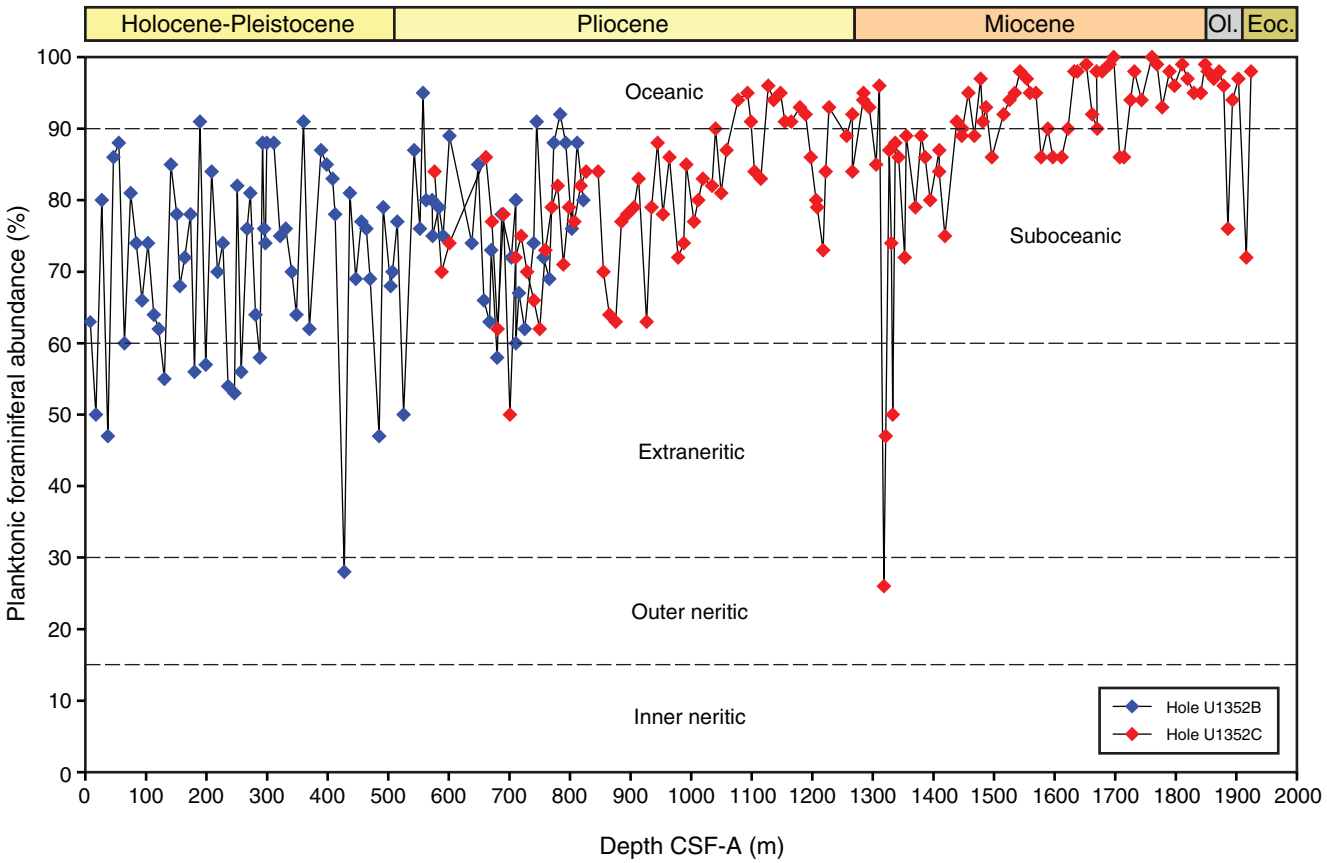

Figure F26. Thin section photomicrograph of sparry calcite and glauconite-infilled planktonic foraminifer in a limestone nodule (Sample 317-U1352B-19X-CC [147.55 m]).

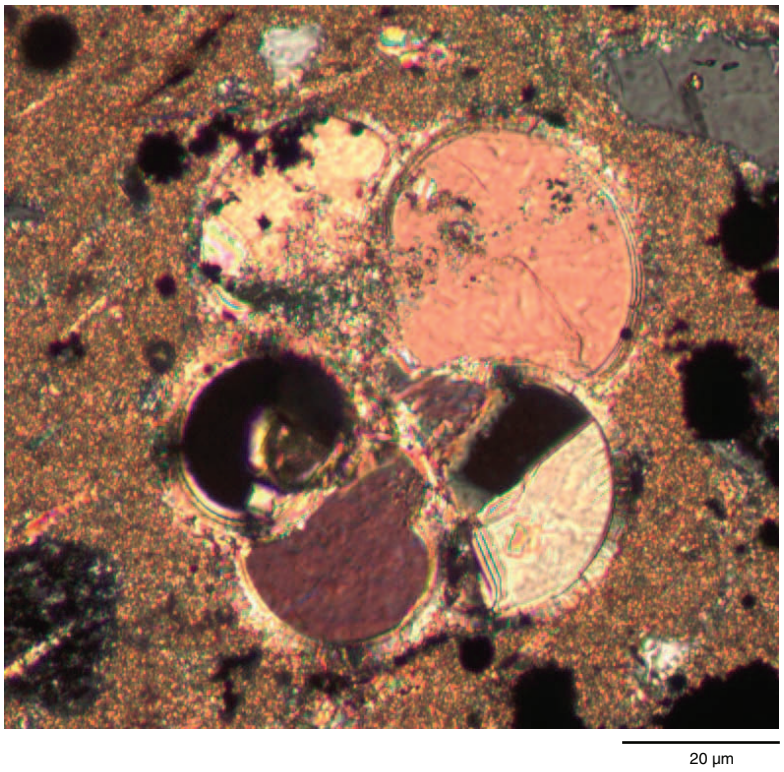

Figure F27. Paleodepth interpretation based on the composition of benthic foraminiferal assemblages, Site U1352. The presence of rare but persistent bathyal marker species, especially in the upper part of the section, suggests that shelfal taxa composing the bulk of the benthic assemblage were transported downslope. In this context, the actual paleowater depths are closer to the deep end of the depth limits shown.

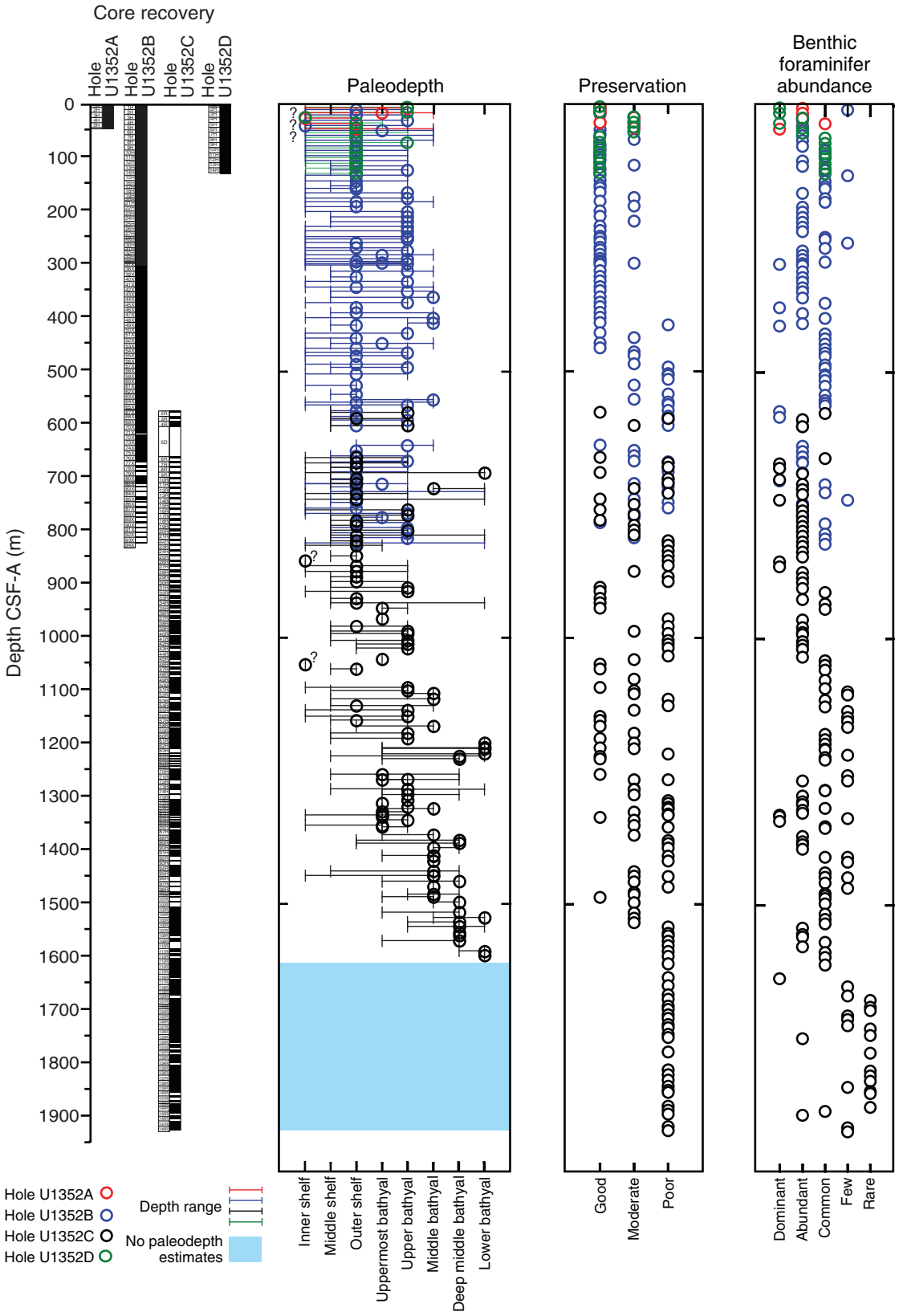

Figure F28. Natural remanent magnetization (NRM) paleomagnetic record for Hole U1352B. Dashed line = Unit I/II boundary, solid horizontal lines = changes in coring system. APC = advanced piston corer, XCB = extended core barrel.

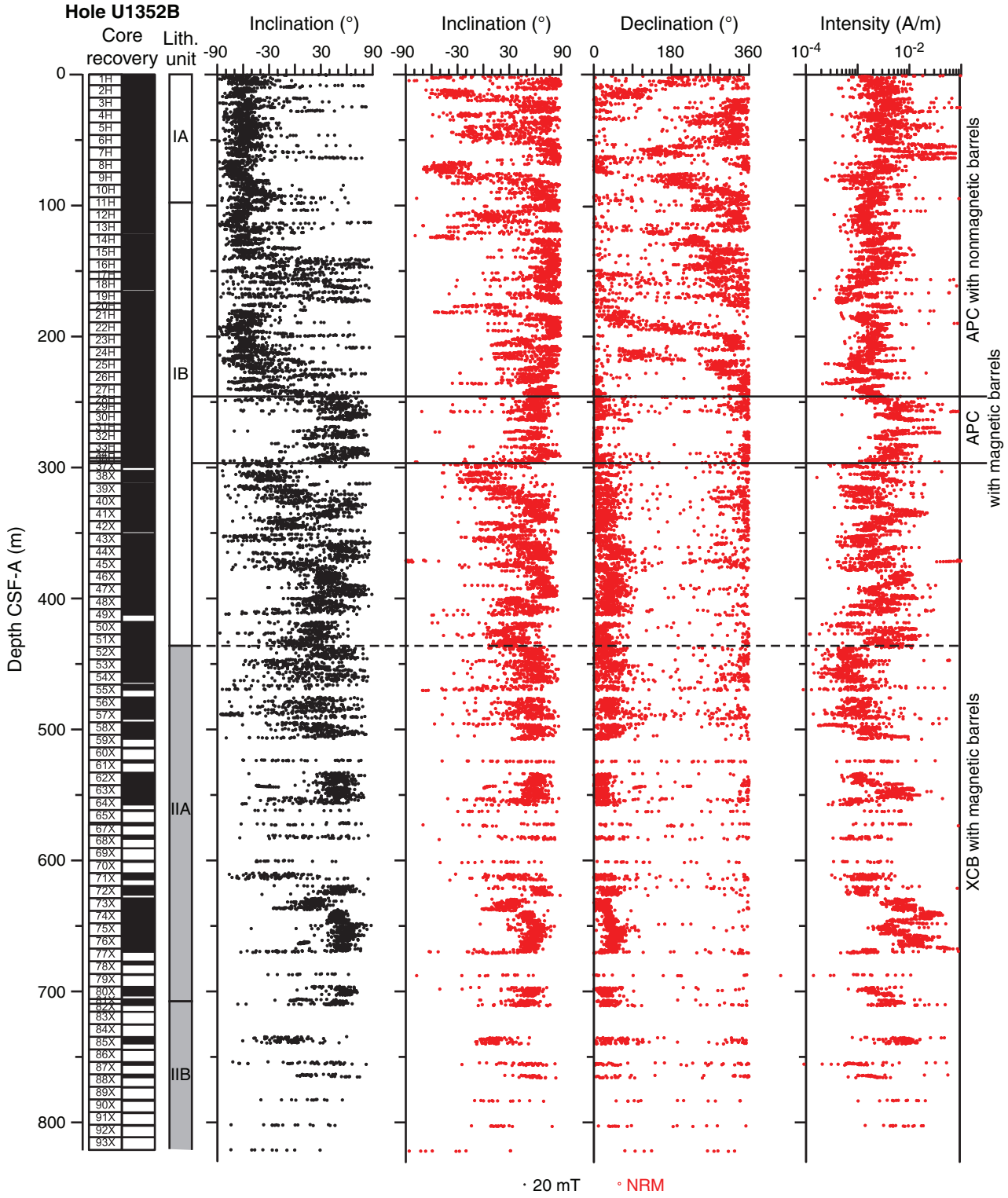

Figure F29. Natural remanent magnetization (NRM) paleomagnetic record of the 0–320 m depth interval in Hole U1352B. WRMSL magnetic susceptibility is also shown. Solid horizontal lines = changes in coring system. APC = advanced piston corer, XCB = extended core barrel.

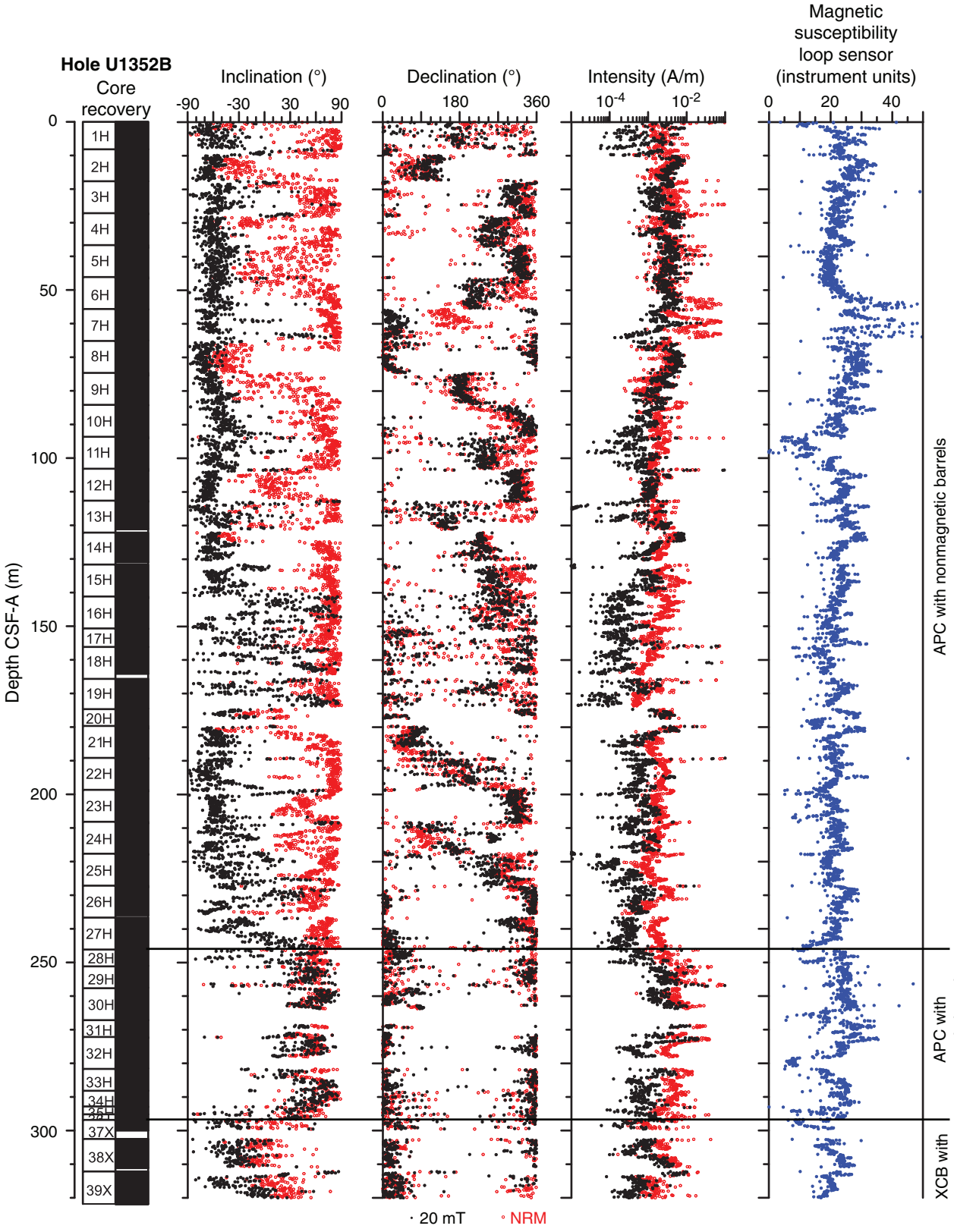

Figure F30. Oriented data from Hole U1352B. Declination is shown before (archive coordinates) and after (Flexit tool corrected) orientation. Equal-area stereoplots show natural remanent magnetization (NRM) directions after AF demagnetization at 20 mT both before and after orientation. Open circles = data from the upper hemisphere (upward negative inclinations), solid red circles = directions from the lower hemisphere (downward positive inclinations). The mean direction of oriented NRM after 20 mT demagnetization is given together with statistical parameters.

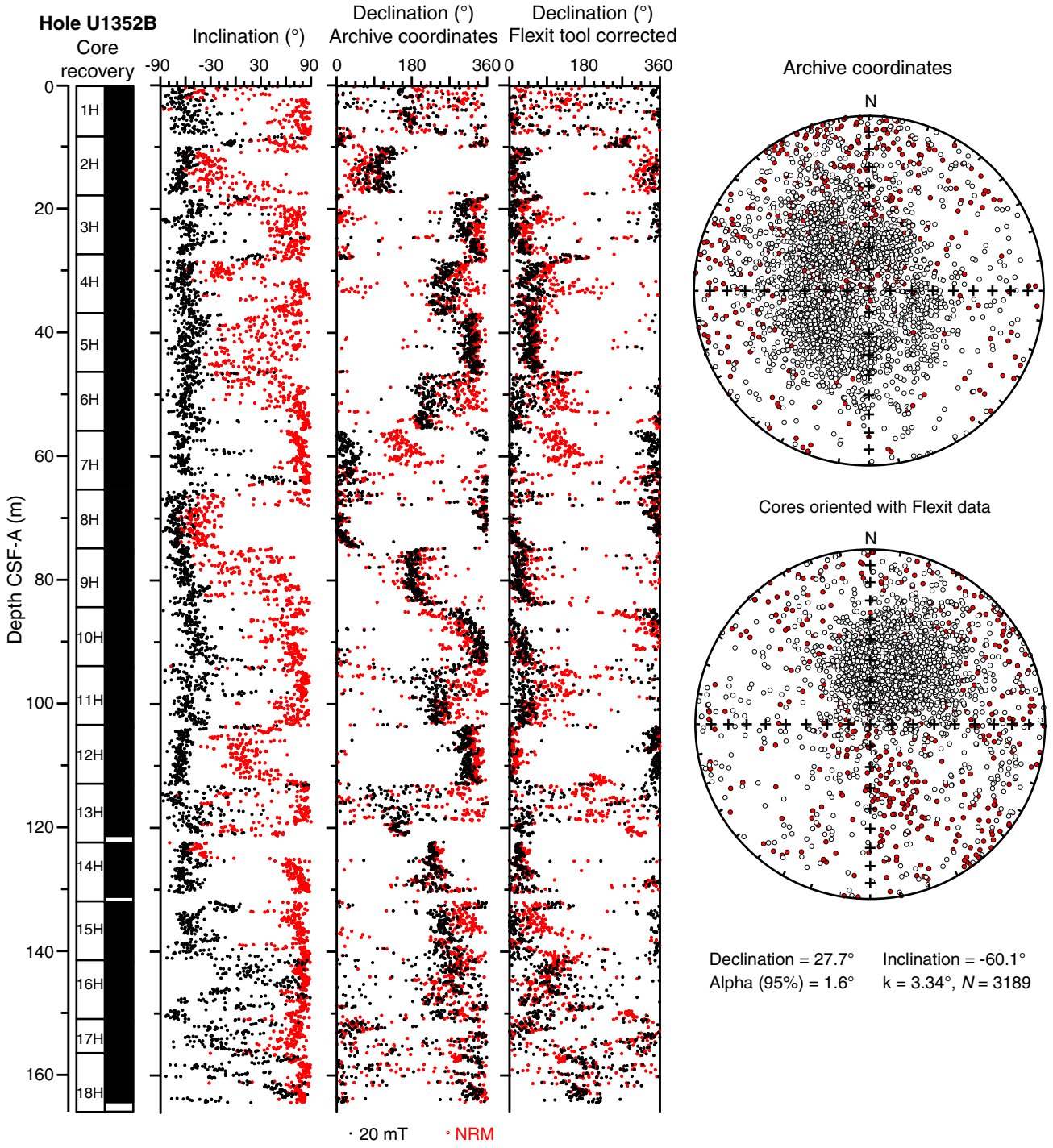

Figure F31. Natural remanent magnetization (NRM) paleomagnetic record for Hole U1352C. WRMSL magnetic susceptibility is also shown. Dashed horizontal line = Unit II/III boundary or the Marshall Paraconformity.

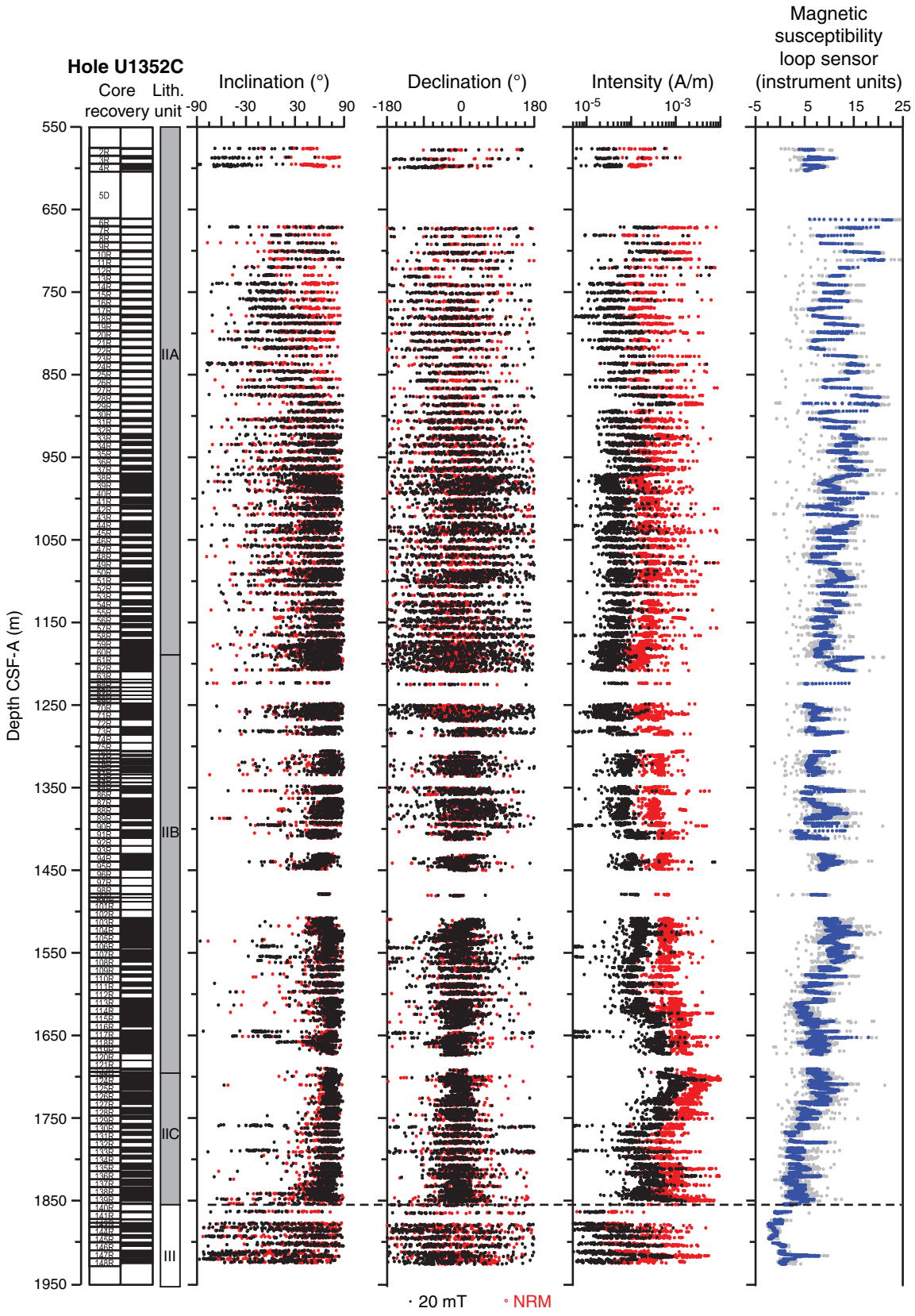

Figure F32. Orthogonal demagnetization plots of AF and thermal demagnetization of samples from Holes U1352B and U1352C. Open circles = projection on the vertical plane, solid circles = projection on the horizontal plane. NRM = natural remanent magnetization. **A, C, E, F.** AF demagnetization. (A) Sample 317-U1352B-8H-4, 62 cm (70.32 m). (C) Sample 317-U1352B-29H-3, 79 cm (254.99 m). (E) Sample 317-U1352C-44R-1, 44 cm (1026.54 m). (F) Sample 317-U1352C-79R-1, 132 cm (1319.22 m). **B, D.** Thermal demagnetization. (B) Sample 317-U1352B-8H-4, 65 cm (70.35 m). (D) Sample 317-U1352B-29H-3, 83 cm (255.03 m). **G.** Magnetic susceptibility variation of thermally demagnetized Samples 317-U1352B-29H-3, 83 cm (255.03 m; red), and 8H-4, 65 cm (70.35 m; black), after each heating step.

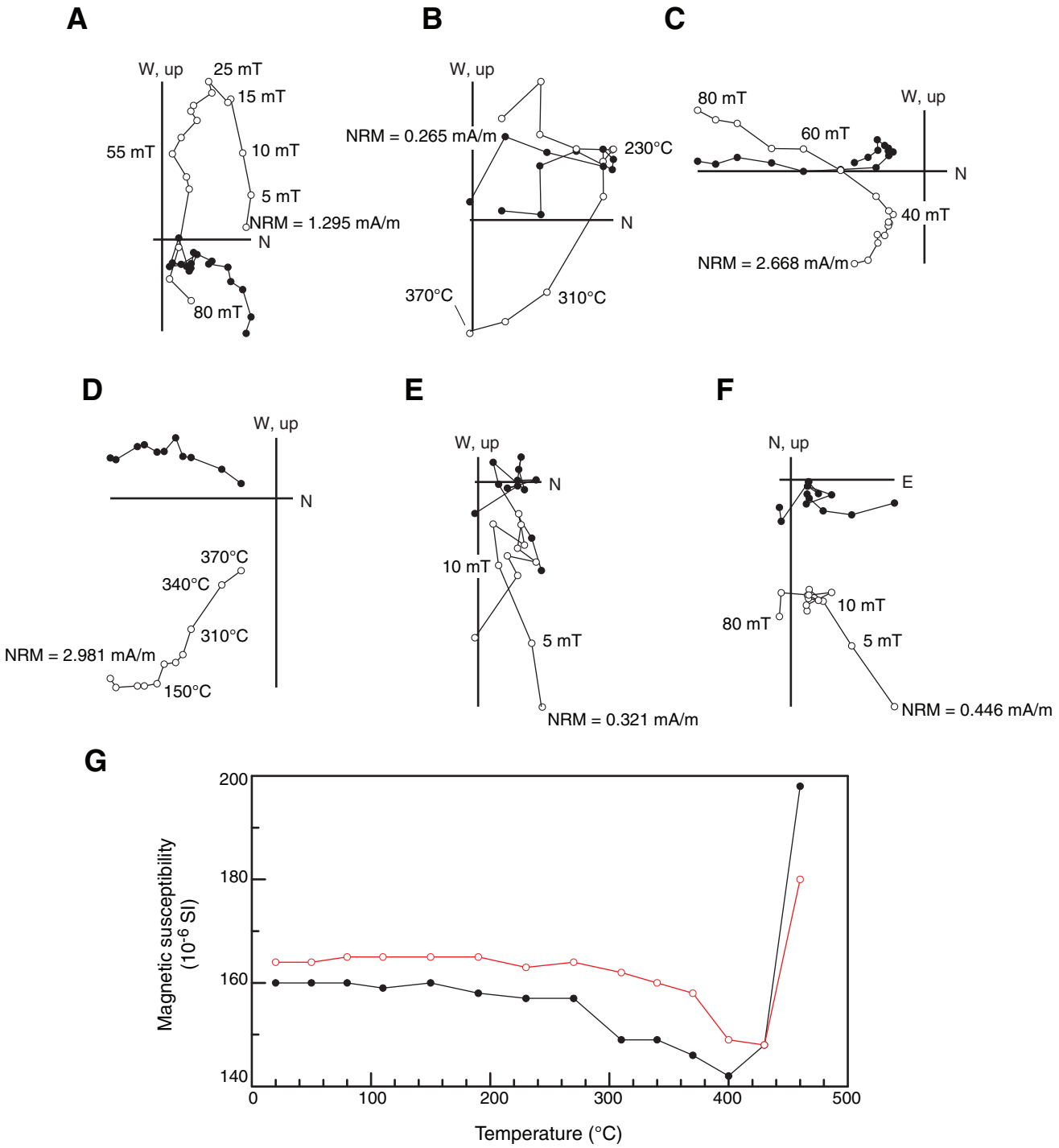

Figure F33. A. Isothermal remanent magnetization (IRM) and backfield acquisition curves for 10 discrete samples from Hole U1352B. Samples reach saturation between 400 and 600 mT, and coercivity of remanence (B_{cr}) ranges between 40 and 75 mT. **B.** AF demagnetization of IRM of the same 10 samples. **C.** Same as B, but intensities are normalized to saturation IRM for each sample.

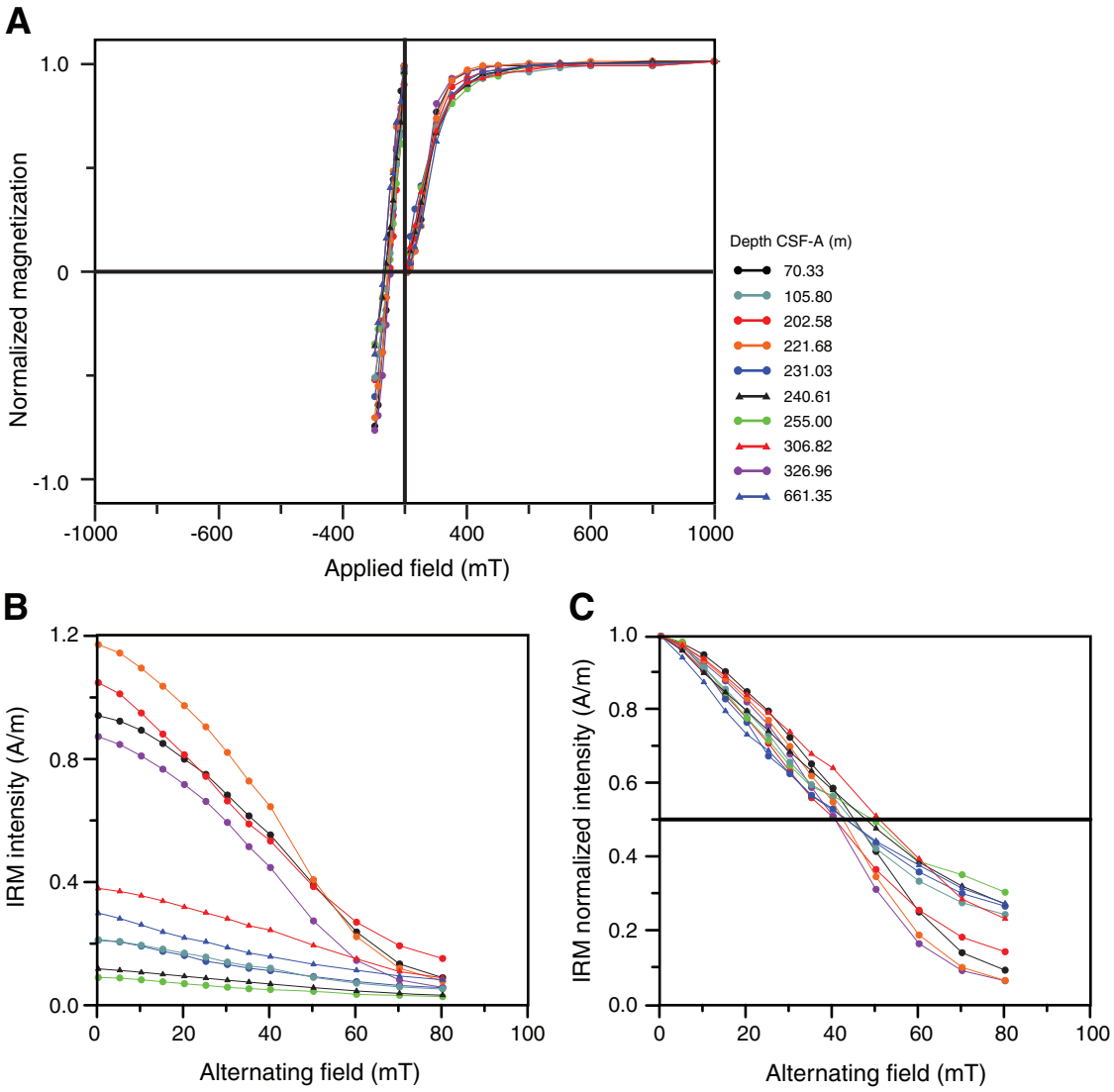

Figure F34. Raw data (gray) and Gaussian low-pass filtered data (red and black) for magnetic susceptibility (loop and point sensors), natural gamma radiation (NGR), gamma ray attenuation (GRA) bulk density, and color reflectance parameter b*, Holes U1352B and U1352C. Extreme high and low values interpreted as noise are not shown.

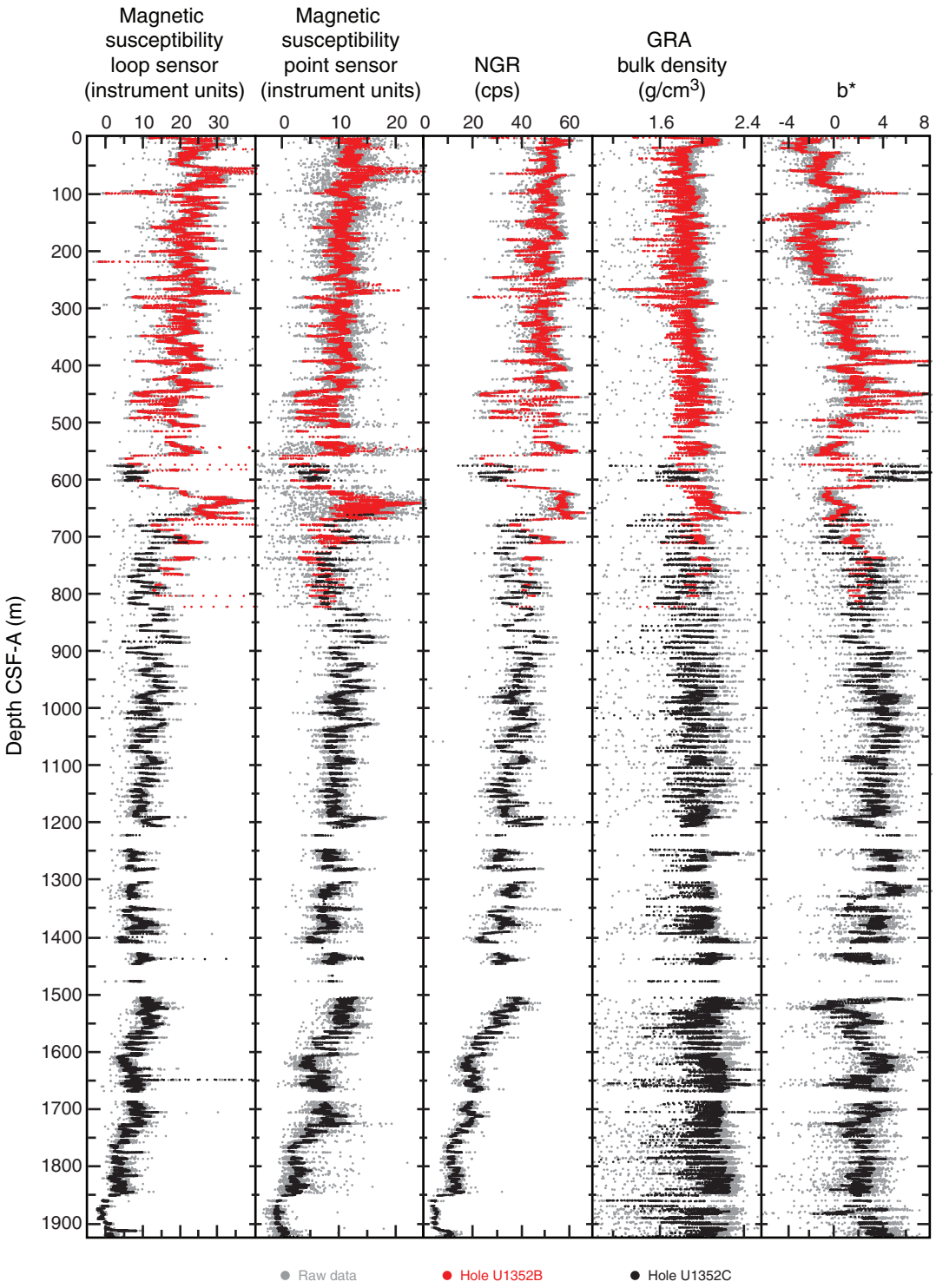

Figure F35. A, B. Comparison of GRA bulk density (red), MAD bulk density (green), and density from downhole logs (black) in Hole U1352B. Lithologic units are indicated in the vertical columns to the left and by the dashed lines. Core recovery information (black = recovered intervals) is also shown. (A) 0–800 m. (B) 100–500 m. **C.** Hole size, based on caliper measurements during downhole logging. Note that depth (m) refers to CSF-A for GRA core data and MAD results and to WMSF for downhole logging data.

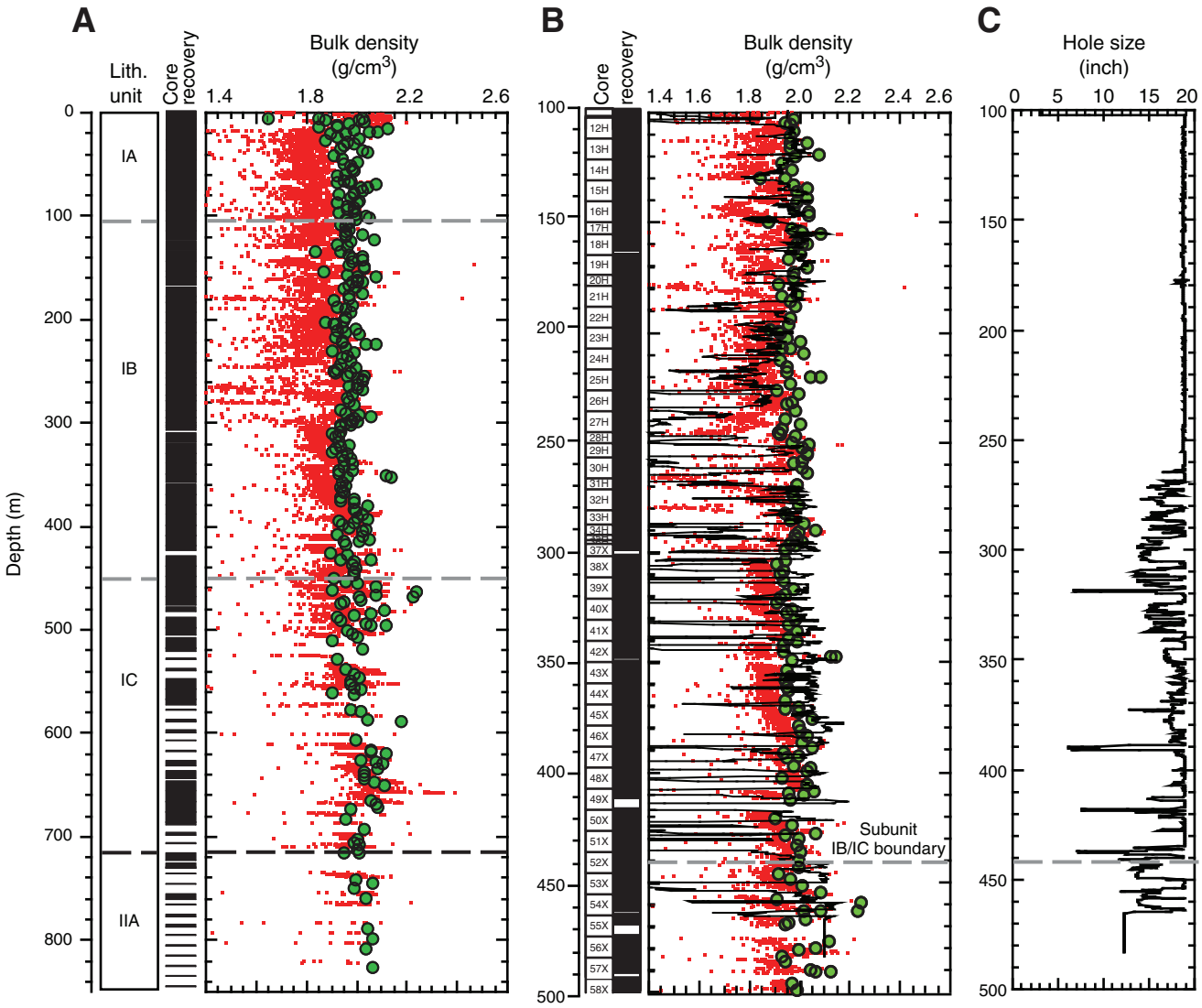

Figure F36. Comparison of GRA bulk density (red) and MAD bulk density (green) in Hole U1352C. Lithologic units are indicated in the vertical column to the left and by the dashed lines in A. Core recovery information (black = recovered intervals) is also shown. **A.** 550–1950 m CSF-A. **B.** 920–945 m CSF-A. **C.** 1500–1550 m CSF-A. In B and C, MAD estimates made on sediments (yellow circles) are differentiated from those made on indurated samples (green circles).

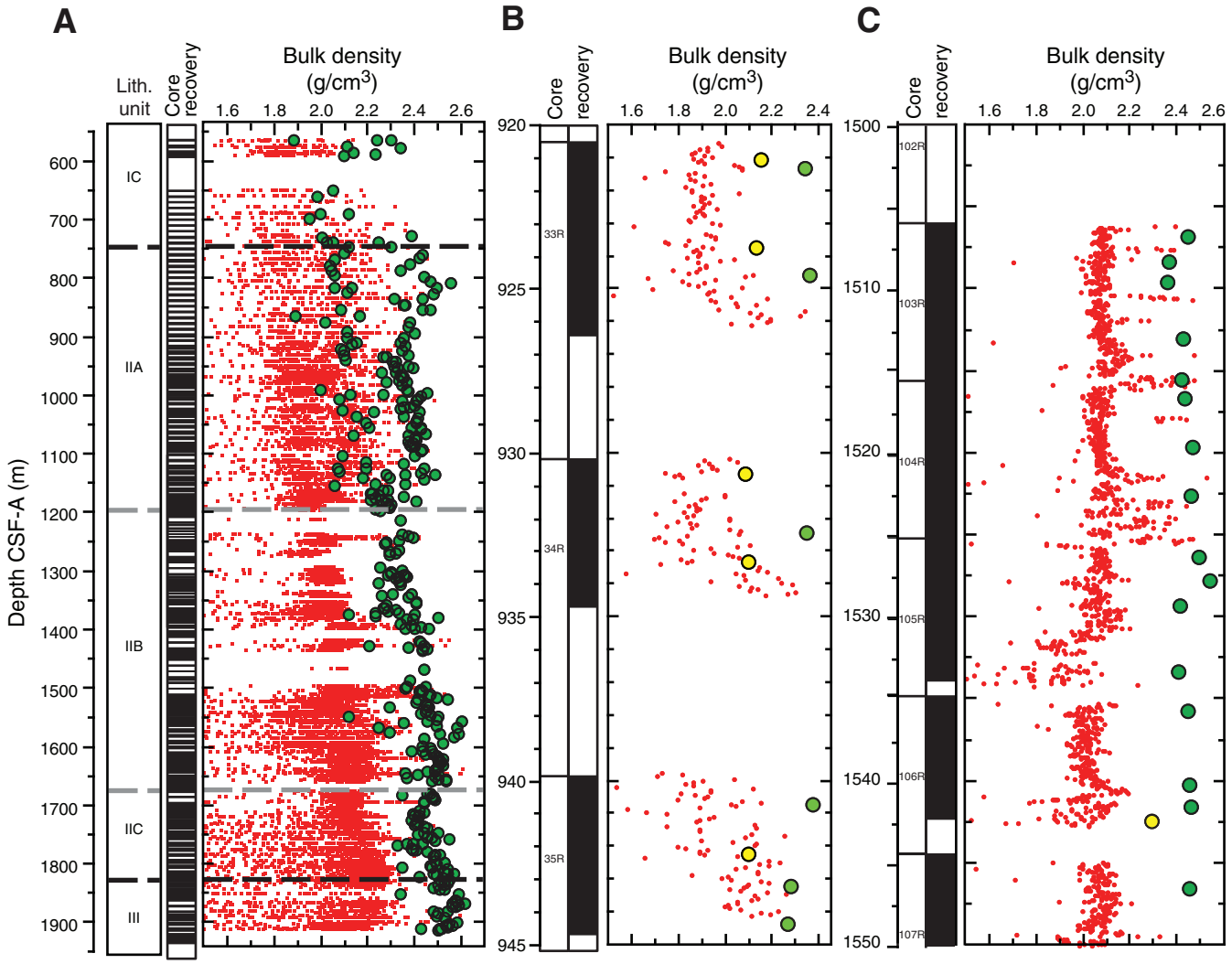

Figure F37. L*a*b* color parameters, Holes U1352B and U1352C. Gray circles = raw data, solid line = smoothed data. Smoothed data were created by applying a 30-pass Gaussian filter to the raw data. See main text for discussion. MP = Marshall Paraconformity.

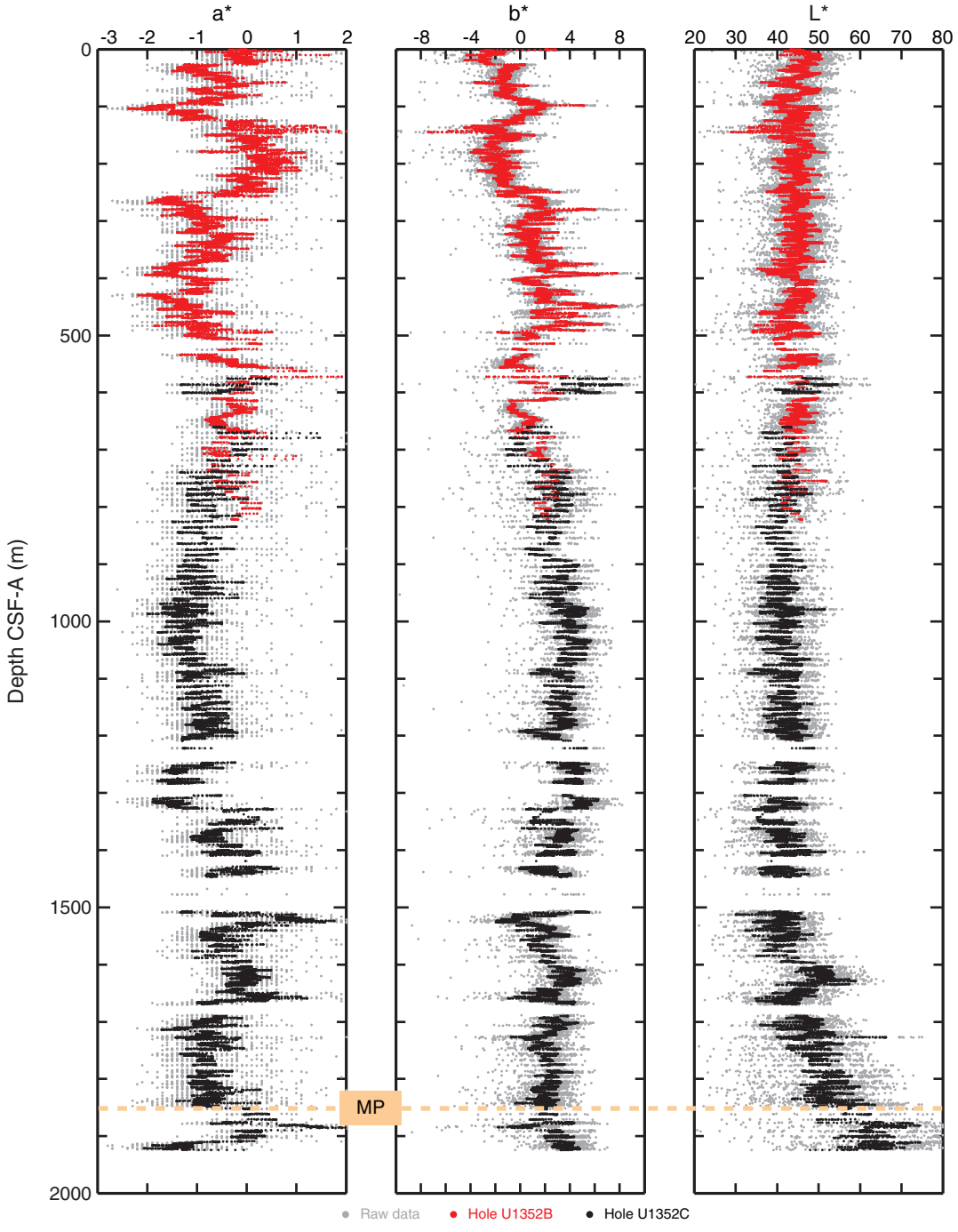

Figure F38. Comparison of raw (red) and Gaussian low-pass filtered (black) magnetic susceptibility and natural gamma radiation (NGR) from Hole U1352B with Ocean Drilling Program (ODP) Hole 1119C (Leg 181).

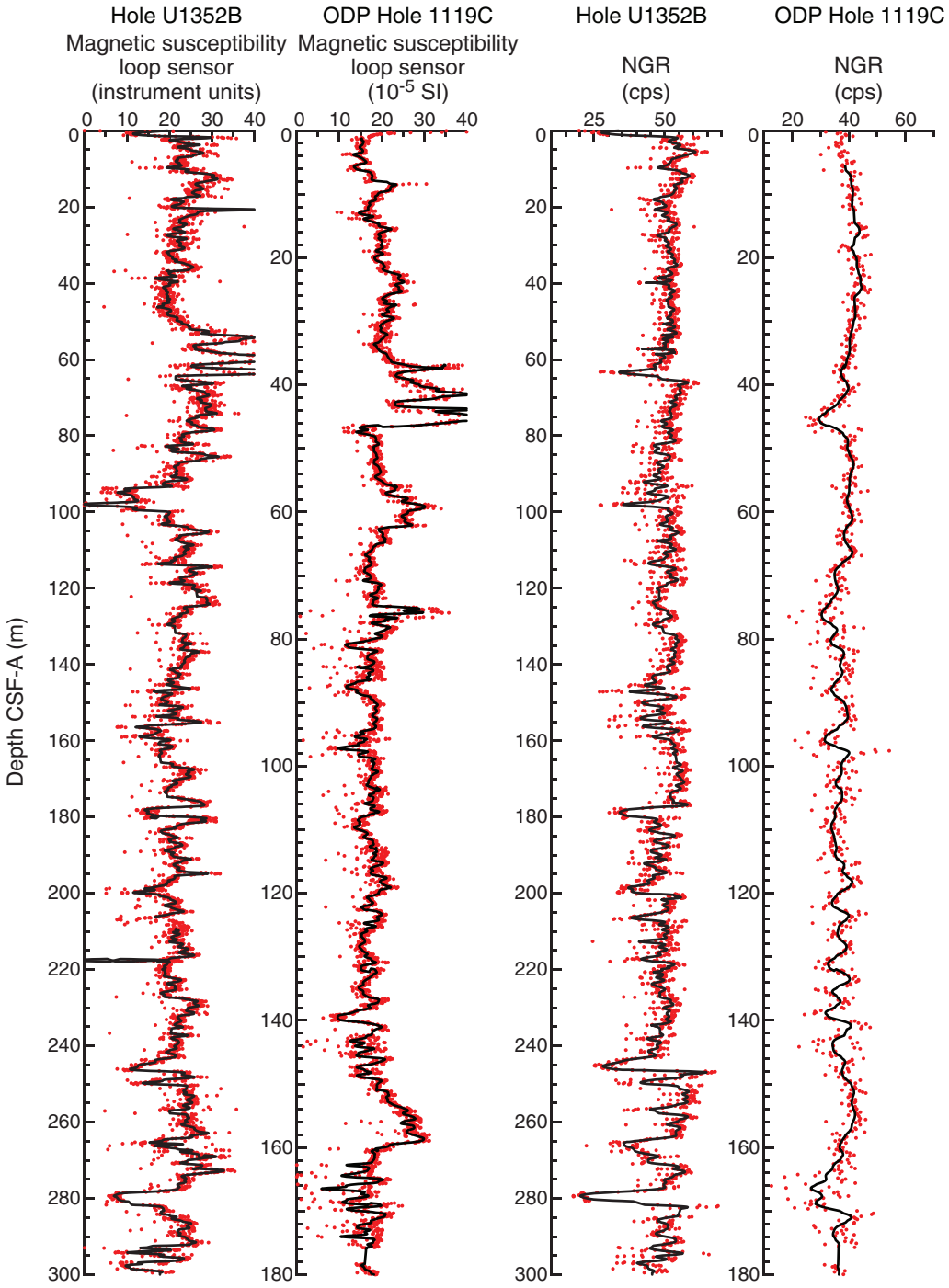

Figure F39. Comparison of (**A**, **B**) whole-round and (**C**) section-half *P*-wave velocities (*x*-, *y*-, and *z*-axis) in the uppermost 20 m of Holes U1352A and U1352B. PWL = *P*-wave logger, PWC = *P*-wave caliper, PWB = *P*-wave bayonets.

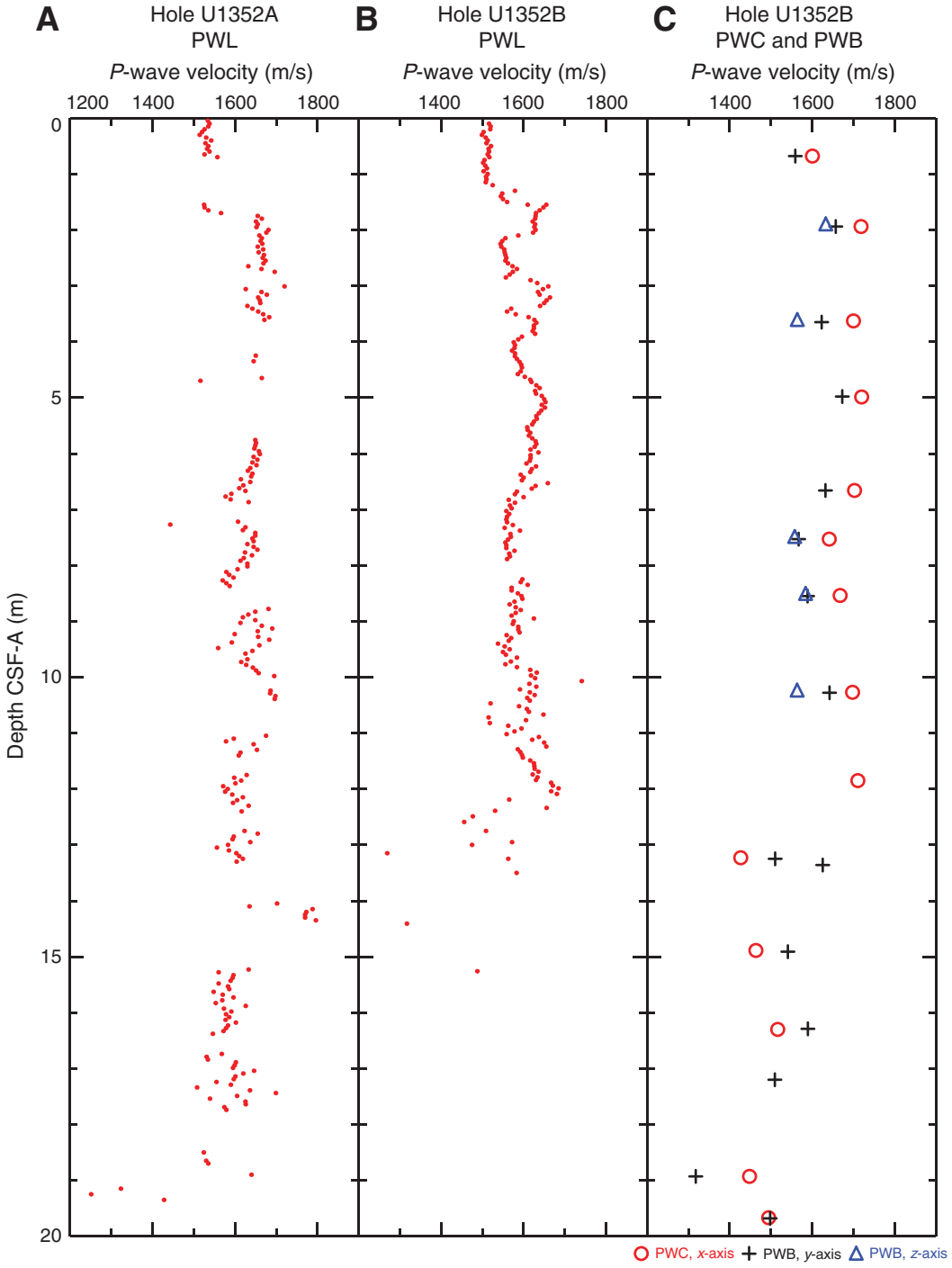

Figure F40. (**A**) Section-half *P*-wave velocity (*x*-axis), (**B**) moisture and density Method D (MAD [D]) porosity, and (**C**) correlation of *P*-wave velocity and MAD porosity in Hole U1352C. PWC = *P*-wave caliper.

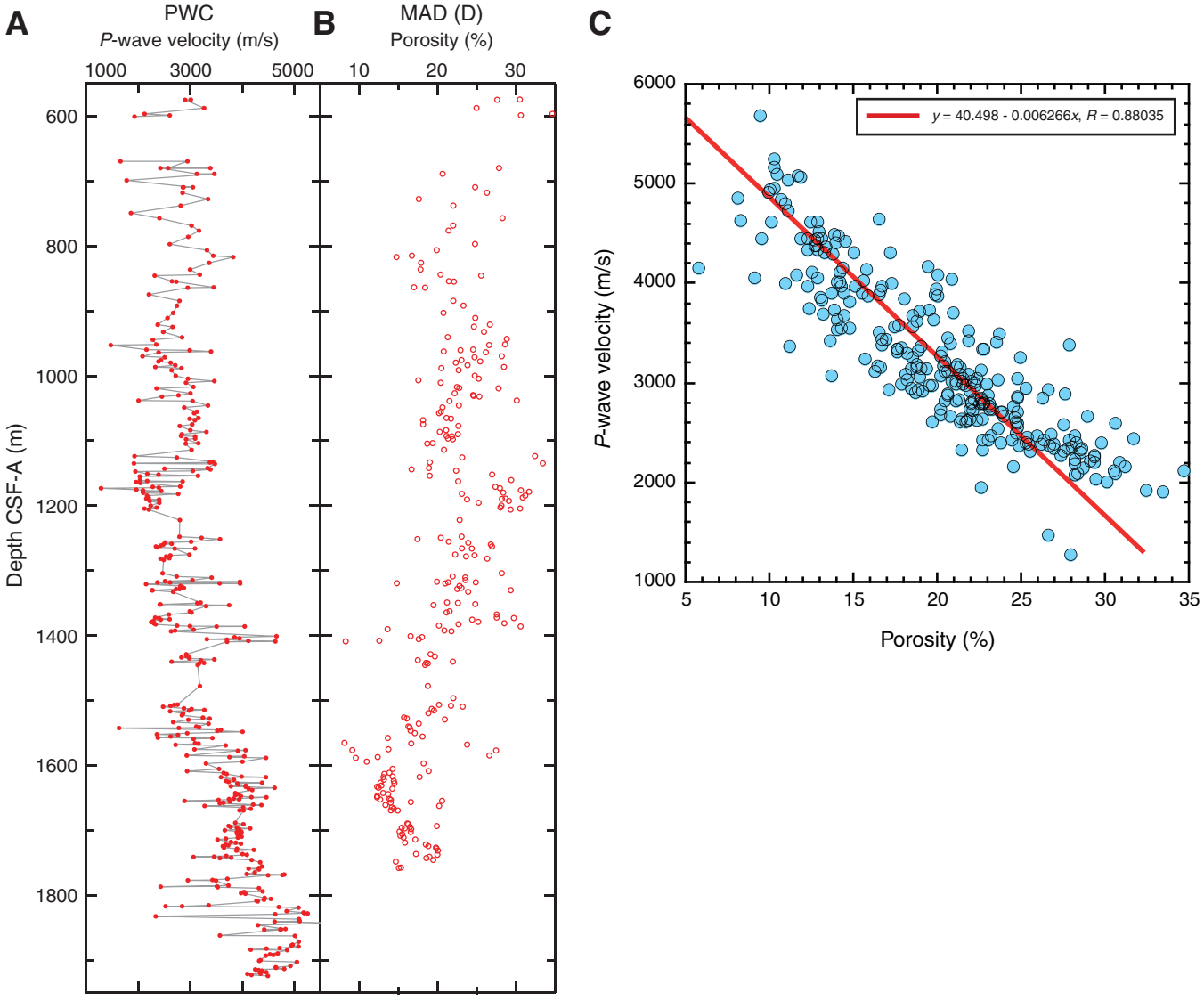

Figure F41. A. Relationship between two methods of porosity calculation: Method C (measurement of wet mass, dry mass, and dry volume) and Method D (measurement of wet volume, dry volume, and dry mass). Both methods yield similar results (within a few percent), but Method D tends to yield higher porosities. **B.** Method C porosities of samples in Hole U1352C, separated into indurated samples collected with the minicorer (blue circles) and soft samples collected with a syringe (yellow circles).

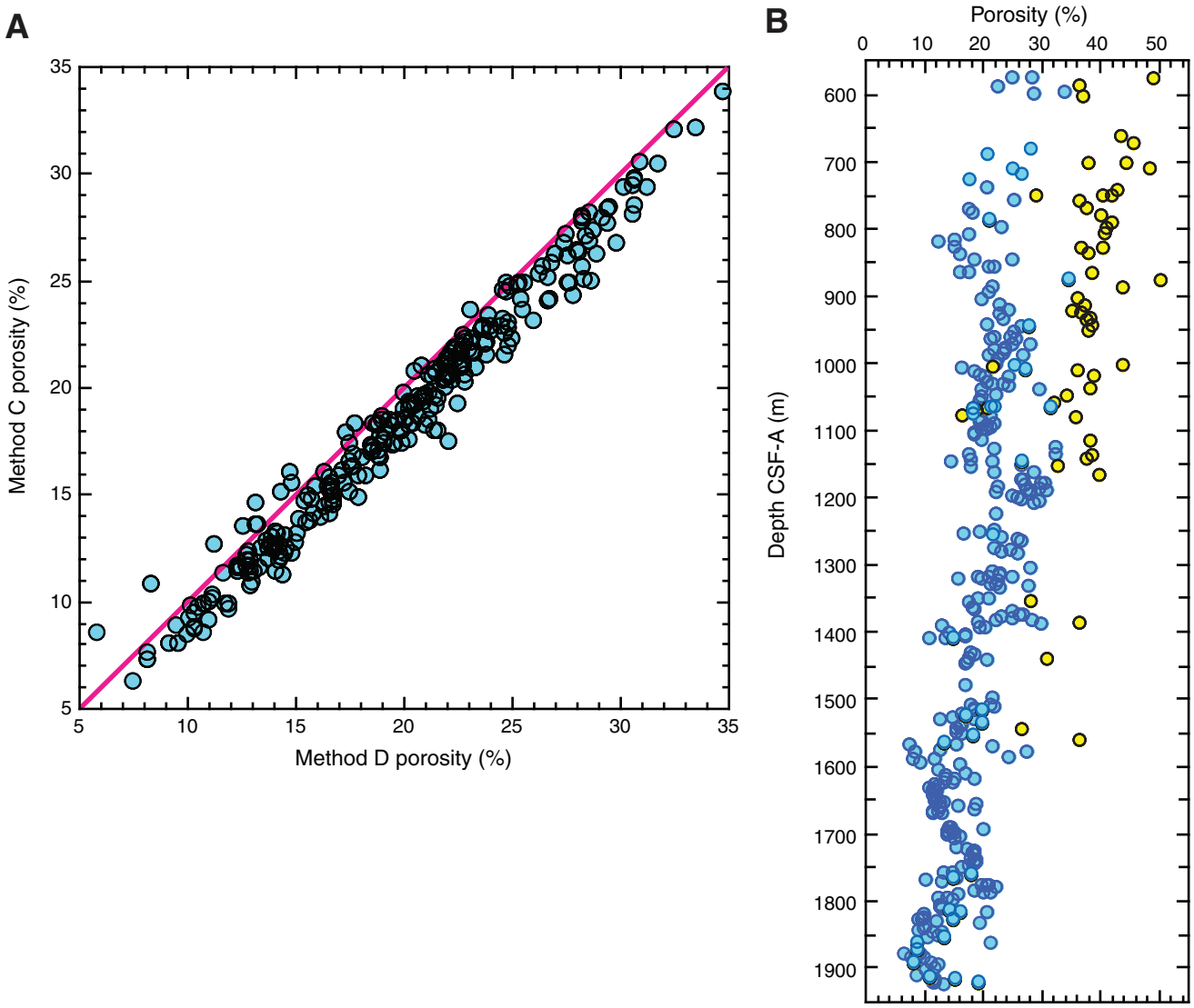

Figure F42. Bulk density, grain density, porosity, and void ratio generated by Method C for samples from Holes U1352B (red-rimmed circles) and U1352C (black-rimmed circles). All indexes show a strong relationship with depth.

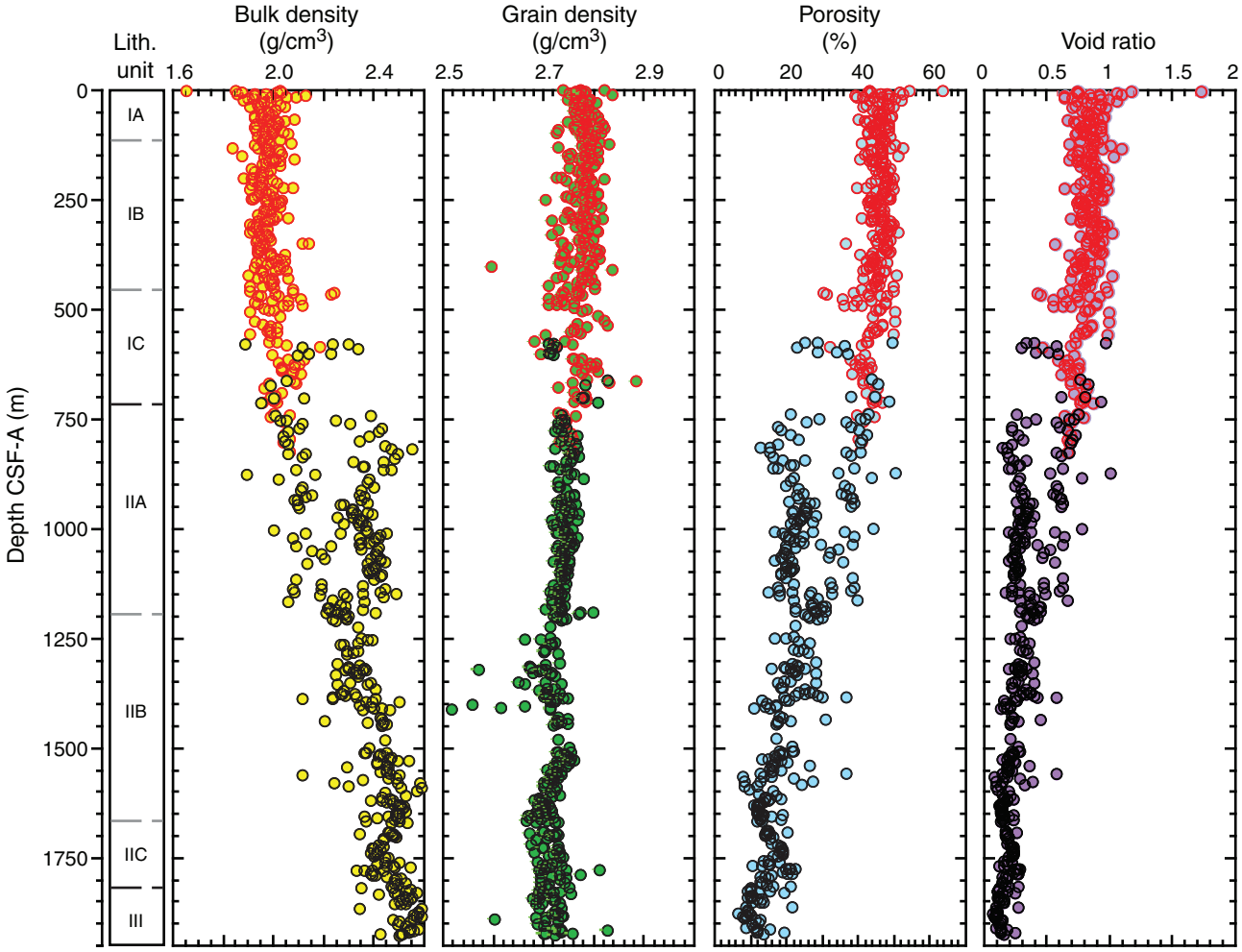

Figure F43. Comparison of moisture and density (MAD) porosity (blue circles), neutron porosity from downhole logs (green curves), and porosity derived from downhole density logs (black curves), Hole U1352B. Hole size, based on caliper measurements during downhole logging, is shown by the red curve. **A.** The entire cored interval for which downhole logging results are available, 100–500 m. **B.** Detail of the top portion of the logged interval, 100–200 m. **C.** Detail of the lower portion of the logged interval, 350–450 m. Core recovery data (black = recovered intervals) are shown to the left. Note that depth (m) refers to CSF-A for core data and to WMSF for logging data.

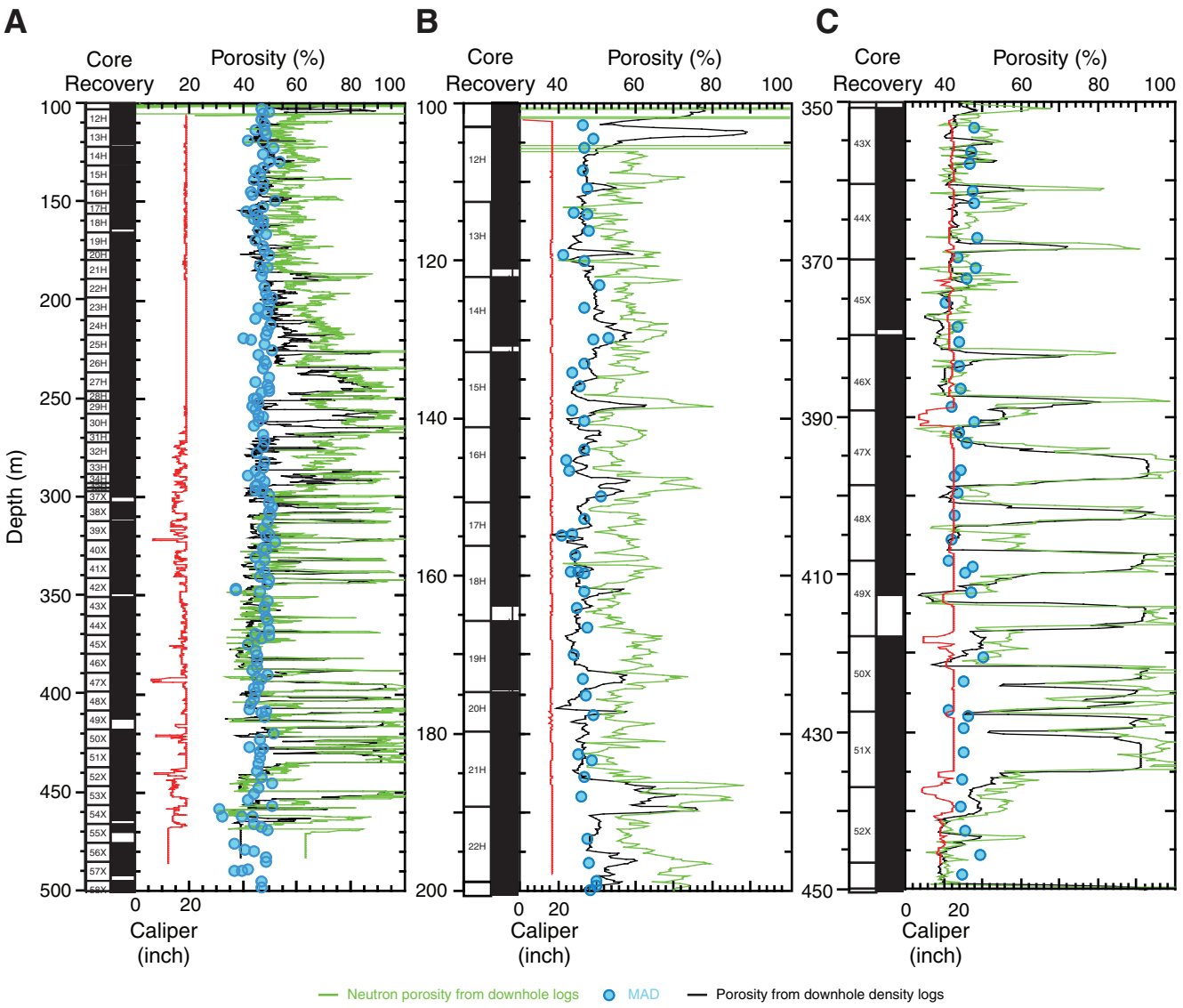

Figure F44. (**A**) Automated vane shear (AVS) and (**B**) fall cone penetrometer (FCP) shear strength for Hole U1352B, (**C**) AVS data for Ocean Drilling Program (ODP) Hole 1119B (Leg 181), and (**D**) cross-plot of AVS and FCP data for Hole U1352B. AVS test results are given as a function of pressure in pascals (kPa = kN/m^2), whereas FCP test results are given in terms of newtons of kN/m^2.

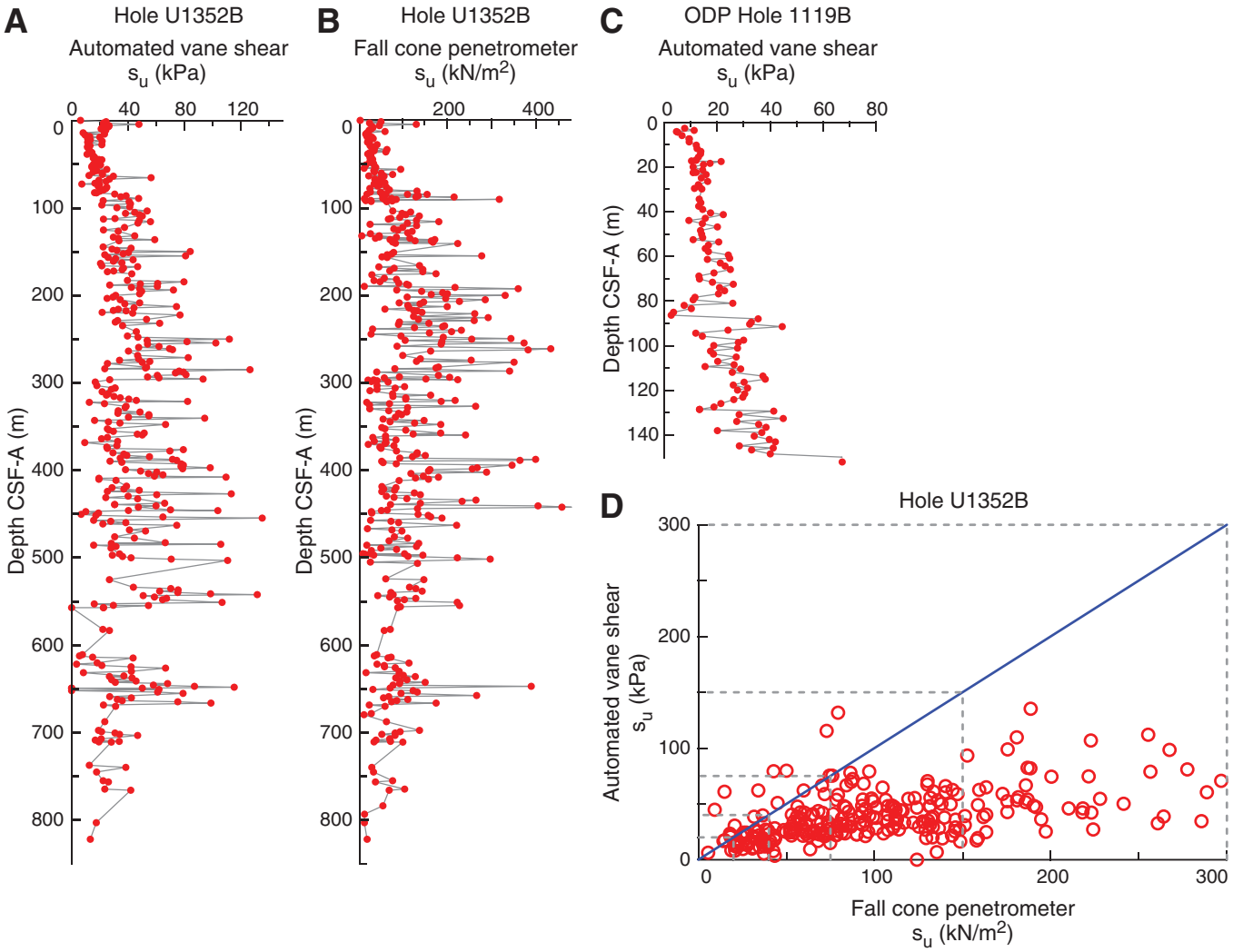

Figure F45. Plots of gas concentrations vs. depth. **A, B.** Methane (C_1), ethane (C_2), and propane (C_3) in (A) headspace (HS) gas and (B) core void gas sampled by syringe (VAC), Holes U1352A (open circles and squares), U1352B (solid circles, squares, and diamonds), and U1352C (solid triangles). **C.** Plots of C_1/C_2 gas ratios from both HS gas and core void gas.

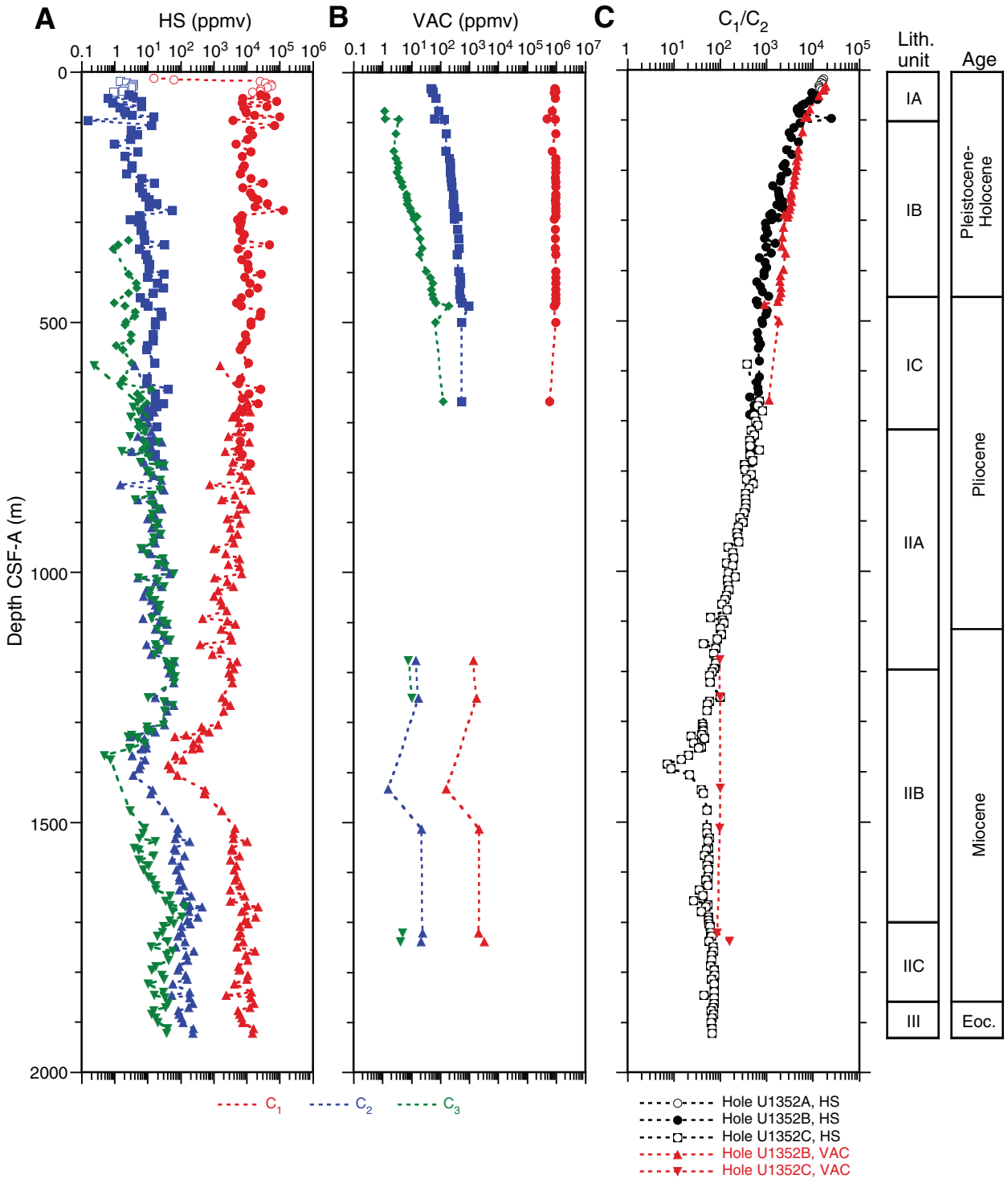

Figure F46. A–E. Plots of concentrations of headspace gas (solid circles) and core void gas (open circles) vs. depth, Holes U1352B (black) and U1352C (red). (A) Total butanes (C_4). (B) Total pentanes (C_5). (C) Total hexanes (C_6). (D) Ethene ($C_{2=}$). (E) Carbon dioxide. **F.** Plots of ratios of normal/(normal + iso) isomers vs. depth for butanes (blue) and pentanes (red) for headspace gas (solid symbols) and core void gas (open symbols) for Holes U1352B (triangles) and U1352C (circles). Some samples contain no detectable *n*-C_5 but do contain measurable *i*-C_5; these zero values are omitted. Cross = air.

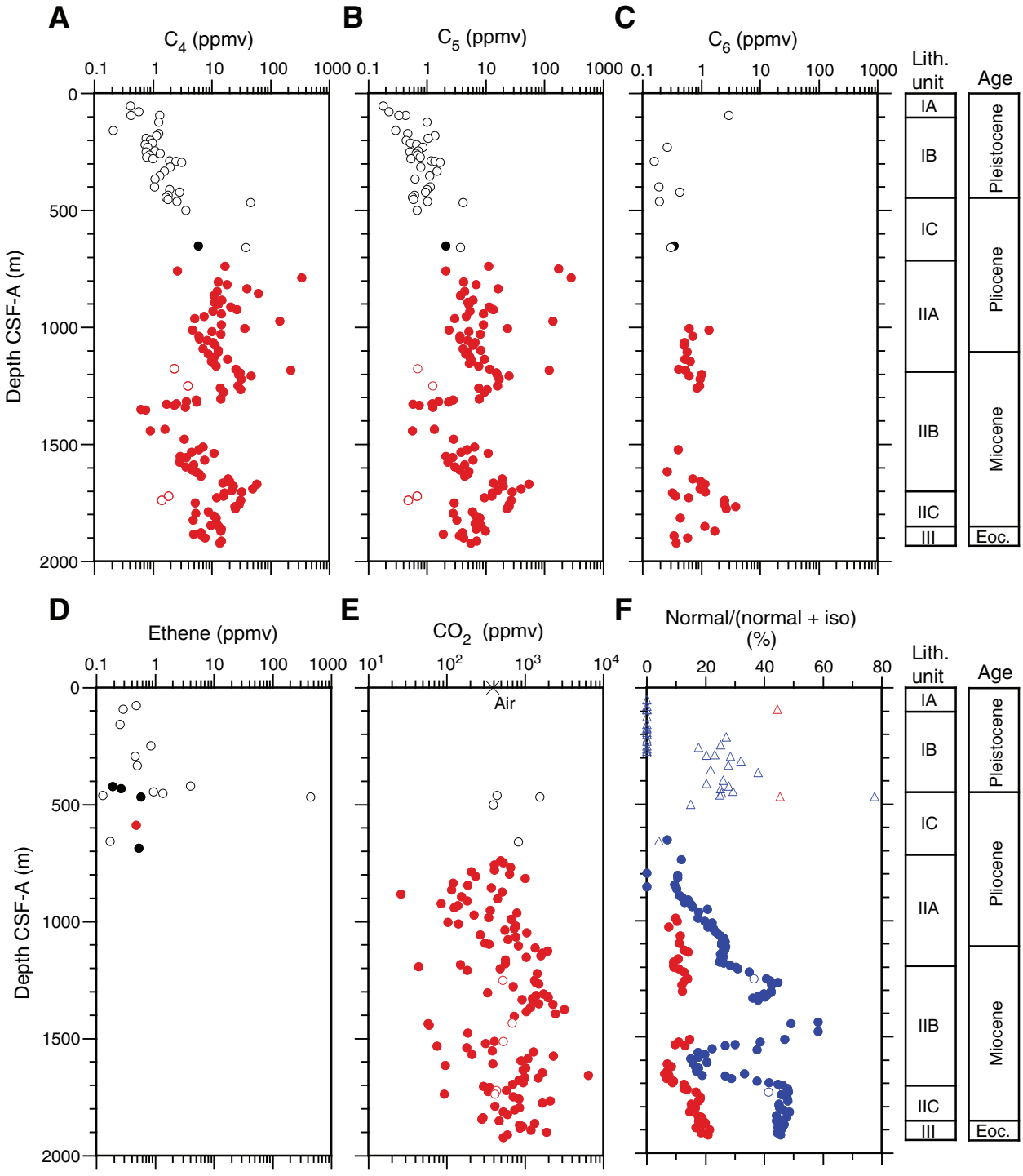

Figure F47. Chromatograms (flame ionization detector [FID]) of Section 317-U1352B-55X-1 (467.37 m CSF-A) showing core void gas composition based on (**A**) the Agilent/HP 6890 Series II gas chromatography system (GC3) and (**B**) the natural gas analyzer (NGA). GC3 identifications and quantifications were confirmed by standards. NGA separation is expanded to show details of butanes, butenes, pentanes, and pentenes. Alkenes could be only tentatively identified.

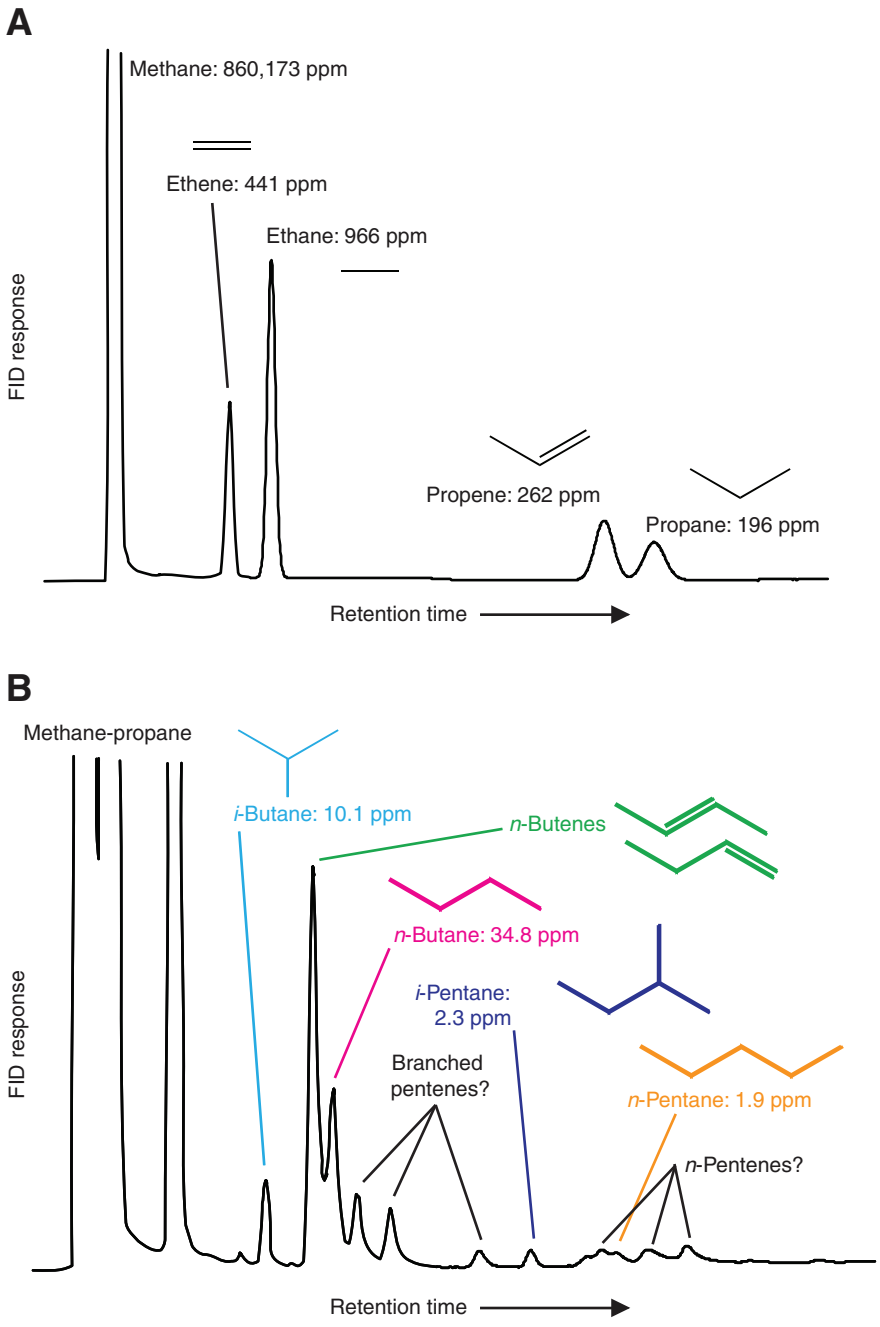

Figure F48. Plots of carbon variation vs. depth, Holes U1352A/B (black) and U1352C (green). **A.** Carbonate carbon (as $CaCO_3$). **B.** Total carbon. **C.** Total organic carbon by difference (TOC_{DIFF}). **D.** Total organic carbon from the source rock analyzer (TOC_{SRA}).

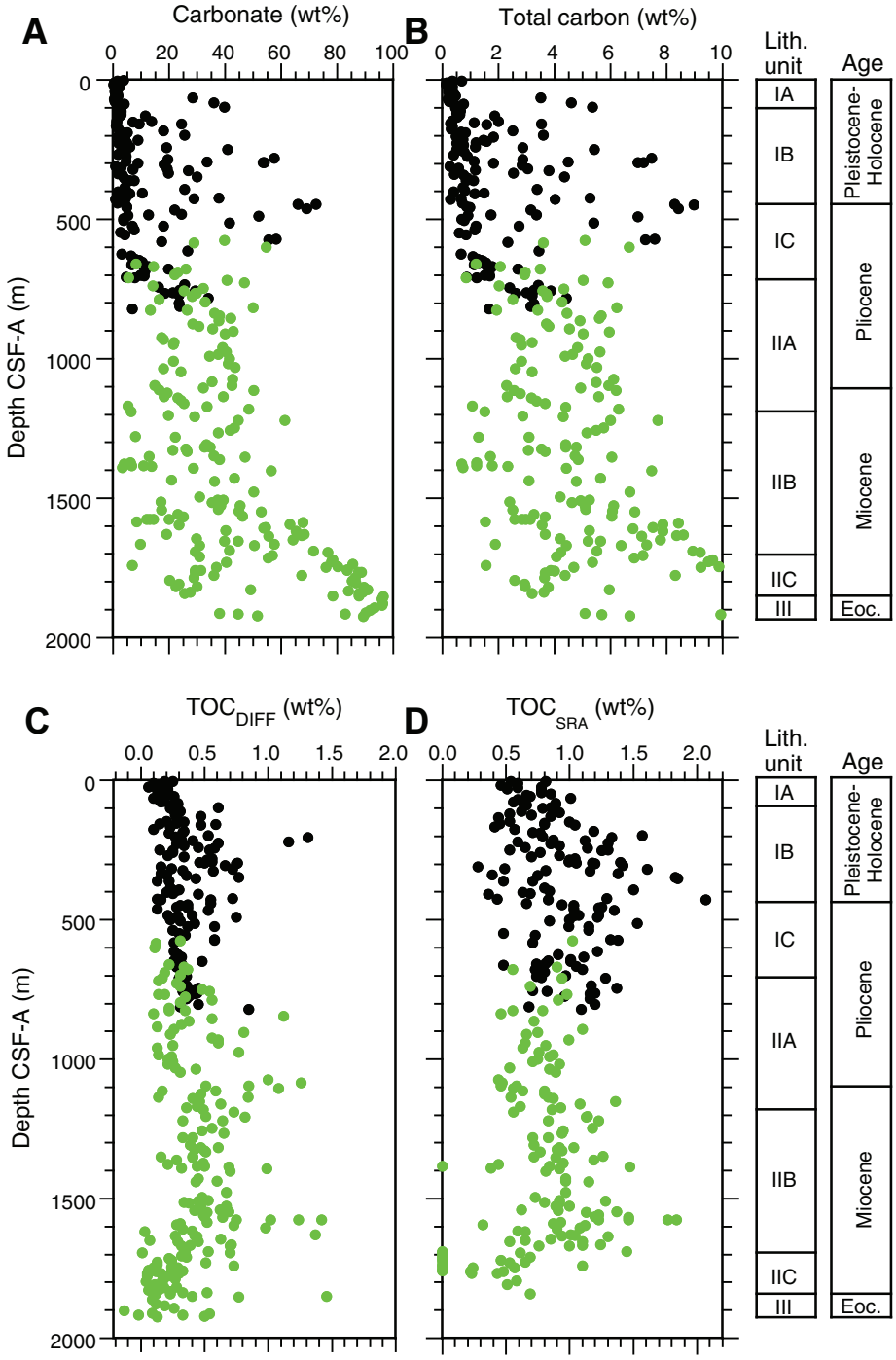

Figure F49. Cross-plot of total carbon measured using two approaches: (1) direct measurement with the CHNS elemental analyzer and (2) the sum of inorganic carbon measured by the coulometer (IC_{COUL}) and total organic carbon measured by the source rock analyzer (TOC_{SRA}). Black line = 1:1 line, dashed red line = correlation line for all data.

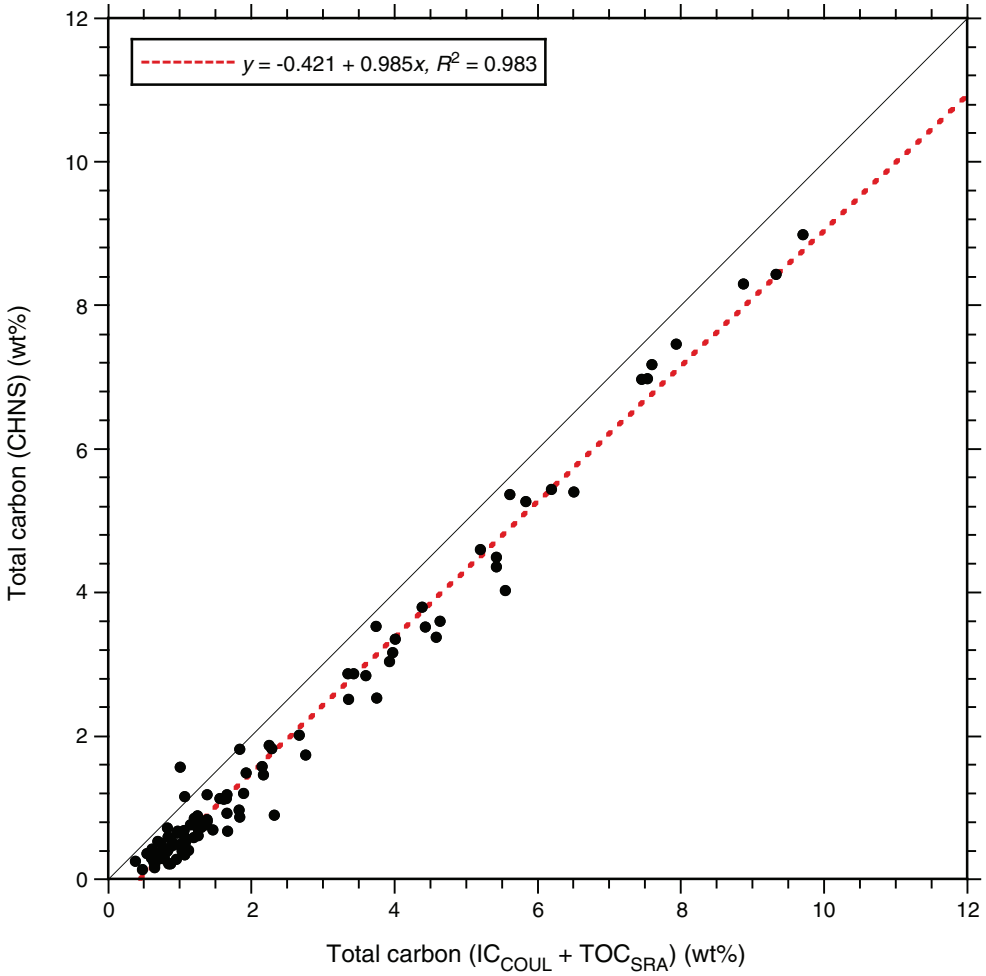

Figure F50. Plots of sediment elemental concentrations vs. depth, Holes U1352A/B (black) and U1352C (green). **A.** Total organic carbon by difference (TOC_{DIFF})/total nitrogen ratio. **B.** TOC_{DIFF}/total sulfur ratio. **C.** Total nitrogen. **D.** Total sulfur.

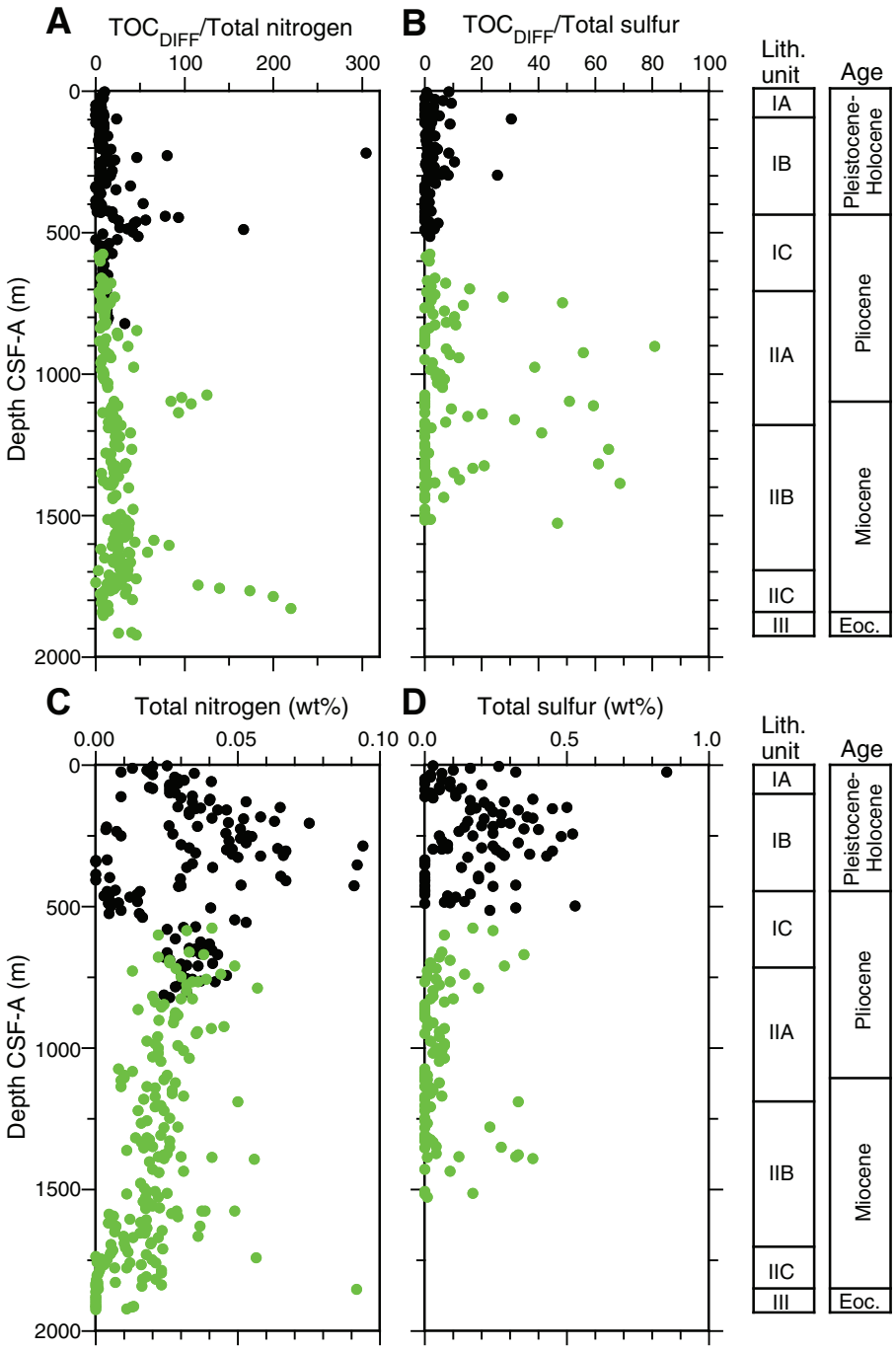

Figure F51. Plots of source rock analyzer data vs. depth, Holes U1352A/B (black) and U1352C (green). **A.** Volatile hydrocarbons (S_1). **B.** Pyrolyzable kerogen (S_2). **C.** Oxidized kerogen (S_3) at <390°C. **D.** Pyrolysis carbon (PC).

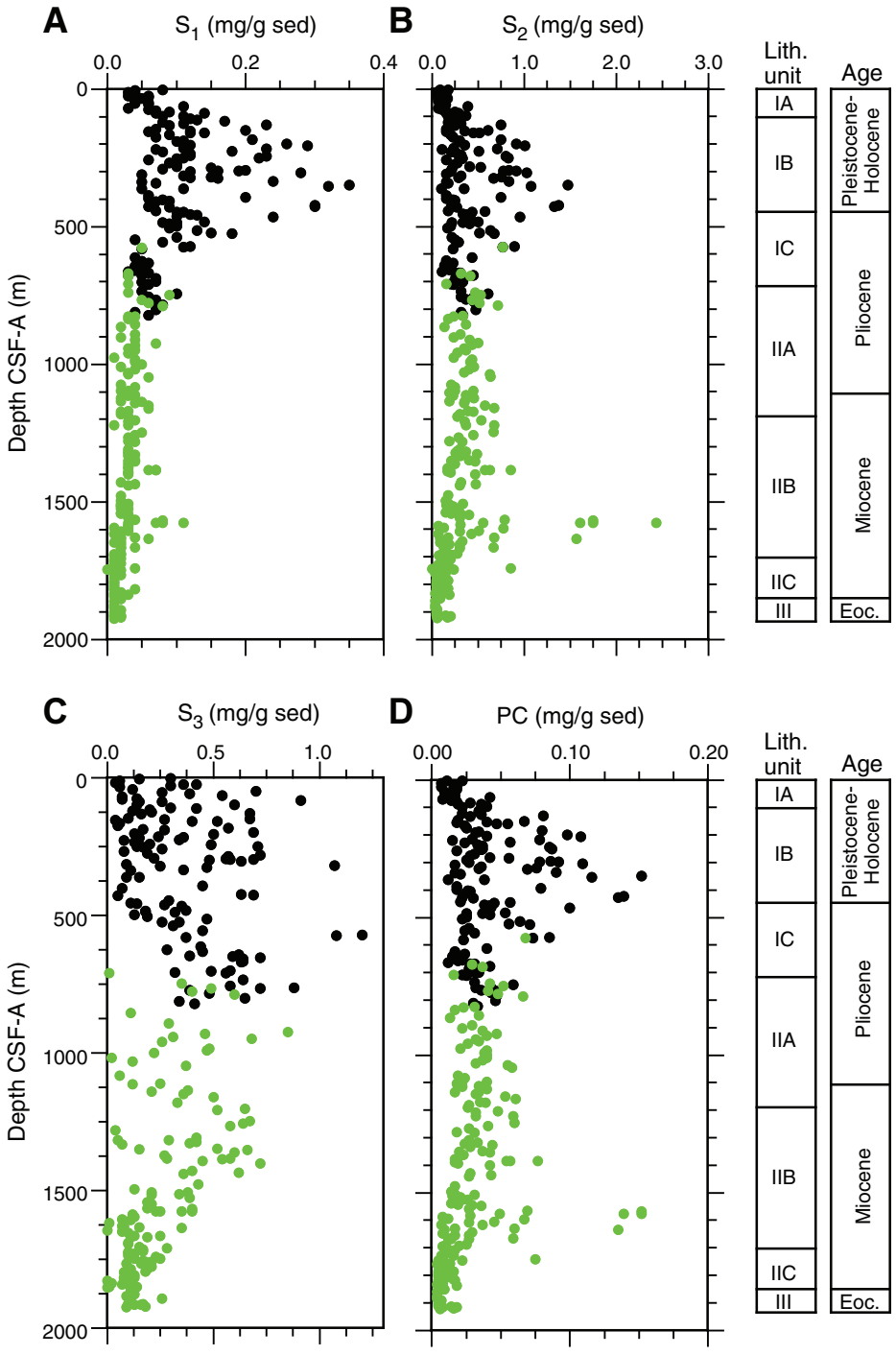

Figure F52. Plots of source rock analyzer (SRA) parameters vs. depth, Holes U1352A/B (black) and U1352C (green). **A.** Hydrogen index. **B.** Oxygen index. **C.** T_{max}. **D.** Production index. HC = hydrocarbons, TOC = total organic carbon from SRA.

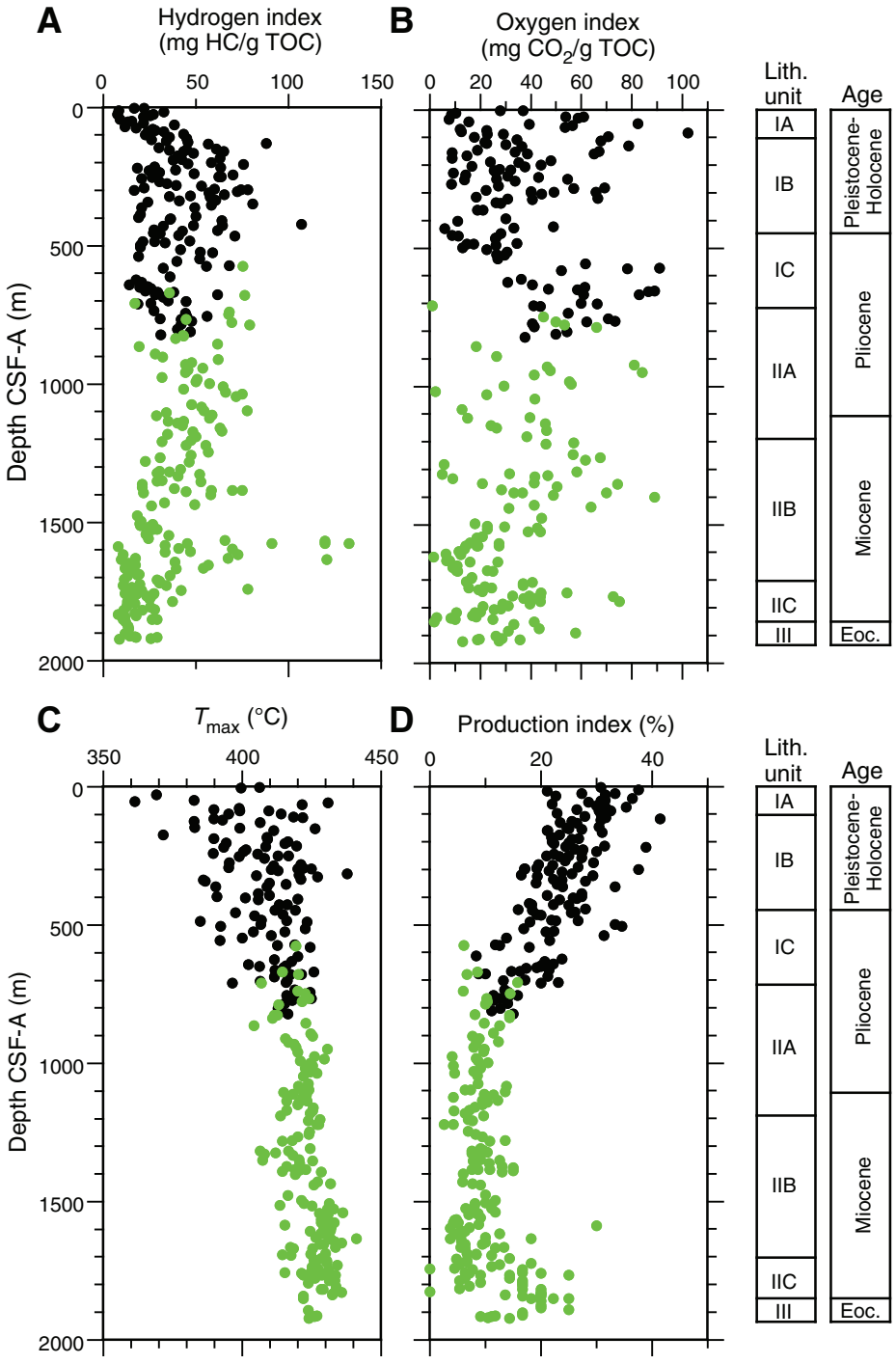

Figure F53. Modified and enlarged van Krevelen diagram based on a cross-plot of hydrogen index vs. oxygen index, showing trend lines for kerogen Types III and IV, Holes U1352A/B (black) and U1352C (green). Trend lines are not shown for kerogen Types I and II. TOC = total organic carbon from SRA.

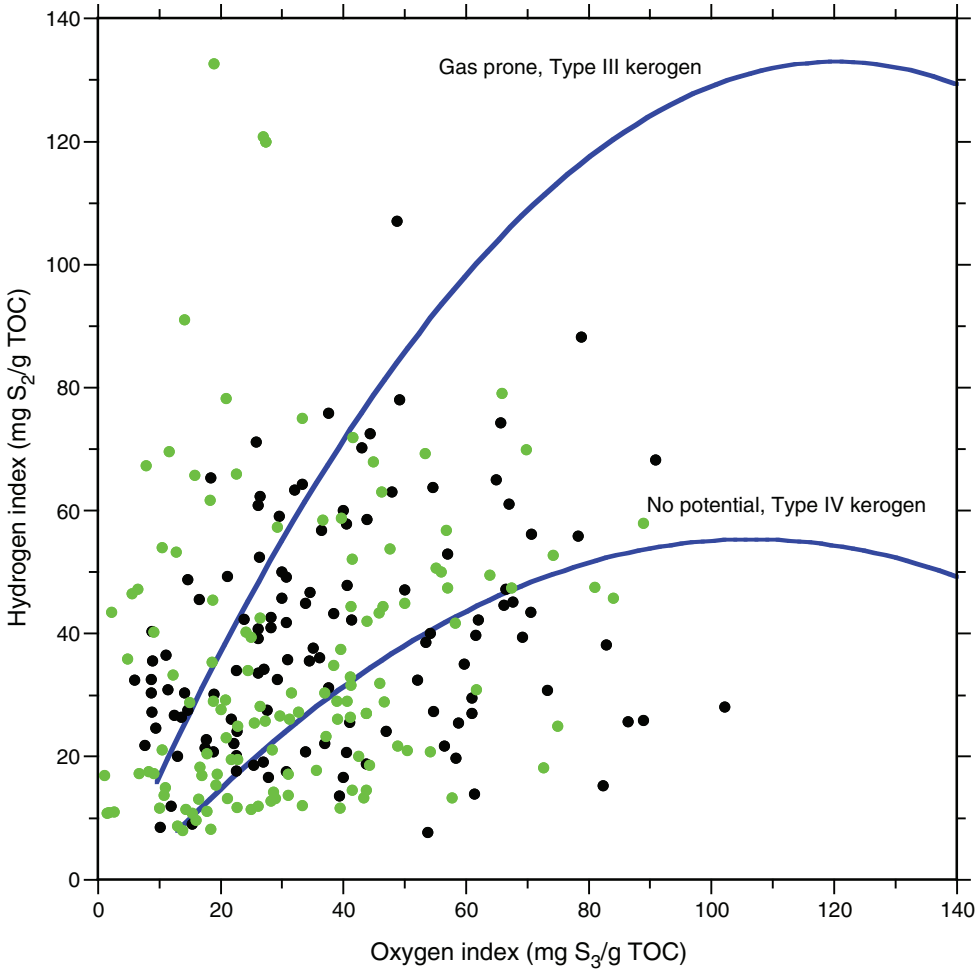

Figure F54. Plot of variation in yield of interstitial water per centimeter of squeezed whole-round cores vs. depth, Holes U1352A (red), U1352B (black), and U1352C (green).

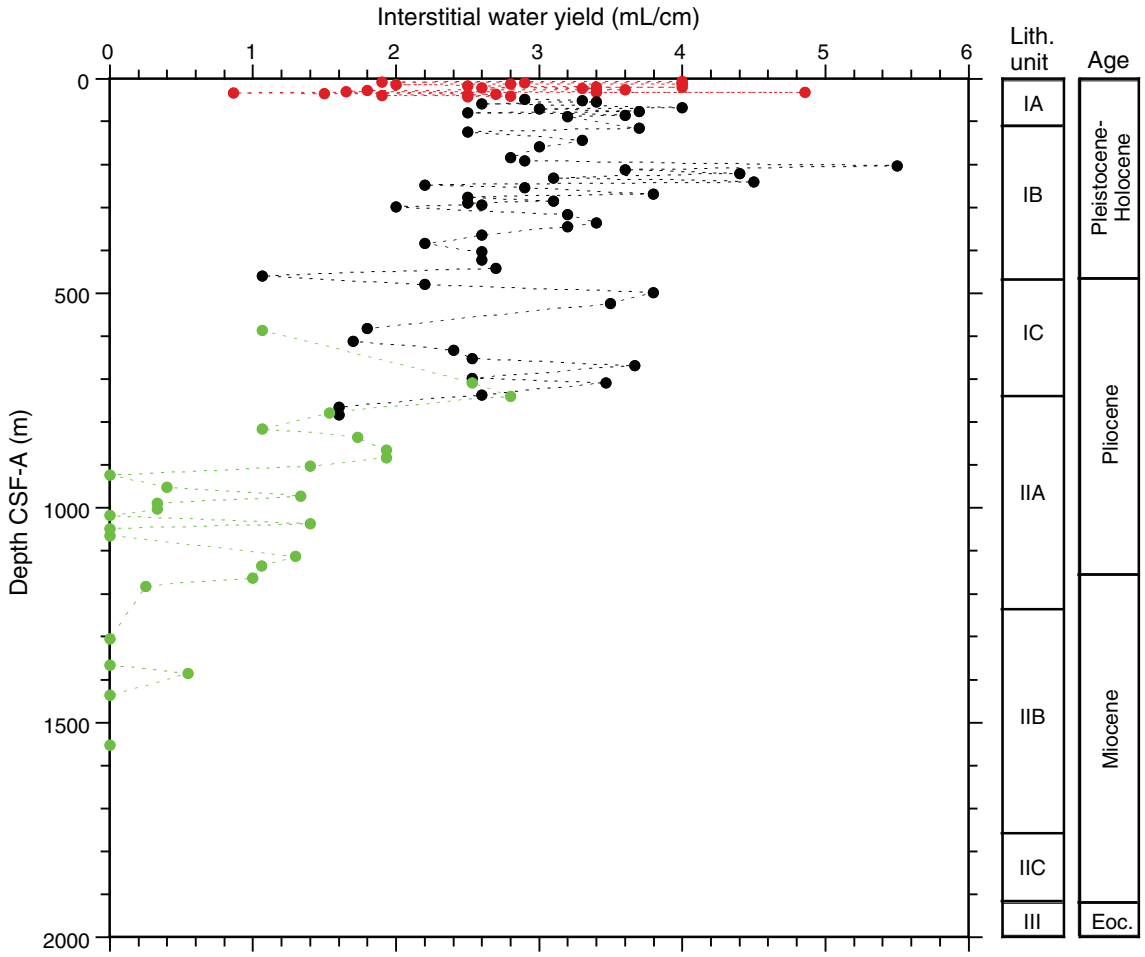

Figure F55. Plots of ionic constituents of interstitial water vs. depth, Holes U1352A (red), U1352B (black), and U1352C (green). **A, C.** Chloride. **B, D.** Salinity. Bottom panels show total depth and top panels show uppermost 100 m. SW = IAPSO seawater values.

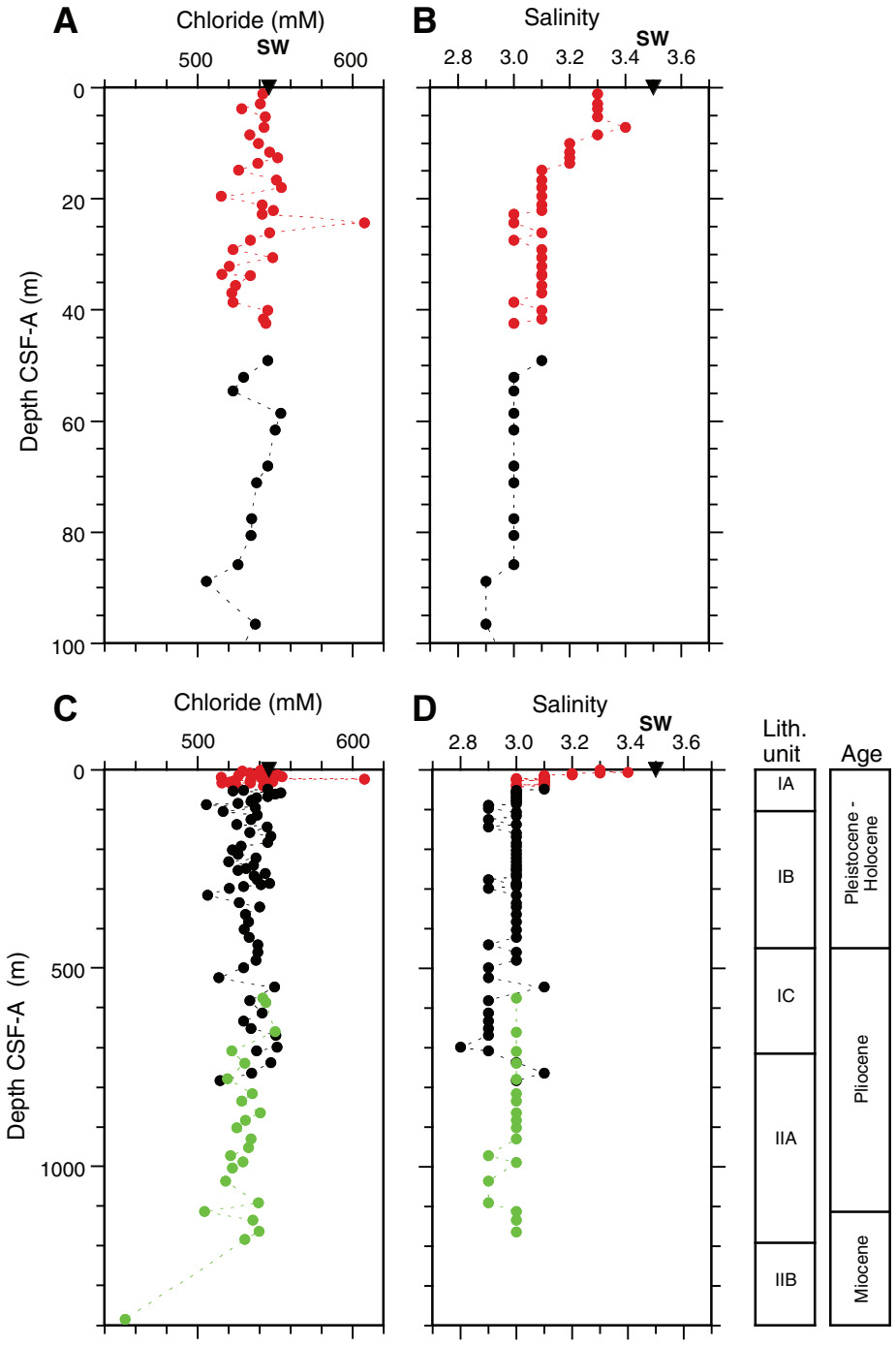

Figure F56. Plots of ionic constituents of interstitial water vs. depth, Holes U1352A (red), U1352B (black), and U1352C (green). **A.** Strontium. **B.** Strontium/calcium ratio. **C.** pH. **D.** Calcium. **E.** Magnesium. **F.** Magnesium/calcium ratio. SW = IAPSO seawater values.

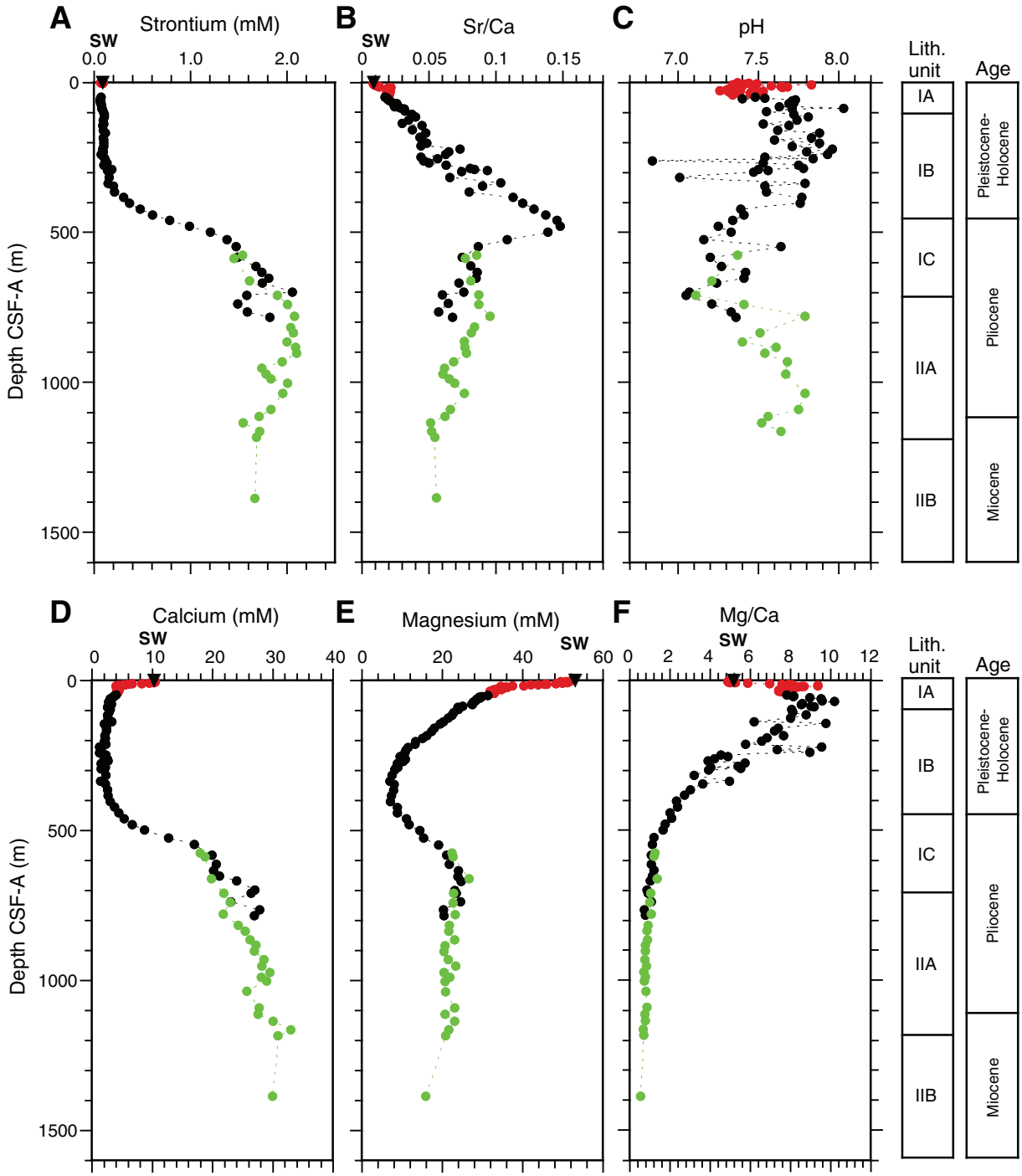

Figure F57. Plots of ionic constituents of interstitial water vs. depth, Holes U1352A (red), U1352B (black), and U1352C (green). **A, C.** Alkalinity. **B, D.** Sulfate. Bottom panels show total depth and top panels show uppermost 100 m. SW = IAPSO seawater values.

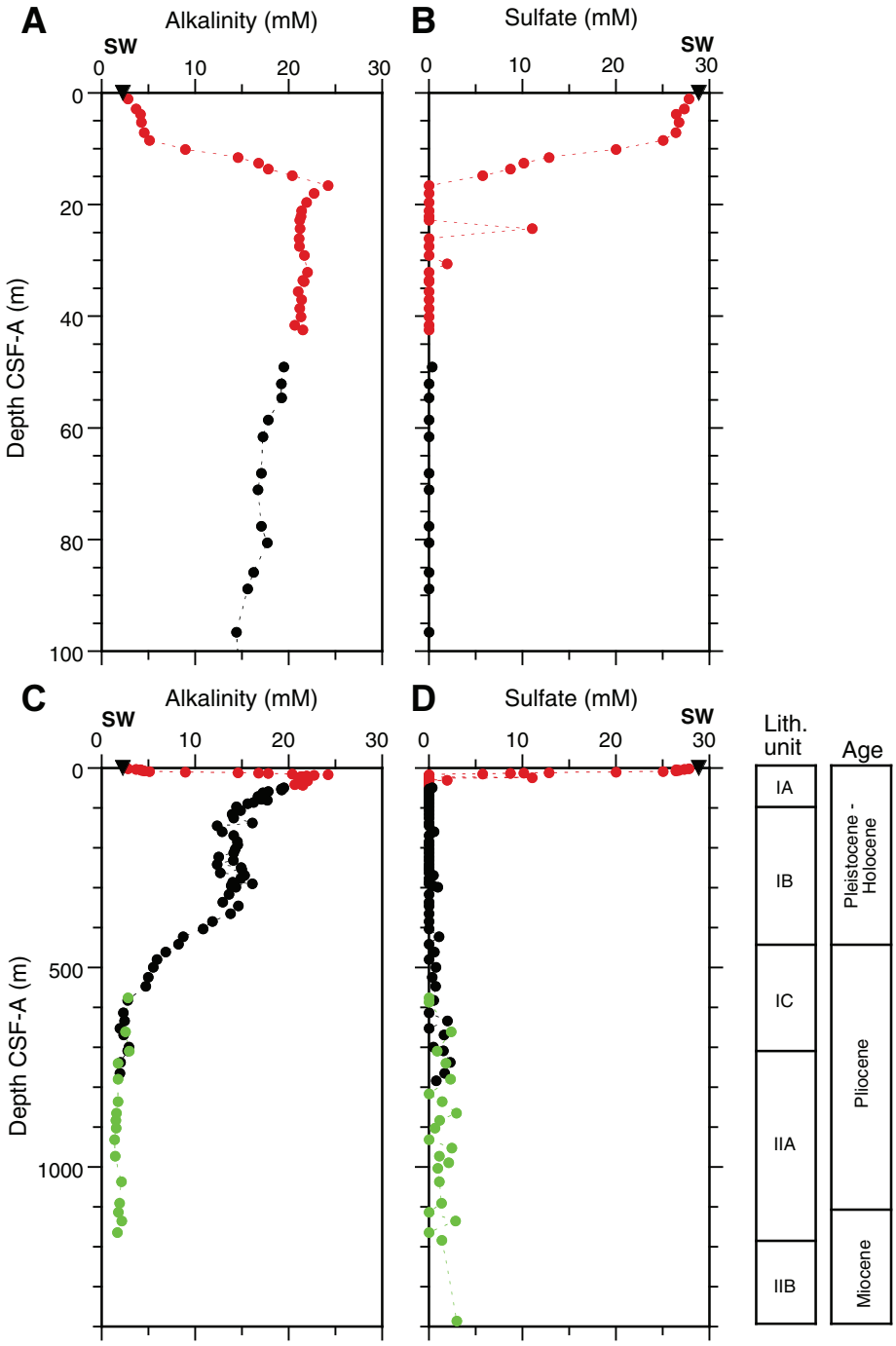

Figure F58. Plots of ionic constituents of interstitial water vs. depth, Holes U1352A (red), U1352B (black), and U1352C (green). **A.** Phosphate. **B.** Dissolved silica. **C.** Ammonium. **D.** Silicon from inductively coupled plasma spectroscopy (ICP). SW = IAPSO seawater values.

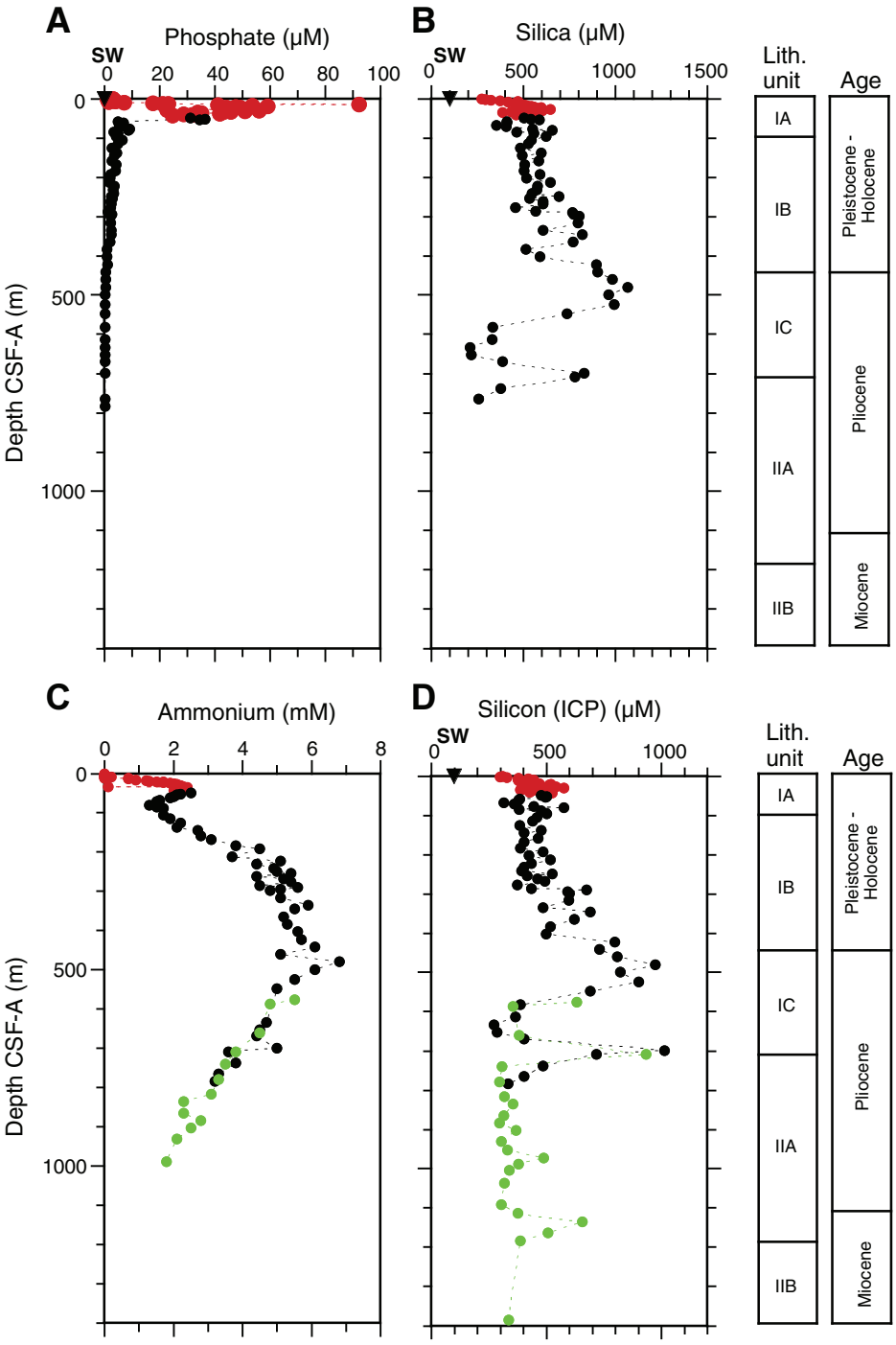

Figure F59. Plots of ionic constituents of interstitial water vs. depth, Holes U1352A (red), U1352B (black), and U1352C (green). **A.** Lithium. **B.** Potassium. **C.** Sodium. **D.** Barium. SW = IAPSO seawater values.

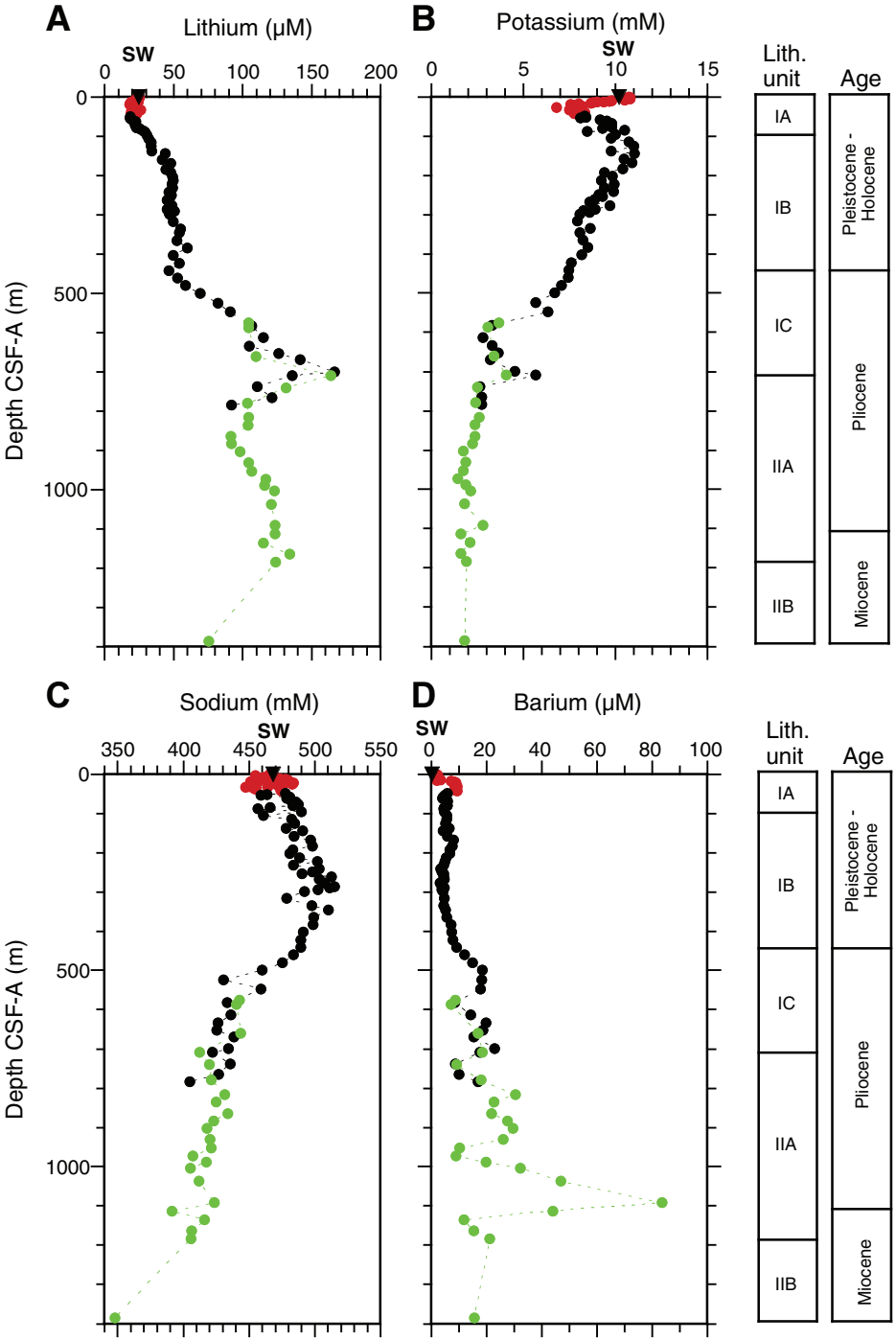

Figure F60. Plots of ionic constituents of interstitial water vs. depth, Holes U1352A (red), U1352B (black), and U1352C (green). **A.** Boron. **B.** Iron. **C.** Manganese. SW = IAPSO seawater values.

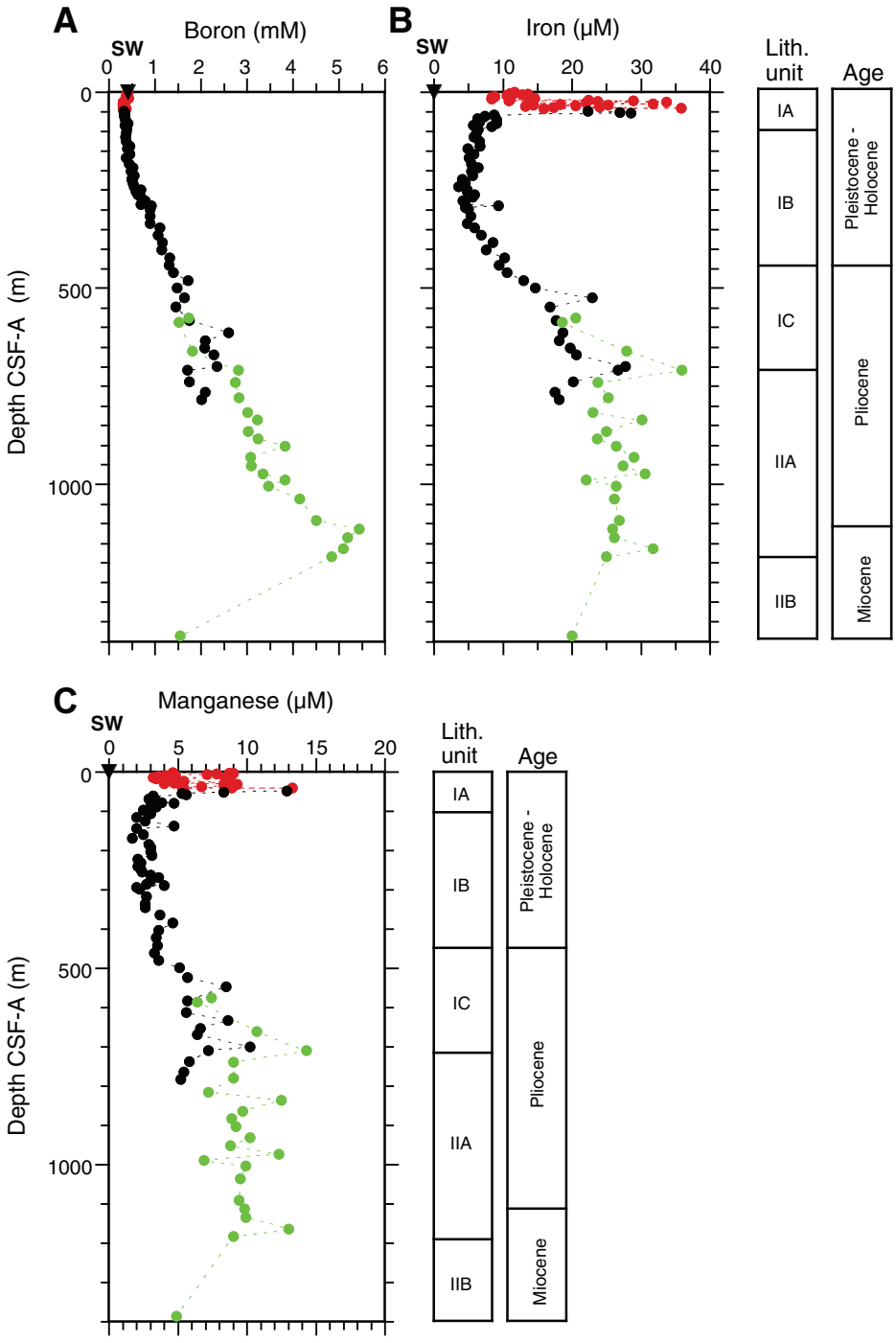

Figure F61. Top 100 m depth profiles for Holes U1352A (open symbols) and U1352B (solid symbols). Blue shading = sulfate–methane transition zone. **A.** Methane, alkalinity, sulfate, calcium, and magnesium. **B.** Phosphate. **C.** Dissolved silica. **D.** Barium.

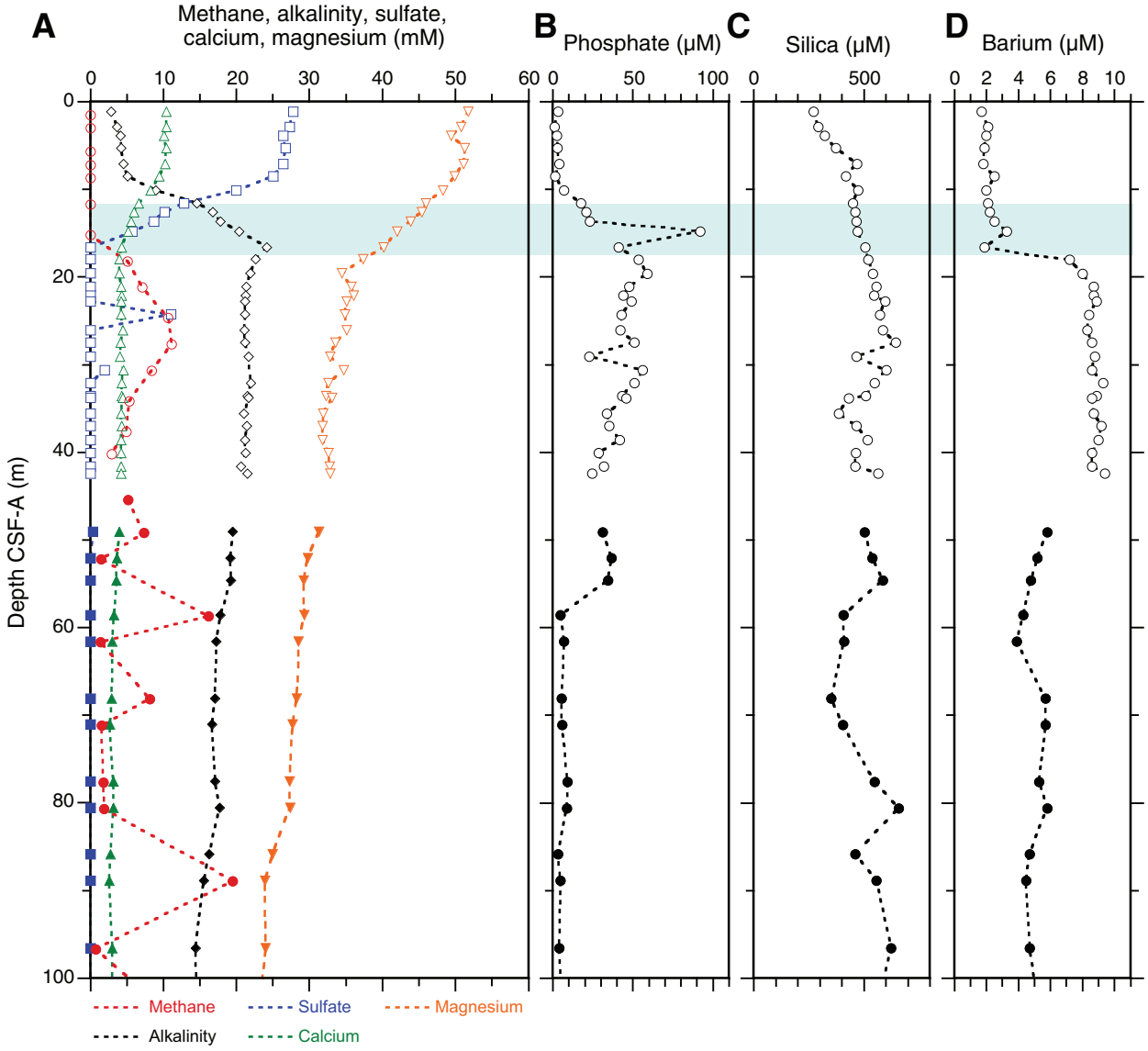

Figure F62. Plot showing stoichiometry of the sulfate-reduction zone for the 12 samples shallower than 17 m in Hole U1352A. Equations for methane oxidation (bottom) and organic matter oxidation (top) are shown. Data from Hole U1352A plot close to the 1.5:1 line (correlation line and equation shown in red).

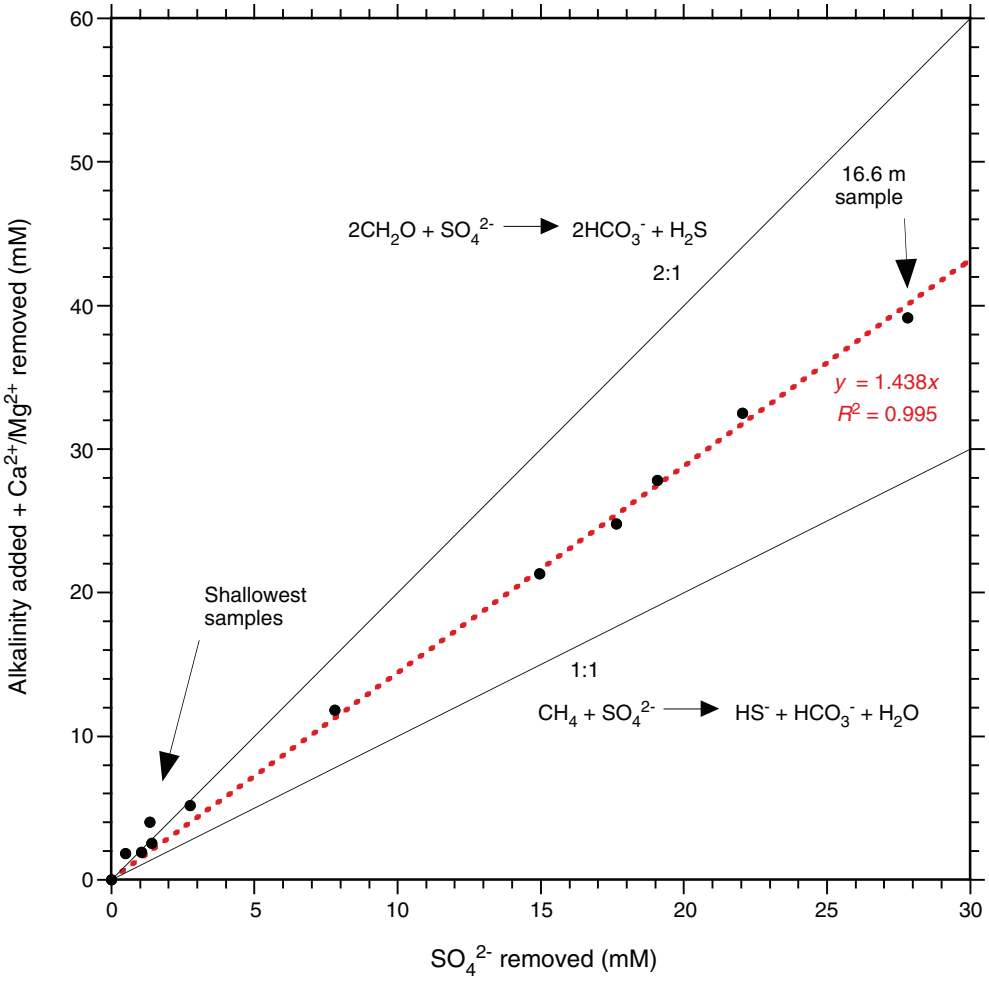

Figure F63. Distribution of microspheres along the core liner, Site U1352. **A.** Contamination degree in the inner part of the core. **B.** Dispersion of microspheres along the core liner. Blue circles = total microsphere count for APC cores, red circles = total microsphere count for XCB cores, black diamonds = total microsphere count for RCB cores.

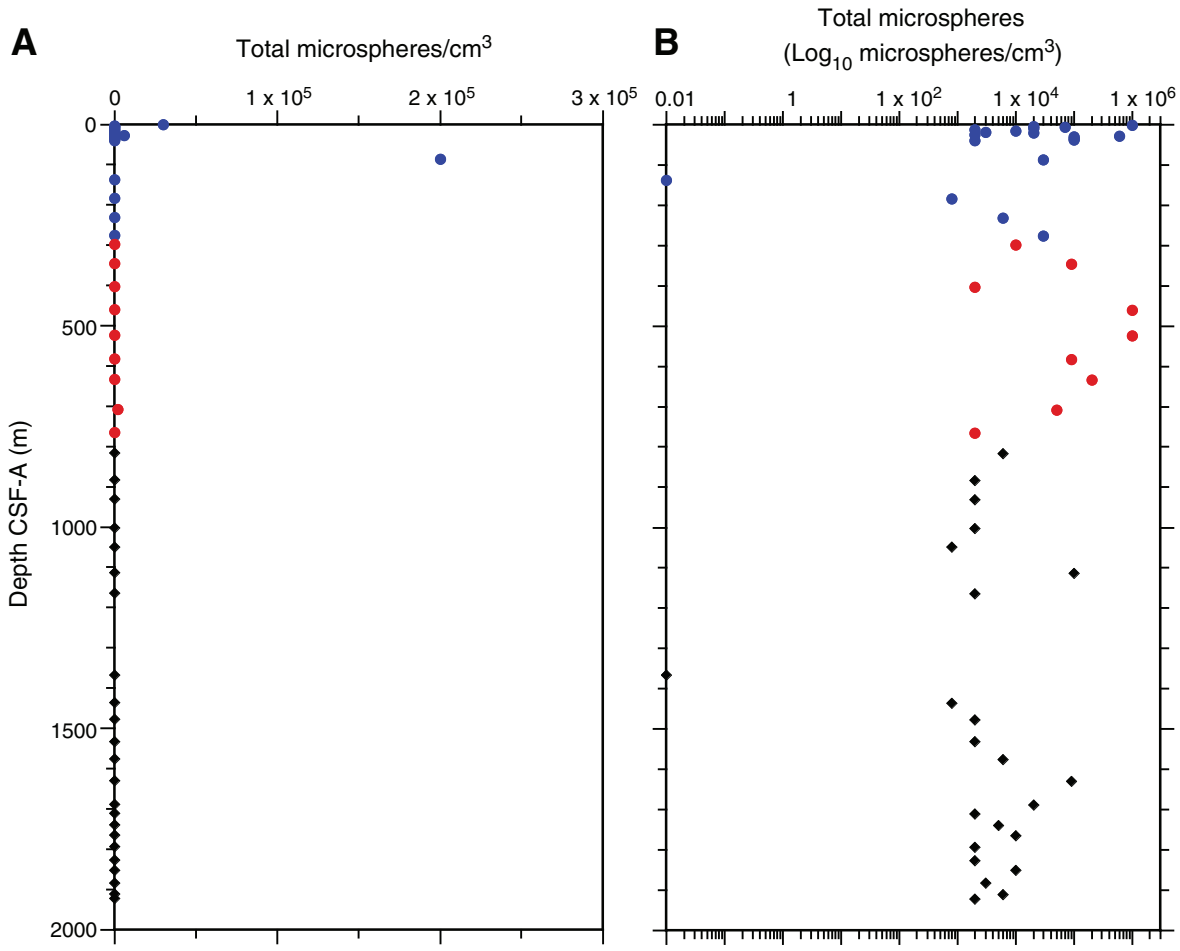

Figure F64. A. Temperature data for Site U1352. An exponential decrease in temperature is expected for the time interval shown and used to estimate ambient temperature. This decrease is evident in Cores 317-U1352B-10H, 15H, 20H, and 38X. Data for the time interval t_i to t_f (solid circles) were used to estimate asymptotic temperature. See Table T27 for these values. **B.** Resulting geothermal gradient (46.0°C/km). Solid circles = reliable temperature measurements. APCT-3 = third-generation advanced piston corer temperature tool, SET = Sediment Temperature tool.

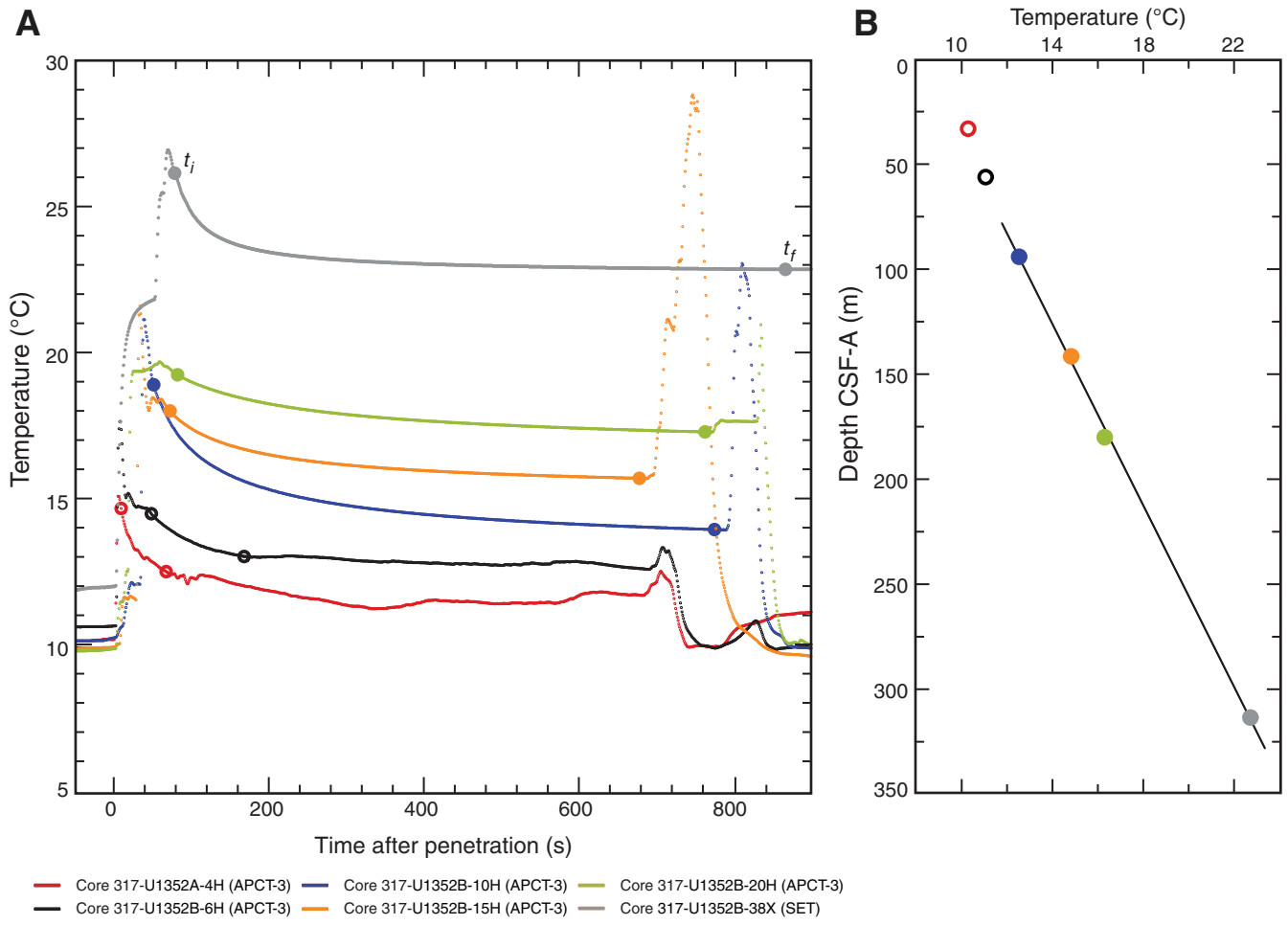

Figure F65. Thermal conductivity for Site U1352 vs. (**A**) depth, (**B**) porosity, and (**C**) bulk density. Thermal conductivity measurements for Holes U1352A, U1352B, and U1352C were used to determine the relationship between thermal conductivity and depth. Linear fits represent increasing thermal conductivity within each depth interval. Thermal conductivity exhibits a negative relationship with porosity and a positive relationship with bulk density. Variation with lithology is weak but detectable. MAD (C) = moisture and density Method C.

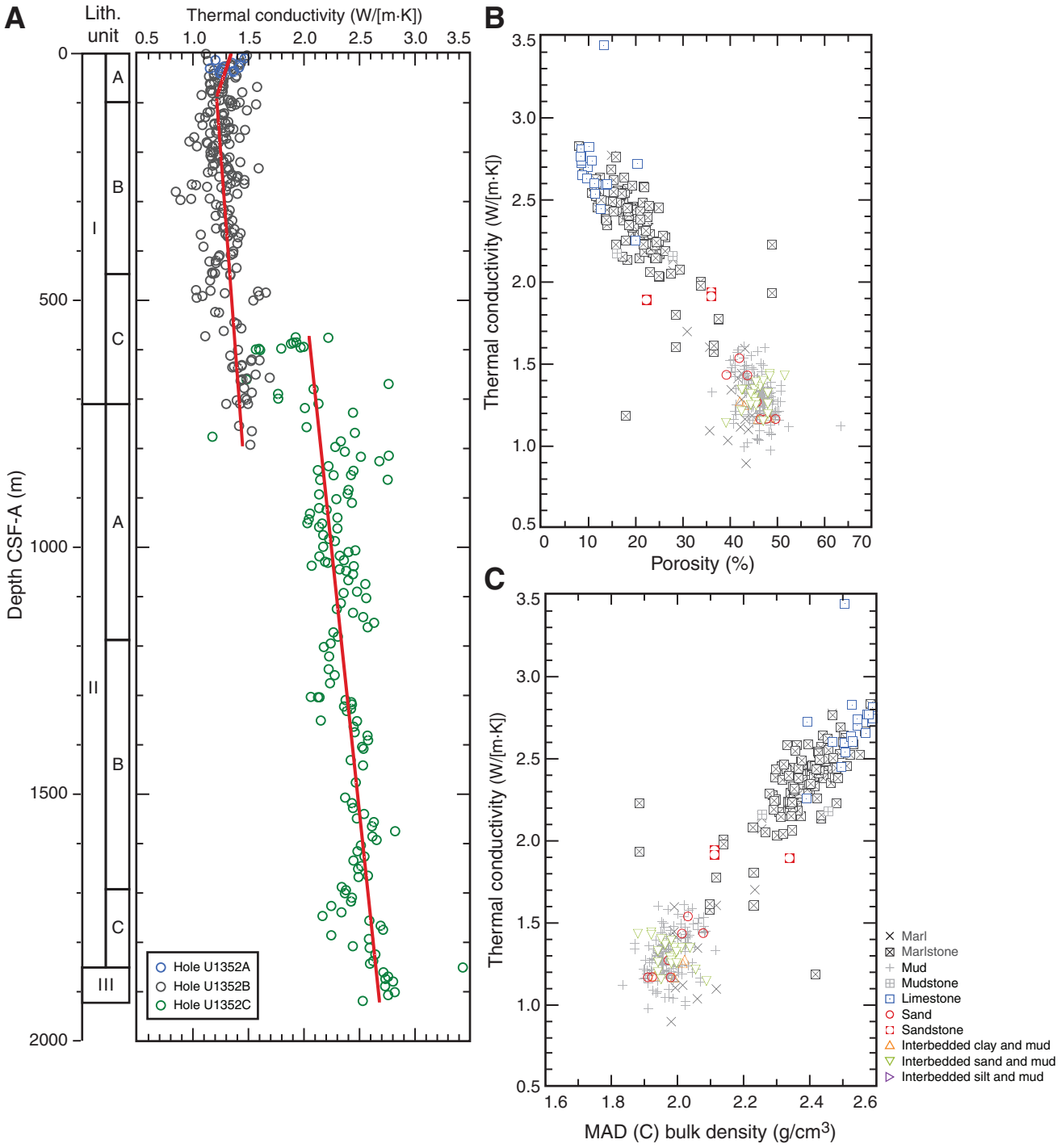

Figure F66. Bullard plot for Site U1352. Thermal resistance is derived from the linearly increasing trend of thermal conductivity with depth in the 94–313 m CSF-A depth interval, where the geothermal gradient was successfully established. The estimated heat flow is 57.8 mW/m^2, which is consistent with the regional heat flow distribution in New Zealand (Reyes, 2007). Solid circles = reliable data points. APCT-3 = third-generation advanced piston corer temperature tool, SET = Sediment Temperature tool.

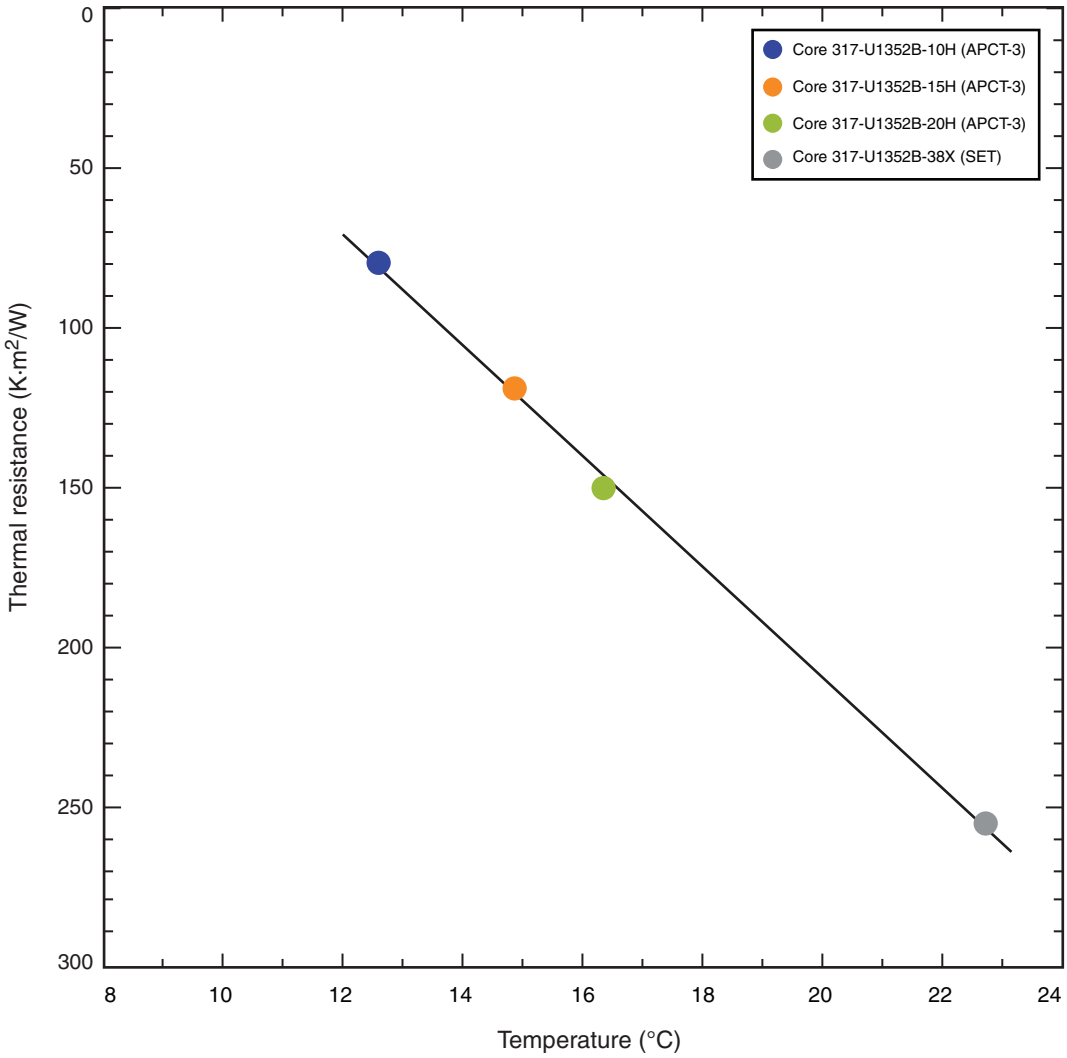

Figure F67. Predicted temperature profiles at Site U1352 based on the geothermal gradient established in the uppermost portion of the hole and variable thermal conductivity with depth. At 661 m CSF-A, the temperature gradient (d*T*/d*z*) is about one-half that of the above depth interval for sediments. The predicted bottom-hole temperature in Hole U1352C, assuming variable thermal conductivity with depth, is ~60°C, which is ~40°C lower than that obtained by assuming a constant geothermal gradient of 46.0°C/km.

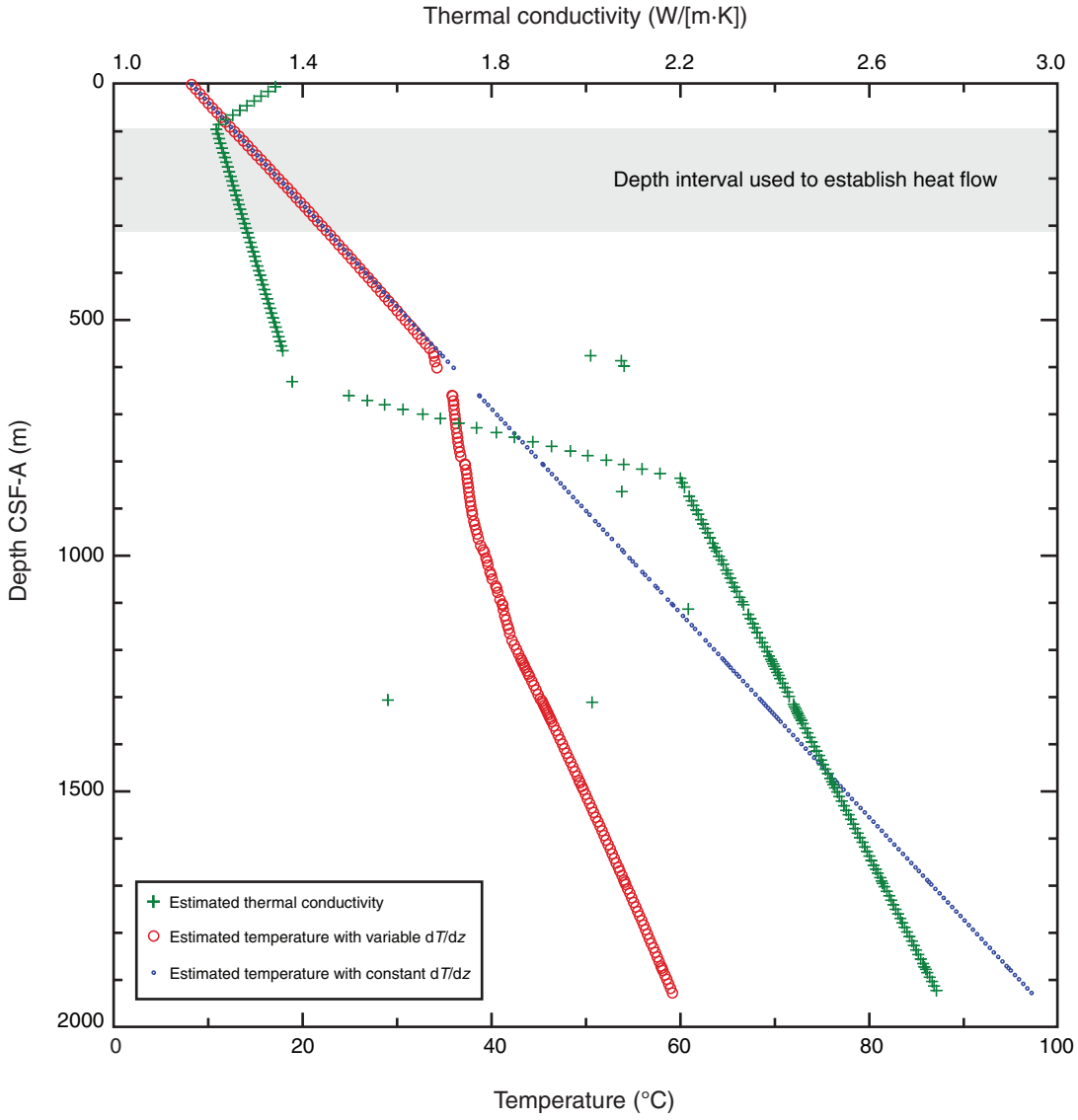

Figure F68. Summary of logs recorded by the triple combination tool string in Hole U1352B and comparison to physical property data measured on recovered cores. Resistivity-derived density and porosity were calculated from the phasor deep induction log (IDPH). HLDS = Hostile Environment Litho-Density Sonde, NGR = natural gamma radiation core measurements, MAD = moisture and density core data, GRA = gamma ray attenuation bulk density core measurements, IMPH = phasor medium induction log.

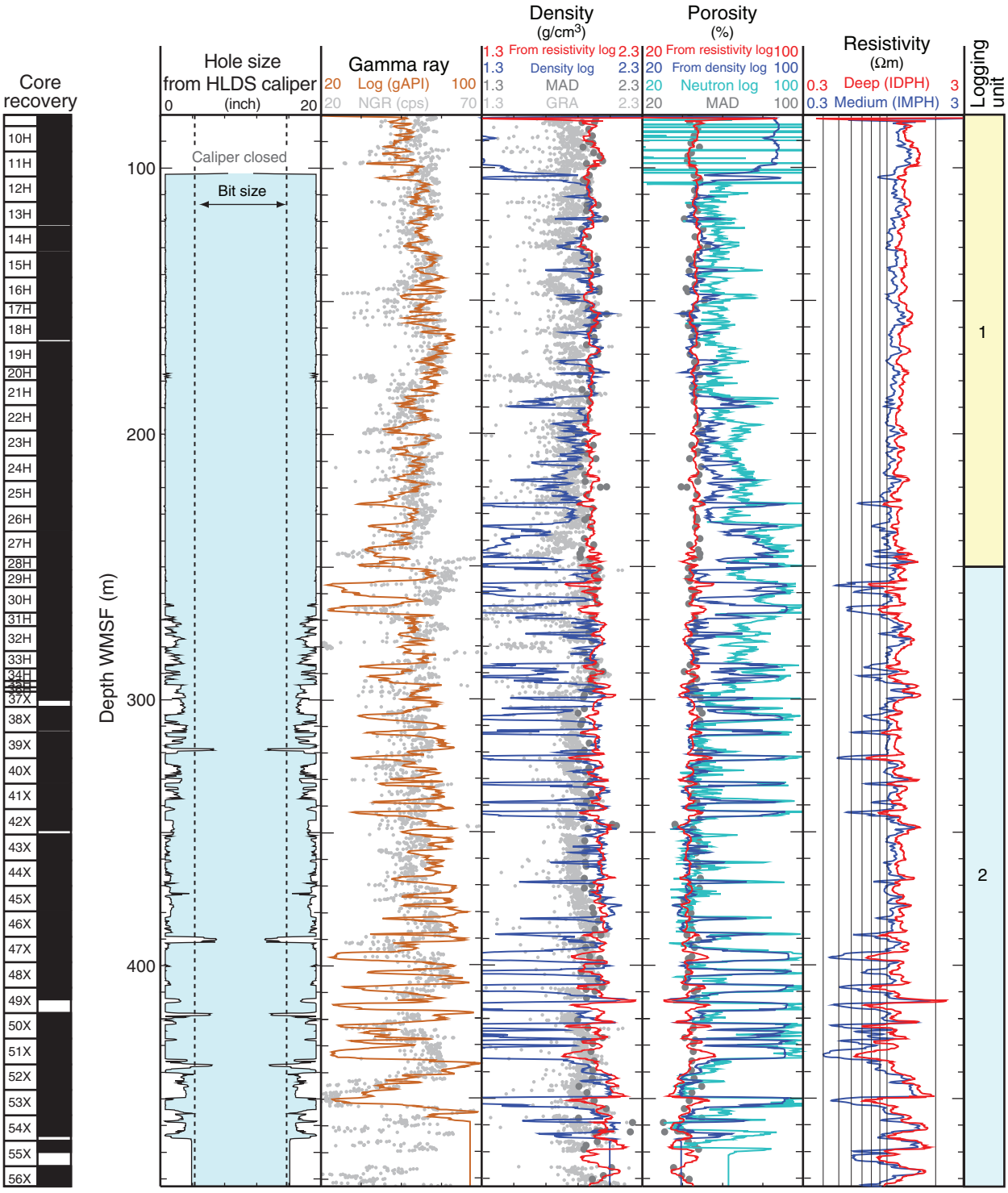

Figure F69. Summary of logs recorded by the Formation MicroScanner (FMS)-sonic tool string in Hole U1352B. Hole size was calculated by the two orthogonal calipers of the FMS (C1 and C2). In the gamma ray track, gamma ray recorded in Pass 2 with the FMS-sonic tool string is compared to gamma ray recorded with the triple combination (TC) tool string in the same hole. Sonic waveform (WF) amplitude is shown as an indicator of the quality of the data. High waveform coherence, shown in red in the two velocity tracks, is a measure of the reliability of the slowness/time coherence algorithm used to derive compressional (V_P) and shear (V_S) velocities from the monopole and lower dipole sonic waveforms, respectively. (**Figure shown on next page.**)

Figure F69 (continued). (Caption shown on previous page.)

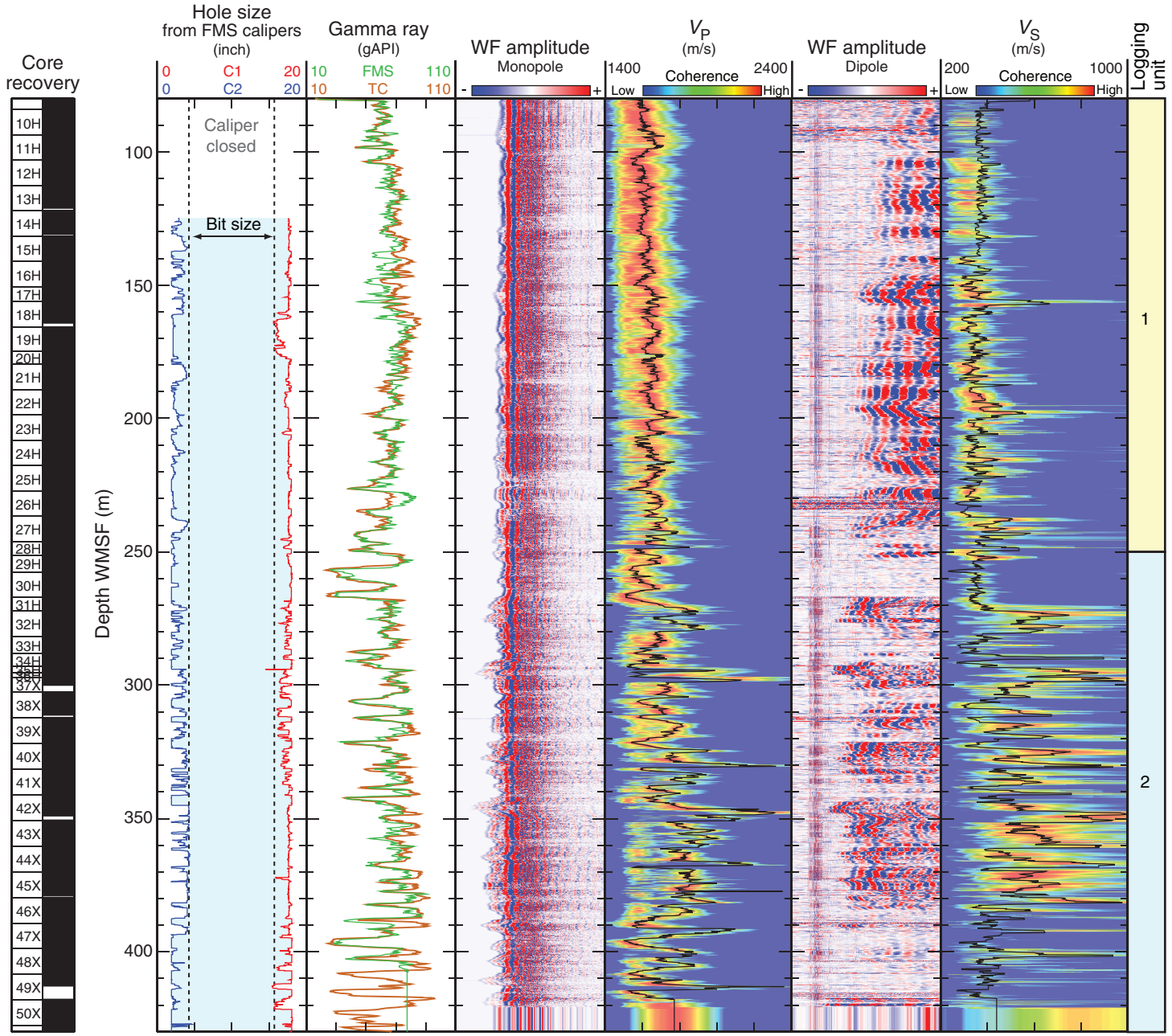

Figure F70. Summary of spectral natural gamma ray measurements in Hole U1352B. SGR = total gamma ray, CGR = computed gamma ray (gamma ray without uranium contribution). The CGR and SGR curves define an envelope (colored green), and the area between the two curves shows the contribution of uranium, a common indicator of organic content.

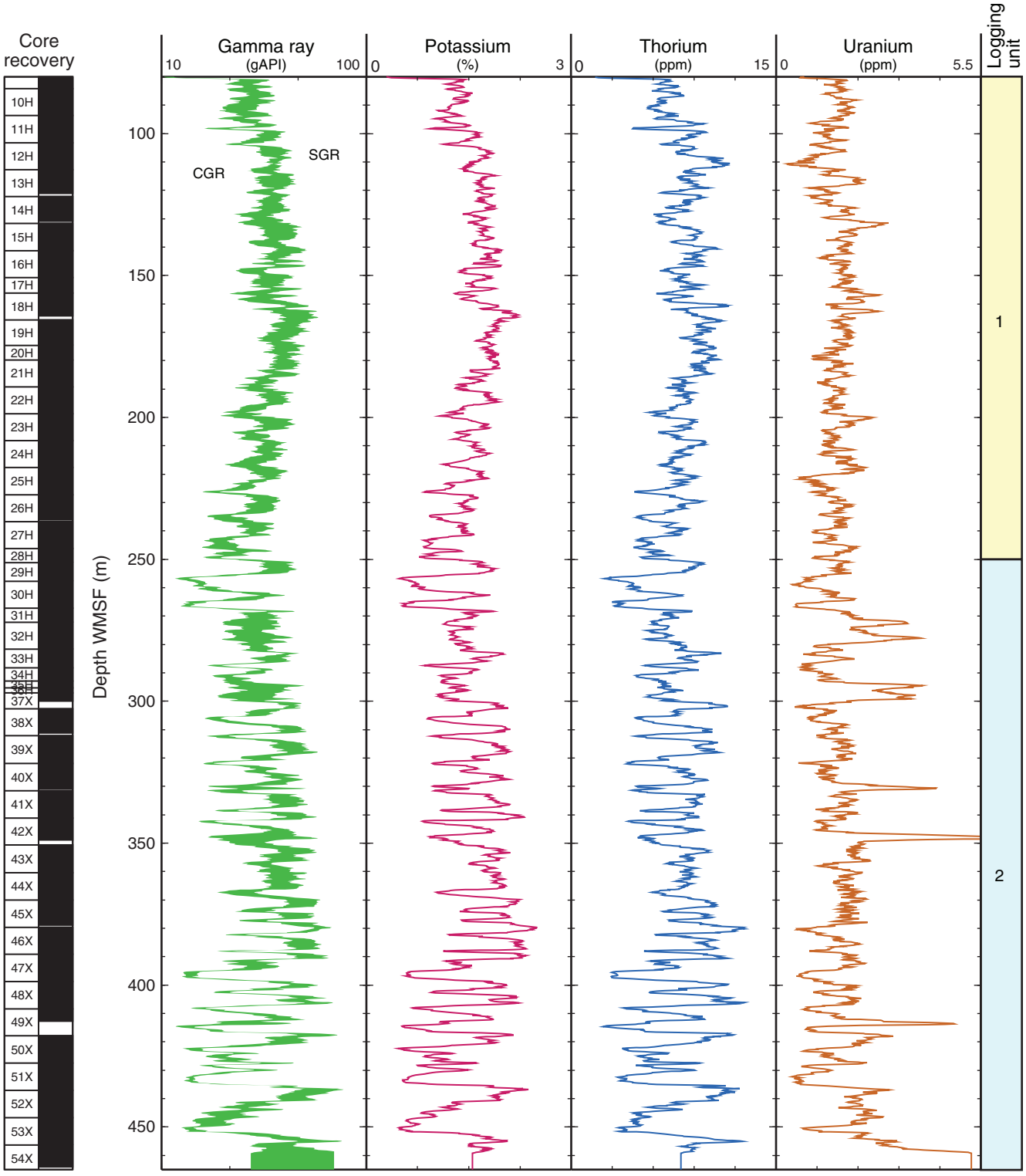

Figure F71. Comparison of logging data recorded in Holes U1352B and U1352C. Because no nuclear sources were used in Hole U1352C, the only comparable measurements are hole size from the HLDS caliper and data from the gamma ray, gamma ray spectroscopy, and resistivity logs.

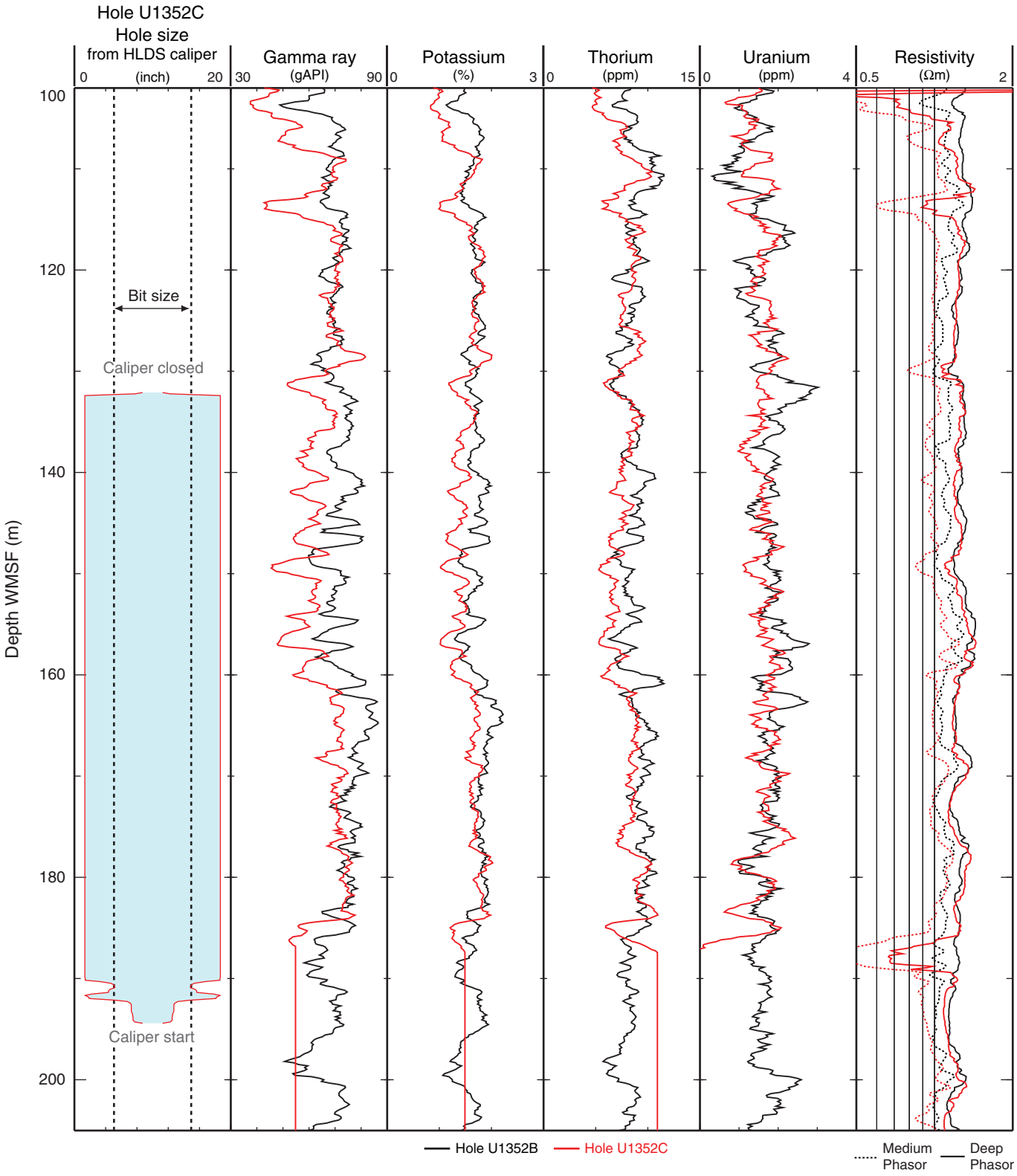

Figure F72. Formation MicroScanner (FMS) images and corresponding core photographs from Hole U1352B showing layers associated with high uranium, resistivity, and velocity in logging Unit 2. High resistivity is apparent as brighter colors in the FMS images. **A.** Dark greenish gray sandy calcareous mud and olive calcareous sandy marl (Sections 317-U1352B-35H-1, 35H-2, and 36H-1). **B.** Olive sandy marl (Sections 317-U1352B-36H-2, 37X-1, and 37X-2). **C.** Olive sandy mud with calcareous concretions (Sections 317-U1352B-42X-4 and 42X-5). Contrast in core photographs has been adjusted to enhance color variation. (**Figure shown on next page.**)

Figure F72 (continued). (Caption shown on previous page.)

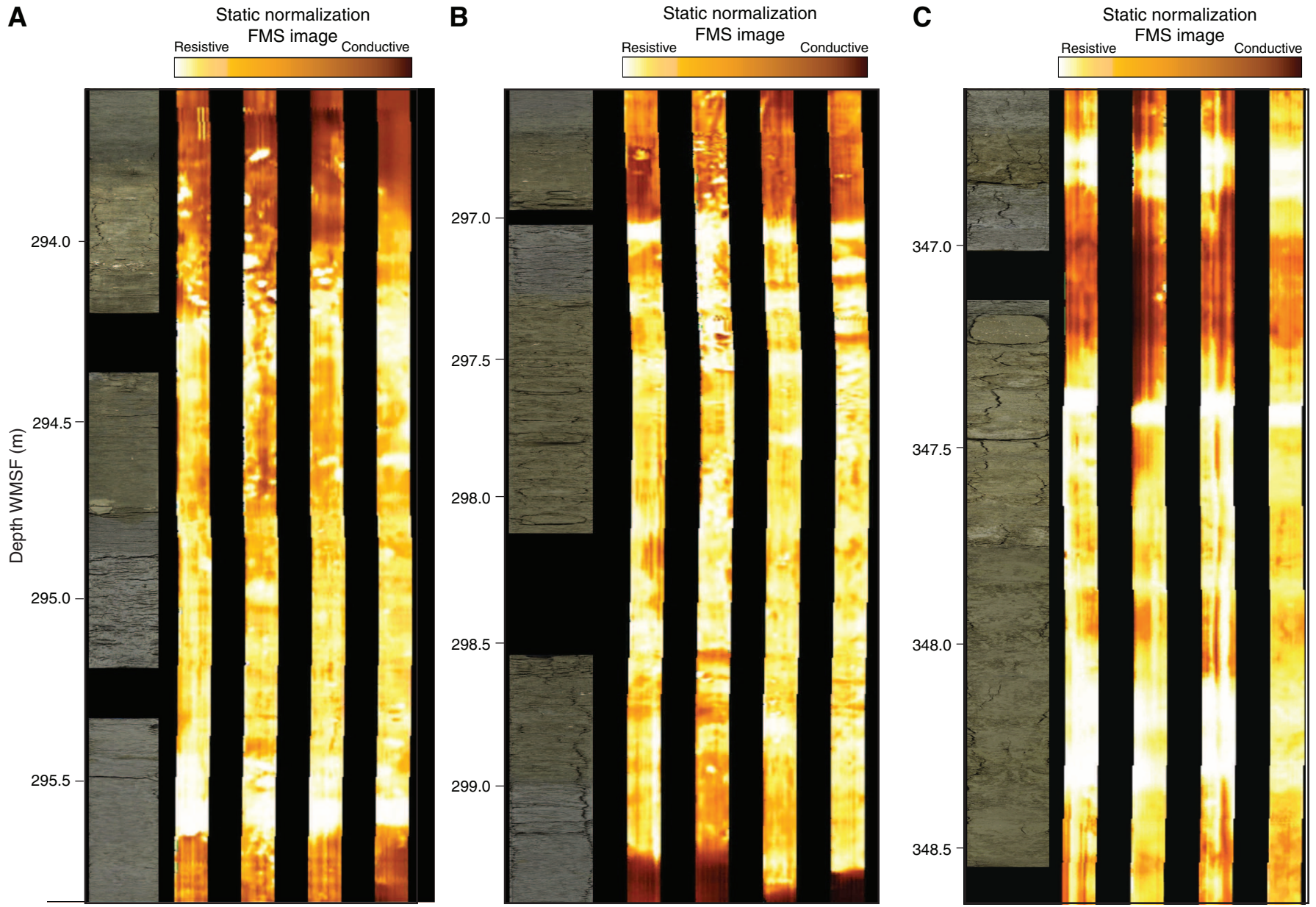

Figure F73. Comparison of synthetic seismogram calculated from density and V_P logs in Hole U1352B with EW00-01 Line 60 across Site U1352. The gamma ray log is shown as a reference to the other logs and logging units at this site. Density was computed from the resistivity log using Archie's equation and MAD grain density. The V_P log used in the calculation was recorded during the downlog. See **"Downhole logging"** for details. FMS = Formation MicroScanner-sonic tool string, TC = triple combination tool string. IDPH = phasor deep induction log. CDP = common depth point. (**Figure shown on next page.**)

Figure F73 (continued). (Caption shown on previous page.)

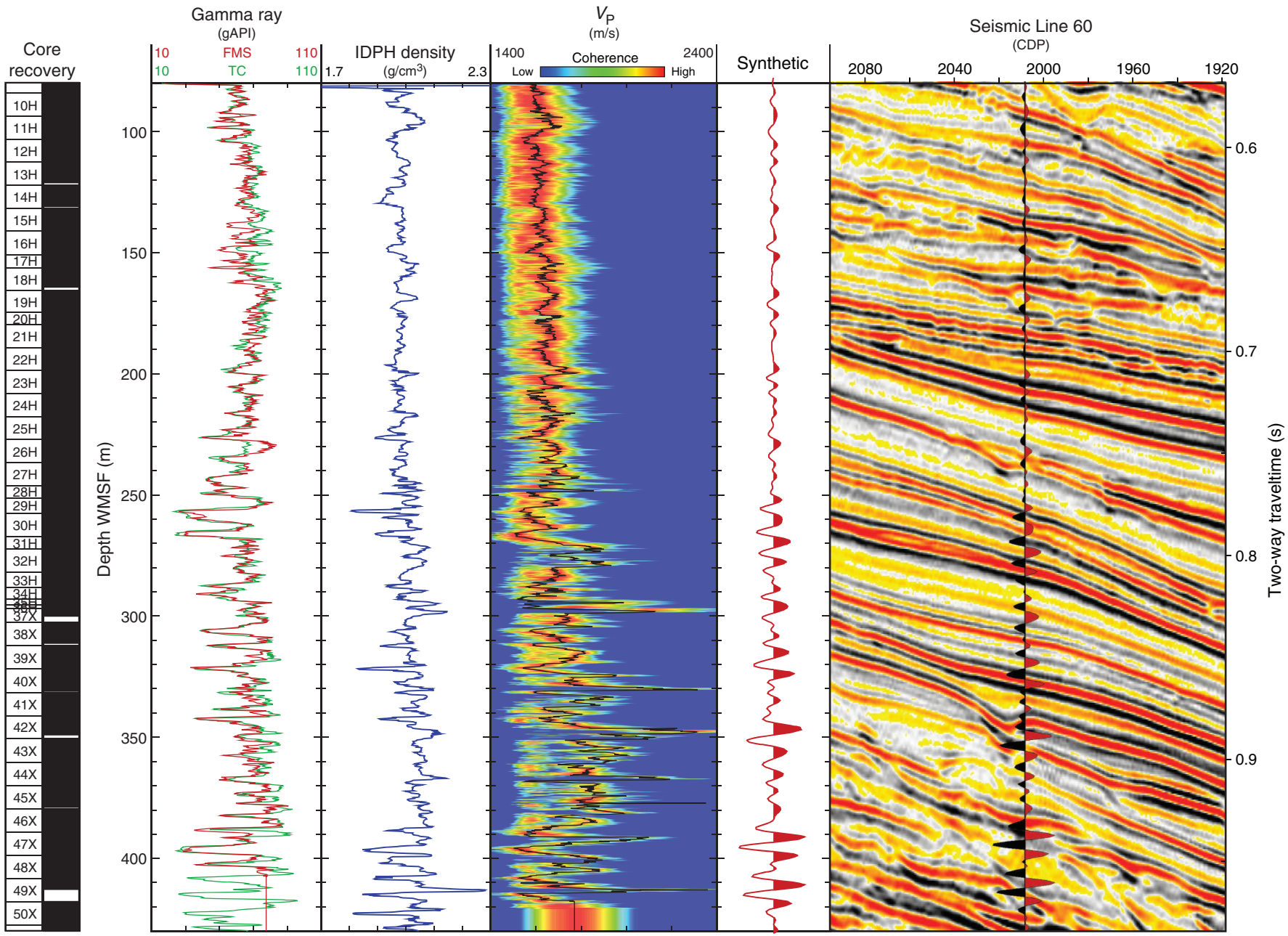

Figure F74. Comparison of velocity data and time vs. depth relationships between Site U1352, ODP Site 1119, the Clipper-1 well, and velocity models used to predict drilling targets during Expedition 317.

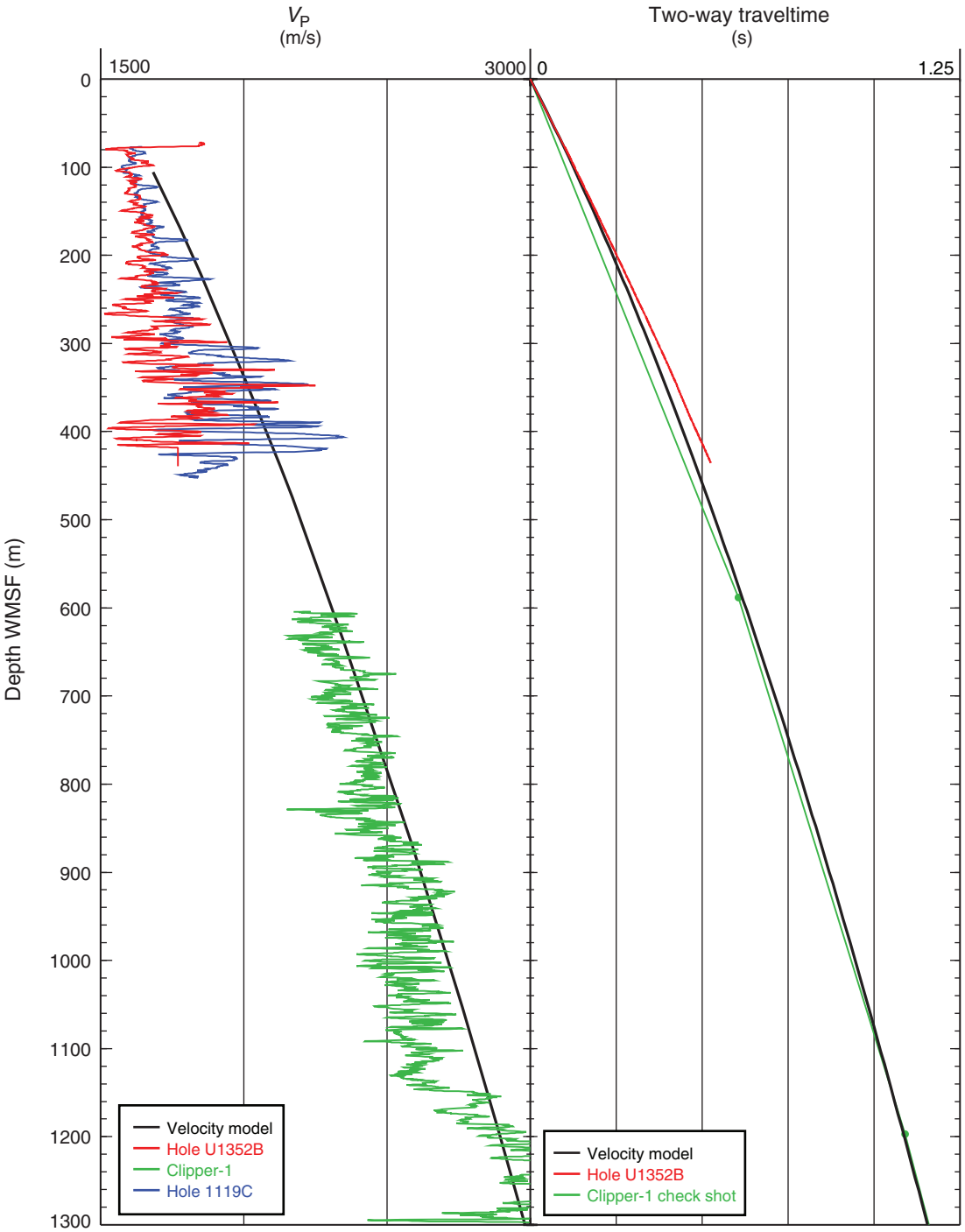

Figure F75. Depth-adjusted records and resultant splice of WRMSL magnetic susceptibility (loop sensor) measurements and natural gamma radiation (NGR) data for Holes U1352B and U1352D. Gaps in the records represent positions where depth adjustments have been made to correlate key features. Solid lines = key correlative horizons.

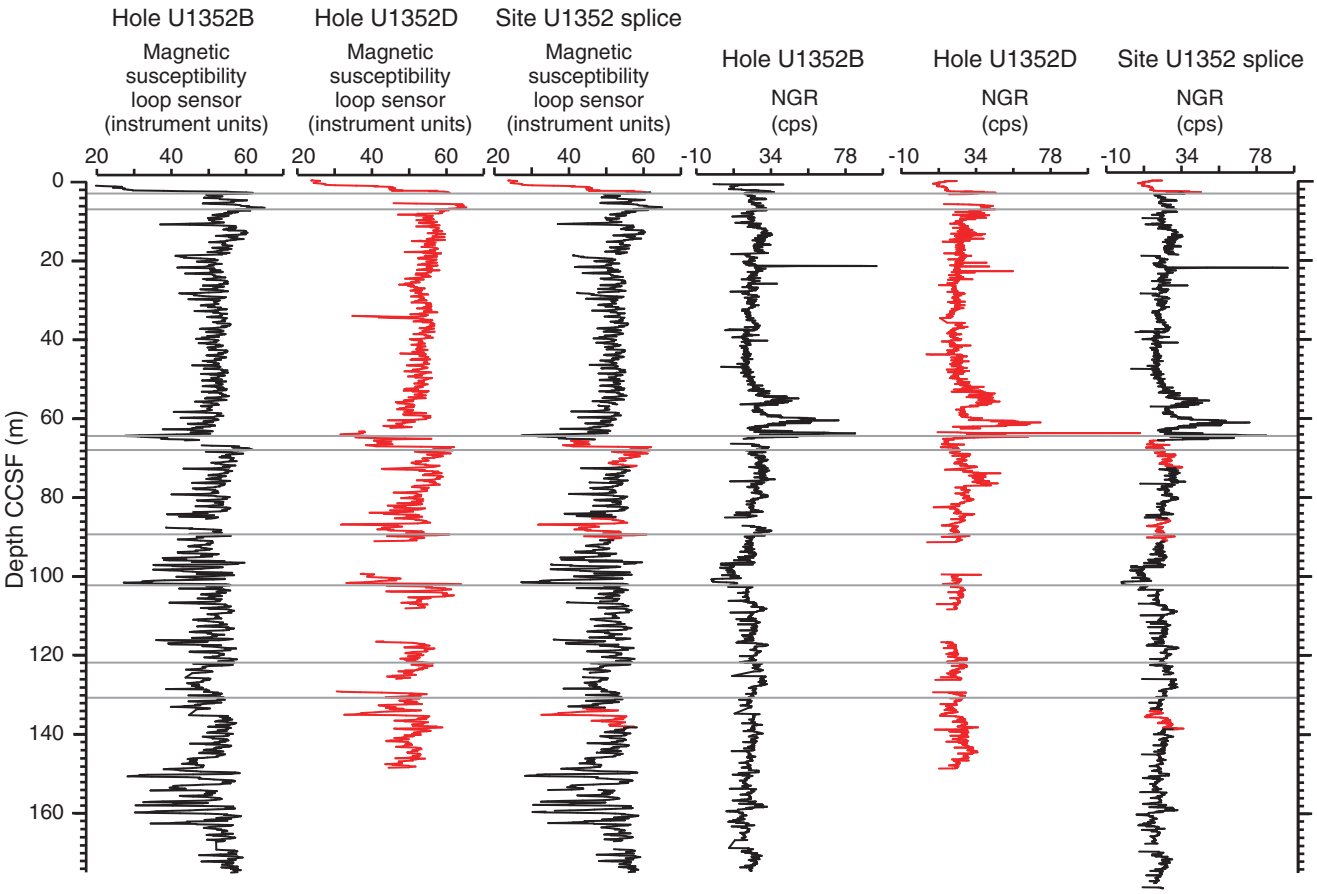

Table T1. Coring summary, Site U1352. (See table notes.) (Continued on next four pages.)

Hole U1352A
Latitude: 44°56.2440′S
Longitude: 172°1.3615′E
Time on hole (d): 0.16 (30 Nov, 1145 h–1530 h)
Seafloor (drill pipe measurement from rig floor, m DRF): 354.8 (APC mudline)
Distance between rig floor and sea level (m): 11.0
Water depth (drill pipe measurement from sea level, m): 343.8
Total depth (drill pipe measurement from rig floor, m DRF): 397.0
Total penetration (m DSF): 42.2
Total length of cored section (m): 42.2
Total core recovered (m): 43.92
Core recovery (%): 104
Total number of cores: 5

Hole U1352B
Latitude: 44°56.2558′S
Longitude: 172°1.3630′E
Time on hole (d): 5.03 (30 Nov, 1530 h–5 Dec, 1615)
Seafloor (drill pipe measurement from rig floor, m DRF): 354.6
Distance between rig floor and sea level (m): 11.0
Water depth (drill pipe measurement from sea level, m): 343.6
Total depth (drill pipe measurement from rig floor, m DRF): 1185.5
Total penetration (m DSF): 830.9
Total length of cored section (m): 830.9
Total core recovered (m): 613.87
Core recovery (%): 74
Total number of cores: 94

Hole U1352C
Latitude: 44°56.2662′S
Longitude: 172°1.3630′E
Time on hole (d): 15.07 (5 Dec, 2015 h–20 Dec, 2200 h)
Seafloor (drill pipe measurement from rig floor, m DRF): 354.5 (tagging seafloor)
Distance between rig floor and sea level (m): 11.0
Water depth (drill pipe measurement from sea level, m): 343.5
Total depth (drill pipe measurement from rig floor, m DRF): 2282.0
Total penetration (m DSF): 1927.5
Total length of cored section (m): 1296.4
Total core recovered (m): 655.02
Core recovery (%): 51
Total number of cores: 146

Hole U1352D
Latitude: 44°56.2326′S
Longitude: 172°1.3611′E
Time on hole (d): 0.61 (21 Dec, 0615 h–2100 h)
Seafloor (drill pipe measurement from rig floor, m DRF): 345.2 (APC mudline)
Distance between rig floor and sea level (m): 11.0
Water depth (drill pipe measurement from sea level, m): 344.2
Total depth (drill pipe measurement from rig floor, m DRF): 472.2
Total penetration (m DSF): 127.0
Total length of cored section (m): 127.0
Total core recovered (m): 130.84
Core recovery (%): 103
Total number of cores: 14

Core	Date (2009)	UTC (h)	Top of cored interval (m DSF)	Bottom of cored interval (m DSF)	Interval advanced (m)	Top of recovered cored (m CSF-A)	Bottom of recovered cored (m CSF-A)	Length of core recovered (m)	Recovery (%)
317-U1352A-									
1H	29 Nov	2255	0.0	4.2	4.2	0.0	4.26	4.26	101
2H	29 Nov	2335	4.2	13.7	9.5	4.2	13.72	9.52	100
3H	30 Nov	0025	13.7	23.2	9.5	13.7	23.15	9.45	99
4H	30 Nov	0125	23.2	32.7	9.5	23.2	33.48	10.28	108
5H	30 Nov	0155	32.7	42.2	9.5	32.7	43.11	10.41	110
				Advanced total:	42.2			43.92	104
				Total interval cored:	42.2				
317-U1352B-									
1H	30 Nov	0310	0.0	8.2	8.2	0	8.21	8.21	100
2H	30 Nov	0350	8.2	17.7	9.5	8.2	17.75	9.55	101
3H	30 Nov	0420	17.7	27.2	9.5	17.7	27.46	9.76	103
4H	30 Nov	0515	27.2	36.7	9.5	27.2	37.43	10.23	108

Table T1 (continued). (Continued on next page.)

Core	Date (2009)	UTC (h)	Top of cored interval (m DSF)	Bottom of cored interval (m DSF)	Interval advanced (m)	Top of recovered cored (m CSF-A)	Bottom of recovered cored (m CSF-A)	Length of core recovered (m)	Recovery (%)
5H	30 Nov	0605	36.7	46.2	9.5	36.7	46.75	10.05	106
6H	30 Nov	0650	46.2	55.7	9.5	46.2	55.81	9.61	101
7H	30 Nov	0720	55.7	65.2	9.5	55.7	64.97	9.27	98
8H	30 Nov	0750	65.2	74.7	9.5	65.2	75.39	10.19	107
9H	30 Nov	0820	74.7	84.2	9.5	74.7	84.27	9.57	101
10H	30 Nov	0920	84.2	93.7	9.5	84.2	94.17	9.97	105
11H	30 Nov	1005	93.7	103.2	9.5	93.7	103.79	10.09	106
12H	30 Nov	1030	103.2	112.7	9.5	103.2	113.03	9.83	103
13H	30 Nov	1110	112.7	122.2	9.5	112.7	121.12	8.42	89
14H	30 Nov	1150	122.2	131.7	9.5	122.2	130.91	8.71	92
15H	30 Nov	1250	131.7	141.2	9.5	131.7	141.75	10.05	106
16H	30 Nov	1340	141.2	150.7	9.5	141.2	150.84	9.64	101
17H	30 Nov	1420	150.7	156.2	5.5	150.7	156.15	5.45	99
18H	30 Nov	1640	156.2	165.7	9.5	156.2	163.80	7.60	80
19H	30 Nov	1735	165.7	174.7	9.0	165.7	174.39	8.69	97
20H	30 Nov	1850	174.7	179.7	5.0	174.7	180.43	5.73	115
21H	30 Nov	2110	179.7	189.2	9.5	179.7	189.47	9.77	103
22H	30 Nov	2155	189.2	198.7	9.5	189.2	199.13	9.93	105
23H	30 Nov	2240	198.7	208.2	9.5	198.7	208.72	10.02	105
24H	30 Nov	2310	208.2	217.7	9.5	208.2	218.01	9.81	103
25H	30 Nov	2340	217.7	227.2	9.5	217.7	227.63	9.93	105
26H	1 Dec	0005	227.2	236.7	9.5	227.2	236.05	8.85	93
27H	1 Dec	0040	236.7	246.2	9.5	236.7	246.13	9.43	99
28H	1 Dec	0145	246.2	251.2	5.0	246.2	250.91	4.71	94
29H	1 Dec	0230	251.2	257.7	6.5	251.2	257.45	6.25	96
30H	1 Dec	0320	257.7	267.2	9.5	257.7	267.21	9.51	100
31H	1 Dec	0415	267.2	272.2	5.0	267.2	272.49	5.29	106
32H	1 Dec	0540	272.2	281.7	9.5	272.2	281.55	9.35	98
33H	1 Dec	0645	281.7	288.2	6.5	281.7	288.22	6.52	100
34H	1 Dec	0940	288.2	292.9	4.7	288.2	292.91	4.71	100
35H	1 Dec	1025	292.9	295.3	2.4	292.9	295.29	2.39	100
36H	1 Dec	1125	295.3	297.0	1.7	295.3	297.06	1.76	104
37X	1 Dec	1230	297.0	302.6	5.6	297.0	299.92	2.92	52
38X	1 Dec	1355	302.6	312.2	9.6	302.6	311.14	8.54	89
39X	1 Dec	1550	312.2	321.9	9.7	312.2	321.90	9.70	100
40X	1 Dec	1630	321.9	331.5	9.6	321.9	330.89	8.99	94
41X	1 Dec	1700	331.5	341.1	9.6	331.5	341.33	9.83	102
42X	1 Dec	1745	341.1	350.7	9.6	341.1	348.92	7.82	81
43X	1 Dec	1815	350.7	360.4	9.7	350.7	360.44	9.74	100
44X	1 Dec	1930	360.4	370.0	9.6	360.4	370.21	9.81	102
45X	1 Dec	2025	370.0	379.6	9.6	370.0	378.88	8.88	93
46X	1 Dec	2115	379.6	389.2	9.6	379.6	389.47	9.87	103
47X	1 Dec	2150	389.2	398.7	9.5	389.2	399.03	9.83	103
48X	1 Dec	2230	398.7	408.3	9.6	398.7	408.43	9.73	101
49X	1 Dec	2315	408.3	417.9	9.6	408.3	412.69	4.39	46
50X	2 Dec	0040	417.9	427.5	9.6	417.9	427.54	9.64	100
51X	2 Dec	0120	427.5	437.1	9.6	427.5	437.17	9.67	101
52X	2 Dec	0200	437.1	446.7	9.6	437.1	446.90	9.8	102
53X	2 Dec	0230	446.7	456.3	9.6	446.7	456.09	9.39	98
54X	2 Dec	0315	456.3	465.9	9.6	456.3	464.08	7.78	81
55X	2 Dec	0355	465.9	475.5	9.6	465.9	470.11	4.21	44
56X	2 Dec	0425	475.5	485.1	9.6	475.5	485.64	10.14	106
57X	2 Dec	0555	485.1	494.7	9.6	485.1	492.17	7.07	74
58X	2 Dec	0635	494.7	504.3	9.6	494.7	504.67	9.97	104
59X	2 Dec	0730	504.3	513.9	9.6	504.3	507.48	3.18	33
60X	2 Dec	0820	513.9	523.5	9.6	513.9	514.99	1.09	11
61X	2 Dec	0900	523.5	533.1	9.6	523.5	525.74	2.24	23
62X	2 Dec	1000	533.1	542.7	9.6	533.1	542.97	9.87	103
63X	2 Dec	1130	542.7	552.2	9.5	542.7	552.61	9.91	104
64X	2 Dec	1220	552.2	561.8	9.6	552.2	557.67	5.47	57
65X	2 Dec	1330	561.8	571.4	9.6	561.8	562.72	0.92	10
66X	2 Dec	1505	571.4	572.7	1.3	571.4	572.68	1.28	98
67X	2 Dec	1620	572.7	581.1	8.4	572.7	573.67	0.97	12
68X	2 Dec	1705	581.1	590.7	9.6	581.1	583.96	2.86	30
69X	2 Dec	1750	590.7	600.3	9.6	590.7	591.18	0.48	5
70X	2 Dec	1855	600.3	609.9	9.6	600.3	601.53	1.23	13
71X	2 Dec	1945	609.9	619.5	9.6	609.9	614.93	5.03	52
72X	2 Dec	2120	619.5	629.1	9.6	619.5	626.63	7.13	74

Table T1 (continued). (Continued on next page.)

Core	Date (2009)	UTC (h)	Top of cored interval (m DSF)	Bottom of cored interval (m DSF)	Interval advanced (m)	Top of recovered cored (m CSF-A)	Bottom of recovered cored (m CSF-A)	Length of core recovered (m)	Recovery (%)
73X	2 Dec	2320	629.1	638.7	9.6	629.1	638.27	9.17	96
74X	3 Dec	0045	638.7	648.3	9.6	638.7	648.60	9.90	103
75X	3 Dec	0200	648.3	657.9	9.6	648.3	658.33	10.03	104
76X	3 Dec	0305	657.9	667.6	9.7	657.9	667.84	9.94	102
77X	3 Dec	0415	667.6	677.3	9.7	667.6	670.21	2.61	27
78X	3 Dec	0515	677.3	686.9	9.6	677.3	679.91	2.61	27
79X	3 Dec	0630	686.9	696.5	9.6	686.9	687.89	0.99	10
80X	3 Dec	0800	696.5	706.1	9.6	696.5	703.64	7.14	74
81X	3 Dec	1000	706.1	709.7	3.6	706.1	710.78	4.68	130
82X	3 Dec	1145	709.7	715.7	6.0	709.7	710.79	1.09	18
83X	3 Dec	1345	715.7	725.3	9.6	715.7	716.14	0.44	5
84X	3 Dec	1545	725.3	734.9	9.6	725.3	725.90	0.60	6
85X	3 Dec	1720	734.9	744.5	9.6	734.9	740.24	5.34	56
86X	3 Dec	1840	744.5	754.1	9.6	744.5	745.33	0.83	9
87X	3 Dec	1955	754.1	763.6	9.5	754.1	756.54	2.44	26
88X	3 Dec	2120	763.6	773.2	9.6	763.6	766.15	2.55	27
89X	3 Dec	2230	773.2	782.9	9.7	773.2	773.99	0.79	8
90X	4 Dec	0005	782.9	792.5	9.6	782.9	784.02	1.12	12
91X	4 Dec	0130	792.5	802.1	9.6	792.5	793.43	0.93	10
92X	4 Dec	0300	802.1	811.7	9.6	802.1	803.18	1.08	11
93X	4 Dec	0420	811.7	821.3	9.6	811.7	812.23	0.53	6
94X	4 Dec	0555	821.3	830.9	9.6	821.3	822.13	0.83	9
				Advanced total:	830.9			613.87	74
				Total interval cored:	830.9				
317-U1352C-									
1D	6 Dec	0605			***** Drilled from 0.0 to 574.7 m *****				
2R	6 Dec	0650	574.7	584.4	9.7	574.7	576.52	1.82	19
3R	6 Dec	0740	584.4	594.0	9.6	584.4	588.09	3.69	38
4R	6 Dec	0835	594.0	603.6	9.6	594.0	601.28	7.28	76
5D	6 Dec	1400			***** Drilled from 603.6 to 660.0 m *****				
6R	6 Dec	1525	660.0	669.6	9.6	660.0	661.21	1.21	13
7R	6 Dec	1635	669.6	679.3	9.7	669.6	671.34	1.74	18
8R	6 Dec	1730	679.3	689.0	9.7	679.3	680.29	0.99	10
9R	6 Dec	1815	689.0	698.7	9.7	689.0	690.08	1.08	11
10R	6 Dec	1915	698.7	708.4	9.7	698.7	701.05	2.35	24
11R	6 Dec	2000	708.4	718.1	9.7	708.4	709.78	1.38	14
12R	6 Dec	2100	718.1	727.8	9.7	718.1	719.51	1.41	15
13R	6 Dec	2200	727.8	737.5	9.7	727.8	728.98	1.18	12
14R	6 Dec	2255	737.5	747.2	9.7	737.5	740.19	2.69	28
15R	7 Dec	0000	747.2	756.9	9.7	747.2	749.82	2.62	27
16R	7 Dec	0050	756.9	766.6	9.7	756.9	759.43	2.53	26
17R	7 Dec	0150	766.6	776.3	9.7	766.6	769.75	3.15	32
18R	7 Dec	0250	776.3	786.0	9.7	776.3	779.92	3.62	37
19R	7 Dec	0410	786.0	795.7	9.7	786.0	788.99	2.99	31
20R	7 Dec	0510	795.7	805.4	9.7	795.7	798.36	2.66	27
21R	7 Dec	0600	805.4	815.0	9.6	805.4	807.40	2.00	21
22R	7 Dec	0650	815.0	824.6	9.6	815.0	817.52	2.52	26
23R	7 Dec	0800	824.6	834.2	9.6	824.6	826.58	1.98	21
24R	7 Dec	0905	834.2	843.8	9.6	834.2	836.84	2.64	28
25R	7 Dec	1010	843.8	853.4	9.6	843.8	846.27	2.47	26
26R	7 Dec	1018	853.4	863.0	9.6	853.4	855.34	1.94	20
27R	7 Dec	1155	863.0	872.6	9.6	863.0	864.99	1.99	21
28R	7 Dec	1325	872.6	882.2	9.6	872.6	875.46	2.86	30
29R	7 Dec	1430	882.2	891.8	9.6	882.2	884.96	2.76	29
30R	7 Dec	1530	891.8	901.3	9.5	891.8	894.42	2.62	28
31R	7 Dec	1645	901.3	910.9	9.6	901.3	905.53	4.23	44
32R	7 Dec	1740	910.9	920.5	9.6	910.9	913.08	2.18	23
33R	7 Dec	1945	920.5	930.1	9.6	920.5	926.36	5.86	61
34R	7 Dec	2040	930.1	939.7	9.6	930.1	934.58	4.48	47
35R	7 Dec	2135	939.7	949.4	9.7	939.7	944.50	4.80	49
36R	7 Dec	2300	949.4	959.0	9.6	949.4	953.54	4.14	43
37R	8 Dec	0020	959.0	968.5	9.5	959.0	964.44	5.44	57
38R	8 Dec	0200	968.5	978.1	9.6	968.5	978.54	10.04	105
39R	8 Dec	0320	978.1	987.7	9.6	978.1	987.79	9.69	101
40R	8 Dec	0425	987.7	997.3	9.6	987.7	992.23	4.53	47
41R	8 Dec	0600	997.3	1006.9	9.6	997.3	1005.00	7.70	80
42R	8 Dec	1620	1006.9	1016.5	9.6	1006.9	1011.74	4.84	50
43R	8 Dec	1745	1016.5	1026.1	9.6	1016.5	1019.74	3.24	34

Table T1 (continued). (Continued on next page.)

Core	Date (2009)	UTC (h)	Top of cored interval (m DSF)	Bottom of cored interval (m DSF)	Interval advanced (m)	Top of recovered cored (m CSF-A)	Bottom of recovered cored (m CSF-A)	Length of core recovered (m)	Recovery (%)
44R	8 Dec	1855	1026.1	1035.7	9.6	1026.1	1034.58	8.48	88
45R	8 Dec	2000	1035.7	1045.3	9.6	1035.7	1040.65	4.95	52
46R	8 Dec	2115	1045.3	1054.9	9.6	1045.3	1049.77	4.47	47
47R	8 Dec	2225	1054.9	1064.4	9.5	1054.9	1058.54	3.64	38
48R	8 Dec	2325	1064.4	1073.8	9.4	1064.4	1068.98	4.58	49
49R	9 Dec	0045	1073.8	1083.3	9.5	1073.8	1077.69	3.89	41
50R	9 Dec	0150	1083.3	1092.9	9.6	1083.3	1093.21	9.91	103
51R	9 Dec	0300	1092.9	1102.5	9.6	1092.9	1098.92	6.02	63
52R	9 Dec	0410	1102.5	1112.1	9.6	1102.5	1104.82	2.32	24
53R	9 Dec	0520	1112.1	1121.7	9.6	1112.1	1115.12	3.02	31
54R	9 Dec	0705	1121.7	1131.3	9.6	1121.7	1127.62	5.92	62
55R	9 Dec	0820	1131.3	1140.9	9.6	1131.3	1136.24	4.94	51
56R	9 Dec	0940	1140.9	1150.5	9.6	1140.9	1147.46	6.56	68
57R	9 Dec	1115	1150.5	1160.1	9.6	1150.5	1155.08	4.58	48
58R	9 Dec	1235	1160.1	1169.7	9.6	1160.1	1165.54	5.44	57
59R	9 Dec	1400	1169.7	1179.4	9.7	1169.7	1179.57	9.87	102
60R	9 Dec	1610	1179.4	1189.0	9.6	1179.4	1188.8	9.40	98
61R	9 Dec	1750	1189.0	1198.6	9.6	1189.0	1197.62	8.62	90
62R	9 Dec	1915	1198.6	1208.2	9.6	1198.6	1206.32	7.72	80
63R	9 Dec	2050	1208.2	1217.8	9.6	1208.2	1208.50	0.30	3
64R	9 Dec	2205	1217.8	1221.4	3.6	1217.8	1217.85	0.05	1
65R	10 Dec	0125	1221.4	1227.4	6.0	1221.4	1222.26	0.86	14
66R	10 Dec	0320	1227.4	1232.0	4.6	1227.4	1227.55	0.15	3
67R	10 Dec	0655	1232.0	1237.0	5.0	1232.0	1232.04	0.04	1
68R	10 Dec	0910	1237.0	1241.7	4.7	1237.0	1237.00	0.00	0
69R	10 Dec	1215	1241.7	1246.7	5.0	1241.7	1241.70	0.00	0
70R	10 Dec	1505	1246.7	1256.3	9.6	1246.7	1256.67	9.97	104
71R	10 Dec	1710	1256.3	1265.8	9.5	1256.3	1266.21	9.91	104
72R	10 Dec	1850	1265.8	1275.0	9.2	1265.8	1266.43	0.63	7
73R	10 Dec	2025	1275.0	1284.6	9.6	1275.0	1284.00	9.00	94
74R	10 Dec	2230	1284.6	1294.3	9.7	1284.6	1284.66	0.06	1
75R	11 Dec	0045	1294.3	1303.9	9.6	1294.3	1294.38	0.08	1
76R	11 Dec	0205	1303.9	1308.4	4.5	1303.9	1305.34	1.44	32
77R	11 Dec	0325	1308.4	1313.4	5.0	1308.4	1310.80	2.40	48
78R	11 Dec	0450	1313.4	1317.9	4.5	1313.4	1318.20	4.80	107
79R	11 Dec	0610	1317.9	1322.9	5.0	1317.9	1321.35	3.45	69
80R	11 Dec	0730	1322.9	1327.5	4.6	1322.9	1327.10	4.20	91
81R	11 Dec	0900	1327.5	1332.5	5.0	1327.5	1330.50	3.00	60
82R	11 Dec	1010	1332.5	1337.1	4.6	1332.5	1333.01	0.51	11
83R	11 Dec	1230	1337.1	1342.1	5.0	1337.1	1337.19	0.09	2
84R	11 Dec	1410	1342.1	1346.7	4.6	1342.1	1342.50	0.40	9
85R	11 Dec	1600	1346.7	1351.7	5.0	1346.7	1352.44	5.74	115
86R	11 Dec	1840	1351.7	1361.4	9.7	1351.7	1355.36	3.66	38
87R	11 Dec	2105	1361.4	1371.0	9.6	1361.4	1370.21	8.81	92
88R	11 Dec	2230	1371.0	1380.6	9.6	1371.0	1379.93	8.93	93
89R	12 Dec	0030	1380.6	1390.2	9.6	1380.6	1386.09	5.49	57
90R	12 Dec	0310	1390.2	1399.8	9.6	1390.2	1394.67	4.47	47
91R	12 Dec	0635	1399.8	1409.4	9.6	1399.8	1409.71	9.91	103
92R	12 Dec	0915	1409.4	1419.0	9.6	1409.4	1409.63	0.23	2
93R	12 Dec	1205	1419.0	1428.6	9.6	1419.0	1419.11	0.11	1
94R	12 Dec	1510	1428.6	1438.3	9.7	1428.6	1438.48	9.88	102
95R	12 Dec	1805	1438.3	1448.0	9.7	1438.3	1446.96	8.66	89
96R	12 Dec	2030	1448.0	1457.7	9.7	1448.0	1448.02	0.02	0
97R	12 Dec	2240	1457.7	1467.3	9.6	1457.7	1457.77	0.07	1
98R	13 Dec	0250	1467.3	1477.0	9.7	1467.3	1467.54	0.24	2
99R	13 Dec	0435	1477.0	1481.7	4.7	1477.0	1478.03	1.03	22
100R	13 Dec	0705	1481.7	1486.7	5.0	1481.7	1481.79	0.09	2
101R	13 Dec	1025	1486.7	1496.4	9.7	1486.7	1486.83	0.13	1
102R	13 Dec	1320	1496.4	1506.1	9.7	1496.4	1496.54	0.14	1
103R	13 Dec	1550	1506.1	1515.8	9.7	1506.1	1515.99	9.89	102
104R	13 Dec	1905	1515.8	1525.5	9.7	1515.8	1525.71	9.91	102
105R	13 Dec	2215	1525.5	1535.2	9.7	1525.5	1534.25	8.75	90
106R	14 Dec	0015	1535.2	1544.9	9.7	1535.2	1542.75	7.55	78
107R	14 Dec	0235	1544.9	1554.6	9.7	1544.9	1554.02	9.12	94
108R	14 Dec	0410	1554.6	1564.4	9.8	1554.6	1559.53	4.93	50
109R	14 Dec	0630	1564.4	1574.1	9.7	1564.4	1569.35	4.95	51
110R	14 Dec	0810	1574.1	1583.8	9.7	1574.1	1577.64	3.54	36
111R	14 Dec	1000	1583.8	1593.5	9.7	1583.8	1588.82	5.02	52

Table T1 (continued).

Core	Date (2009)	UTC (h)	Top of cored interval (m DSF)	Bottom of cored interval (m DSF)	Interval advanced (m)	Top of recovered cored (m CSF-A)	Bottom of recovered cored (m CSF-A)	Length of core recovered (m)	Recovery (%)
112R	14 Dec	1200	1593.5	1603.2	9.7	1593.5	1597.13	3.63	37
113R	14 Dec	1440	1603.2	1612.9	9.7	1603.2	1611.77	8.57	88
114R	14 Dec	1815	1612.9	1622.7	9.8	1612.9	1622.20	9.30	95
115R	14 Dec	2140	1622.7	1632.4	9.7	1622.7	1632.66	9.96	103
116R	15 Dec	0100	1632.4	1642.1	9.7	1632.4	1637.81	5.41	56
117R	15 Dec	0420	1642.1	1651.8	9.7	1642.1	1652.30	10.20	105
118R	15 Dec	0920	1651.8	1661.5	9.7	1651.8	1661.88	10.08	104
119R	15 Dec	2030	1661.5	1668.9	7.4	1661.5	1670.46	8.96	121
120R	15 Dec	2345	1668.9	1678.5	9.6	1668.9	1669.41	0.51	5
121R	16 Dec	0230	1678.5	1688.1	9.6	1678.5	1678.65	0.15	2
122R	16 Dec	0430	1688.1	1692.5	4.4	1688.1	1690.49	2.39	54
123R	16 Dec	0655	1692.5	1697.5	5.0	1692.5	1697.44	4.94	99
124R	16 Dec	1040	1697.5	1707.0	9.5	1697.5	1707.68	10.18	107
125R	16 Dec	1335	1707.0	1716.6	9.6	1707.0	1714.47	7.47	78
126R	16 Dec	1615	1716.6	1726.2	9.6	1716.6	1725.50	8.90	93
127R	16 Dec	1830	1726.2	1735.8	9.6	1726.2	1731.76	5.56	58
128R	16 Dec	2055	1735.8	1745.4	9.6	1735.8	1743.55	7.75	81
129R	16 Dec	2325	1745.4	1755.0	9.6	1745.4	1749.71	4.31	45
130R	17 Dec	0225	1755.0	1764.6	9.6	1755.0	1760.74	5.74	60
131R	17 Dec	0500	1764.6	1774.2	9.6	1764.6	1769.23	4.63	48
132R	17 Dec	0700	1774.2	1783.8	9.6	1774.2	1777.64	3.44	36
133R	17 Dec	0955	1783.8	1793.4	9.6	1783.8	1789.65	5.85	61
134R	17 Dec	1230	1793.4	1803.0	9.6	1793.4	1797.75	4.35	45
135R	17 Dec	1515	1803.0	1812.7	9.7	1803.0	1810.45	7.45	77
136R	17 Dec	1750	1812.7	1822.3	9.6	1812.7	1819.61	6.91	72
137R	17 Dec	2045	1822.3	1831.9	9.6	1822.3	1829.80	7.50	78
138R	17 Dec	2340	1831.9	1841.5	9.6	1831.9	1841.59	9.69	101
139R	18 Dec	0255	1841.5	1851.1	9.6	1841.5	1848.54	7.04	73
140R	18 Dec	0510	1851.1	1860.8	9.7	1851.1	1852.76	1.66	17
141R	18 Dec	0700	1860.8	1870.4	9.6	1860.8	1862.62	1.82	19
142R	18 Dec	0940	1870.4	1875.0	4.6	1870.4	1871.51	1.11	24
143R	18 Dec	1230	1875.0	1880.0	5.0	1875.0	1878.90	3.90	78
144R	18 Dec	1530	1880.0	1889.5	9.5	1880.0	1885.90	5.90	62
145R	18 Dec	1825	1889.5	1898.7	9.2	1889.5	1893.55	4.05	44
146R	18 Dec	2145	1898.7	1908.3	9.6	1898.7	1903.34	4.64	48
147R	19 Dec	0115	1908.3	1917.9	9.6	1908.3	1916.68	8.38	87
148R	19 Dec	0440	1917.9	1927.5	9.6	1917.9	1924.31	6.41	67
				Advanced total:	1296.4			655.02	51
				Total interval cored:	1927.5				
317-U1352D-									
1H	20 Dec	1740	0.0	3.5	3.5	0.0	3.60	3.60	103
2H	20 Dec	1835	3.5	13.0	9.5	3.5	13.37	9.87	104
3H	20 Dec	1915	13.0	22.5	9.5	13.0	22.38	9.38	99
4H	20 Dec	1950	22.5	32.0	9.5	22.5	32.65	10.15	107
5H	20 Dec	2040	32.0	41.5	9.5	32.0	42.03	10.03	106
6H	20 Dec	2125	41.5	51.0	9.5	41.5	51.31	9.81	103
7H	20 Dec	2220	51.0	60.5	9.5	51.0	60.82	9.82	103
8H	20 Dec	2325	60.5	70.0	9.5	60.5	70.05	9.55	101
9H	21 Dec	0030	70.0	79.5	9.5	70.0	79.85	9.85	104
10H	21 Dec	0120	79.5	89.0	9.5	79.5	88.97	9.47	100
11H	21 Dec	0215	89.0	98.5	9.5	89.0	98.28	9.28	98
12H	21 Dec	0315	98.5	108.0	9.5	98.5	108.60	10.10	106
13H	21 Dec	0400	108.0	117.5	9.5	108.0	117.77	9.77	103
14H	21 Dec	0450	117.5	127.0	9.5	117.5	127.66	10.16	107
				Advanced total:	127.0			130.84	103
				Total interval cored:	127.0				

Notes: APC = advanced piston corer. DRF = drilling depth below rig floor, DSF = drilling depth below seafloor, CSF-A = core depth below seafloor. UTC = Universal Time Coordinated.

Table T2. Lithostratigraphic summary, Site U1352. (See table note.)

Lith. unit	Age	Interval	Depth (m)	Lithologies (decreasing order of importance)
		317-		
IA	Holocene to Pleistocene	U1352A-1H though 5H (TD) U1352B-1H to 11H-4, 23 cm U1352D-1H to 11H-4, 13 cm	0–43.11 0–98.41 0–93.63	Mud, interbedded sand and mud, interbedded clay and mud, sandy mud, interbedded silt and mud, muddy sand
IB	Pleistocene	U1352B-11H-4, 23 cm, to 53X-1, 18 cm U1352D-11H-4, 13 cm, though 14H (TD)	98.41–446.88 93.63–127.66	Mud, marl, sandy mud, muddy sand, interbedded sand and mud
IC	Pleistocene to middle Pliocene	U1352B-53X-1, 18 cm, through 81X (base) U1352C-2R to 11R-1, 92 cm	574.70–709.32 446.88–710.78	Mud, marl, marlstone, sandy mud, muddy sand, muddy sandstone
IIA	middle Pliocene to early Pliocene	U1352B-81X (base) though 94X (TD) U1352C-11R-1, 92 cm, to 61R-1, 30 cm	710.78–822.13 709.32–1189.30	Marlstone, sandy mud, mud, muddy sand, marls, muddy sandstone, chalk
IIB	early Pliocene to late early Miocene	U1352C-61R-1, 30 cm, to 123R-1, 142 cm	1189.30–1693.92	Marlstone, marl, sandy mudstone, mudstone, muddy sandstone, very fine to fine sandstone, medium to coarse sandstone
IIC	early Miocene	U1352C-123R-1, 142 cm, to 140R-2, 47 cm	1693.92–1852.63	Limestone, marlstone, mudstone, very fine to fine sandstone
III	Oligocene to Eocene	U1352C-140R-2, 47 cm, to base 148R (TD)	1852.63–1924.31	Limestone, mudstone, chert

Note: TD = total depth.

Table T3. Lithologic surface types, Site U1352.

Type A		Type B		Type C
Contact depth (m)	Deposit thickness (m)	Contact depth (m)	Package thickness (m)	Contact depth (m)
1.6	1.6	26	16	207
64	2	34	2	217
84	1.5	98	6	220
114	1	148	2.5	447
200	1.3	159	3	476
250	6.5	331	2	514
282	4	348	1	557
299	1.2	428	5	614
453	6	1035	8	990
468	1.5	1095	11	1188
483	4.5	1113	1	1550
708	2	1263	2	1777
1279	2.9	1278	1	1852
1376	6	1390	10	
1440	3	1730	8	
1541	13			

Table T4. Lithologic surfaces and interpretation, Site U1352. (See table notes.)

Lithologic surface	Hole, core, section, interval (cm)	Depth CSF-A (m)	Overlying lithology	Nature of significant surface	Seismic sequence boundary	Predicted depth (m)	Preliminary biostratigraphy (Ma)
	317-						
U1352B-S1	U1352B-7H-6, 96	64.16	Muddy sand	Sharp basal contact burrowed	U19	68	<0.29 (CN), possibly <0.1 (CN)
U1352D-S1	U1352D-8H-3, 88	64.38	Muddy sand	Sharp basal contact burrowed	U19	68	
U1352B-S2	U1352B-16H-5, 5	147.22	Muddy sand	Sharp basal contact burrowed	U18	142	0.29–0.44 (CN)
U1352B-S3	U1352B-23H-1, 130	200.00	Muddy sand	Sharp basal contact burrowed	U17	195	0.44–0.91 (CN)
U1352B-S4	U1352B-28H-4, 7	250.20	Muddy sand	Sharp basal contact burrowed	U16	249	0.44–0.91 (CN)–0.91 at 266.92 m
U1352B-S5	U1352B-51X-1, 131	428.81	Sandy mud	Sharp basal contact	U15	428	1.56–1.69 (CN)
U1352B-S5.1	U1352B-53X-5, 30	453.00	Shelly sand	Sharp basal contact burrowed	U14	448	1.56–1.69 (CN)
U1352B-S6	U1352B-56X-5, 70	482.20	Sand	Sharp basal contact burrowed	U13	500	1.69–1.81 (CN)
U1352C-S9	U1352C-40R-3, 5	990.56	Limestone	Sharp scoured basal contact	U9	970	3.7 (CN)–4.3 (PF)
U1352C-S10	U1352C-53R-1, 90	1113.00	Calcareous shelly muddy sandstone	Sharp basal contact	U8	1136	3.7 (CN)–4.3 (PF)
U1352C-S11	U1352C-73R-4, 20	1279.70	Sandy marlstone	Sharp basal contact burrowed	U7	1251	4.49–5.30 (PF) Miocene/Pliocene boundary (5.3) picked between 1266.38–1283.95 m
U1352C-S12	U1352C-94R-7, 60	1438.20	Mass flow deposit	Sharp basal contact	U6	1428	10.58-10.91 (PF)
U1352C-S13	U1352C-140R-2, 48	1852.64	Rubble	Sharp contact with rubble layer above	MP	1824	Above UC at 1848.49 m, age is ~19; below UC at 1852.71 m, age is 30.1–32.0

Notes: CN = calcareous nannofossil, PF = planktonic foraminifer. UC = unconformity. MP = Marshall Paraconformity.

Table T5. Microfossil bioevents, Site U1352. This table is available in an oversized format.

Table T6. Calcareous nannofossil abundance, Site U1352. This table is available in an oversized format.

Table T7. Planktonic foraminifer and bolboformid summary, Hole U1352A. (See table notes.)

Core, section	Top depth CSF-A (m)	Interpreted age	NN zone	NZ stage correlation	NZ stage	Age (Ma)	Planktonic foraminifer (%)	Oceanicity	Key species and comments
317-U1352A-									
1H-1, 0	0.00	Holocene	NN21	Haweran (Wq)	Wq–uWc	0–1.1	78	Suboceanic	*Truncorotalia truncatulinoides, Globoconella inflata*; temperate
1H-CC	4.21	middle-late Pleistocene			Wq–uWc	0–1.1	68		*Truncorotalia truncatulinoides, Globoconella inflata*; temperate?
2H-CC	13.67				Wq–uWc	0–1.1	79		*Truncorotalia truncatulinoides, Globoconella inflata*; cold
3H-CC	23.10				Wq–uWc	0–1.1	77		*Truncorotalia truncatulinoides, Globoconella inflata*; cold
4H-CC	33.43				Wq–uWc	0–1.1	65		*Truncorotalia truncatulinoides, Globoconella inflata*; cold?
5H-CC	43.06				Wq–uWo	0–4.3	83		*Globoconella inflata*; cold

Notes: For New Zealand (NZ) stage abbreviations, see Figure F5 in the "Methods" chapter. This table is also available in ASCII.

Table T8. Planktonic foraminifer and bolboformid summary, Hole U1352B. This table is available in an **oversized format.**

Table T9. Planktonic foraminifer and bolboformid summary, Hole U1352C. This table is available in an **oversized format.**

Table T10. Planktonic foraminifer and bolboformid summary, Hole U1352D. (**See table notes.**)

Core, section, interval (cm)	Top depth CSF-A (m)	Interpreted age	NN zone	NZ stage correlation	NZ stage	Age (Ma)	Planktonic foraminifer (%)	Oceanicity	Key species and comments
317-U1352D-									
1H-1, 0	0.00	Holocene	NN21a	Haweran (Wq)	Wq–uWc	0–1.1	66	Suboceanic	*Truncorotalia truncatulinoides* (11S:0D), *Globoconella inflata;* [Holocene; 1.2 m thick (inferred from lithostratigraphy data)]
1H-CC	3.55	Pleistocene			Wq	0–0.34	56	Extraneritic	*Truncorotalia truncatulinoides* (0S:1D), *Globoconella inflata,* [*Loxostomum karrerianum,* 0–0.34 Ma]
2H-CC	13.32				Wq–uWc	0–1.1	72	Suboceanic	*Truncorotalia truncatulinoides* (5S:1D), *Globoconella inflata*
3H-CC	22.33				Wq–uWo	0–4.3	64		*Globoconella inflata*
4H-CC	32.60				Wq–uWc	0–1.1	70		*Truncorotalia truncatulinoides* (3S:0D), *Globoconella inflata*
5H-CC	41.98				Wq–uWc	0–1.1	86		*Truncorotalia truncatulinoides* (7S:0D), *Globoconella inflata*
6H-CC	51.26				Wq–uWc	0–1.1	81		*Truncorotalia truncatulinoides* (1S:0D), *Globoconella inflata*
7H-CC	60.32				Wq–uWc	0–1.1	55	Extraneritic	*Truncorotalia truncatulinoides* (4S:0D), *Globoconella inflata*
8H-CC	70.00				Wq–uWc	0–1.1	82	Suboceanic	*Truncorotalia truncatulinoides* (11S:0D), *Globoconella inflata, Globigerinella aequilateralis*?
9H-CC	79.80				Wq–uWc	0–1.1	80		*Truncorotalia truncatulinoides* (2S:0D), *Globoconella inflata*
10H-CC	88.92				Wq–uWc	0–1.1	63		*Truncorotalia truncatulinoides* (4S:0D), *Globoconella inflata*
11H-CC	98.23				Wq–uWc	0–1.1	80		*Truncorotalia truncatulinoides* (3S:0D), *Globoconella inflata*
12H-CC	108.55				Wq–Wn	0–2.4?	56	Extraneritic	*Truncorotalia crassula*?, *Globoconella inflata*
13H-CC	117.72				Wq–uWc	0–1.1	62	Suboceanic	*Truncorotalia truncatulinoides* (10S:0D), *Globoconella* cf. *puncticuloides, Globoconella inflata*
14H-CC	127.61				Wq	0–0.34	74		*Hirsutella hirsuta, Truncorotalia crassula*?, *Truncorotalia truncatulinoides* (2S:0D), *Globoconella inflata*

Notes: For New Zealand (NZ) stage abbreviations, see Figure **F5** in the "Methods" chapter. This table is also available in **ASCII**.

Table T11. Planktonic foraminifer and bolboformid distribution and microfossil abundance and preservation, Hole U1352A. This table is available in an **oversized format.**

Table T12. Planktonic foraminifer and bolboformid distribution and microfossil abundance and preservation, Hole U1352B. This table is available in an **oversized format.**

Table T13. Planktonic foraminifer and bolboformid distribution and microfossil abundance and preservation, Hole U1352C. This table is available in an **oversized format.**

Table T14. Planktonic foraminifer and bolboformid distribution and microfossil abundance and preservation, Hole U1352D. This table is available in an **oversized format.**

Table T15. Benthic foraminifer abundance, preservation, and distribution, Site U1352. This table is available in an **oversized format.**

Table T16. Diatom abundance, preservation, and distribution, Site U1352. This table is available in an **oversized format.**

Table T17. Invertebrate macrofossils. This table is available in an **oversized format.**

Table T18. Headspace gas composition from sediments, Site U1352. (See table note.) (Continued on next three pages.)

Core, section interval (cm)	Depth CSF-A (m)	C_1 (ppmv)	C_2 (ppmv)	$C_{2=}$ (ppmv)	C_3 (ppmv)	C_1 (mM)	C_1/C_2	$C_2/(C_2 + C_{2=})$ (%)
317-U1352A-								
1H-2, 0	1.50	0	0.0	0.00	0.00	0.000	ND	ND
1H-3, 0	3.00	0	0.0	0.00	0.00	0.000	ND	ND
2H-2, 0	5.70	0	0.0	0.00	0.00	0.000	ND	ND
2H-3, 0	7.20	0	0.0	0.00	0.00	0.000	ND	ND
2H-4, 0	8.70	0	0.0	0.00	0.00	0.000	ND	ND
2H-6, 0	11.70	15	0.0	0.00	0.00	0.003	ND	ND
3H-2, 0	15.20	61	0.0	0.00	0.00	0.018	ND	ND
3H-4, 0	18.20	25,494	2.0	0.00	0.00	7.648	16,914	100.0
3H-6, 0	21.20	35,792	2.0	0.00	0.00	10.738	15,882	100.0
4H-2, 0	24.70	53,436	4.0	0.00	0.00	16.031	15,058	100.0
4H-4, 0	27.70	55,636	3.0	0.00	0.00	16.691	16,100	100.0
4H-6, 0	30.70	42,035	3.0	0.00	0.00	12.610	13,484	100.0
5H-2, 0	34.20	26,854	2.0	0.00	0.00	8.056	13,735	100.0
5H-4, 0	37.70	24,874	2.0	0.00	0.00	7.462	14,092	100.0
5H-6, 0	40.20	14,588	1.0	0.00	0.00	4.376	15,863	100.0
317-U1352B-								
5H-8, 0	45.42	26,151	3.0	0.00	0.00	ND	9,562	100.0
6H-3, 0	49.20	36,924	4.0	0.00	0.00	ND	10,044	100.0
6H-5, 0	52.20	7,583	1.0	0.00	0.00	ND	11,855	100.0
7H-3, 0	58.70	81,015	6.0	0.00	0.00	ND	12,542	100.0
7H-5, 0	61.70	7,154	1.0	0.00	0.00	ND	8,257	100.0
8H-3, 0	68.20	40,972	6.0	0.00	0.00	ND	6,393	100.0
8H-5, 0	71.20	7,944	1.0	0.00	0.00	ND	5,595	100.0
9H-3, 0	77.70	9,221	2.0	0.00	0.00	ND	4,627	100.0
9H-5, 0	80.70	9,560	2.0	0.00	0.00	ND	4,567	100.0
10H-3, 0	85.96	17,014	3.0	0.00	0.00	ND	4,984	100.0
10H-5, 0	88.96	97,557	15.0	0.00	0.00	ND	6,431	100.0
11H-3, 0	96.70	3,799	0.0	0.00	0.00	ND	24,964	100.0
12H-3, 0	106.16	68,756	13.0	0.00	0.00	ND	5,210	100.0
13H-3, 0	115.68	12,224	3.0	0.00	0.00	ND	3,891	100.0
14H-3, 0	125.20	14,603	5.0	0.00	0.00	ND	3,056	100.0
15H-3, 0	134.63	10,296	3.0	0.00	0.00	ND	3,359	100.0
16H-3, 0	144.17	4,705	1.0	0.00	0.00	ND	4,931	100.0
18H-3, 0	159.20	13,452	5.0	0.00	0.00	ND	2,703	100.0
19H-3, 0	168.70	7,305	2.0	0.00	0.00	ND	3,513	100.0
21H-6, 0	187.20	8,165	3.0	0.00	0.00	ND	2,460	100.0
22H-3, 0	192.20	7,417	3.0	0.00	0.00	ND	2,269	100.0
23H-4, 0	203.20	6,353	2.0	0.00	0.00	ND	2,744	100.0
24H-4, 0	212.70	13,307	7.0	0.00	0.00	ND	2,011	100.0
25H-4, 0	222.20	30,961	15.0	0.00	0.00	ND	2,000	100.0
26H-4, 0	231.62	7,464	6.0	0.00	0.00	ND	1,346	100.0
27H-4, 0	241.20	12,611	7.0	0.00	0.00	ND	1,802	100.0
28H-3, 0	249.13	15,172	8.0	0.00	0.00	ND	1,805	100.0
29H-3, 0	254.20	20,873	11.0	0.00	0.00	ND	1,872	100.0
30H-4, 0	262.20	42,306	19.0	0.00	0.00	ND	2,273	100.0
31H-2, 0	268.70	17,785	11.0	0.00	0.00	ND	1,656	100.0
32H-4, 0	276.70	128,320	56.0	0.00	0.00	ND	2,292	100.0
33H-5, 0	286.14	7,080	6.0	0.00	0.00	ND	1,287	100.0
34H-3, 0	289.89	7,084	6.0	0.00	0.00	ND	1,172	100.0
35H-2, 0	294.34	5,273	3.0	0.00	0.00	ND	1,772	100.0
37X-2, 0	298.50	6,651	5.0	0.00	0.00	ND	1,268	100.0
38X-3, 0	305.60	6,301	7.0	0.00	0.00	ND	938	100.0
39X-4, 0	316.70	5,960	6.0	0.00	0.00	ND	974	100.0
40X-3, 0	324.90	8,172	8.0	0.00	0.00	ND	1,046	100.0
41X-4, 0	336.00	7,148	8.0	0.00	2.60	ND	901	100.0
42X-3, 115	345.25	48,623	32.0	0.00	1.30	ND	1,512	100.0
43X-3, 0	353.70	5,483	6.0	0.00	0.90	ND	985	100.0
44X-4, 0	364.90	10,832	9.0	0.00	0.00	ND	1,245	100.0
45X-4, 0	374.50	6,890	10.0	0.00	0.00	ND	705	100.0
46X-4, 0	384.08	10,472	11.0	0.00	0.00	ND	926	100.0
47X-4, 0	393.70	11,307	11.0	0.00	0.00	ND	1,006	100.0
48X-4, 0	403.20	27,242	31.0	0.00	2.63	ND	879	100.0
49X-2, 0	409.80	8,649	10.0	0.00	0.00	ND	871	100.0
50X-4, 0	422.40	12,184	20.0	0.19	4.53	ND	616	99.1
51X-4, 0	432.00	21,641	30.0	0.26	4.72	ND	732	99.1
52X-4, 0	441.60	11,991	15.0	0.00	2.66	ND	817	100.0

Table T18 (continued). (Continued on next page.)

Core, section interval (cm)	Depth CSF-A (m)	C_1 (ppmv)	C_2 (ppmv)	$C_{2=}$ (ppmv)	C_3 (ppmv)	C_1 (mM)	C_1/C_2	$C_2/(C_2 + C_{2=})$ (%)
53X-4, 0	451.20	6,579	6.0	0.00	0.00	ND	1,106	100.0
54X-4, 0	460.80	4,880	8.0	0.00	0.96	ND	602	100.0
55X-2, 0	467.40	6,623	10.0	0.57	2.03	ND	648	94.8
56X-4, 0	480.00	25,963	25.0	0.00	4.18	ND	1,025	100.0
57X-3, 0	488.10	25,570	27.0	0.00	4.04	ND	961	100.0
58X-5, 0	499.42	13,012	17.0	0.00	2.19	ND	787	100.0
59X-2, 0	505.80	13,628	17.0	0.00	2.07	ND	816	100.0
61X-2, 0	524.50	9,095	15.0	0.00	3.17	ND	627	100.0
62X-4, 0	537.60	9,569	15.0	0.00	3.07	ND	652	100.0
63X-4, 0	547.20	7,234	10.0	0.00	1.09	ND	730	100.0
64X-3, 0	555.20	6,224	9.0	0.00	1.77	ND	664	100.0
68X-2, 0	581.10	11,330	16.0	0.00	3.20	ND	703	100.0
71X-3, 0	612.90	6,502	9.0	0.00	1.86	ND	686	100.0
72X-3, 0	622.47	5,582	9.0	0.00	1.49	ND	607	100.0
73X-4, 0	633.60	26,614	42.0	0.00	12.48	ND	636	100.0
74X-4, 0	643.20	11,395	17.0	0.00	4.87	ND	657	100.0
75X-4, 0	652.80	7,364	17.0	0.00	6.44	ND	433	100.0
76X-4, 0	662.40	21,834	30.0	0.00	9.69	ND	722	100.0
77X-2, 0	669.10	10,013	19.0	0.00	7.80	ND	539	100.0
78X-2, 0	678.80	7,445	14.0	0.00	6.79	ND	538	100.0
79X-1, 51	687.41	4,523	11.0	0.53	8.11	ND	423	95.3
81X-3, 0	709.10	12,034	19.0	0.00	5.12	ND	643	100.0
85X-3, 0	737.90	6,292	13.0	0.00	7.82	ND	468	100.0
87X-1, 0	755.35	5,706	11.0	0.00	6.82	ND	531	100.0
88X-2, 0	765.10	7,367	17.0	0.00	12.21	ND	437	100.0
90X-1, 51	783.41	12,780	27.0	0.00	20.43	ND	471	100.0
317-U1352C-								
3R-3, 0	587.10	1,539	4.0	0.48	0.23	ND	376	89.4
6R-1, 0	660.80	10,742	16.0	0.00	4.99	ND	683	100.0
7R-2, 0	670.26	6,056	9.0	0.00	3.71	ND	638	100.0
8R-1, 49	679.79	12,729	16.0	0.00	5.28	ND	803	100.0
9R-1, 79	689.79	3,675	7.0	0.00	3.05	ND	543	100.0
10R-2, 145	700.79	5,874	10.0	0.00	4.97	ND	584	100.0
11R-1, 72	709.12	11,124	17.0	0.00	7.11	ND	645	100.0
12R-1, 130	719.40	5,817	13.0	0.00	8.43	ND	464	100.0
13R-1, 105	728.85	2,690	5.0	0.00	2.97	ND	539	100.0
14R-2, 79	739.79	11,821	27.0	0.00	21.54	ND	431	100.0
15R-2, 102	749.58	5,593	13.0	0.00	9.42	ND	436	100.0
16R-2, 0	758.27	2,201	3.0	0.00	1.66	ND	687	100.0
17R-2, 0	768.07	6,361	15.0	0.00	11.26	ND	437	100.0
18R-3, 87	779.68	3,851	8.0	0.00	6.06	ND	501	100.0
19R-2, 0	787.50	10,336	31.0	0.00	31.38	ND	330	100.0
20R-2, 0	797.09	3,310	10.0	0.00	9.42	ND	337	100.0
21R-2, 0	806.80	7,071	15.0	0.00	12.21	ND	459	100.0
22R-2, 0	816.42	9,388	26.0	0.00	24.39	ND	361	100.0
23R-2, 0	825.60	756	1.0	0.00	0.00	ND	516	100.0
24R-2, 0	835.63	12,979	31.0	0.00	23.53	ND	418	100.0
25R-2, 0	845.30	4,490	13.0	0.00	12.03	ND	344	100.0
26R-2, 70	855.28	1,718	5.0	0.00	4.24	ND	345	100.0
27R-2, 56	864.56	6,285	18.0	0.00	14.26	ND	353	100.0
28R-1, 126	873.86	9,454	27.0	0.00	22.03	ND	344	100.0
29R-2, 0	883.23	5,046	16.0	0.00	13.58	ND	322	100.0
30R-1, 148	893.28	2,543	10.0	0.00	12.62	ND	261	100.0
31R-1, 124	902.54	6,316	21.0	0.00	21.11	ND	303	100.0
32R-1, 120	912.10	3,173	13.0	0.00	16.80	ND	243	100.0
33R-3, 0	923.25	5,267	23.0	0.00	25.42	ND	228	100.0
34R-2, 0	931.17	3,604	15.0	0.00	15.33	ND	236	100.0
35R-2, 0	941.20	4,132	17.0	0.00	14.89	ND	250	100.0
36R-3, 0	952.40	993	7.0	0.00	6.20	ND	145	100.0
37R-3, 115	962.81	2,284	12.0	0.00	9.28	ND	184	100.0
38R-4, 0	973.00	6,013	31.0	0.00	28.96	ND	195	100.0
39R-5, 0	984.10	2,687	20.0	0.00	21.97	ND	136	100.0
40R-2, 0	989.01	6,032	33.0	0.00	32.95	ND	181	100.0
41R-5, 0	1003.30	7,078	47.0	0.00	60.72	ND	151	100.0
42R-4, 0	1010.94	1,047	5.0	0.00	5.19	ND	210	100.0
43R-2, 0	1017.93	2,555	18.0	0.00	20.34	ND	144	100.0
44R-3, 0	1029.10	3,972	27.0	0.00	31.04	ND	148	100.0
45R-2, 0	1037.11	1,342	9.0	0.00	12.07	ND	153	100.0
46R-2, 148	1048.22	998	7.0	0.00	11.08	ND	134	100.0

Table T18 (continued). (Continued on next page.)

Core, section interval (cm)	Depth CSF-A (m)	C_1 (ppmv)	C_2 (ppmv)	$C_{2=}$ (ppmv)	C_3 (ppmv)	C_1 (mM)	C_1/C_2	$C_2/(C_2 + C_{2=})$ (%)
47R-2, 0	1056.18	1,587	13.0	0.00	16.37	ND	124	100.0
48R-2, 0	1065.88	1,818	17.0	0.00	23.36	ND	108	100.0
49R-3, 0	1076.77	2,480	18.0	0.00	22.36	ND	138	100.0
50R-6, 0	1092.25	449	7.0	0.00	13.08	ND	62	100.0
51R-3, 145	1097.32	2,585	23.0	0.00	29.40	ND	110	100.0
52R-2, 0	1103.90	4,579	39.0	0.00	38.56	ND	118	100.0
53R-2, 0	1113.54	1,684	17.0	0.00	19.58	ND	98	100.0
54R-4, 0	1126.18	3,135	30.0	0.00	31.54	ND	104	100.0
55R-4, 0	1135.50	3,453	40.0	0.00	47.44	ND	86	100.0
56R-4, 0	1145.28	384	9.0	0.00	17.24	ND	42	100.0
57R-2, 149	1153.49	1,590	20.0	0.00	23.72	ND	80	100.0
58R-5, 0	1164.57	913	13.0	0.00	16.34	ND	72	100.0
59R-7, 0	1178.70	5,057	63.0	0.00	64.03	ND	80	100.0
60R-4, 0	1183.90	3,193	40.0	0.00	38.36	ND	79	100.0
61R-4, 0	1193.50	4,052	54.0	0.00	54.66	ND	74	100.0
62R-3, 0	1201.60	2,908	44.0	0.00	49.65	ND	66	100.0
63R-CC, 0	1208.20	3,376	58.0	0.00	69.87	ND	58	100.0
65R-1, 0	1221.40	3,629	60.0	0.00	64.19	ND	60	100.0
70R-4, 0	1251.03	1,747	17.0	0.00	10.25	ND	101	100.0
71R-3, 0	1259.30	2,238	38.0	0.00	31.51	ND	59	100.0
72R-1, 0	1265.80	3,195	62.0	0.00	56.90	ND	52	100.0
73R-3, 0	1278.00	1,990	39.0	0.00	31.95	ND	52	100.0
76R-1, 107	1304.97	1,331	33.0	0.00	30.19	ND	41	100.0
77R-1, 145	1309.85	420	10.0	0.00	9.47	ND	42	100.0
78R-2, 145	1316.29	518	13.0	0.00	9.43	ND	41	100.0
79R-1, 145	1319.35	719	17.0	0.00	12.93	ND	42	100.0
80R-2, 145	1325.85	145	4.0	0.00	3.29	ND	40	100.0
81R-2, 0	1329.00	68	3.0	0.00	2.57	ND	23	100.0
82R-1, 41	1332.91	358	8.0	0.00	5.06	ND	45	100.0
84R-CC, 5	1342.15	240	9.0	0.00	8.06	ND	27	100.0
85R-3, 149	1351.19	369	9.0	0.00	2.94	ND	39	100.0
86R-2, 0	1353.16	224	7.0	0.00	2.76	ND	34	100.0
87R-5, 0	1367.40	68	3.0	0.00	0.49	ND	20	100.0
88R-4, 0	1375.50	116	8.0	0.00	0.76	ND	14	100.0
89R-4, 0	1384.89	42	6.0	0.00	0.00	ND	7	100.0
90R-3, 0	1393.20	49	6.0	0.00	0.00	ND	9	100.0
91R-5, 0	1405.70	78	4.0	0.00	0.00	ND	21	100.0
94R-6, 0	1436.10	551	14.0	0.00	0.00	ND	38	100.0
95R-4, 0	1442.80	514	12.0	0.00	0.00	ND	42	100.0
99R-1, 0	1477.00	1,710	33.0	0.00	2.92	ND	51	100.0
103R-5, 0	1512.10	4,282	83.0	0.00	7.92	ND	52	100.0
104R-5, 0	1521.80	3,909	77.0	0.00	7.11	ND	50	100.0
105R-6, 0	1532.73	3,961	68.0	0.00	5.46	ND	58	100.0
106R-3, 0	1538.20	10,228	189.0	0.00	16.89	ND	54	100.0
107R-6, 0	1552.37	3,546	64.0	0.00	3.95	ND	56	100.0
108R-2, 0	1556.05	3,540	72.0	0.00	5.29	ND	49	100.0
109R-3, 0	1567.24	6,001	133.0	0.00	15.30	ND	45	100.0
110R-2, 0	1575.57	3,220	56.0	0.00	5.31	ND	57	100.0
111R-2, 1.4	1586.63	4,880	96.0	0.00	10.48	ND	51	100.0
112R-1, 1.4	1594.91	4,066	73.0	0.00	7.42	ND	55	100.0
113R-4, 1.4	1609.14	4,893	91.0	0.00	10.63	ND	54	100.0
114R-2, 1.5	1615.89	4,446	92.0	0.00	13.81	ND	48	100.0
115R-4, 0	1627.20	6,534	121.0	0.00	17.37	ND	54	100.0
116R-2, 1.4	1635.38	3,178	92.0	0.00	17.39	ND	35	100.0
117R-5, 0	1647.27	8,769	206.0	0.00	47.46	ND	42	100.0
118R-6, 0	1658.02	3,151	122.0	0.00	34.42	ND	26	100.0
119R-4, 0	1666.00	9,951	184.0	0.00	47.85	ND	54	100.0
120R-CC, 0.5	1669.36	21,832	445.0	0.00	136.97	ND	49	100.0
121R-CC, 0.1	1678.60	6,817	175.0	0.00	58.16	ND	39	100.0
122R-2, 0	1689.60	18,311	333.0	0.00	108.49	ND	55	100.0
123R-3, 0.1	1696.41	8,713	159.0	0.00	46.16	ND	55	100.0
124R-4, 1.5	1703.43	11,331	197.0	0.00	61.48	ND	57	100.0
125R-2, 0	1708.50	6,200	106.0	0.00	29.55	ND	59	100.0
126R-4, 0	1721.00	6,526	106.0	0.00	28.04	ND	61	100.0
127R-1, 1.5	1727.69	5,394	83.0	0.00	19.24	ND	65	100.0
128R-3, 0	1738.80	7,763	135.0	0.00	40.38	ND	57	100.0
129R-3, 0	1749.48	4,986	71.0	0.00	12.73	ND	70	100.0
130R-3, 0	1757.98	17,588	247.0	0.00	56.95	ND	71	100.0
131R-2, 0	1766.02	9,421	144.0	0.00	36.71	ND	65	100.0

Table T18 (continued).

Core, section interval (cm)	Depth CSF-A (m)	C_1 (ppmv)	C_2 (ppmv)	$C_{2=}$ (ppmv)	C_3 (ppmv)	C_1 (mM)	C_1/C_2	$C_2/(C_2 + C_{2=})$ (%)
132R-2, 0	1775.67	10,727	165.0	0.00	43.07	ND	65	100.0
133R-4, 0	1788.08	5,580	90.0	0.00	17.47	ND	62	100.0
134R-2, 114	1795.77	5,942	82.0	0.00	13.21	ND	73	100.0
135R-3, 0	1805.89	10,613	141.0	0.00	27.16	ND	75	100.0
136R-2, 0	1814.12	10,058	155.0	0.00	30.81	ND	65	100.0
137R-2, 0	1823.80	4,250	58.0	0.00	10.22	ND	73	100.0
138R-6, 0	1839.39	13,890	187.0	0.00	29.73	ND	74	100.0
139R-4, 0	1845.89	2,385	54.0	0.00	15.51	ND	44	100.0
140R-1, 0	1851.10	13,605	183.0	0.00	33.42	ND	74	100.0
141R-2, 0	1862.02	16,754	234.0	0.00	41.65	ND	72	100.0
142R-1, 0	1870.40	12,163	176.0	0.00	35.06	ND	69	100.0
143R-1, 149	1876.49	5,301	84.0	0.00	15.42	ND	63	100.0
144R-3, 101	1883.96	6,144	87.0	0.00	13.05	ND	71	100.0
145R-1, 144	1890.94	7,065	105.0	0.00	17.42	ND	67	100.0
146R-2, 5	1900.25	7,412	118.0	0.00	20.19	ND	63	100.0
147R-4, 0	1912.68	15,971	239.0	0.00	39.71	ND	67	100.0
148R-4, 0	1922.35	14,976	227.0	0.00	37.39	ND	66	100.0

Note: ND = not determined.

Table T19. Headspace wet gas composition, Site U1352. (See table notes.) (Continued on next two pages.)

Core, section, interval (cm)	Depth CSF-A (m)	C_1 (ppmv)	C_2 (ppmv)	C_3 (ppmv)	*n*-C_4 (ppmv)	*i*-C_4 (ppmv)	*n*-C_5 (ppmv)	*i*-C_5 (ppmv)	*br*-C_6 (ppmv)	CO_2 (ppmv)	C_1/C_2	*n*-C_4/(*i*-C_4 + *n*-C_4) (%)	*n*-C_5/(*i*-C_5 + *n*-C_5) (%)
317-U1352B-													
75X-4, 0	652.80	7,364	17.0	6.4	0.41	5.40	0.00	2.06	0.34	ND	433	7.0	0.0
317-U1352C-													
14R-2, 79	739.79	11,821	27.4	21.5	1.95	14.62	0.00	11.22	0.00	487	431	11.8	0.0
15R-2, 102	749.58	5,593	12.8	9.4	0.00	0.00	0.00	174.12	0.00	532	436	ND	0.0
16R-2, 0	758.27	2,201	3.2	1.7	0.00	2.57	0.00	2.10	0.00	410	687	0.0	0.0
17R-2, 0	768.07	6,361	14.6	11.3	0.00	0.00	0.00	0.00	0.00	658	437	ND	ND
18R-3, 87	779.68	3,851	7.7	6.1	0.00	0.00	0.00	0.00	0.00	406	501	ND	ND
19R-2, 0	787.50	10,336	31.3	31.4	0.00	336.06	0.00	284.88	0.00	207	330	0.0	0.0
20R-2, 0	797.09	3,310	9.8	9.4	0.00	0.00	0.00	0.00	0.00	632	337	ND	ND
21R-2, 0	806.80	7,071	15.4	12.2	1.35	11.41	0.00	4.17	0.00	234	459	10.6	0.0
22R-2, 0	816.42	9,388	26.0	24.4	1.91	16.07	0.00	6.93	0.00	1,003	361	10.6	0.0
24R-2, 0	835.63	12,979	31.0	23.5	0.00	39.78	0.00	16.15	0.00	121	418	0.0	0.0
25R-2, 0	845.30	4,490	13.0	12.0	1.15	10.98	0.00	4.34	0.00	186	344	9.5	0.0
26R-2, 70	855.28	1,718	5.0	4.2	0.00	61.97	0.00	0.00	0.00	372	345	0.0	ND
27R-2, 56	864.56	6,285	17.8	14.3	1.09	9.63	0.00	3.70	0.00	116	353	10.1	0.0
28R-1, 126	873.86	9,454	27.5	22.0	0.00	0.00	0.00	0.00	0.00	517	344	ND	ND
29R-2, 0	883.23	5,046	15.7	13.6	0.00	14.61	0.00	6.05	0.00	26	322	0.0	0.0
30R-1, 148	893.28	2,543	9.7	12.6	1.25	9.92	0.00	4.91	0.00	154	261	11.2	0.0
31R-1, 124	902.54	6,316	20.9	21.1	1.58	11.31	0.00	5.14	0.00	449	303	12.2	0.0
32R-1, 120	912.10	3,173	13.1	16.8	2.92	17.86	0.00	11.35	0.00	184	243	14.1	0.0
33R-3, 0	923.25	5,267	23.1	25.4	3.46	23.26	0.00	13.39	0.00	85	228	12.9	0.0
34R-2, 0	931.17	3,604	15.3	15.3	1.57	8.77	0.00	5.37	0.00	140	236	15.2	0.0
35R-2, 0	941.20	4,132	16.5	14.9	2.25	12.26	0.00	9.06	0.00	125	250	15.5	0.0
36R-3, 0	952.40	993	6.8	6.2	1.51	5.80	0.00	4.65	0.00	364	145	20.7	0.0
37R-3, 115	962.81	2,284	12.4	9.3	0.91	4.22	0.00	2.96	0.00	789	184	17.7	0.0
38R-4, 0	973.00	6,013	30.9	29.0	0.00	142.90	0.00	140.55	0.00	225	195	0.0	0.0
39R-5, 0	984.10	2,687	19.8	22.0	0.00	0.00	0.00	0.00	0.00	342	136	ND	ND
40R-2, 0	989.01	6,032	33.3	32.9	2.53	11.99	0.91	8.31	0.62	668	181	17.5	9.8
41R-5, 0	1003.30	7,078	46.8	60.7	7.24	29.31	2.42	21.00	1.34	104	151	19.8	10.3
42R-4, 0	1010.94	1,047	5.0	5.2	1.04	3.63	0.00	2.38	0.00	141	210	22.2	0.0
43R-2, 0	1017.93	2,555	17.7	20.3	2.12	7.92	0.00	5.17	0.00	770	144	21.1	0.0
44R-3, 0	1029.10	3,972	26.9	31.0	2.96	11.18	0.61	7.50	0.72	733	148	20.9	7.5
45R-2, 0	1037.11	1,342	8.8	12.1	1.35	4.61	0.00	3.64	0.00	557	153	22.7	0.0
46R-2, 148	1048.22	998	7.5	11.1	1.43	4.72	0.00	3.65	0.00	1,063	134	23.3	0.0
47R-2, 0	1056.18	1,587	12.8	16.4	1.98	6.28	0.00	4.98	0.51	269	124	24.0	0.0
48R-2, 0	1065.88	1,818	16.9	23.4	2.58	7.73	0.74	5.79	0.50	769	108	25.0	11.4
49R-3, 0	1076.77	2,480	18.0	22.4	2.97	8.31	0.00	6.09	0.00	608	138	26.3	0.0
50R-6, 0	1092.25	449	7.2	13.1	1.87	5.14	0.00	4.09	0.00	310	62	26.7	0.0
51R-3, 145	1097.32	2,585	23.4	29.4	3.26	9.50	0.91	7.31	0.57	348	110	25.5	11.1
52R-2, 0	1103.90	4,579	38.8	38.6	3.21	9.45	0.00	4.89	0.00	832	118	25.4	0.0
53R-2, 0	1113.54	1,684	17.1	19.6	2.31	6.28	0.00	4.55	0.00	1,348	98	26.9	0.0
54R-4, 0	1126.18	3,135	30.1	31.5	2.89	8.00	0.68	4.72	0.52	1,962	104	26.5	12.7
55R-4, 0	1135.50	3,453	40.3	47.4	4.72	13.58	1.34	8.18	0.64	1,681	86	25.8	14.1
56R-4, 0	1145.28	384	9.1	17.2	2.45	7.32	0.00	5.83	0.00	1,607	42	25.0	0.0
57R-2, 149	1153.49	1,590	20.0	23.7	2.82	8.07	0.00	5.26	0.00	1,041	80	25.9	0.0
58R-5, 0	1164.57	1,208	17.1	22.6	2.96	8.71	0.81	6.81	0.41	561	71	25.3	10.7
59R-7, 0	1178.70	5,057	63.2	64.0	6.42	19.42	1.07	10.67	0.54	559	80	24.8	9.1
60R-4, 0	1183.90	3,193	40.3	38.4	57.75	163.06	0.00	119.41	0.00	150	79	26.2	0.0
61R-4, 0	1193.50	4,052	54.5	54.7	8.57	21.51	1.40	13.93	1.01	44	74	28.5	9.1

Table T19 (continued). (Continued on next page.)

Core, section, interval (cm)	Depth CSF-A (m)	C_1 (ppmv)	C_2 (ppmv)	C_3 (ppmv)	*n*-C_4 (ppmv)	*i*-C_4 (ppmv)	*n*-C_5 (ppmv)	*i*-C_5 (ppmv)	*br*-C_6 (ppmv)	CO_2 (ppmv)	C_1/C_2	*n*-C_4/(*i*-C_4 + *n*-C_4) (%)	*n*-C_5/(*i*-C_5 + *n*-C_5) (%)
62R-3, 0	1201.60	2,908	44.4	49.6	8.63	19.70	1.44	14.20	0.62	486	66	30.5	9.2
63R-CC, 0	1208.20	3,376	58.3	69.9	14.36	32.00	2.69	22.18	0.94	183	58	31.0	10.8
65R-1, 0	1221.40	3,629	60.4	64.2	10.90	20.34	2.10	14.63	0.92	1,440	60	34.9	12.6
70R-4, 0	1251.16	1,747	17.4	10.2	11.33	16.44	2.20	13.68	0.84	1,338	101	40.8	13.9
71R-3, 0	1259.30	2,238	38.2	31.5	5.75	7.96	0.97	6.57	0.00	1,367	59	41.9	12.9
72R-1, 0	1265.80	3,195	61.7	56.9	13.85	17.21	0.00	10.56	0.00	1,515	52	44.6	0.0
73R-3, 0	1278.00	1,990	38.6	31.9	6.61	8.96	1.14	8.41	0.00	704	52	42.5	12.0
76R-1, 107	1304.97	1,331	32.5	30.2	5.99	8.18	0.94	6.77	0.00	333	41	42.3	12.2
77R-1, 145	1309.85	420	10.1	9.5	2.30	3.12	0.00	2.77	0.00	1,726	42	42.4	0.0
78R-2, 145	1316.29	518	12.8	9.4	1.45	2.18	0.00	1.56	0.00	1,394	41	39.9	0.0
79R-1, 145	1319.35	719	17.0	12.9	2.26	3.27	0.00	2.31	0.00	1,958	42	40.9	0.0
80R-2, 145	1325.85	145	3.7	3.3	0.95	1.54	0.00	1.24	0.00	1,979	40	38.0	0.0
81R-2, 0	1329.00	68	2.9	2.6	0.68	1.01	0.00	0.58	0.00	1,255	23	40.2	0.0
82R-1, 41	1332.91	358	7.9	5.1	0.82	1.46	0.00	0.73	0.00	923	45	36.1	0.0
84R-CC, 5	1342.15	240	9.0	8.1	1.33	2.18	0.00	1.26	0.00	1,272	27	37.9	0.0
85R-3, 149	1351.19	369	9.4	2.9	0.00	0.62	0.00	0.00	0.00	1,510	39	0.0	ND
86R-2, 0	1353.16	224	6.6	2.8	0.00	0.74	0.00	0.00	0.00	2,291	34	0.0	ND
87R-5, 0	1367.40	68	3.4	0.5	0.00	0.00	0.00	0.00	0.00	1,183	20	ND	ND
88R-4, 0	1375.50	116	8.3	0.8	0.00	0.00	0.00	0.00	0.00	3,173	14	ND	ND
89R-4, 0	1384.89	42	5.9	0.0	0.00	0.00	0.00	0.00	0.00	1,039	7	ND	ND
90R-3, 0	1393.20	49	5.7	0.0	0.00	0.00	0.00	0.00	0.00	2,477	9	ND	ND
91R-5, 0	1405.70	78	3.6	0.0	0.00	0.00	0.00	0.00	0.00	728	21	ND	ND
94R-6, 0	1436.10	551	14.4	0.0	0.93	0.66	0.00	1.32	0.00	58	38	58.3	0.0
95R-4, 0	1442.80	514	12.2	0.0	0.44	0.45	0.00	0.56	0.00	60	42	49.0	0.0
99R-1, 0	1477.00	1,710	33.2	2.9	1.99	1.42	0.00	2.85	0.00	186	51	58.3	0.0
103R-5, 0	1512.10	4,282	83.0	7.9	3.29	3.71	0.93	5.51	0.40	410	52	47.0	14.5
104R-5, 0	1521.80	3,909	77.5	7.1	2.30	3.64	0.52	4.29	0.00	316	50	38.7	10.9
105R-6, 0	1532.73	3,961	68.3	5.5	1.36	3.15	0.37	3.45	0.00	75	58	30.1	9.7
106R-3, 0	1538.20	10,228	188.7	16.9	2.91	7.97	1.44	9.62	0.00	182	54	26.7	13.0
107R-6, 0	1552.37	3,546	63.8	3.9	0.64	2.25	0.00	2.11	0.00	386	56	22.3	0.0
108R-2, 0	1556.05	3,540	71.8	5.3	1.39	2.30	0.00	2.74	0.00	1290	49	37.5	0.0
109R-3, 0	1567.24	6,001	133.2	15.3	1.30	6.12	0.00	6.12	0.00	211	45	17.5	0.0
110R-2, 0	1575.57	3,220	56.2	5.3	0.55	2.24	0.00	2.29	0.00	2,314	57	19.8	0.0
111R-2, 1.4	1586.63	4,880	96.2	10.5	0.86	4.01	0.00	4.40	0.00	1,092	51	17.7	0.0
112R-1, 1.4	1594.91	4,066	73.3	7.4	0.54	3.08	0.00	2.96	0.00	894	55	14.9	0.0
113R-4, 1.4	1609.14	4,893	91.3	10.6	0.93	3.65	0.00	3.65	0.00	393	54	20.4	0.0
114R-2, 1.5	1615.89	4,446	91.8	13.8	0.85	4.48	0.35	4.78	0.26	96	48	15.9	6.9
115R-4, 0	1627.20	6,534	120.8	17.4	1.01	5.12	0.41	4.52	0.00	1,029	54	16.5	8.3
116R-2, 1.4	1635.38	3,178	92	17.39	1.14	5.31	0.00	4.41	0.00	947	35	17.7	0.0
117R-5, 0	1647.27	8,769	206	47.46	3.21	15.75	1.32	17.86	0.72	1,677	42	16.9	6.9
118R-6, 0	1658.02	3,151	122	34.42	6.60	13.27	1.14	17.66	0.96	6,480	26	33.2	6.1
119R-4, 0	1666.00	9,951	184	47.85	2.88	12.40	1.02	12.46	0.00	989	54	18.9	7.5
120R-CC, 0.5	1669.36	21,832	445	136.97	15.35	42.13	3.61	50.72	1.15	1,487	49	26.7	6.7
121R-CC, 0.1	1678.60	6,817	175	58.16	6.63	16.37	1.33	18.50	0.00	837	39	28.8	6.7
122R-2, 0	1689.60	18,311	333	108.49	18.50	30.88	3.63	36.42	0.95	949	55	37.5	9.1
123R-3, 0.1	1696.41	8,713	159	46.16	9.01	12.63	1.39	14.43	0.00	703	55	41.6	8.8
124R-4, 1.5	1703.43	11,331	197	61.48	14.39	17.78	3.50	24.33	1.17	294	57	44.7	12.6
125R-2, 0	1708.50	6,200	106	29.55	7.55	8.79	1.64	11.29	0.32	355	59	46.2	12.6
126R-4, 0	1721.00	6,526	106	28.04	7.51	8.21	1.61	11.02	0.36	580	61	47.8	12.7
127R-1, 1.5	1727.69	5,394	83	19.24	5.80	6.27	1.30	8.16	0.60	339	65	48.1	13.7
128R-3, 0	1738.80	7,763	135	40.38	14.71	15.83	4.49	22.45	2.47	94	57	48.2	16.7

Table T19 (continued).

Core, section, interval (cm)	Depth CSF-A (m)	C_1 (ppmv)	C_2 (ppmv)	C_3 (ppmv)	*n*-C_4 (ppmv)	*i*-C_4 (ppmv)	*n*-C_5 (ppmv)	*i*-C_5 (ppmv)	*br*-C_6 (ppmv)	CO_2 (ppmv)	C_1/C_2	*n*-C_4/(*i*-C_4 + *n*-C_4) (%)	*n*-C_5/(*i*-C_5 + *n*-C_5) (%)
129R-3, 114	1749.48	4,986	71	12.73	2.37	2.80	0.00	2.90	0.00	710	70	45.8	0.0
130R-3, 0	1757.98	17,588	247	56.95	13.77	15.13	4.48	20.30	2.50	834	71	47.6	18.1
131R-2, 0	1766.02	9,421	144	36.71	11.73	12.78	4.52	20.45	3.84	2,120	65	47.9	18.1
132R-2, 0	1775.67	10,727	165	43.07	12.06	13.00	4.07	19.03	2.64	1,669	65	48.1	17.6
133R-4, 0	1788.08	5,580	90	17.47	3.91	4.79	0.91	5.07	0.00	417	62	45.0	15.2
134R-2, 114	1795.77	5,942	82	13.21	2.40	2.93	0.00	2.76	0.00	854	73	45.0	0.0
135R-3, 0	1805.89	10,613	141	27.16	4.88	5.93	1.11	5.56	0.00	742	75	45.1	16.6
136R-2, 0	1814.12	10,058	155	30.81	5.50	6.31	1.20	6.75	0.44	528	65	46.5	15.1
137R-2, 0	1823.80	4,250	58	10.22	2.33	2.46	0.47	2.75	0.00	600	73	48.6	14.5
138R-6, 0	1839.39	13,890	187	29.73	5.26	6.64	1.15	5.44	0.00	290	74	44.2	17.5
139R-4, 0	1845.89	2,385	54	15.51	4.58	5.04	1.52	6.67	0.00	283	44	47.6	18.6
140R-1, 0	1851.10	13,605	183	33.42	5.82	7.18	1.59	6.85	1.15	470	74	44.7	18.8
141R-2, 0	1862.02	16,754	234	41.65	6.33	8.00	1.21	5.64	0.00	1,325	72	44.2	17.6
142R-1, 0	1870.40	12,163	176	35.06	6.43	7.59	1.97	7.94	1.69	849	69	45.9	19.9
143R-1, 149	1876.49	5,301	84	15.42	3.01	3.42	0.76	3.29	0.00	931	63	46.8	18.9
144R-3, 101	1883.96	6,144	87	13.05	2.25	2.59	0.00	1.90	0.00	867	71	46.5	0.0
145R-1, 144	1890.94	7,065	105	17.42	3.00	3.73	0.59	2.95	0.34	1,190	67	44.6	16.7
146R-2, 5	1900.25	7,412	118	20.19	3.51	4.17	0.91	3.33	0.58	1,898	63	45.7	21.4
147R-4, 0	1912.68	15,971	239	39.71	6.37	7.94	1.28	5.68	0.00	598	67	44.5	18.5
148R-4, 0	1922.35	14,976	227	37.39	6.16	7.37	1.17	4.44	0.37	530	66	45.5	20.8

Notes: C_1–C_3 analyzed on GC3. C_1 and C_4–C_6 analyzed on natural gas analyzer (NGA) and normalized to methane in GC3 analysis. Exception: Core 317-U1352C-72R-1 normalized to ethane. CO_2 analyzed by thermal conductivity detector on NGA. *br*-C_6 is the peak eluting before *n*-C_6, which may include as many as five branched C_6 alkane isomers. ND = not determined.

Table T20. Core void gas composition, Site U1352. (See table notes.)

Core, section, interval (cm)	Depth CSF-A (m)	C_1 (ppmv)	C_2 (ppmv)	$C_{2=}$ (ppmv)	C_3 (ppmv)	$C_{3=}$ (ppmv)	*n*-C_4 (ppmv)	*i*-C_4 (ppmv)	*n*-C_5 (ppmv)	*i*-C_5 (ppmv)	*n*-C_6 (ppmv)	*br*-C_6 (ppmv)	CO_2 (ppmv)	C_1/C_2	*n*-C_4/(*i*-C_4 + *n*-C_4) (%)	*n*-C_5/(*i*-C_5 + *n*-C_5) (%)	*n*-C_6/(*i*-C_6 + *n*-C_6) (%)	$C_2/(C_2 + C_{2=})$ (%)	$C_3/(C_3 + C_{3=})$ (%)
317-U1352B-																			
4H-7, 29	32.49	869,603	46.0	0.00	0.0	0.00	0.00	0.00	0.00	0.00	0.00	0.00	ND	18,969	ND	ND	ND	100.00	ND
5H-1, 37	33.07	910,149	50.0	0.00	0.0	0.00	0.00	0.00	0.00	0.00	0.00	0.00	ND	18,314	ND	ND	ND	100.00	ND
5H-5, 28	38.98	940,365	53.0	0.00	0.0	0.00	0.00	0.00	0.00	0.00	0.00	0.00	ND	17,596	ND	ND	ND	100.00	ND
5H-4, 26	40.18	845,453	52.0	0.00	0.0	0.00	0.00	0.00	0.00	0.00	0.00	0.00	ND	16,373	ND	ND	ND	100.00	ND
6H-5, 3	52.23	927,165	69.0	0.00	0.0	0.00	0.00	0.41	0.00	0.18	0.00	0.00	ND	13,481	0.0	0.0	ND	100.00	ND
9H-3, 26	77.96	718,475	84.0	0.48	1.2	0.00	0.00	0.57	0.00	0.22	0.00	0.00	ND	8,573	0.0	0.0	ND	99.43	100.00
10H-8, 11	93.07	467,881	61.0	0.28	1.2	0.00	0.00	0.41	0.19	0.24	2.43	0.51	ND	7,699	0.0	44.5	82.6	99.54	100.00
11H-1, 95	94.65	909,977	137.0	0.00	3.7	0.00	0.00	1.28	0.00	0.33	0.00	0.00	ND	6,661	0.0	0.0	ND	100.00	100.00
14H-1, 92	123.12	961,209	161.0	0.00	2.8	0.00	0.00	1.23	0.00	0.99	0.00	0.00	ND	5,979	0.0	0.0	ND	100.00	100.00
18H-2, 5	157.75	730,810	148.0	0.25	2.4	0.00	0.00	0.21	0.00	0.30	0.00	0.00	ND	4,926	0.0	0.0	ND	99.83	100.00
19H-5, 35	172.05	960,020	201.0	0.00	2.9	0.00	0.00	1.24	0.00	0.47	0.00	0.00	ND	4,778	0.0	0.0	ND	100.00	100.00
21H-1, 135	181.05	956,075	217.0	0.00	3.3	0.00	0.00	1.13	0.00	1.36	0.00	0.00	ND	4,404	0.0	0.0	ND	100.00	100.00
22H-2, 26	190.96	960,680	216.0	0.00	3.6	0.00	0.00	0.76	0.00	1.05	0.00	0.00	ND	4,441	0.0	0.0	ND	100.00	100.00
23H-1, 121	199.91	950,445	223.0	0.00	3.1	0.00	0.00	0.90	0.00	0.44	0.00	0.00	ND	4,258	0.0	0.0	ND	100.00	100.00
24H-2, 125	210.95	920,891	228.0	0.00	3.6	0.00	0.26	0.70	0.00	0.53	0.00	0.00	ND	4,036	27.1	0.0	ND	100.00	100.00
25H-2, 29	219.49	944,804	240.0	0.00	4.5	0.00	0.00	0.73	0.00	0.67	0.00	0.00	ND	3,944	0.0	0.0	ND	100.00	100.00
26H-2, 41	229.03	957,125	250.0	0.00	4.8	0.00	0.00	0.81	0.00	0.85	0.26	0.00	ND	3,825	0.0	0.0	100.0	100.00	100.00
27H-6, 25	244.45	955,414	282.0	0.00	6.8	0.00	0.27	0.80	0.00	0.71	0.00	0.00	ND	3,390	25.0	0.0	ND	100.00	100.00
28H-3, 90	250.03	953,728	280.0	0.84	6.6	0.00	0.00	0.75	0.00	0.51	0.00	0.00	ND	3,407	0.0	0.0	ND	99.70	100.00
29H-4, 44	256.14	921,538	283.0	0.00	7.2	0.00	0.23	1.08	0.00	0.65	0.00	0.00	ND	3,259	17.6	0.0	ND	100.00	100.00
30H-4, 114	263.34	939,056	274.0	0.00	6.9	0.00	0.00	0.85	0.00	0.70	0.00	0.00	ND	3,422	0.0	0.0	ND	100.00	100.00
31H-5, 61	271.62	963,948	302.0	0.00	8.9	0.00	0.00	0.77	0.00	0.76	0.00	0.00	ND	3,187	0.0	0.0	ND	100.00	100.00
32H-4, 144	278.14	943,942	301.0	0.00	9.4	0.00	0.00	0.98	0.00	0.53	0.00	0.00	ND	3,137	0.0	0.0	ND	100.00	100.00
33H-5, 124	287.38	967,438	321.0	0.00	11.7	0.00	0.44	1.46	0.00	1.17	0.00	0.00	ND	3,017	23.1	0.0	ND	100.00	100.00
34H-2, 38	288.84	940,614	400.0	0.00	15.0	0.00	0.50	1.95	0.00	1.37	0.00	0.16	ND	2,350	20.2	0.0	0.0	100.00	100.00
35H-1, 07	293.87	856,279	303.0	0.45	11.9	0.00	0.87	2.20	0.00	1.68	0.00	0.00	ND	2,822	28.4	0.0	ND	99.85	100.00
39X-2, 27	313.97	917,689	392.0	0.00	15.7	0.00	0.62	1.31	0.00	0.79	0.00	0.00	ND	2,340	32.0	0.0	ND	100.00	100.00
41X-2, 0	333.00	930,406	425.0	0.50	19.4	0.00	0.43	1.12	0.00	1.49	0.00	0.00	ND	2,191	27.7	0.0	ND	99.88	100.00
43X-1, 105	351.75	930,744	439.0	0.03	23.1	0.00	0.28	1.02	0.00	1.12	0.00	0.00	ND	2,119	21.8	0.0	ND	99.99	100.00
44X-3, 139	364.79	960,430	377.0	0.00	19.0	0.00	0.41	0.67	0.00	0.63	0.00	0.00	ND	2,550	37.9	0.0	ND	100.00	100.00
47X-7, 47	398.47	960,508	420.0	0.00	31.4	0.00	0.27	0.77	0.00	1.14	0.19	0.00	ND	2,289	26.0	0.0	100.0	100.00	100.00
49X-2, 77	410.57	963,567	486.0	0.00	45.3	0.00	0.38	1.51	0.00	1.00	0.00	0.00	ND	1,983	20.3	0.0	ND	100.00	100.00
50X-3, 78	421.68	965,701	494.0	3.99	53.0	1.56	0.78	2.01	0.00	0.95	0.23	0.19	ND	1953	28.0	0.0	55.0	99.20	97.14
51X-5, 57	434.07	957,477	466.0	0.00	47.8	0.00	0.45	1.34	0.00	0.61	0.00	0.00	ND	2,054	25.0	0.0	ND	100.00	100.00
52X-6, 30	444.90	951,964	469.0	0.94	52.6	0.00	0.48	1.16	0.00	0.56	0.00	0.00	ND	2,032	29.4	0.0	ND	99.80	100.00
53X-4, 114	452.34	954,944	502.0	1.36	58.2	0.00	0.46	1.34	0.00	0.59	0.00	0.00	ND	1,901	25.5	0.0	ND	99.73	100.00
54X-4, 38	461.18	963,698	558.0	0.13	70.3	0.00	0.63	1.91	0.00	1.03	0.00	0.19	439	1,728	24.9	0.0	0.0	99.98	100.00
55X-1, 147	467.37	860,173	966.0	440.53	196.0	262.46	34.75	10.11	1.88	2.26	0.00	0.00	1,543	891	77.5	45.4	ND	68.67	42.75
58X-5, 116	500.58	969,448	536.0	0.00	67.6	0.00	0.55	3.08	0.00	0.68	0.00	0.00	397	1,808	15.0	0.0	ND	100.00	100.00
76X-1, 82	658.72	592,919	529.0	0.17	123.5	0.00	1.57	36.33	0.00	3.69	0.00	0.30	821	1,121	4.2	0.0	0.0	99.97	100.00
317-U1352C-																			
59R-5, 83	1,176.53	1,360	14.0	0.00	7.8	0.00	0.61	1.70	0.00	0.70	0.00	0.00	ND	98	26.3	0.0	ND	100.00	100.00
70R-4, 0	1,251.16	1,747	17.0	0.00	10.2	0.00	1.41	2.46	0.00	1.25	0.00	0.00	525	101	36.5	0.0	ND	100.00	100.00
94R-4, 32	1,433.42	153	2.0	0.00	0.0	0.00	0.00	0.00	0.00	0.00	0.00	0.00	691	98	ND	ND	ND	100.00	ND
103R-5, 114	1,513.24	2,139	22.0	0.00	0.0	0.00	0.00	0.00	0.00	0.00	0.00	0.00	529	96	ND	ND	ND	100.00	ND
126R-4-VAC 0.35	1,721.35	2,028	24.0	0.00	4.8	0.00	0.86	0.99	0.00	0.68	0.00	0.00	435	84	46.49	ND	ND	100.00	ND
128R-2, 1.4	1,738.65	3,232	21.0	0.00	4.1	0.00	0.58	0.82	0.00	0.48	0.00	0.00	413	157	41.41	ND	ND	100.00	ND

Notes: Samples from Hole U1352B: C_2–C_3 analyzed on GC3. C_1 and C_4–C_6 analyzed on natural gas analyzer (NGA) and normalized to methane from GC3 analysis. Cores 317-U1352C-59R through 103R: C_1–C_3 analyzed on GC3. C_4–C_6 analyzed on NGA and normalized to methane in GC3 analysis. Cores 317-U1352C-126R and 128R: all components analyzed on NGA. CO_2 analyzed by thermal conductivity detector on NGA. *br*-C_6 is the peak eluting before *n*-C_6, which may include as many as five branched alkane isomers. ND = not determined.

Table T21. Carbon, nitrogen, and sulfur analyses of sediments, Site U1352. (See table notes.) (Continued on next four pages.)

Core, section, interval (cm)	Depth CSF-A (m)	IC (wt%)	$CaCO_3$ (wt%)	TC (wt%)	TN (wt%)	TS (wt%)	TOC_{DIFF} (wt%)	TOC_{SRA} (wt%)	TOC_{DIFF}/TN	TOC_{DIFF}/TS
317-U1352B-										
1H-3, 29	3.29	0.45	3.71	0.70	0.030	0.030	0.25	0.81	10	8.5
1H-3, 91	3.91	0.18	1.49	0.37	0.020	0.260	0.19	0.54	10	0.7
2H-3, 80	12.00	0.06	0.48	0.16	0.010	0.160	0.10	0.59	8	0.6
2H-7, 9	16.79	0.02	0.16	0.14	0.020	0.100	0.12	0.46	7	1.2
3H-5, 143	25.13	0.29	2.38	0.35	0.010	0.850	0.06	0.78	7	0.1
3H-6, 66	25.86	0.13	1.07	0.29	0.020	0.320	0.16	0.59	8	0.5
4H-2, 139	30.09	0.12	0.96	0.32	0.030	0.060	0.21	0.51	6	3.5
4H-6, 17	34.87	0.09	0.77	0.22	0.020	0.020	0.13	0.78	6	6.4
5H-6, 71	43.63	0.07	0.58	0.22	0.030	0.020	0.15	0.78	5	9.3
6H-3, 84	50.04	0.18	1.52	0.40	0.030	0.000	0.22	0.85	ND	ND
6H-5, 55	52.75	0.11	0.90	0.29	0.030	0.060	0.18	0.66	6	3.1
7H-2, 16	57.36	0.22	1.82	0.48	0.040	0.090	0.26	0.69	6	2.9
7H-6, 72	63.92	3.42	28.47	3.52	0.030	0.000	0.10	1.01	ND	ND
8H-3, 82	69.02	0.06	0.49	0.20	0.030	0.200	0.14	0.59	5	0.7
8H-CC, 46	75.02	0.13	1.07	0.32	0.030	0.090	0.19	0.62	7	2.1
9H-3, 75	78.45	0.08	0.64	0.24	0.020	0.050	0.16	0.56	9	3.3
9H-6, 34	82.54	4.31	35.94	4.60	0.020	0.130	0.29	0.89	ND	ND
10H-3, 118	87.14	0.47	3.89	0.76	0.030	0.000	0.29	0.89	ND	ND
10H-4, 53	87.99	0.19	1.60	0.44	0.030	0.050	0.25	0.66	9	5.0
11H-3, 130	98.00	4.76	39.68	5.37	0.030	0.020	0.61	0.85	23	30.4
11H-4, 127	99.45	0.24	2.01	0.47	0.030	0.110	0.23	0.79	8	2.1
12H-4, 84	108.50	0.32	2.64	0.58	0.030	0.110	0.26	0.87	8	2.4
12H-6, 100	111.66	0.34	2.85	0.65	0.010	0.000	0.31	0.62	ND	ND
13H-3, 44	116.12	0.34	2.86	0.61	0.030	0.030	0.27	0.92	9	8.9
13H-6, 46	120.64	0.21	1.72	0.50	0.040	0.380	0.29	0.53	7	0.8
14H-3, 75	125.95	0.35	2.95	0.62	0.040	0.160	0.27	0.70	7	1.7
14H-5, 143	129.63	1.40	11.65	1.87	0.050	0.280	0.47	0.85	9	1.7
15H-1, 122	132.92	0.25	2.11	0.53	0.030	0.210	0.28	0.44	8	1.3
16H-4, 92	146.59	0.17	1.39	0.37	0.030	0.230	0.20	0.53	7	0.9
16H-7, 43	150.47	1.67	13.88	2.01	0.070	0.500	0.34	1.00	5	0.7
17H-2, 42	152.62	0.85	7.11	1.13	0.040	0.180	0.28	0.80	7	1.5
17H-4, 77	155.26	0.15	1.22	0.30	0.040	0.450	0.15	0.45	4	0.3
18H-2, 115	158.85	2.94	24.52	3.53	0.040	0.160	0.59	0.80	14	3.7
18H-3, 34	159.54	1.11	9.28	1.58	0.050	0.330	0.47	1.04	10	1.4
19H-1, 78	166.48	0.13	1.11	0.36	0.030	0.240	0.23	0.41	7	0.9
20H-1, 43	175.13	0.21	1.78	0.31	0.030	0.270	0.10	0.57	3	0.4
21H-3, 62	183.32	2.17	18.07	2.51	0.060	0.360	0.34	1.19	6	0.9
21H-6, 43	187.63	0.35	2.93	0.68	0.040	0.380	0.33	0.71	8	0.9
22H-1, 112	190.32	0.61	5.08	0.83	0.050	0.210	0.22	0.77	4	1.0
22H-7, 52	198.72	3.07	25.59	3.60	0.060	0.150	0.53	1.57	8	3.5
23H-3, 117	202.87	0.21	1.76	0.49	0.050	0.270	0.27	0.79	6	1.0
23H-5, 130	206.00	0.51	4.26	1.82	0.080	0.300	1.31	1.33	17	4.4
24H-5, 94	215.14	0.41	3.44	0.73	0.030	0.200	0.32	0.87	12	1.6
24H-6, 139	217.09	1.05	8.76	1.46	0.040	0.240	0.41	1.12	11	1.7
25H-2, 70	219.90	0.42	3.46	1.57	0.000	0.140	1.16	0.59	304	8.4
25H-6, 72	225.92	0.59	4.96	1.20	0.050	0.350	0.61	1.30	12	1.7
26H-1, 77	227.97	0.23	1.94	0.51	0.000	0.400	0.28	0.85	80	0.7
26H-6, 41	235.03	0.42	3.49	0.76	0.010	0.120	0.34	0.92	46	2.9
27H-3, 120	240.90	0.73	6.08	1.18	0.050	0.240	0.45	0.65	10	1.9
27H-5, 78	243.48	2.29	19.11	2.87	0.030	0.520	0.58	1.14	21	1.1
28H-3, 75	249.88	4.89	40.76	5.43	0.050	0.050	0.54	1.30	10	10.5
28H-4, 41	250.54	0.37	3.10	0.52	0.010	0.170	0.15	0.53	16	0.9
29H-1, 117	252.37	0.42	3.51	0.67	0.060	0.480	0.25	1.25	5	0.5
30H-1, 78	258.48	0.53	4.41	0.78	0.050	1.110	0.25	0.77	5	0.2
31H-2, 26	268.96	0.20	1.69	0.41	0.050	0.060	0.21	0.92	4	3.4
32H-2, 102	274.72	0.55	4.58	0.89	0.050	0.330	0.34	0.70	6	1.0
32H-CC, 56	281.40	6.90	57.49	7.46	0.030	0.080	0.56	1.04	19	7.0
33H-4, 68	285.32	2.35	19.59	2.87	0.090	0.240	0.52	1.00	6	2.2
34H-5, 95	292.09	0.57	4.76	1.13	0.030	0.200	0.56	0.99	17	2.8
35H-2, 31	294.65	4.03	33.57	4.49	0.060	0.080	0.46	1.40	7	5.7
36H-2, 39-CARB	296.89	6.42	53.45	7.18	0.050	0.030	0.76	1.18	16	25.5
36H-2, 39-CHNS	296.89	6.48	54.01	6.98	0.050	0.060	0.50	1.05	11	8.3
37X-2, 57	299.07	1.08	8.97	1.83	0.050	0.250	0.75	1.20	16	3.0
38X-2, 88	304.98	2.18	18.14	2.84	0.070	0.450	0.66	1.42	10	1.5
38X-5, 128	309.88	0.10	0.87	0.26	0.040	0.270	0.16	0.28	4	0.6
39X-3, 97	316.17	0.35	2.92	0.59	0.050	0.370	0.24	0.49	5	0.6

Table T21 (continued). (Continued on next page.)

Core, section, interval (cm)	Depth CSF-A (m)	IC (wt%)	$CaCO_3$ (wt%)	TC (wt%)	TN (wt%)	TS (wt%)	TOC_{DIFF} (wt%)	TOC_{SRA} (wt%)	TOC_{DIFF}/TN	TOC_{DIFF}/TS
39X-6, 29	319.99	2.32	19.36	3.04	0.070	0.280	0.72	1.61	11	2.6
40X-1, 82	322.72	0.85	7.10	1.18	0.060	0.430	0.33	0.81	6	0.8
40X-3, 49	325.39	3.23	26.93	3.80	0.050	0.150	0.57	1.16	11	3.8
41X-3, 82	335.32	2.37	19.76	2.53	0.000	0.000	0.16	1.38	40	ND
41X-5, 72	338.22	0.22	1.81	0.42	0.000	0.000	0.20	0.39	ND	ND
42X-1, 92	342.02	0.40	3.35	0.76	0.000	0.000	0.36	0.75	ND	ND
42X-5, 140	348.50	3.59	29.87	4.36	0.030	0.000	0.77	1.83	23	ND
43X-2, 87	353.07	0.47	3.90	0.90	0.090	0.000	0.43	1.85	5	ND
44X-2, 77	362.67	0.72	6.04	0.85	0.030	0.230	0.13	0.48	4	0.5
44X-2, 80	362.70	0.90	7.49	1.12	0.040	0.130	0.22	0.71	5	1.8
46X-5, 73	386.31	0.50	4.18	0.73	0.000	0.000	0.23	0.80	ND	ND
47X-3, 87	393.07	3.08	25.62	3.38	0.070	0.190	0.30	1.50	5	1.6
47X-6, 72	397.42	0.54	4.54	0.81	0.010	0.000	0.27	0.84	53	ND
48X-3, 64	402.34	0.20	1.69	0.40	0.030	0.190	0.20	0.63	7	1.0
48X-5, 123	405.93	1.24	10.33	1.49	0.000	0.000	0.25	0.69	ND	ND
49X-1, 62	408.92	0.71	5.95	1.16	0.070	0.000	0.45	0.36	7	ND
50X-4, 95	423.35	4.55	37.87	5.27	0.050	0.320	0.72	1.29	14	2.3
50X-6, 110	426.50	0.54	4.52	0.67	0.090	0.000	0.13	0.43	1	ND
51X-1, 33	427.83	3.48	28.95	4.03	0.030	0.000	0.55	2.07	18	ND
51X-2, 35	429.35	0.12	0.97	0.28	0.030	0.240	0.16	0.83	6	0.7
52X-4, 70	442.30	0.17	1.45	0.72	0.010	0.000	0.55	0.66	78	ND
52X-7, 56	446.36	7.93	66.03	8.30	0.000	0.000	0.37	0.94	93	ND
53X-1, 118	447.88	8.68	72.33	8.99	0.020	0.000	0.31	1.03	20	ND
53X-6, 87	455.04	0.59	4.94	0.87	0.010	0.160	0.28	1.25	56	ND
54X-1, 112	457.42	0.60	4.98	0.97	0.010	0.000	0.37	1.23	26	ND
54X-5, 28	462.58	8.30	69.12	8.43	0.000	0.080	0.13	1.03	46	1.6
55X-1, 9	465.99	2.63	21.89	3.16	0.010	0.110	0.53	1.35	44	4.8
56X-6, 33	483.33	2.94	24.52	3.35	0.010	0.140	0.40	1.07	27	2.9
56X-7, 57	484.67	1.53	12.74	1.74	0.010	0.070	0.21	1.23	38	2.8
57X-1, 85	485.95	0.63	5.28	0.92	0.010	0.090	0.29	1.03	35	3.3
57X-4, 43	490.03	6.23	51.86	6.97	0.000	0.000	0.75	1.22	166	ND
58X-4, 72	498.64	0.46	3.84	0.69	0.010	0.530	0.23	1.00	42	0.4
59X-1, 104	505.34	0.46	3.83	0.77	0.040	0.320	0.31	0.84	8	1.0
60X-1, 29	514.19	4.98	41.50	5.40	0.010	0.230	0.42	1.53	48	1.8
61X-1, 42	523.92	0.82	6.82	1.19	0.020	0.380	0.37	0.99	24	1.0
61X-2, 63	525.13	2.17	18.06	2.74	0.000	0.020	0.58	1.15	ND	ND
62X-4, 84	538.44	0.91	7.55	1.15	0.020	0.120	0.25	1.15	15	2.1
63X-4, 83	548.03	0.31	2.59	0.61	0.050	0.470	0.30	0.48	6	0.6
64X-3, 81	556.01	0.49	4.10	0.84	0.050	0.540	0.35	0.73	7	0.6
66X-1, 58	571.98	7.00	58.33	7.58	0.040	0.050	0.58	1.32	17	11.6
67X-CC, 16	573.49	6.66	55.46	7.24	0.030	0.050	0.58	1.38	19	11.6
68X-1, 71	581.81	2.07	17.23	2.33	0.030	0.180	0.26	0.71	10	1.5
71X-3, 42	613.32	3.19	26.55	3.45	0.030	0.200	0.26	1.22	9	1.3
72X-4, 80	624.77	0.37	3.09	0.66	0.040	0.540	0.29	0.91	8	0.5
73X-3, 57	632.67	0.76	6.31	1.08	0.040	0.270	0.32	1.11	8	1.2
74X-3, 76	642.46	0.94	7.83	1.24	0.040	0.160	0.30	1.01	8	1.9
74X-7, 10	647.60	1.12	9.34	1.38	0.030	0.100	0.26	0.83	8	2.6
75X-1, 130	649.60	0.97	8.10	1.45	0.040	0.240	0.48	1.01	14	2.0
75X-5, 71	655.01	1.26	10.51	1.55	0.040	0.130	0.29	0.81	7	2.2
76X-1, 40	658.30	0.99	8.25	1.31	0.030	0.070	0.32	0.74	9	4.6
76X-4, 75	663.15	0.81	6.73	1.13	0.030	0.130	0.32	0.48	13	2.5
77X-1, 61	668.21	1.29	10.75	1.58	0.040	0.070	0.29	1.05	8	4.1
77X-2, 46	669.56	1.51	12.58	1.79	0.040	0.140	0.28	0.76	7	2.0
78X-1, 38	677.68	2.37	19.77	2.70	0.030	0.040	0.33	0.73	13	8.2
78X-1, 55	677.85	2.37	19.77	2.71	0.020	0.050	0.34	1.10	14	6.7
79X-1, 43	687.33	1.36	11.32	1.68	0.030	0.180	0.32	0.80	12	1.8
80X-3, 74	700.24	1.16	9.63	1.50	0.040	0.370	0.34	0.97	8	0.9
80X-5, 13	702.63	1.34	11.13	1.70	0.030	0.210	0.36	0.74	12	1.7
81X-2, 90	708.50	0.56	4.67	0.87	0.030	0.250	0.31	0.78	10	1.2
81X-3, 78	709.88	0.93	7.75	1.23	0.040	0.250	0.30	1.28	8	1.2
85X-1, 83	735.73	3.06	25.52	3.42	0.030	0.180	0.36	1.17	12	2.0
86X-1, 15	744.65	1.94	16.20	2.39	0.050	0.100	0.45	1.37	10	4.5
87X-1, 73	754.83	2.86	23.84	3.27	0.030	0.180	0.41	0.71	13	2.3
87X-2, 60	756.00	3.53	29.42	3.86	0.030	0.070	0.33	0.82	10	4.7
88X-1, 70	764.30	2.56	21.29	3.00	0.040	0.040	0.44	1.20	12	11.1
88X-2, 57	765.67	2.20	18.36	2.62	0.040	0.200	0.42	1.16	10	2.1
89X-CC, 44	773.64	2.83	23.57	3.21	0.030	0.160	0.38	0.96	13	2.4
90X-1, 40	783.30	4.07	33.90	4.43	0.030	0.150	0.36	1.16	13	2.4
92X-1, 44	802.54	2.82	23.50	3.27	0.030	0.110	0.45	1.20	14	4.1

Table T21 (continued). (Continued on next page.)

Core, section, interval (cm)	Depth CSF-A (m)	IC (wt%)	$CaCO_3$ (wt%)	TC (wt%)	TN (wt%)	TS (wt%)	TOC_{DIFF} (wt%)	TOC_{SRA} (wt%)	TOC_{DIFF}/TN	TOC_{DIFF}/TS
93X-CC, 18	811.88	2.84	23.67	3.15	0.020	0.120	0.31	0.68	13	2.6
94X-1, 15	821.45	0.81	6.77	1.66	0.030	0.260	0.85	1.09	33	3.3
317-U1352C-										
2R-1, 76	575.46	4.77	39.73	5.08	0.040	0.170	0.31	1.02	8	1.8
3R-1, 114	585.54	3.48	28.98	3.60	0.030	0.240	0.12	ND	4	0.5
4R-6, 20	600.78	6.56	54.64	6.67	0.020	0.070	0.11	ND	5	1.6
6R-1, 73	660.73	0.97	8.11	1.19	0.030	0.060	0.22	ND	7	3.6
7R-2, 43	670.69	1.72	14.34	2.06	0.040	0.350	0.34	0.90	9	1.0
8R-1, 1	679.31	3.12	26.00	3.49	0.020	0.050	0.37	0.55	17	7.4
9R-C, 7	689.91	2.77	23.04	2.96	0.030	0.090	0.19	ND	7	2.2
10R-1, 46	699.16	2.63	21.88	2.94	0.030	0.020	0.31	ND	12	15.7
11R-1, 66	709.06	0.67	5.54	0.84	0.050	0.280	0.17	0.94	4	0.6
12R-1, 8	718.18	4.89	40.70	5.03	0.030	0.040	0.14	ND	5	3.6
13R-1, 18	727.98	5.63	46.94	5.91	0.010	0.010	0.28	ND	21	27.5
14R-2, 73	739.73	1.71	14.22	2.02	0.040	0.140	0.31	0.69	7	2.2
15R-2, 60	749.16	3.86	32.12	4.34	0.030	0.010	0.48	0.78	16	48.4
16R-1, 27	757.17	3.04	25.34	3.58	0.040	0.040	0.54	ND	14	13.5
17R-1, 31-CARB	766.91	3.57	29.77	3.71	0.030	0.090	0.14	0.98	4	1.5
17R-1, 31-XRD	766.91	3.53	29.44	3.72	0.040	0.000	0.19	ND	5	ND
18R-1, 91	777.21	3.39	28.24	3.74	0.030	0.050	0.35	0.75	11	7.0
19R-2, 11	787.61	1.96	16.33	2.52	0.060	0.190	0.56	0.91	10	2.9
20R-2, 5	797.14	3.96	32.96	4.27	0.030	0.030	0.31	ND	10	10.5
22R-2, 95	817.37	6.00	49.95	6.22	0.020	0.030	0.22	ND	11	7.5
23R-2, 25	825.85	1.59	13.21	1.94	0.030	0.100	0.35	0.79	10	3.5
23R-CC, 12	826.46	3.17	26.44	3.39	0.030	0.020	0.22	0.55	7	10.8
24R-2, 75	836.38	4.34	36.13	4.44	0.020	0.070	0.10	0.46	5	1.5
25R-2, 47	845.77	4.55	37.94	5.67	0.020	0.000	1.12	ND	46	ND
26R-2, 37	854.95	5.04	41.98	5.60	0.020	0.000	0.56	0.60	24	ND
27R-1, 79	863.79	4.53	37.77	4.91	0.020	0.000	0.38	0.72	25	ND
28R-2, 82	874.73	3.40	28.35	3.72	0.030	0.000	0.32	ND	11	ND
29R-3, 21	884.54	3.68	30.64	3.81	0.030	0.000	0.13	ND	5	ND
30R-1, 32	892.12	4.27	35.57	4.53	0.030	0.000	0.26	1.10	9	ND
31R-2, 44	903.20	5.15	42.90	5.96	0.020	0.010	0.81	0.75	37	81.0
32R-1, 14	911.04	4.80	40.00	5.03	0.030	0.030	0.23	0.66	8	7.6
33R-3, 50	923.75	2.07	17.25	2.63	0.050	0.010	0.56	1.05	12	55.9
34R-1, 47	930.57	2.16	17.96	2.77	0.040	0.070	0.61	0.99	15	8.8
35R-2, 99	942.19	2.60	21.69	3.21	0.040	0.050	0.61	0.65	17	12.1
36R-1, 70	950.10	2.58	21.52	2.83	0.040	0.000	0.25	0.81	7	ND
37R-1, 86	959.86	4.70	39.15	4.83	0.020	0.050	0.13	0.63	6	2.6
38R-5, 145	975.95	4.85	40.38	5.62	0.020	0.020	0.77	0.76	43	38.6
39R-4, 128	983.88	4.51	37.59	4.65	0.020	0.070	0.14	0.87	7	2.0
40R-3, 100	991.51	4.14	34.46	4.38	0.030	0.070	0.24	0.84	8	3.5
41R-2, 118	999.98	4.99	41.55	5.20	0.020	0.040	0.21	0.75	10	5.3
42R-3, 14	1009.58	2.58	21.51	2.83	0.030	0.060	0.25	0.71	8	4.1
43R-2, 78	1018.71	4.93	41.07	5.14	0.020	0.030	0.21	0.92	10	7.0
44R-4- 39	1030.87	5.24	43.63	5.51	0.020	0.060	0.27	0.53	14	4.5
45R-1, 79	1036.49	2.17	18.08	2.60	0.030	0.070	0.43	0.84	13	6.1
46R-2, 16	1046.90	2.90	24.13	3.21	0.020	0.050	0.31	0.89	14	6.3
49R-1, 108	1074.88	5.12	42.66	6.12	0.010	0.000	1.00	0.44	125	ND
50R-1, 59	1083.89	4.23	35.25	5.49	0.010	0.000	1.26	0.47	97	ND
51R-3, 15	1096.02	1.79	14.92	2.30	0.030	0.010	0.51	0.58	20	50.8
51R-3, 84	1096.71	5.08	42.34	5.93	0.010	0.000	0.85	0.46	85	ND
52R-2, 64	1104.54	3.86	32.19	4.94	0.010	0.000	1.08	0.56	108	ND
53R-1, 52	1112.62	1.96	16.30	2.55	0.020	0.010	0.59	0.63	25	59.3
53R-2, 52	1114.06	6.03	50.25	6.20	0.010	0.000	0.17	0.80	19	ND
54R-2, 57	1123.77	2.31	19.22	2.78	0.030	0.050	0.47	0.80	17	9.4
55R-4, 23	1135.73	4.73	39.38	5.57	0.010	0.000	0.84	0.54	94	ND
55R-4, 33	1135.83	2.18	18.16	2.32	0.020	0.000	0.14	0.83	8	ND
56R-1, 50	1141.40	2.77	23.10	3.18	0.020	0.020	0.41	0.87	19	20.3
57R-1, 24	1150.74	2.89	24.10	3.35	0.030	0.030	0.46	1.36	17	15.2
58R-1, 49	1160.59	3.05	25.39	3.68	0.030	0.020	0.63	1.08	23	31.6
59R-1, 85	1170.55	0.63	5.25	1.07	0.030	0.060	0.44	0.61	14	7.3
59R-3, 76	1173.46	4.03	33.55	4.39	0.020	0.000	0.36	0.93	17	ND
60R-2, 91	1181.81	5.81	48.41	6.30	0.020	0.000	0.49	0.86	29	ND
61R-1, 98	1189.98	0.77	6.44	1.50	0.050	0.330	0.73	0.56	15	2.2
62R-4, 136	1204.46	2.36	19.63	2.87	0.020	0.000	0.51	1.14	22	ND
63R-CC, 14	1208.34	3.50	29.14	4.32	0.020	0.020	0.82	1.13	39	41.1
65R-1, 26	1221.66	7.37	61.41	7.70	0.020	0.000	0.33	0.83	22	ND
65R-1, 75	1222.15	5.37	44.69	6.01	0.020	0.000	0.64	1.23	27	ND

Table T21 (continued). (Continued on next page.)

Core, section, interval (cm)	Depth CSF-A (m)	IC (wt%)	$CaCO_3$ (wt%)	TC (wt%)	TN (wt%)	TS (wt%)	TOC_{DIFF} (wt%)	TOC_{SRA} (wt%)	TOC_{DIFF}/TN	TOC_{DIFF}/TS
70R-1, 112	1247.82	5.20	43.28	5.76	0.030	0.000	0.56	1.18	22	ND
71R-1, 85	1257.15	5.01	41.76	5.49	0.020	0.000	0.48	0.95	26	ND
72R-1, 26	1266.06	4.51	37.60	5.16	0.020	0.010	0.65	0.94	40	64.7
73R-4 80	1280.30	0.96	7.99	1.29	0.030	0.230	0.33	0.83	11	1.4
73R-5, 69	1281.69	2.67	22.21	3.08	0.020	0.000	0.41	0.71	17	ND
77R-1, 60	1309.00	4.00	33.35	4.39	0.020	0.000	0.39	0.72	17	ND
78R-3, 86	1317.20	3.93	32.72	4.40	0.010	0.000	0.47	0.92	34	ND
79R-1, 20	1318.10	4.16	34.63	4.77	0.020	0.010	0.61	1.03	34	61.2
80R-1, 79	1323.69	3.11	25.94	3.53	0.020	0.020	0.42	0.90	22	20.8
81R-1, 81	1328.31	2.57	21.37	3.07	0.030	0.000	0.50	0.94	19	ND
82R-1, 25	1332.75	3.17	26.40	3.68	0.020	0.030	0.51	0.77	32	17.0
85R-2, 101	1349.21	4.32	35.99	4.73	0.020	0.040	0.41	1.26	20	10.2
85R-4, 21	1351.41	1.56	12.96	1.72	0.030	0.270	0.16	0.72	6	0.6
86R-2, 13	1353.29	5.64	47.02	6.05	0.020	0.000	0.41	0.89	24	ND
87R-1, 135	1362.75	4.57	38.06	4.85	0.010	ND	0.28	1.19	25	ND
88R-2, 57	1373.07	0.74	6.14	1.23	0.030	0.040	0.49	0.95	20	12.3
88R-5, 129	1378.29	0.48	4.02	0.69	0.020	0.330	0.21	0.44	9	0.6
89R-3, 93	1384.35	0.78	6.53	1.22	0.020	0.120	0.44	0.83	20	3.6
89R-4, 15	1385.04	1.29	10.75	1.79	0.030	0.320	0.50	0.84	17	1.6
89R-4, 82	1385.71	1.64	13.69	2.33	0.040	0.010	0.69	1.47	17	68.6
90R-1, 32	1390.52	0.41	3.42	0.73	0.020	0.380	0.32	0.38	13	0.8
90R-3, 20	1393.40	3.44	28.62	4.43	0.060	ND	0.99	0.92	18	ND
91R-1, 126	1401.06	6.76	56.31	7.46	0.020	ND	0.70	0.81	37	ND
94R-1, 32	1428.92	5.20	43.31	5.65	0.020	0.000	0.45	0.97	23	ND
94R-6, 49	1436.59	2.50	20.82	3.10	0.030	0.090	0.60	0.97	19	6.7
95R-2, 41	1440.21	4.35	36.27	4.79	0.020	ND	0.43	1.15	19	ND
99R-1, 64	1477.64	6.02	50.18	6.69	0.020	ND	0.67	0.97	42	ND
102R-CC, 7	1496.47	3.71	30.92	4.19	0.020	ND	0.48	0.73	28	ND
103R-1, 60	1506.70	4.72	39.31	5.25	0.020	0.000	0.53	0.92	30	ND
103R-2, 63	1508.23	4.49	37.37	4.94	0.020	0.000	0.45	1.28	22	ND
103R-5, 114	1513.24	2.05	17.07	2.39	0.030	0.170	0.34	0.80	14	2.0
104R-1, 75	1516.55	4.24	35.34	4.62	0.010	ND	0.38	0.92	34	ND
105R-1, 67	1526.17	4.62	38.50	5.09	0.020	0.010	0.47	1.00	21	46.8
105R-1, 70	1526.20	5.44	45.32	6.11	0.020	ND	0.67	0.89	38	ND
106R-4, 45	1540.15	4.49	37.44	5.11	0.020	ND	0.62	0.62	35	ND
106R-6, 29	1542.35	2.07	17.26	2.50	0.020	ND	0.42	0.91	25	ND
107R-2, 8	1546.48	5.38	44.77	6.07	0.020	ND	0.69	1.37	37	ND
107R-3, 131	1549.21	6.35	52.93	6.87	0.020	ND	0.52	1.13	30	ND
108R-4, 24	1558.94	2.77	23.07	3.26	0.020	ND	0.49	1.23	24	ND
109R-1, 89	1565.29	5.54	46.18	6.04	0.020	ND	0.50	1.20	22	ND
109R-3, 81	1568.05	3.02	25.18	3.66	0.020	ND	0.64	1.46	36	ND
110R-2, 26-A	1575.83	1.73	14.43	2.97	0.040	ND	1.24	1.77	33	ND
110R-2, 26-B	1575.83	1.43	11.93	2.85	0.050	ND	1.42	1.84	29	ND
110R-2, 26-GEO	1575.83	1.57	13.12	2.59	0.040	ND	1.02	1.46	26	ND
110R-3, 7	1577.08	2.39	19.90	3.14	0.030	ND	0.75	1.23	26	ND
111R-1, 94	1584.74	1.01	8.41	1.53	0.030	ND	0.52	0.93	20	ND
111R-4, 34	1588.45	8.12	67.65	8.43	0.000	ND	0.31	0.87	65	ND
112R-1, 61	1594.11	7.58	63.14	7.86	0.010	ND	0.28	0.32	44	ND
112R-3, 26	1596.68	2.82	23.50	3.55	0.030	ND	0.73	1.12	25	ND
113R-2, 53	1605.23	6.54	54.49	7.52	0.010	ND	0.98	1.08	82	ND
113R-4, 111	1608.81	6.47	53.87	6.80	0.020	ND	0.33	0.90	19	ND
114R-3, 113	1617.03	4.84	40.30	5.24	0.020	ND	0.40	0.59	26	ND
114R-4, 63	1618.03	7.84	65.35	7.87	0.000	ND	0.03	0.65	6	ND
115R-6, 15	1630.35	2.30	19.18	3.67	0.040	ND	1.37	1.01	37	ND
115R-6, 82	1631.02	8.18	68.14	8.60	0.010	ND	0.42	1.04	59	ND
116R-2, 40	1634.30	8.09	67.37	8.36	0.010	ND	0.27	0.94	39	ND
116R-3, 27	1635.67	6.67	55.55	7.11	0.020	ND	0.44	1.30	25	ND
117R-3, 52	1644.79	3.56	29.68	4.19	0.020	ND	0.63	0.85	27	ND
117R-6, 29	1649.06	7.71	64.23	7.78	0.010	ND	0.07	0.65	10	ND
118R-3, 67	1654.38	5.36	44.64	5.65	0.020	ND	0.29	1.10	19	ND
118R-3, 114	1654.85	4.76	39.68	5.21	0.020	ND	0.45	0.53	26	ND
119R-4, 45	1666.45	1.17	9.78	1.88	0.040	ND	0.71	1.24	20	ND
119R-4, 68	1666.68	6.90	57.51	7.29	0.010	ND	0.39	1.10	39	ND
120R-CC, 0	1668.90	3.72	30.97	4.42	0.020	ND	0.70	0.76	32	ND
120R-CC, 34	1669.24	6.06	50.52	6.38	0.010	ND	0.32	1.00	24	ND
122R-1, 77	1688.87	4.97	41.44	5.50	0.020	ND	0.53	1.45	27	ND
122R-2, 66	1690.26	8.59	71.56	8.94	0.010	ND	0.35	0.60	35	ND
123R-1, 73	1693.23	3.53	29.39	4.23	0.020	ND	0.70	0.61	36	ND
123R-2, 65	1694.65	9.20	76.59	9.21	0.010	ND	0.01	0.61	3	ND

Table T21 (continued).

Core, section, interval (cm)	Depth CSF-A (m)	IC (wt%)	$CaCO_3$ (wt%)	TC (wt%)	TN (wt%)	TS (wt%)	TOC_{DIFF} (wt%)	TOC_{SRA} (wt%)	TOC_{DIFF}/TN	TOC_{DIFF}/TS
124R-6, 102	1705.96	6.83	56.91	7.15	0.010	ND	0.32	1.04	31	ND
125R-2, 91	1709.41	3.70	30.86	4.06	0.020	ND	0.36	0.69	15	ND
125R-5, 116	1714.16	6.63	55.25	6.85	0.010	ND	0.22	0.46	36	ND
126R-3, 101	1720.51	9.41	78.36	9.65	0.010	ND	0.24	0.46	21	ND
126R-6, 54	1724.31	9.38	78.14	9.62	0.010	ND	0.24	0.46	46	ND
127R-2, 36	1728.06	9.36	77.95	9.49	0.010	ND	0.13	0.65	26	ND
127R-3, 111	1730.22	4.85	40.39	5.36	0.020	ND	0.51	0.53	29	ND
128R-1, 58	1736.38	10.27	85.58	10.40	0.000	ND	0.13	0.52	ND	ND
128R-5, 12	1741.69	0.82	6.87	1.55	0.060	ND	0.73	1.10	13	ND
129R-1, 4	1745.44	9.62	80.16	9.86	0.000	ND	0.24	ND	115	ND
129R-2, 104*	1747.88	9.13	76.06	9.23	0.000	ND	0.10	0.24	24	ND
129R-2, 104†	1747.88	4.41	36.77	4.70	0.020	ND	0.29	0.57	14	ND
130R-2, 70	1757.20	10.02	83.45	10.08	0.000	ND	0.06	0.43	140	ND
130R-3, 65	1758.63	3.53	29.39	3.86	0.020	ND	0.33	0.55	16	ND
130R-4, 103*	1760.44	10.04	83.65	10.16	0.000	ND	0.12	0.22	35	ND
130R-4, 103†	1760.44	3.77	31.36	4.01	0.010	ND	0.24	0.48	20	ND
131R-2, 96*	1766.98	10.65	88.71	10.70	0.000	ND	0.05	0.23	17	ND
131R-2, 96†	1766.98	3.51	29.25	3.67	0.020	ND	0.16	0.43	10	ND
131R-2, 111	1767.13	10.51	87.52	10.81	0.000	ND	0.30	0.41	174	ND
132R-3, 9	1776.86	8.09	67.38	8.31	0.010	ND	0.22	0.48	33	ND
132R-3, 61	1777.38	4.33	36.04	4.38	0.010	ND	0.05	0.24	5	ND
133R-2, 144	1786.74	3.46	28.83	3.64	0.020	ND	0.18	0.48	8	ND
133R-3, 61	1787.37	10.38	86.49	10.65	0.000	ND	0.27	0.38	200	ND
134R-1, 78	1794.18	2.41	20.11	2.58	0.020	ND	0.17	0.58	7	ND
134R-3, 70	1796.58	10.24	85.31	10.28	0.000	ND	0.04	0.38	41	ND
135R-1, 84	1803.84	10.40	86.60	10.57	0.000	ND	0.17	0.39	343	ND
135R-4, 52	1807.91	2.82	23.47	2.93	0.020	ND	0.11	0.51	6	ND
136R-3, 127	1816.86	2.68	22.32	2.96	0.020	ND	0.28	0.65	13	ND
136R-4, 141	1818.50	3.60	29.98	3.77	0.020	ND	0.17	0.76	10	ND
136R-5, 27	1818.86	10.75	89.59	10.93	0.000	ND	0.18	0.45	747	ND
137R-4, 119	1827.88	10.90	90.82	11.04	0.000	ND	0.14	ND	220	ND
137R-5, 63	1828.82	5.90	49.17	5.96	0.010	ND	0.06	0.47	8	ND
138R-1, 94	1832.84	10.07	83.92	10.30	0.000	ND	0.23	0.49	ND	ND
138R-4, 13	1836.52	10.70	89.15	11.22	0.000	ND	0.52	0.73	877	ND
138R-4, 134	1837.73	3.29	27.44	3.62	0.020	ND	0.33	1.08	14	ND
139R-1, 60	1842.10	3.08	25.64	3.20	0.020	ND	0.12	0.69	7	ND
139R-1, 86	1842.36	10.52	87.66	10.75	0.000	ND	0.23	0.44	ND	ND
140R-1, 16	1851.26	10.54	87.79	10.94	0.000	ND	0.40	0.34	499	ND
140R-1, 35	1851.45	9.42	78.44	10.88	0.000	ND	1.46	0.55	1,514	ND
140R-2, 53	1852.69	11.58	96.44	12.35	0.090	ND	0.77	0.24	8	ND
141R-1, 89	1861.69	11.51	95.88	11.60	0.000	ND	0.09	0.33	ND	ND
143R-2, 70	1877.20	11.54	96.16	11.66	0.000	ND	0.12	0.30	ND	ND
144R-4 7	1884.24	11.53	96.08	11.72	0.000	ND	0.19	0.29	ND	ND
145R-3, 45	1892.90	11.20	93.30	11.46	0.000	ND	0.26	0.45	ND	ND
146R-3 77	1902.47	11.01	91.68	10.88	0.000	ND	–0.13	0.42	ND	ND
147R-3, 35	1911.56	10.82	90.12	10.91	0.000	ND	0.09	0.35	ND	ND
147R-4, 55	1913.23	4.55	37.89	5.09	0.010	ND	0.54	0.87	40	ND
147R-6, 71*	1916.31	9.96	82.94	9.94	0.000	ND	–0.02	0.45	ND	ND
147R-6, 71†	1916.31	5.36	44.67	5.69	0.010	ND	0.33	0.69	26	ND
148R-3, 56	1921.41	6.19	51.59	6.69	0.010	ND	0.50	0.66	45	ND
148R-5, 59	1924.03	10.73	89.41	10.86	0.000	ND	0.13	0.69	ND	ND

Notes: * = white layer, † = black layer. Inorganic carbon (IC) is from coulometric measurement of acid-evolved CO_2. $CaCO_3$ is calculated from IC × 8.33. Total carbon (TC), total nitrogen (TN), and total sulfur (TS) are from elemental analysis of sediments. TOC_{DIFF} = total organic carbon from difference of TC and IC. TOC_{SRA} = total organic carbon from source rock analyzer pyrolysis (see Table T22). ND = not determined. CARB, CHNS, XRD, A, B, and GEO refer to separate aliquots of the same sample that were analyzed separately.

Table T22. Source rock analyzer pyrolysis evaluation of organic matter in sediments, Site U1352. (See table notes.) (Continued on next six pages.)

Core, section, interval (cm)	Depth CSF-A (m)	S_1 (mg HC/g rock)	S_2 (mg HC/g rock)	S_3 (mg HC/g rock)	T_{max} (°C)	TOC_{SRA} (wt%)	Hydrogen index (mg S_2/g TOC)	Oxygen index (mg S_3/g TOC)	Pyrolysis carbon	Production index
317-U1352B-										
1H-3, 29	3.29	0.08	0.18	0.30	406.2	0.81	22.2	37.0	0.022	30.8
1H-3, 91	3.91	0.04	0.09	0.15	399.6	0.54	16.7	27.8	0.011	30.8
2H-3, 80	12.00	0.03	0.05	0.06	ND	0.59	8.5	10.2	0.007	37.5
2H-7, 9	16.79	0.04	0.15	0.04	ND	0.46	32.6	8.7	0.016	21.1
3H-5, 143	25.13	0.03	0.06	0.42	ND	0.78	7.7	53.8	0.007	33.3
3H-6, 66	25.86	0.06	0.16	0.36	ND	0.59	27.1	61.0	0.018	27.3
4H-2, 139	30.09	0.06	0.13	0.30	369.2	0.51	25.5	58.8	0.016	31.6
4H-6, 17	34.87	0.05	0.17	0.06	ND	0.78	21.8	7.7	0.018	22.7
5H-6, 71	43.63	0.04	0.07	0.12	ND	0.78	9.0	15.4	0.009	36.4
6H-3, 84	50.04	0.06	0.13	0.70	382.8	0.85	15.3	82.4	0.016	31.6
6H-5, 55	52.75	0.04	0.09	0.26	361.3	0.66	13.6	39.4	0.011	30.8
7H-2, 16	57.36	0.06	0.15	0.39	430.9	0.69	21.7	56.5	0.017	28.6
7H-6, 72	63.92	0.11	0.39	0.54	421.6	1.01	38.6	53.5	0.042	22.0
8H-3, 82	69.02	0.03	0.07	0.07	ND	0.59	11.9	11.9	0.008	30.0
8H-CC, 46	75.02	0.06	0.11	0.14	ND	0.62	17.7	22.6	0.014	35.3
9H-3, 75	78.45	0.07	0.15	0.07	398.9	0.56	26.8	12.5	0.018	31.8
9H-6, 34	82.54	0.09	0.25	0.91	389.9	0.89	28.1	102.2	0.028	26.5
10H-3, 118	87.14	0.14	0.29	0.26	399.1	0.89	32.6	29.2	0.036	32.6
10H-4, 53	87.99	0.07	0.16	0.15	409.5	0.66	24.2	22.7	0.019	30.4
11H-3, 130	98.00	0.11	0.37	0.60	414.1	0.85	43.5	70.6	0.040	22.9
11H-4, 127	99.45	0.08	0.18	0.14	395.2	0.79	22.8	17.7	0.022	30.8
12H-4, 84	108.50	0.12	0.31	0.30	418.5	0.87	35.6	34.5	0.036	27.9
12H-6, 100	111.66	0.13	0.28	0.42	421.9	0.62	45.2	67.7	0.034	31.7
13H-3, 44	116.12	0.17	0.24	0.20	389.8	0.92	26.1	21.7	0.034	41.5
13H-6, 46	120.64	0.08	0.18	0.12	393.0	0.53	34.0	22.6	0.022	30.8
14H-3, 75	125.95	0.11	0.32	0.21	382.6	0.70	45.7	30.0	0.036	25.6
14H-5, 143	129.63	0.23	0.75	0.67	406.5	0.85	88.2	78.8	0.081	23.5
15H-1, 122	132.92	0.09	0.25	0.16	ND	0.44	56.8	36.4	0.028	26.5
16H-4, 92	146.59	0.07	0.16	0.10	383.0	0.53	30.2	18.9	0.019	30.4
16H-7, 43	150.47	0.20	0.61	0.67	399.1	1.00	61.0	67.0	0.067	24.7
17H-2, 42	152.62	0.12	0.36	0.27	426.2	0.80	45.0	33.8	0.040	25.0
17H-4, 77	155.26	0.06	0.16	0.04	ND	0.45	35.6	8.9	0.018	27.3
18H-2, 115	158.85	0.14	0.52	0.52	ND	0.80	65.0	65.0	0.055	21.2
18H-3, 34	159.54	0.12	0.45	0.40	411.4	1.04	43.3	38.5	0.047	21.1
19H-1, 78	166.48	0.09	0.20	0.06	ND	0.41	48.8	14.6	0.024	31.0
20H-1, 43	175.13	0.07	0.23	0.05	371.7	0.57	40.4	8.8	0.025	23.3
21H-3, 62	183.32	0.21	0.75	0.57	409.0	1.19	63.0	47.9	0.080	21.9
21H-6, 43	187.63	0.11	0.30	0.17	389.8	0.71	42.3	23.9	0.034	26.8
22H-1, 112	190.32	0.10	0.29	0.27	409.2	0.77	37.7	35.1	0.032	25.6
22H-7, 52	198.72	0.26	0.92	0.69	416.5	1.57	58.6	43.9	0.098	22.0
23H-3, 117	202.87	0.12	0.36	0.13	394.3	0.79	45.6	16.5	0.040	25.0
23H-5, 130	206.00	0.29	1.01	0.50	415.3	1.33	75.9	37.6	0.108	22.3
24H-5, 94	215.14	0.11	0.24	0.24	419.6	0.87	27.6	27.6	0.029	31.4
24H-6, 139	217.09	0.23	0.71	0.36	408.5	1.12	63.4	32.1	0.078	24.5
25H-2, 70	219.90	0.07	0.11	0.15	393.3	0.59	18.6	25.4	0.015	38.9
25H-6, 72	225.92	0.18	0.51	0.34	ND	1.30	39.2	26.2	0.057	26.1
26H-1, 77	227.97	0.08	0.21	0.08	401.3	0.85	24.7	9.4	0.024	27.6
26H-6, 41	235.03	0.12	0.28	0.13	400.6	0.92	30.4	14.1	0.033	30.0

Table T22 (continued). (Continued on next page.)

Core, section, interval (cm)	Depth CSF-A (m)	S_1 (mg HC/g rock)	S_2 (mg HC/g rock)	S_3 (mg HC/g rock)	T_{max} (°C)	TOC_{SRA} (wt%)	Hydrogen index (mg S_2/g TOC)	Oxygen index (mg S_3/g TOC)	Pyrolysis carbon	Production index
27H-3, 120	240.90	0.12	0.32	0.20	389.5	0.65	49.2	30.8	0.037	27.3
27H-5, 78	243.48	0.23	0.80	0.49	405.6	1.14	70.2	43.0	0.085	22.3
28H-3, 75	249.88	0.22	0.83	0.71	416.8	1.30	63.8	54.6	0.087	21.0
28H-4, 41	250.54	0.11	0.33	0.14	413.0	0.53	62.3	26.4	0.037	25.0
29H-1, 117	252.37	0.10	0.33	0.17	398.9	1.25	26.4	13.6	0.036	23.3
30H-1, 78	258.48	0.06	0.16	0.26	408.0	0.77	20.8	33.8	0.018	27.3
31H-2, 26	268.96	0.09	0.28	0.08	ND	0.92	30.4	8.7	0.031	24.3
32H-2, 102	274.72	0.10	0.24	0.19	395.4	0.70	34.3	27.1	0.028	29.4
32H-CC, 56	281.40	0.10	0.41	0.72	421.1	1.04	39.4	69.2	0.042	19.6
33H-4, 68	285.32	0.15	0.53	0.57	411.4	1.00	53.0	57.0	0.056	22.1
34H-5, 95	292.09	0.08	0.22	0.22	395.2	0.99	22.2	22.2	0.025	26.7
35H-2, 31	294.65	0.20	0.84	0.56	422.0	1.40	60.0	40.0	0.086	19.2
36H-2, 39-CARB	296.89	0.19	0.92	0.58	420.0	1.18	78.0	49.2	0.092	17.1
36H-2, 39-CHNS	296.89	0.16	0.78	0.69	424.9	1.05	74.3	65.7	0.078	17.0
37X-2, 57	299.07	0.12	0.20	0.48	410.4	1.20	16.7	40.0	0.027	37.5
38X-2, 88	304.98	0.28	1.03	0.63	412.9	1.42	72.5	44.4	0.109	21.4
38X-5, 128	309.88	0.05	0.16	ND	ND	0.28	57.1	ND	0.017	23.8
39X-3, 97	316.17	0.11	0.32	0.09	437.9	0.49	65.3	18.4	0.036	25.6
39X-6, 29	319.99	0.15	0.76	1.07	420.4	1.61	47.2	66.5	0.076	16.5
40X-1, 82	322.72	0.12	0.29	0.25	405.2	0.81	35.8	30.9	0.034	29.3
40X-3, 49	325.39	0.16	0.67	0.47	427.2	1.16	57.8	40.5	0.069	19.3
41X-3, 82	335.32	0.24	0.84	0.36	421.2	1.38	60.9	26.1	0.090	22.2
41X-5, 72	338.22	0.05	0.16	0.11	386.1	0.39	41.0	28.2	0.017	23.8
42X-1, 92	342.02	0.07	0.18	ND	386.8	0.75	24.0	ND	0.021	28.0
42X-5, 140	348.50	0.35	1.48	ND	409.9	1.83	80.9	ND	0.152	19.1
43X-2, 87	353.07	0.32	1.08	ND	415.8	1.85	58.4	ND	0.116	22.9
44X-2, 77	362.67	0.05	0.10	0.09	409.0	0.48	20.8	18.8	0.012	33.3
44X-2, 80	362.70	0.11	0.35	0.15	390.5	0.71	49.3	21.1	0.038	23.9
46X-5, 73	386.31	0.06	0.16	ND	405.8	0.80	20.0	ND	0.018	27.3
47X-3, 87	393.07	0.20	0.75	0.45	409.9	1.50	50.0	30.0	0.079	21.1
47X-6, 72	397.42	0.06	0.16	ND	391.0	0.84	19.0	ND	0.018	27.3
48X-3, 64	402.34	0.08	0.23	0.07	401.1	0.63	36.5	11.1	0.026	25.8
48X-5, 123	405.93	0.09	0.25	ND	420.1	0.69	36.2	ND	0.028	26.5
49X-1, 62	408.92	0.07	0.23	ND	405.9	0.36	63.9	ND	0.025	23.3
50X-4, 95	423.35	0.30	1.38	0.63	ND	1.29	107.0	48.8	0.139	17.9
50X-6, 110	426.50	0.06	0.21	ND	413.3	0.43	48.8	ND	0.022	22.2
51X-1, 33	427.83	0.30	1.33	0.69	416.3	2.07	64.3	33.3	0.135	18.4
51X-2, 35	429.35	0.09	0.27	0.05	ND	0.83	32.5	6.0	0.030	25.0
52X-4, 70	442.30	0.07	0.18	ND	412.7	0.66	27.3	ND	0.021	28.0
52X-7, 56	446.36	0.11	0.58	ND	419.2	0.94	61.7	ND	0.057	15.9
53X-1, 118	447.88	0.10	0.44	0.29	411.8	1.03	42.7	28.2	0.045	18.5
53X-6, 87	455.04	0.12	0.34	0.11	397.6	1.25	27.2	8.8	0.038	26.1
54X-1, 112	457.42	0.13	0.38	0.14	ND	1.23	30.9	11.4	0.042	25.5
54X-5, 28	462.58	0.10	0.42	0.27	414.8	1.03	40.8	26.2	0.043	19.2
55X-1, 9	465.99	0.24	0.96	0.35	404.4	1.35	71.1	25.9	0.100	20.0
56X-6, 33	483.33	0.14	0.50	0.37	407.0	1.07	46.7	34.6	0.053	21.9
56X-7, 57	484.67	0.10	0.34	0.18	416.1	1.23	27.6	14.6	0.037	22.7
57X-1, 85	485.95	0.08	0.22	0.18	385.0	1.03	21.4	17.5	0.025	26.7
57X-4, 43	490.03	0.09	0.41	0.32	423.5	1.22	33.6	26.2	0.042	18.0
58X-4, 72	498.64	0.10	0.20	0.13	406.8	1.00	20.0	13.0	0.025	33.3
59X-1, 104	505.34	0.09	0.17	0.19	392.3	0.84	20.2	22.6	0.022	34.6

Table T22 (continued). (Continued on next page.)

Core, section, interval (cm)	Depth CSF-A (m)	S_1 (mg HC/g rock)	S_2 (mg HC/g rock)	S_3 (mg HC/g rock)	T_{max} (°C)	TOC_{SRA} (wt%)	Hydrogen index (mg S_2/g TOC)	Oxygen index (mg S_3/g TOC)	Pyrolysis carbon	Production index
60X-1, 29	514.19	0.13	0.64	0.47	422.7	1.53	41.8	30.7	0.064	16.9
61X-1, 42	523.92	0.15	0.52	0.26	404.1	0.99	52.5	26.3	0.056	22.4
61X-2, 63	525.13	0.18	0.68	0.34	415.3	1.15	59.1	29.6	0.071	20.9
62X-4, 84	538.44	0.10	0.22	0.31	410.5	1.15	19.1	27.0	0.027	31.3
63X-4, 83	548.03	0.04	0.25	ND	400.1	0.48	52.1	ND	0.024	13.8
64X-3, 81	556.01	0.08	0.29	0.45	392.0	0.73	39.7	61.6	0.031	21.6
66X-1, 58	571.98	0.12	0.90	1.20	419.0	1.32	68.2	90.9	0.085	11.8
67X-CC, 16	573.49	0.11	0.77	1.08	412.8	1.38	55.8	78.3	0.073	12.5
68X-1, 71	581.81	0.05	0.23	0.37	424.4	0.71	32.4	52.1	0.023	17.9
71X-3, 42	613.32	0.04	0.44	0.44	420.0	1.22	36.1	36.1	0.040	8.3
72X-4, 80	624.77	0.05	0.16	0.28	411.5	0.91	17.6	30.8	0.017	23.8
73X-3, 57	632.67	0.06	0.23	0.45	417.8	1.11	20.7	40.5	0.024	20.7
74X-3, 76	642.46	0.04	0.14	0.62	402.2	1.01	13.9	61.4	0.015	22.2
74X-7, 10	647.60	0.05	0.20	0.39	415.9	0.83	24.1	47.0	0.021	20.0
75X-1, 130	649.60	0.05	0.20	0.59	406.2	1.01	19.8	58.4	0.021	20.0
75X-5, 71	655.01	0.05	0.21	0.72	415.0	0.81	25.9	88.9	0.022	19.2
76X-1, 40	658.30	0.04	0.19	0.64	415.4	0.74	25.7	86.5	0.019	17.4
76X-4, 75	663.15	0.03	0.11	ND	411.9	0.48	22.9	ND	0.012	21.4
77X-1, 61	668.21	0.06	0.31	0.64	415.5	1.05	29.5	61.0	0.031	16.2
77X-2, 46	669.56	0.05	0.29	0.63	425.9	0.76	38.2	82.9	0.028	14.7
78X-1, 38	677.68	0.05	0.45	ND	421.4	0.73	61.6	ND	0.042	10.0
78X-1, 55	677.85	0.03	0.31	ND	417.4	1.10	28.2	ND	0.028	8.8
79X-1, 43	687.33	0.07	0.26	ND	411.7	0.80	32.5	ND	0.027	21.2
80X-3, 74	700.24	0.07	0.34	0.58	416.2	0.97	35.1	59.8	0.034	17.1
80X-5, 13	702.63	0.05	0.33	0.49	406.6	0.74	44.6	66.2	0.032	13.2
81X-2, 90	708.50	0.06	0.20	0.32	415.8	0.78	25.6	41.0	0.022	23.1
81X-3, 78	709.88	0.06	0.24	0.56	396.4	1.28	18.8	43.8	0.025	20.0
85X-1, 83	735.73	0.05	0.32	0.64	419.0	1.17	27.4	54.7	0.031	13.5
86X-1, 15	744.65	0.10	0.61	ND	424.5	1.37	44.5	ND	0.059	14.1
87X-1, 73	754.83	0.06	0.32	ND	416.0	0.71	45.1	ND	0.032	15.8
87X-2, 60	756.00	0.06	0.46	0.58	418.7	0.82	56.1	70.7	0.043	11.5
88X-1, 70	764.30	0.06	0.37	0.88	417.7	1.20	30.8	73.3	0.036	14.0
88X-2, 57	765.67	0.07	0.49	0.72	425.0	1.16	42.2	62.1	0.046	12.5
89X-CC, 44	773.64	0.06	0.46	0.39	418.0	0.96	47.9	40.6	0.043	11.5
90X-1, 40	783.30	0.08	0.49	0.48	415.4	1.16	42.2	41.4	0.047	14.0
92X-1, 44	802.54	0.07	0.48	0.65	413.0	1.20	40.0	54.2	0.046	12.7
93X-CC, 18	811.88	0.04	0.32	0.34	414.5	0.68	47.1	50.0	0.030	11.1
94X-1, 15	821.45	0.06	0.34	0.41	416.5	1.09	31.2	37.6	0.033	15.0
317-U1352C-										
2R-1, 76	575.46	0.05	0.77	ND	419.4	1.02	75.5	ND	0.068	6.1
3R-1, 114	585.54	ND	ND	ND	ND	ND	ND	ND	ND	ND
4R-6, 20	600.78	ND	ND	ND	ND	ND	ND	ND	ND	ND
6R-1, 73	660.73	ND	ND	ND	ND	ND	ND	ND	ND	ND
7R-2, 43	670.69	0.03	0.32	ND	414.5	0.90	35.6	ND	0.029	8.6
8R-1, 1	679.31	0.03	0.42	ND	420.2	0.55	76.4	ND	0.037	6.7
9R-CC, 7	689.91	ND	ND	ND	ND	ND	ND	ND	ND	ND
10R-1, 46	699.16	ND	ND	ND	ND	ND	ND	ND	ND	ND
11R-1, 66	709.06	0.03	0.16	0.01	406.9	0.94	17.0	1.1	0.016	15.8
12R-1, 8	718.18	ND	ND	ND	ND	ND	ND	ND	ND	ND
13R-1, 18	727.98	ND	ND	ND	ND	ND	ND	ND	ND	ND
14R-2, 73	739.73	0.03	0.47	ND	420.0	0.69	68.1	ND	0.042	6.0

Table T22 (continued). (Continued on next page.)

Core, section, interval (cm)	Depth CSF-A (m)	S_1 (mg HC/g rock)	S_2 (mg HC/g rock)	S_3 (mg HC/g rock)	T_{max} (°C)	TOC_{SRA} (wt%)	Hydrogen index (mg S_2/g TOC)	Oxygen index (mg S_3/g TOC)	Pyrolysis carbon	Production index
15R-2, 60	749.16	0.09	0.53	0.35	422.70	0.78	67.9	44.9	0.052	14.5
16R-1, 27	757.17	ND	ND	ND	ND	ND	ND	ND	ND	ND
17R-1, 3-CARB	766.91	0.05	0.44	0.49	424.0	0.98	44.9	50.0	0.041	10.2
17R-1, 3-XRD	766.91	ND	ND	ND	ND	ND	ND	ND	ND	ND
18R-1, 91	777.21	0.06	0.52	0.40	421.60	0.75	69.3	53.3	0.048	10.3
19R-2, 11	787.61	0.08	0.72	0.60	413.2	0.91	79.1	65.9	0.066	10.0
20R-2, 5	797.14	ND	ND	ND	ND	ND	ND	ND	ND	ND
22R-2, 95	817.37	ND	ND	ND	ND	ND	ND	ND	ND	ND
23R-2, 25	825.85	0.03	0.34	ND	411.7	0.79	43.0	ND	0.031	8.1
23R-CC, 12	826.46	0.04	0.24	ND	412.6	0.55	43.6	ND	0.023	14.3
24R-2, 75	836.38	0.03	0.18	ND	411.0	0.46	39.1	ND	0.017	14.3
25R-2, 47	845.77	ND	ND	ND	ND	ND	ND	ND	ND	ND
26R-2, 37	854.95	0.04	0.37	0.11	423.00	0.60	61.7	18.3	0.034	9.8
27R-1, 79	863.79	0.02	0.14	ND	404.2	0.72	19.4	ND	0.013	12.5
28R-2, 82	874.73	ND	ND	ND	ND	ND	ND	ND	ND	ND
29R-3, 21	884.54	ND	ND	ND	ND	ND	ND	ND	ND	ND
30R-1, 32	892.12	0.04	0.31	0.29	424.7	1.10	28.2	26.4	0.029	11.4
31R-2, 44	903.20	0.02	0.24	ND	425.4	0.75	32.0	ND	0.022	7.7
32R-1, 14	911.04	0.04	0.41	ND	415.6	0.66	62.1	ND	0.037	8.9
33R-3, 50	923.75	0.07	0.50	0.85	416.80	1.05	47.6	81.0	0.047	12.3
34R-1, 47	930.57	0.04	0.44	0.46	418.8	0.99	44.4	46.5	0.040	8.3
35R-2, 99	942.19	0.03	0.35	0.31	419.4	0.65	53.8	47.7	0.032	7.9
36R-1, 70	950.10	0.04	0.37	0.68	430.7	0.81	45.7	84.0	0.034	9.8
37R-1, 86	959.86	0.03	0.28	0.26	420.0	0.63	44.4	41.3	0.026	9.7
38R-5, 145	975.95	0.01	0.24	ND	426.0	0.76	31.6	ND	0.021	4.0
39R-4, 128	983.88	0.04	0.44	0.48	429.7	0.87	50.6	55.2	0.040	8.3
40R-3, 100	991.51	0.04	0.42	0.47	420.9	0.84	50.0	56.0	0.038	8.7
41R-2, 118	999.98	0.05	0.43	0.22	424.4	0.75	57.3	29.3	0.040	10.4
42R-3, 14	1009.58	0.02	0.46	ND	425.5	0.71	64.8	ND	0.040	4.2
43R-2, 78	1018.71	0.04	0.40	0.02	422.7	0.92	43.5	2.2	0.037	9.1
44R-4- 39	1030.87	0.03	0.35	0.12	424.4	0.53	66.0	22.6	0.032	7.9
45R-1, 79	1036.49	0.03	0.63	ND	426.9	0.84	75.0	ND	0.055	4.5
46R-2, 16	1046.90	0.06	0.64	0.37	422.1	0.89	71.9	41.6	0.058	8.6
49R-1, 108	1074.88	0.02	0.21	ND	423.8	0.44	47.7	ND	0.019	8.7
50R-1, 59	1083.89	0.04	0.25	0.06	420.3	0.47	53.2	12.8	0.024	13.8
51R-3, 15	1096.02	0.03	0.45	ND	421.6	0.58	77.6	ND	0.040	6.3
51R-3, 84	1096.71	0.02	0.25	ND	424.1	0.46	54.3	ND	0.022	7.4
52R-2, 64	1104.54	0.03	0.19	ND	414.9	0.56	33.9	ND	0.018	13.6
53R-1, 52	1112.62	0.04	0.37	0.25	418.3	0.63	58.7	39.7	0.034	9.8
53R-2, 52	1114.06	0.03	0.23	0.12	423.2	0.80	28.8	15.0	0.022	11.5
54R-2, 57	1123.77	0.02	0.46	ND	421.8	0.80	57.5	ND	0.040	4.2
55R-4, 23	1135.73	0.02	0.19	ND	416.0	0.54	35.2	ND	0.017	9.5
55R-4, 33	1135.83	0.05	0.36	0.38	423.5	0.83	43.4	45.8	0.034	12.2
56R-1, 50	1141.40	0.04	0.35	0.21	420.4	0.87	40.2	24.1	0.032	10.3
57R-1, 24	1150.74	0.06	0.58	0.36	420.1	1.36	42.6	26.5	0.053	9.4
58R-1, 49	1160.59	0.06	0.68	0.50	425.6	1.08	63.0	46.3	0.061	8.1
59R-1, 85	1170.55	0.03	0.39	ND	416.0	0.61	63.9	ND	0.035	7.1
59R-3, 76	1173.46	0.02	0.45	ND	425.3	0.93	48.4	ND	0.039	4.3
60R-2, 91	1181.81	0.02	0.30	0.33	424.4	0.86	34.9	38.4	0.027	6.3
61R-1, 98	1189.98	0.03	0.28	ND	413.9	0.56	50.0	ND	0.026	9.7
62R-4, 136	1204.46	0.04	0.54	0.65	428.1	1.14	47.4	57.0	0.048	6.9

Table T22 (continued). (Continued on next page.)

Core, section, interval (cm)	Depth CSF-A (m)	S_1 (mg HC/g rock)	S_2 (mg HC/g rock)	S_3 (mg HC/g rock)	T_{max} (°C)	TOC_{SRA} (wt%)	Hydrogen index (mg S_2/g TOC)	Oxygen index (mg S_3/g TOC)	Pyrolysis carbon	Production index
63R-CC, 14	1208.34	0.03	0.36	0.52	423.9	1.13	31.9	46.0	0.032	7.7
65R-1, 26	1221.66	0.01	0.37	ND	427.6	0.83	44.6	ND	0.032	2.6
65R-1, 75	1222.15	0.03	0.68	ND	426.9	1.23	55.3	ND	0.059	4.2
70R-1, 112	1247.82	0.05	0.67	0.67	424.2	1.18	56.8	56.8	0.060	6.9
71R-1, 85	1257.15	0.04	0.45	0.64	424.1	0.95	47.4	67.4	0.041	8.2
72R-1, 26	1266.06	0.03	0.29	0.58	420.1	0.94	30.9	61.7	0.027	9.4
73R-4 80	1280.30	0.03	0.19	ND	418.1	0.83	22.9	ND	0.018	13.6
73R-5, 69	1281.69	0.04	0.33	0.04	414.5	0.71	46.5	5.6	0.031	10.8
77R-1, 60	1309.00	0.03	0.30	0.42	424.5	0.72	41.7	58.3	0.027	9.1
78R-3, 86	1317.20	0.03	0.28	0.29	406.5	0.92	30.4	31.5	0.026	9.7
79R-1, 20	1318.10	0.03	0.37	0.05	416.8	1.03	35.9	4.9	0.033	7.5
80R-1, 79	1323.69	0.03	0.26	0.42	412.0	0.90	28.9	46.7	0.024	10.3
81R-1, 81	1328.31	0.04	0.49	0.39	408.0	0.94	52.1	41.5	0.044	7.5
82R-1, 25	1332.75	0.03	0.31	0.07	418.3	0.77	40.3	9.1	0.028	8.8
85R-2, 101	1349.21	0.04	0.40	0.52	420.6	1.26	31.7	41.3	0.037	9.1
85R-4, 21	1351.41	0.03	0.21	0.15	407.4	0.72	29.2	20.8	0.020	12.5
86R-2, 13	1353.29	0.04	0.47	0.66	425.5	0.89	52.8	74.2	0.042	7.8
87R-1, 135	1362.75	0.03	0.25	0.60	420.8	1.19	21.0	50.4	0.023	10.7
88R-2, 57	1373.07	0.03	0.20	0.27	416.0	0.95	21.1	28.4	0.019	13.0
88R-5, 129	1378.29	0.03	0.17	ND	ND	0.44	38.6	ND	0.017	15.0
89R-3, 93	1384.35	0.07	0.58	0.58	422.90	0.83	69.9	69.9	0.054	10.8
89R-4, 15	1385.04	0.06	0.63	0.28	419.0	0.84	75.0	33.3	0.057	8.7
89R-4, 82	1385.71	0.07	0.86	0.54	420.8	1.47	58.5	36.7	0.077	7.5
90R-1, 32	1390.52	0.03	0.17	ND	414.6	0.38	44.7	ND	0.017	15.0
90R-3, 20	1393.40	0.03	0.20	0.45	428.6	0.92	21.7	48.9	0.019	13.0
91R-1, 126	1401.06	0.03	0.47	0.72	419.1	0.81	58.0	88.9	0.042	6.0
94R-1, 32	1428.92	0.02	0.32	0.40	427.1	0.97	33.0	41.2	0.028	5.9
94R-6, 49	1436.59	0.04	0.48	0.62	431.8	0.97	49.5	63.9	0.043	7.7
95R-2, 41	1440.21	0.03	0.30	0.36	425.8	1.15	26.1	31.3	0.027	9.1
99R-1, 64	1477.64	0.02	0.18	0.43	416.6	0.97	18.6	44.3	0.017	10.0
102R-CC, 7	1496.47	0.02	0.15	0.13	421.3	0.73	20.5	17.8	0.014	11.8
103R-1, 60	1506.70	0.02	0.18	0.21	422.3	0.92	19.6	22.8	0.017	10.0
103R-2, 63	1508.23	0.03	0.34	0.38	431.4	1.28	26.6	29.7	0.031	8.1
103R-5, 114	1513.24	0.02	0.16	0.34	413.7	0.80	20.0	42.5	0.015	11.1
104R-1, 75	1516.55	0.02	0.23	0.21	425.2	0.92	25.0	22.8	0.021	8.0
105R-1, 67	1526.17	0.02	0.29	0.39	432.9	1.00	29.0	39.0	0.026	6.5
105R-1, 70	1526.20	0.03	0.24	0.39	430.7	0.89	27.0	43.8	0.022	11.1
106R-4, 45	1540.15	0.02	0.15	ND	436.3	0.62	24.2	ND	0.014	11.8
106R-6, 29	1542.35	0.02	0.21	0.19	427.8	0.91	23.1	20.9	0.019	8.7
107R-2, 8	1546.48	0.03	0.32	ND	430.9	1.37	23.4	ND	0.029	8.6
107R-3, 131	1549.21	0.03	0.40	0.21	430.5	1.13	35.4	18.6	0.036	7.0
108R-4, 24	1558.94	0.03	0.30	ND	430.5	1.23	24.4	ND	0.027	9.1
109R-1, 89	1565.29	0.04	0.79	0.19	428.4	1.20	65.8	15.8	0.069	4.8
109R-3, 81	1568.05	0.08	1.75	0.40	429.3	1.46	119.9	27.4	0.152	4.4
110R-2, 26-A	1575.83	0.07	1.61	0.25	428.6	1.77	91.0	14.1	0.139	4.2
110R-2, 26-B	1575.83	0.11	2.44	0.35	433.2	1.84	132.6	19.0	0.212	4.3
110R-2, 26-GEO	1575.83	0.08	1.75	0.40	429.3	1.46	119.9	27.4	0.152	4.4
110R-3, 7	1577.08	0.03	0.56	0.23	429.3	1.23	45.5	18.7	0.049	5.1
111R-1, 94	1584.74	0.03	0.31	ND	415.3	0.93	33.3	ND	0.028	8.8
111R-4, 34	1588.45	0.03	0.07	0.12	ND	0.87	8.0	13.8	0.008	30.0
112R-1, 61	1594.11	0.01	0.13	ND	432.0	0.32	40.6	ND	0.012	7.1

Table T22 (continued). (Continued on next page.)

Core, section, interval (cm)	Depth CSF-A (m)	S_1 (mg HC/g rock)	S_2 (mg HC/g rock)	S_3 (mg HC/g rock)	T_{max} (°C)	TOC_{SRA} (wt%)	Hydrogen index (mg S_2/g TOC)	Oxygen index (mg S_3/g TOC)	Pyrolysis carbon	Production index
112R-3, 26	1596.68	0.03	0.78	0.13	429.4	1.12	69.6	11.6	0.067	3.7
113R-2, 53	1605.23	0.03	0.51	0.07	431.9	1.08	47.2	6.5	0.045	5.6
113R-4, 111	1608.81	0.02	0.30	0.11	424.5	0.90	33.3	12.2	0.027	6.3
114R-3, 113	1617.03	0.02	0.43	ND	428.3	0.59	72.9	ND	0.037	4.4
114R-4, 63	1618.03	0.01	0.07	0.01	ND	0.65	10.8	1.5	0.007	12.5
115R-6, 15	1630.35	0.04	0.68	0.08	426.5	1.01	67.3	7.9	0.060	5.6
115R-6, 82	1631.02	0.02	0.18	0.07	431.2	1.04	17.3	6.7	0.017	10.0
116R-2, 40	1634.30	0.02	0.09	0.15	441.1	0.94	9.6	16.0	0.009	18.2
116R-3, 27	1635.67	0.06	1.57	0.35	432.0	1.30	120.8	26.9	0.135	3.7
117R-3, 52	1644.79	0.02	0.33	ND	433.4	0.85	38.8	ND	0.029	5.7
117R-6, 29	1649.06	0.01	0.09	0.07	435.8	0.65	13.8	10.8	0.008	10.0
118R-3, 67	1654.38	0.02	0.19	0.10	428.1	1.10	17.3	9.1	0.017	9.5
118R-3, 114	1654.85	0.02	0.30	ND	429.4	0.53	56.6	ND	0.027	6.3
119R-4, 45	1666.45	0.04	0.67	0.13	433.6	1.24	54.0	10.5	0.059	5.6
119R-4, 68	1666.68	0.02	0.13	0.25	417.3	1.10	11.8	22.7	0.012	13.3
120R-CC, 0	1668.90	0.02	0.30	0.19	425.3	0.76	39.5	25.0	0.027	6.3
120R-CC, 34	1669.24	0.02	0.15	0.11	418.4	1.00	15.0	11.0	0.014	11.8
122R-1, 77	1688.87	0.02	0.28	ND	430.1	1.45	19.3	ND	0.025	6.7
122R-2, 66	1690.26	0.01	0.11	0.10	424.7	0.60	18.3	16.7	0.010	8.3
123R-1, 73	1693.23	0.02	0.22	ND	414.4	0.61	36.1	ND	0.020	8.3
123R-2, 65	1694.65	0.01	0.08	0.10	417.5	0.61	13.1	16.4	0.008	11.1
124R-6, 102	1705.96	0.02	0.12	0.15	428.6	1.04	11.5	14.4	0.012	14.3
125R-2, 91	1709.41	0.01	0.20	0.28	425.8	0.69	29.0	40.6	0.017	4.8
125R-5, 116	1714.16	0.01	0.14	0.17	430.6	0.46	30.4	37.0	0.012	6.7
126R-3, 101	1720.51	0.01	0.14	0.17	430.6	0.46	30.4	37.0	0.012	6.7
126R-6, 54	1724.31	0.02	0.09	0.10	426.1	0.46	19.6	21.7	0.009	18.2
127R-2, 36	1728.06	0.01	0.07	0.10	ND	0.65	10.8	15.4	0.007	12.5
127R-3, 111	1730.22	0.01	0.18	0.13	434.3	0.53	34.0	24.5	0.016	5.3
128R-1, 58	1736.38	0.01	0.08	0.10	425.1	0.52	15.4	19.2	0.008	11.1
128R-5, 12	1741.69	0.04	0.86	0.23	427.1	1.10	78.2	20.9	0.075	4.4
129R-1, 4	1745.44	ND	ND	ND	ND	ND	ND	ND	ND	ND
129R-2, 104*	1747.88	0.01	0.05	0.13	427.6	0.24	20.8	54.2	0.005	16.7
129R-2, 104†	1747.88	0.02	0.24	0.25	431.2	0.57	42.1	43.9	0.022	7.7
130R-2, 70	1757.20	0.01	0.05	0.17	415.4	0.43	11.6	39.5	0.005	16.7
130R-3, 65	1758.63	0.01	0.15	0.18	424.6	0.55	27.3	32.7	0.013	6.3
130R-4, 103*	1760.44	0.01	0.04	0.16	426.9	0.22	18.2	72.7	0.004	20.0
130R-4, 103†	1760.44	0.01	0.13	0.21	421.4	0.48	27.1	43.8	0.012	7.1
131R-2, 96*	1766.98	0.02	0.06	0.09	433.7	0.23	26.1	39.1	0.007	25.0
131R-2, 96†	1766.98	0.01	0.10	0.16	422.1	0.43	23.3	37.2	0.009	9.1
131R-2, 111	1767.13	0.01	0.06	0.17	428.7	0.41	14.6	41.5	0.006	14.3
132R-3, 9	1776.86	0.01	0.15	0.21	426.3	0.48	14.6	43.8	0.013	6.3
132R-3, 61	1777.38	0.01	0.06	0.18	431.9	0.24	25.0	75.0	0.006	14.3
133R-2, 144	1786.74	0.01	0.18	0.19	433.4	0.48	37.5	39.6	0.016	5.3
133R-3, 61	1787.37	0.01	0.05	0.11	431.4	0.38	13.2	28.9	0.005	16.7
134R-1, 78	1794.18	0.01	0.10	0.18	423.9	0.58	17.2	31.0	0.009	9.1
134R-3, 70	1796.58	0.01	0.05	0.08	ND	0.38	13.2	21.1	0.005	16.7
135R-1, 84	1803.84	0.01	0.05	0.11	ND	0.39	12.8	28.2	0.005	16.7
135R-4, 52	1807.91	0.01	0.13	0.13	433.8	0.51	25.5	25.5	0.012	7.1
136R-3, 127	1816.86	0.01	0.18	0.13	429.1	0.65	27.7	20.0	0.016	5.3
136R-4, 141	1818.50	0.04	0.16	0.08	428.5	0.76	21.1	10.5	0.017	20.0
136R-5, 27	1818.86	0.01	0.05	0.08	ND	0.45	11.1	17.8	0.005	16.7

Table T22 (continued).

Core, section, interval (cm)	Depth CSF-A (m)	S_1 (mg HC/g rock)	S_2 (mg HC/g rock)	S_3 (mg HC/g rock)	T_{max} (°C)	TOC_{SRA} (wt%)	Hydrogen index (mg S_2/g TOC)	Oxygen index (mg S_3/g TOC)	Pyrolysis carbon	Production index
137R-4, 119	1827.88	ND	ND	ND	ND	ND	ND	ND	ND	ND
137R-5, 63	1828.82	0.02	0.08	0.08	435.9	0.47	17.0	17.0	0.008	20.0
138R-1, 94	1832.84	0.01	0.04	0.09	432.8	0.49	8.2	18.4	0.004	20.0
138R-4, 13	1836.52	0.02	0.08	0.02	ND	0.73	11.0	2.7	0.008	20.0
138R-4, 134	1837.73	0.03	0.19	0.09	432.5	1.08	17.6	8.3	0.018	13.6
139R-1, 60	1842.10	0.02	0.08	0.07	422.0	0.69	11.6	10.1	0.008	20.0
139R-1, 86	1842.36	0.01	0.05	0.11	ND	0.44	11.4	25.0	0.005	16.7
140R-1, 16	1851.26	0.02	0.09	0.14	422.1	0.34	26.5	41.2	0.009	18.2
140R-1, 35	1851.45	0.02	0.06	0.01	ND	0.55	10.9	1.8	0.007	25.0
140R-2, 53	1852.69	0.02	0.07	0.00	ND	0.24	29.2	0.0	0.008	22.2
141R-1, 89	1861.69	0.01	0.04	0.11	ND	0.33	12.1	33.3	0.004	20.0
143R-2, 70	1877.20	0.01	0.04	0.13	ND	0.30	13.3	43.3	0.004	20.0
144R-4, 7	1884.24	0.01	0.04	0.09	ND	0.29	13.8	31.0	0.004	20.0
145R-3, 45	1892.90	0.02	0.06	0.26	423.9	0.45	13.3	57.8	0.007	25.0
146R-3, 77	1902.47	0.01	0.05	0.11	ND	0.42	11.9	26.2	0.005	16.7
147R-3, 35	1911.56	0.01	0.05	0.10	ND	0.35	14.3	28.6	0.005	16.7
147R-4, 55	1913.23	0.02	0.15	0.17	427.0	0.87	17.2	19.5	0.014	11.8
147R-6, 71*	1916.31	0.01	0.08	0.16	ND	0.45	17.8	35.6	0.008	11.1
147R-6, 71†	1916.31	0.02	0.20	0.13	426.0	0.69	29.0	18.8	0.018	9.1
148R-3, 56	1921.41	0.02	0.17	0.18	424.1	0.66	25.8	27.3	0.016	10.5
148R-5, 59	1924.03	0.01	0.06	0.09	ND	0.69	8.7	13.0	0.006	14.3

Notes: * = white layer, † = black layer. T_{max} is the pyrolysis temperature at which the evolution rate of S_2 is at a maximum. TOC_{SRA} = total organic carbon from source rock analyzer pyrolysis. Pyrolysis carbon = [0.83 × (S_1 + S_2)/10], production index = [S_1/(S_1 + S_2)] × 100. ND = not determined. CARB, CHNS, XRD, A, B, and GEO refer to separate aliquots of the same sample that were analyzed separately.

Table T23. Yield of interstitial water from whole-round cores, Site U1352. (See table notes.) (Continued on next page.)

Core, section, interval (cm)	Depth CSF-A (m)	IW volume (mL)	IW core length (cm)	IW yield (mL/cm)
317-U1352A-				
1H-1, 110	1.10	ND	30	ND
1H-2, 140	2.90	ND	10	ND
1H-3, 86	3.86	ND	10	ND
2H-1, 110	5.30	ND	30	ND
2H-2, 140	7.10	40	10	4.0
2H-3, 130	8.50	19	10	1.9
2H-4, 140	10.10	29	10	2.9
2H-5, 140	11.60	40	10	4.0
2H-6, 90	12.60	40	10	4.0
2H-7, 95	13.65	28	10	2.8
3H-1, 110	14.80	60	30	2.0
3H-2, 140	16.60	25	10	2.5
3H-3, 130	18.00	25	10	2.5
3H-4, 140	19.60	34	10	3.4
3H-5, 140	21.10	40	10	4.0
3H-6, 90	22.10	26	10	2.6
3H-7, 57	22.77	33	10	3.3
4H-1, 110	24.30	102	30	3.4
4H-2, 140	26.10	18	10	1.8
4H-3, 130	27.50	36	10	3.6
4H-4, 140	29.10	17	10	1.7
4H-5, 140	30.60	ND	10	ND
4H-6, 140	32.10	34	10	3.4
4H-7, 140	33.60	34	7	4.9
5H-1, 110	33.80	26	30	0.9
5H-2, 140	35.60	27	10	2.7
5H-3, 130	37.00	15	10	1.5
5H-4, 140	38.60	25	10	2.5
5H-5, 140	40.10	28	10	2.8
5H-6, 140	41.60	25	10	2.5
5H-7, 73	42.43	19	10	1.9
317-U1352B-				
6H-2, 140	49.10	29	10	2.9
6H-4, 140	52.10	33	10	3.3
6H-6, 90	54.60	34	10	3.4
7H-2, 140	58.60	26	10	2.6
7H-4, 140	61.60	ND	10	ND
8H-2, 140	68.10	40	10	4.0
8H-4, 140	71.10	30	10	3.0
9H-2, 140	77.60	37	10	3.7
9H-4, 140	80.60	25	10	2.5
10H-2, 140	85.86	36	10	3.6
10H-4, 140	88.86	32	10	3.2
11H-2, 140	96.60	ND	10	ND
12H-2, 136	106.06	ND	10	ND
13H-2, 140	115.58	37	10	3.7
14H-2, 140	125.10	25	10	2.5
15H-4, 127	137.40	ND	10	ND
16H-2, 137	144.07	33	10	3.3
18H-2, 140	159.10	30	10	3.0
19H-2, 140	168.60	ND	10	ND
21H-3, 140	184.10	28	10	2.8
22H-2, 140	192.10	29	10	2.9
23H-3, 140	203.10	55	10	5.5
24H-3, 140	212.60	36	10	3.6
25H-3, 140	222.10	44	10	4.4
26H-3, 130	231.42	31	10	3.1
27H-3, 140	241.10	45	10	4.5
28H-2, 140	249.03	22	10	2.2
29H-2, 140	254.10	29	10	2.9
30H-3, 140	262.10	ND	10	ND
31H-1, 140	268.60	38	10	3.8
32H-3, 140	276.60	25	10	2.5
33H-4, 140	286.04	31	10	3.1
34H-2, 133	289.79	25	10	2.5
35H-1, 134	294.24	26	10	2.6

Table T23 (continued).

Core, section, interval (cm)	Depth CSF-A (m)	IW volume (mL)	IW core length (cm)	IW yield (mL/cm)
37X-1, 130	298.30	20	10	2.0
39X-3, 140	316.60	32	10	3.2
41X-3, 140	335.90	34	10	3.4
42X-3, 130	345.40	32	10	3.2
44X-3, 140	364.80	26	10	2.6
46X-3, 140	383.98	22	10	2.2
48X-3, 130	403.00	26	10	2.6
50X-3, 140	422.30	26	10	2.6
52X-3, 140	441.50	27	10	2.7
54X-3, 130	460.60	32	30	1.1
56X-3, 140	479.90	22	10	2.2
58X-4, 140	499.32	38	10	3.8
61X-1, 80	524.30	35	10	3.5
63X-3, 140	547.10	ND	10	ND
68X-1, 130	582.40	18	10	1.8
71X-2, 140	612.80	17	10	1.7
73X-3, 130	633.40	24	10	2.4
75X-3, 135	652.65	38	15	2.5
77X-1, 135	668.95	55	15	3.7
80X-2, 135	699.35	38	15	2.5
81X-2, 125	708.85	52	15	3.5
85X-2, 135	737.75	39	15	2.6
88X-1, 125	764.85	24	15	1.6
90X-1, 56	783.46	24	15	1.6
317-U1352C-				
2R-1, 89	575.59	ND	15	ND
3R-2, 135	586.95	16	15	1.1
6R-1, 85	660.85	ND	15	ND
11R-1, 77	709.17	38	15	2.5
14R-2, 84	739.84	42	15	2.8
18R-3, 77	779.58	23	15	1.5
22R-1, 107	816.07	16	15	1.1
24R-1, 128	835.48	26	15	1.7
27R-2, 61	864.61	29	15	1.9
29R-1, 78	882.98	29	15	1.9
31R-1, 126	902.56	28	20	1.4
33R-2, 113	923.05	0	20	0.0
34R-1, 79	930.89	ND	18	ND
36R-2, 135	952.25	6	15	0.4
38R-3, 135	972.85	20	15	1.3
40R-1, 110	988.80	7	21	0.3
41R-4, 135	1003.15	5	15	0.3
43R-1, 120	1017.70	0	23	0.0
45R-1, 121	1036.91	28	20	1.4
46R-3, 129	1049.33	0	19	0.0
48R-1, 128	1065.68	0	20	0.0
50R-5, 130	1090.75	24	ND	ND
53R-1, 104	1113.14	26	20	1.3
55R-3, 133	1135.33	18	17	1.1
58R-4, 100	1164.27	20	20	1.0
60R-3, 130	1183.70	5	20	0.2
76R-1, 112	1305.02	0	20	0.0
87R-4, 115	1367.05	0	25	0.0
89R-4, 82	1385.71	6	11	0.5
94R-5, 115	1435.65	0	25	0.0
107R-6, 120	1553.57	0	28	0.0

Notes: IW = interstitial water. ND = not determined.

Table T24. Composition of interstitial waters, Site U1352. (See table note.) (Continued on next page.)

Core, section, interval (cm)	Depth CSF-A (m)	Salinity	pH	Alkalinity (mM)	Ion chromatograph data (mM)						Mg/Ca
					Cl^-	SO_4^{2-}	Mg^{2+}	Ca^{2+}	Na^+	K^+	
317-U1352A-											
1H-1, 110	1.10	3.3	7.37	2.81	542	27.82	51.8	10.4	466	10.7	4.97
1H-2, 140	2.90	3.3	7.44	3.67	540	27.31	50.8	10.4	465	10.8	4.89
1H-3, 86	3.86	3.3	7.49	4.14	529	26.47	49.4	10.1	455	10.6	4.88
2H-1, 110	5.30	3.3	7.41	4.25	544	26.76	51.3	10.5	469	10.8	4.91
2H-2, 140	7.10	3.4	7.34	4.54	543	26.41	51.1	10.2	469	10.5	4.99
2H-3, 130	8.50	3.3	7.83	5.13	534	25.06	49.9	9.5	461	10.5	5.26
2H-4, 140	10.10	3.2	7.47	8.96	539	20.01	48.3	8.2	464	9.8	5.87
2H-5, 140	11.60	3.2	7.58	14.58	547	12.84	46.0	6.6	473	9.7	6.95
2H-6, 90	12.60	3.2	7.64	16.79	552	10.16	45.4	6.0	478	9.4	7.57
2H-7, 95	13.65	3.2	7.65	17.83	539	8.73	43.9	5.6	465	9.0	7.91
3H-1, 110	14.80	3.1	7.68	20.37	526	5.76	42.0	5.2	459	8.8	8.11
3H-2, 140	16.60	3.1	7.65	24.21	551	0.00	40.2	4.3	480	8.7	9.35
3H-3, 130	18.00	3.1	7.47	22.70	554	0.00	37.4	4.0	474	8.0	9.37
3H-4, 140	19.60	3.1	7.39	21.91	515	0.00	34.5	4.0	451	7.6	8.66
3H-5, 140	21.10	3.1	7.32	21.39	542	0.00	35.8	4.2	476	7.9	8.56
3H-6, 90	22.10	3.1	7.37	21.31	549	0.00	36.1	4.3	484	7.8	8.38
3H-7, 57	22.77	3.0	7.32	21.19	542	0.00	35.1	4.3	478	7.8	8.25
4H-1, 110	24.30	3.0	7.34	21.21	608	11.05	34.9	4.3	483	8.2	8.22
4H-2, 140	26.10	3.1	7.30	21.11	546	0.00	35.1	4.4	483	7.9	7.92
4H-3, 130	27.50	3.0	7.26	21.15	534	0.00	33.6	4.1	471	6.8	8.13
4H-4, 140	29.10	3.1	7.53	21.68	523	0.00	32.9	4.1	453	8.1	8.10
4H-5, 140	30.60	3.1	ND	ND	548	1.95	34.7	4.5	475	7.7	7.70
4H-6, 140	32.10	3.1	7.32	22.01	520	0.00	32.6	4.3	450	7.7	7.55
4H-7, 140	33.60	3.1	7.52	21.52	516	0.00	32.3	4.3	447	7.5	7.53
5H-1, 110	33.80	3.1	7.33	21.64	534	0.00	33.1	4.5	464	7.6	7.42
5H-2, 140	35.60	3.1	7.45	21.01	524	0.00	31.9	4.2	455	8.0	7.55
5H-3, 130	37.00	3.1	7.38	21.40	522	0.00	31.8	4.3	454	7.8	7.41
5H-4, 140	38.60	3.0	7.45	21.19	523	0.00	31.8	4.2	455	7.7	7.54
5H-5, 140	40.10	3.1	7.50	21.32	545	0.00	32.6	4.3	474	8.3	7.67
5H-6, 140	41.60	3.1	7.48	20.66	542	0.00	32.8	4.2	475	8.1	7.76
5H-7, 73	42.43	3.0	7.34	21.52	544	0.00	32.9	4.2	474	7.8	7.84
317-U1352B-											
6H-2, 140	49.10	3.1	7.48	19.48	545	0.34	31.3	4.0	478	8.3	7.82
6H-4, 140	52.10	3.0	7.54	19.20	530	0.00	29.8	3.7	464	8.4	8.16
6H-6, 90	54.60	3.0	7.40	19.26	523	0.00	29.2	3.6	459	8.1	8.12
7H-2, 140	58.60	3.0	7.73	17.82	554	0.00	29.3	3.3	481	9.2	8.96
7H-4, 140	61.60	3.0	7.71	17.25	550	0.00	28.5	3.0	479	9.5	9.52
8H-2, 140	68.10	3.0	7.72	17.09	545	0.00	28.3	3.0	482	9.8	9.58
8H-4, 140	71.10	3.0	7.69	16.70	538	0.00	27.7	2.7	486	9.4	10.18
9H-2, 140	77.60	3.0	7.71	17.08	535	0.00	27.3	3.2	487	9.8	8.58
9H-4, 140	80.60	3.0	7.63	17.71	534	0.00	27.4	3.2	483	9.3	8.52
10H-2, 140	85.86	3.0	8.03	16.25	526	0.00	25.0	2.8	466	10.5	9.01
10H-4, 140	88.86	2.9	7.71	15.60	505	0.00	23.9	2.6	457	8.5	9.18
11H-2, 140	96.60	2.9	7.55	14.43	537	0.00	24.0	3.0	490	10.0	8.04
12H-2, 136	106.06	3.0	7.72	14.84	516	0.00	22.8	2.8	461	9.8	8.11
13H-2, 140	115.58	3.0	7.81	13.96	538	0.00	22.4	2.6	482	10.7	8.77
14H-2, 140	125.10	2.9	7.74	14.11	534	0.00	21.5	2.7	485	11.0	8.00
15H-4, 127	137.40	3.0	7.53	16.10	525	0.00	20.3	3.3	478	9.8	6.20
16H-2, 137	144.07	2.9	7.69	12.36	545	0.00	19.5	2.0	491	11.0	9.76
18H-2, 140	159.10	3.0	7.62	12.90	534	0.54	18.0	2.4	484	10.5	7.39
19H-2, 140	168.60	3.0	7.88	14.13	547	0.00	17.3	2.4	497	10.9	7.21
21H-3, 140	184.10	3.0	7.83	14.52	545	0.00	16.1	2.1	498	10.4	7.66
22H-2, 140	192.10	3.0	7.60	14.53	528	0.00	15.0	2.2	483	9.4	6.83
23H-3, 140	203.10	3.0	7.88	14.30	523	0.00	13.3	2.0	481	9.8	6.56
24H-3, 140	212.60	3.0	7.71	14.10	526	0.00	13.2	2.3	488	9.2	5.77
25H-3, 140	222.10	3.0	7.96	12.52	538	0.00	11.5	1.2	502	9.9	9.55
26H-3, 130	231.42	3.0	7.80	14.09	520	0.00	10.9	1.5	484	9.4	7.34
27H-3, 140	241.10	3.0	7.93	12.36	536	0.00	10.6	1.2	503	9.9	8.96
28H-2, 140	249.03	3.0	7.54	14.91	531	0.00	10.4	2.3	498	9.1	4.54
29H-2, 140	254.10	3.0	7.84	14.99	526	0.00	9.5	2.0	490	9.3	4.88
30H-3, 140	262.10	3.0	6.84	12.67	543	0.00	10.8	2.0	512	8.9	4.22
31H-1, 140	268.60	3.0	7.53	15.29	536	0.49	10.3	2.6	503	8.6	3.89
32H-3, 140	276.60	2.9	7.75	14.88	538	0.00	8.8	1.5	508	9.7	5.74
33H-4, 140	286.04	3.0	7.78	14.01	546	0.00	8.7	1.6	515	8.9	5.38
34H-2, 133	289.79	3.0	7.50	16.10	541	0.00	8.9	2.2	511	8.3	4.03
35H-1, 134	294.24	3.0	7.56	13.85	530	0.41	8.2	1.5	503	8.6	5.53
37X-1, 130	298.30	2.9	7.47	14.34	521	0.97	8.1	2.1	492	8.1	3.92

Table T24 (continued).

Core, section, interval (cm)	Depth CSF-A (m)	Salinity	pH	Alkalinity (mM)	Ion chromatograph data (mM)						Mg/Ca
					Cl^-	SO_4^{2-}	Mg^{2+}	Ca^{2+}	Na^+	K^+	
39X-3, 140	316.60	3.0	7.01	13.61	507	0.00	7.4	2.3	479	7.9	3.20
41X-3, 140	335.90	3.0	7.79	12.97	527	0.00	6.9	1.4	498	8.6	4.95
42X-3, 130	345.40	3.0	7.54	14.62	540	0.00	8.0	2.2	511	8.1	3.62
44X-3, 140	364.80	3.0	7.55	13.79	531	0.00	7.8	2.6	499	8.2	3.00
46X-3, 140	383.98	3.0	7.77	11.85	533	0.00	7.3	2.7	499	8.5	2.72
48X-3, 130	403.00	3.0	7.76	10.84	530	0.00	7.0	3.0	491	8.2	2.32
50X-3, 140	422.30	3.0	7.39	8.73	533	1.07	8.8	3.7	489	7.6	2.38
52X-3, 140	441.50	2.9	7.41	8.20	539	0.00	8.8	4.4	490	7.5	2.00
54X-3, 130	460.60	3.0	7.34	6.84	539	0.59	11.1	5.4	484	7.4	2.08
56X-3, 140	479.90	3.0	7.25	5.92	538	0.00	11.7	6.7	475	7.1	1.75
58X-4, 140	499.32	2.9	7.33	5.51	530	0.76	14.4	8.7	460	6.7	1.65
61X-1, 80	524.30	2.9	7.16	4.98	514	0.34	15.3	12.7	431	5.7	1.21
63X-3, 140	547.10	3.1	7.64	4.73	550	0.71	19.0	16.9	459	6.3	1.12
68X-1, 130	582.40	2.9	7.20	2.80	534	0.51	21.1	19.9	433	3.3	1.06
71X-2, 140	612.80	2.9	7.27	2.32	542	0.00	21.7	20.6	436	2.8	1.06
73X-3, 130	633.40	2.9	7.42	2.44	530	1.99	24.0	20.2	426	3.3	1.19
75X-3, 135	652.65	2.9	7.41	1.94	534	0.00	23.8	21.2	425	3.6	1.12
77X-1, 135	668.95	2.9	7.24	2.34	551	1.62	24.6	24.0	438	3.2	1.02
80X-2, 135	699.35	2.8	7.07	2.93	551	0.49	23.0	27.0	434	4.5	0.85
81X-2, 125	708.85	2.9	7.05	2.80	538	1.54	23.5	26.4	422	5.7	0.89
85X-2, 135	737.75	3.0	7.21	2.01	547	2.30	24.55	23.0	436	2.6	1.07
88X-1, 125	764.85	3.1	7.33	1.95	535	1.68	20.2	27.8	427	2.7	0.73
90X-1, 56	783.46	3.0	7.36	ND	514	0.77	20.4	26.9	405	2.7	0.76
317-U1352C-											
2R-1, 89	575.59	3.0	7.37	2.81	542	0.00	22.4	17.9	443	3.7	1.25
3R-2, 135	586.95	ND	ND	ND	544	0.00	22.7	18.7	441	3.1	1.21
6R-1, 85	660.85	3.0	7.21	2.54	550	2.40	26.7	19.8	444	3.4	1.35
11R-1, 77	709.17	3.0	7.11	2.97	522	0.90	22.8	21.9	412	4.1	1.04
14R-2, 84	739.84	3.0	7.41	1.76	530	1.82	22.6	23.0	420	2.5	0.99
18R-3, 77	779.58	3.0	7.79	1.76	519	2.31	23.2	21.7	421	2.4	1.07
22R-1, 107	816.07	3.0	ND	ND	535	0.00	21.7	24.3	431	2.6	0.90
24R-1, 128	835.48	3.0	7.51	1.75	528	1.43	21.6	25.4	425	2.4	0.85
27R-2, 61	864.61	3.0	7.40	1.58	540	2.95	23.1	26.2	434	2.4	0.88
29R-1, 78	882.98	3.0	7.61	1.50	531	1.14	20.7	27.2	423	2.2	0.76
31R-1, 126	902.56	3.0	7.54	1.55	525	0.66	20.4	26.9	418	1.7	0.76
34R-1, 79	930.89	3.0	7.68	1.37	534	0.00	21.4	28.5	420	1.9	0.75
36R-2, 135	952.25	ND	ND	ND	533	2.47	23.3	28.2	421	1.7	0.83
38R-3, 135	972.85	2.9	7.67	1.44	521	1.12	20.4	29.5	407	1.4	0.69
40R-1, 110	988.80	3.0	ND	ND	529	2.13	21.8	28.1	418	1.9	0.78
41R-4, 135	1003.15	ND	ND	ND	522	0.96	20.6	29.0	405	2.1	0.71
45R-1, 121	1036.91	2.9	7.79	2.10	518	1.11	20.8	25.6	412	1.8	0.81
50R-5, 130	1090.75	2.9	7.75	1.92	539	1.35	23.1	27.7	423	2.8	0.84
53R-1, 104	1113.14	3.0	7.56	1.77	504	0.00	20.7	27.6	391	1.6	0.75
55R-3, 133	1135.33	3.0	7.52	2.14	536	2.85	23.1	30.1	416	2.1	0.77
58R-4, 100	1164.27	3.0	7.64	1.69	539	0.00	21.6	33.0	406	1.6	0.66
60R-3, 130	1183.70	ND	ND	ND	531	1.37	20.8	30.8	406	1.9	0.68
89R-4, 82	1385.71	ND	ND	ND	453	2.99	15.9	30.0	348	1.8	0.53

Note: ND = not determined.

Table T25. Composition of interstitial waters, Site U1352. (See table notes.) (Continued on next page.)

Core, section, interval (cm)	Depth CSF-A (m)	Spectrophotometry data			ICP-AES data							
		NH_4^+ (mM)	HPO_4^{2-} (μM)	$HSiO_4$ (μM)	Mn (μM)	Fe (μM)	B (mM)	Sr^{2+} (mM)	Ba (μM)	Si (μM)	Li^+ (μM)	Sr/Ca*
317-U1352A-												
1H-1, 110	1.10	0.0	3.10	272	4.6	11.6	0.41	0.091	1.70	309	25	0.009
1H-2, 140	2.90	0.0	1.10	294	8.7	11.7	0.40	0.088	2.10	300	24	0.009
1H-3, 86	3.86	0.0	2.60	324	9.0	11.0	0.41	0.090	2.00	328	23	0.009
2H-1, 110	5.30	0.0	2.90	374	7.8	13.6	0.40	0.089	1.90	378	23	0.009
2H-2, 140	7.10	0.0	3.90	471	7.1	12.8	0.39	0.088	1.80	422	22	0.009
2H-3, 130	8.50	0.2	1.60	418	4.8	10.6	0.39	0.088	2.50	375	24	0.009
2H-4, 140	10.10	0.0	7.00	475	4.1	11.2	0.39	0.086	2.00	444	23	0.010
2H-5, 140	11.60	0.0	17.60	451	3.6	8.8	0.37	0.074	2.10	379	25	0.011
2H-6, 90	12.60	0.7	21.00	460	3.5	8.4	0.37	0.072	2.20	404	19	0.012
2H-7, 95	13.65	0.7	23.10	467	3.6	8.7	0.37	0.072	2.50	421	20	0.013
3H-1, 110	14.80	ND	92.20	473	3.2	8.3	0.37	0.066	3.30	418	19	0.013
3H-2, 140	16.60	0.9	41.20	507	8.4	14.6	0.42	0.093	1.90	404	24	0.022
3H-3, 130	18.00	1.2	53.60	521	3.4	8.3	0.36	0.077	7.20	457	18	0.019
3H-4, 140	19.60	1.3	59.20	542	4.2	11.0	0.36	0.081	8.00	470	19	0.020
3H-5, 140	21.10	1.5	47.50	557	4.9	22.4	0.36	0.086	8.70	520	22	0.021
3H-6, 90	22.10	1.7	44.10	546	4.5	10.8	0.36	0.082	8.70	472	21	0.019
3H-7, 57	22.77	1.7	49.10	597	4.9	28.9	0.36	0.085	8.90	512	22	0.020
4H-1, 110	24.30	1.9	42.80	572	5.4	23.7	0.36	0.079	8.40	454	22	0.019
4H-2, 140	26.10	2.0	42.10	588	8.9	33.7	0.30	0.087	8.30	519	20	0.020
4H-3, 130	27.50	2.1	50.80	645	4.7	22.0	0.31	0.088	8.60	540	21	0.021
4H-4, 140	29.10	2.1	22.70	466	4.0	13.6	0.30	0.086	8.80	394	21	0.021
4H-5, 140	30.60	2.2	56.00	604	8.7	31.7	0.31	0.087	8.60	575	23	0.019
4H-6, 140	32.10	2.2	50.80	548	9.3	18.3	0.31	0.089	9.30	514	26	0.021
4H-7, 140	33.60	2.3	43.20	509	8.3	14.4	0.31	0.088	8.90	480	22	0.021
5H-1, 110	33.80	0.1	45.80	433	8.4	25.2	0.30	0.083	8.60	398	19	0.018
5H-2, 140	35.60	2.4	33.70	386	9.0	20.5	0.30	0.082	8.70	388	20	0.019
5H-3, 130	37.00	2.3	35.10	466	6.7	13.2	0.31	0.084	9.20	461	21	0.020
5H-4, 140	38.60	2.3	41.70	518	5.3	24.0	0.31	0.083	9.00	435	20	0.020
5H-5, 140	40.10	2.4	28.70	464	8.9	17.3	0.30	0.079	8.60	499	20	0.019
5H-6, 140	41.60	2.1	31.80	461	13.3	35.8	0.30	0.078	8.60	425	19	0.018
5H-7, 73	42.43	2.0	24.60	566	5.4	15.9	0.37	0.085	9.40	525	23	0.020
317-U1352B-												
6H-2, 140	49.10	2.5	31.20	505	12.9	22.3	0.32	0.069	5.80	477	19	0.017
6H-4, 140	52.10	2.2	36.50	540	8.3	26.9	0.33	0.068	5.20	502	19	0.019
6H-6, 90	54.60	2.1	34.50	587	5.3	28.5	0.34	0.067	4.80	497	19	0.019
7H-2, 140	58.60	2.0	4.90	409	5.6	8.7	0.34	0.064	4.30	383	20	0.020
7H-4, 140	61.60	1.9	6.90	410	3.2	7.4	0.33	0.062	3.90	378	23	0.021
8H-2, 140	68.10	1.6	5.30	352	2.9	6.3	0.34	0.068	5.70	314	23	0.023
8H-4, 140	71.10	1.5	5.80	407	3.33	9.1	0.36	0.071	5.70	360	22	0.026
9H-2, 140	77.60	1.5	9.00	549	3.8	6.6	0.37	0.076	5.30	444	23	0.024
9H-4, 140	80.60	1.3	8.70	658	4.7	9.1	0.41	0.078	5.80	575	26	0.024
10H-2, 140	85.86	1.5	3.40	461	3.0	5.7	0.35	0.078	4.70	382	28	0.028
10H-4, 140	88.86	1.7	4.90	558	3.4	8.3	0.38	0.082	4.50	476	29	0.031
11H-2, 140	96.60	ND	4.10	624	2.5	6.4	0.39	0.095	4.70	500	31	0.032
12H-2, 136	106.06	1.7	6.40	542	3.0	6.1	0.37	0.104	5.50	458	32	0.037
13H-2, 140	115.58	1.9	4.90	527	2.0	5.8	0.36	0.102	5.60	439	34	0.040
14H-2, 140	125.10	2.2	2.70	481	2.6	6.6	0.37	0.094	5.10	385	34	0.035
15H-4, 127	137.40	2.1	4.40	595	4.7	6.7	0.45	0.098	6.30	476	34	0.030
16H-2, 137	144.07	2.7	3.50	494	2.0	4.9	0.40	0.089	4.20	402	44	0.045
18H-2, 140	159.10	2.8	2.70	582	2.5	5.8	0.45	0.092	5.70	462	42	0.038
19H-2, 140	168.60	3.1	4.10	505	1.7	5.1	0.37	0.114	8.00	402	48	0.048
21H-3, 140	184.10	3.8	4.00	502	2.9	5.4	0.44	0.091	7.60	386	44	0.043
22H-2, 140	192.10	4.5	2.30	590	3.0	6.4	0.52	0.098	6.70	486	48	0.045
23H-3, 140	203.10	ND	1.90	517	3.0	5.4	0.48	0.098	6.70	425	49	0.048
24H-3, 140	212.60	3.7	1.80	648	3.1	5.6	0.54	0.101	5.30	516	50	0.044
25H-3, 140	222.10	5.1	3.60	577	2.1	4.1	0.49	0.088	4.80	434	49	0.073
26H-3, 130	231.42	4.4	3.00	574	2.3	4.5	0.52	0.096	4.50	403	49	0.065
27H-3, 140	241.10	4.9	3.20	546	2.1	3.5	0.55	0.074	3.30	393	46	0.062
28H-2, 140	249.03	5.0	2.50	692	2.3	4.8	0.70	0.101	3.80	526	48	0.044
29H-2, 140	254.10	5.4	2.80	533	2.4	4.8	0.58	0.110	4.40	417	48	0.056
30H-3, 140	262.10	4.4	2.30	608	3.0	5.9	0.63	0.118	4.40	461	46	0.046
31H-1, 140	268.60	5.2	2.50	605	3.6	5.6	0.70	0.132	4.60	493	47	0.050
32H-3, 140	276.60	5.4	2.10	456	3.0	4.2	0.79	0.097	3.00	373	49	0.063
33H-4, 140	286.04	4.5	1.30	566	2.7	4.5	0.70	0.131	3.80	434	45	0.081
34H-2, 133	289.79	5.6	1.30	766	4.0	9.3	0.92	0.184	4.60	674	51	0.084
35H-1, 134	294.24	5.1	2.70	772	2.0	4.5	0.89	0.138	3.80	593	47	0.094

Table T25 (continued).

Core, section, interval (cm)	Depth CSF-A (m)	Spectrophotometry data			ICP-AES data							
		NH_4^+ (mM)	HPO_4^{2-} (μM)	$HSiO_4$ (μM)	Mn (μM)	Fe (μM)	B (mM)	Sr^{2+} (mM)	Ba (μM)	Si (μM)	Li^+ (μM)	Sr/Ca*
37X-1, 130	298.30	4.8	2.10	803	2.2	5.0	0.90	0.153	4.10	600	47	0.074
39X-3, 140	316.60	5.1	2.20	796	2.7	5.3	0.89	0.152	4.60	596	50	0.066
41X-3, 140	335.90	5.9	2.50	607	2.6	4.8	0.89	0.145	4.50	485	55	0.104
42X-3, 130	345.40	5.5	2.40	818	2.6	5.9	1.10	0.200	5.00	691	54	0.090
44X-3, 140	364.80	5.2	1.90	769	3.7	6.8	1.07	0.208	5.60	620	52	0.080
46X-3, 140	383.98	5.3	0.90	515	4.6	8.5	1.16	0.303	7.20	517	60	0.113
48X-3, 130	403.00	5.6	0.90	589	3.6	7.5	1.14	0.363	7.30	498	50	0.120
50X-3, 140	422.30	5.7	1.00	897	3.4	10.2	1.32	0.477	7.80	797	54	0.128
52X-3, 140	441.50	6.1	0.50	902	3.5	9.4	1.31	0.606	9.00	730	47	0.137
54X-3, 130	460.60	5.1	0.50	982	3.3	10.6	1.40	0.780	11.90	808	53	0.146
56X-3, 140	479.90	6.8	0.50	1066	3.6	13.0	1.72	0.988	14.90	973	59	0.148
58X-4, 140	499.32	6.1	0.30	963	5.1	14.7	1.48	1.204	18.50	821	70	0.139
61X-1, 80	524.30	5.5	0.10	992	5.7	22.9	1.64	1.374	18.30	902	82	0.108
63X-3, 140	547.10	5.0	0.20	737	8.5	16.8	1.45	1.468	17.70	689	91	0.087
68X-1, 130	582.40	ND	0.20	334	5.7	17.7	1.74	1.488	8.50	385	107	0.075
71X-2, 140	612.80	ND	0.10	329	5.6	18.7	2.60	1.674	14.10	365	115	0.081
73X-3, 130	633.40	4.7	0.10	211	8.6	18.1	2.09	1.738	19.70	271	105	0.086
75X-3, 135	652.65	4.5	0.10	215	6.6	19.7	2.08	1.808	18.60	286	126	0.085
77X-1, 135	668.95	4.4	0.10	386	6.4	20.6	2.28	1.741	15.20	403	142	0.073
80X-2, 135	699.35	5.0	0.10	831	10.2	27.7	2.35	2.056	22.80	1013	166	0.076
81X-2, 125	708.85	3.6	0.00	780	7.2	26.7	1.71	1.583	17.60	717	136	0.060
85X-2, 135	737.75	3.8	ND	375	5.8	20.2	1.75	1.487	8.60	485	111	0.065
88X-1, 125	764.85	3.3	0.10	258	5.4	17.5	2.10	1.589	10.00	403	121	0.057
90X-1, 56	783.46	3.2	0.10	ND	5.2	18.1	2.01	1.820	16.90	332	92	0.068
317-U1352C-												
2R-1, 89	575.59	5.5	ND	ND	7.4	20.5	1.73	1.535	8.70	632	104	0.086
3R-2, 135	586.95	4.8	ND	ND	6.4	18.6	1.52	1.446	7.00	355	105	0.077
6R-1, 85	660.85	4.5	ND	ND	10.7	27.9	1.81	1.608	16.80	380	110	0.081
11R-1, 77	709.17	3.8	ND	ND	14.3	35.9	2.81	1.901	18.50	932	164	0.087
14R-2, 84	739.84	3.5	ND	ND	9.0	23.7	2.74	2.003	9.10	307	131	0.087
18R-3, 77	779.58	3.3	ND	ND	9.0	25.2	2.82	2.078	17.90	295	104	0.096
22R-1, 107	816.07	3.1	ND	ND	7.2	23.0	3.01	2.039	30.50	316	104	0.084
24R-1, 128	835.48	2.3	ND	ND	12.5	30.1	3.22	2.066	22.70	355	104	0.081
27R-2, 61	864.61	2.3	ND	ND	9.7	25.0	3.03	2.000	21.80	314	91	0.076
29R-1, 78	882.98	2.8	ND	ND	8.9	23.6	3.24	2.087	27.60	295	92	0.077
31R-1, 126	902.56	2.5	ND	ND	9.2	26.4	3.82	2.100	29.60	368	98	0.078
34R-1, 79	930.89	2.1	ND	ND	10.2	29.0	3.08	1.951	26.00	303	104	0.068
36R-2, 135	952.25	ND	ND	ND	8.8	27.4	3.10	1.736	10.30	329	107	0.062
38R-3, 135	972.85	ND	ND	ND	12.3	30.6	3.35	1.783	8.90	488	117	0.060
40R-1, 110	988.80	1.8	ND	ND	6.9	22.0	3.82	1.832	19.80	380	116	0.065
41R-4, 135	1003.15	ND	ND	ND	9.9	26.4	3.47	2.006	32.30	337	123	0.069
45R-1, 121	1036.91	ND	ND	ND	9.5	26.1	4.15	1.954	46.90	316	121	0.076
50R-5, 130	1090.75	ND	ND	ND	9.4	26.8	4.51	1.829	83.50	305	124	0.066
53R-1, 104	1113.14	ND	ND	ND	9.8	25.9	5.44	1.710	43.90	376	124	0.062
55R-3, 133	1135.33	ND	ND	ND	9.9	26.1	5.19	1.541	11.80	656	115	0.051
58R-4, 100	1164.27	ND	ND	ND	13.0	31.7	5.09	1.714	15.20	506	134	0.052
60R-3, 130	1183.70	ND	ND	ND	9.0	25.0	4.84	1.680	21.20	387	124	0.055
89R-4, 82	1385.71	ND	ND	ND	4.9	20.0	1.55	1.666	15.60	335	76	0.056

Notes: * = Ca^{2+} data from ion chromatography (see Table **T24**). ICP-AES = inductively coupled plasma–atomic emission spectroscopy. ND = not determined. Mn and Fe concentrations may have been affected by oxidation prior to analysis, as these are redox-sensitive trace elements.

Table T26. Degree of sediment sample contamination (particulate tracer), Site U1352. (See table note.)

Core, section	Depth CSF-A (m)	Microsphere count (beads/cm^3 sediment)		Delivery confirmed
		Inner	Outer	
317-U1352A-				
1H-1	1.40	27,322	1,117,004	Yes
1H-3	3.76	0	24,108	Yes
2H-1	5.60	0	73,931	Yes
2H-3	8.60	161	16,072	Yes
2H-5	11.60	0	2,411	Yes
3H-1	15.10	0	9,643	Yes
3H-3	18.10	161	3,214	Yes
3H-5	21.10	0	16,876	Yes
4H-1	24.60	0	2,411	Yes
4H-3	27.60	6,268	613,950	Yes
4H-5	30.60	0	117,326	Yes
5H-1	34.10	0	123,754	Yes
5H-3	37.10	0	100,450	Yes
5H-5	40.10	161	1,607	Yes
10H-3	87.26	212,150	34,555	Yes
15H-4	137.13	0	0	Yes
21H-3	184.00	0	804	Yes
26H-3	231.52	161	6,429	Yes
32H-3	276.50	161	28,126	Yes
317-U1352B-				
37X-1	298.40	0	14,465	Yes
42X-3	345.50	0	86,789	Yes
48X-3	403.10	0	2,411	Yes
54X-3	460.70	0	988,428	Yes
61X-1	524.40	0	1,024,590	Yes
68X-1	582.50	0	86,789	Yes
73X-3	633.50	0	234,651	Yes
81X-2	709.00	2,411	51,430	Yes
88X-1	765.00	0	1,607	Yes
317-U1352C-				
22R-2	816.32	0	6,429	Yes
29R-2	883.13	0	2,411	Yes
34R-2	931.07	0	1,607	Yes
41R-4	1003.05	0	2,411	Yes
46R-3	1049.43	0	804	Yes
53R-1	1113.44	0	99,646	Yes
58R-5	1164.47	0	2,411	Yes
87R-4	1367.30	0	0	Yes
94R-5	1436.00	0	804	Yes
99R-1	1477.76	0	1,607	Yes
105R-5	1532.63	0	1,607	Yes
110R-2	1576.68	0	5,625	Yes
115R-5	1630.10	0	92,414	Yes
122R-1	1689.50	0	15,268	Yes
125R-3	1711.40	0	1,607	Yes
128R-3	1740.06	161	4,822	Yes
131R-1	1765.88	161	9,643	Yes
134R-1	1794.51	0	2,411	Yes
137R-3	1826.59	0	2,411	Yes
140R-1	1852.00	0	10,447	Yes
144R-3	1884.06	0	3,214	Yes
147R-2	1911.07	0	6,429	Yes
148R-3	1922.27	0	2,411	Yes

Note: Inner = center part of core, outer = part of core in contact with core liner.

Table T27. Temperature data, Site U1352. (See table notes.)

Core	Tool	Depth CSF-A (m)	Temperature (°C)	t_i (s)	t_f (s)	$t_f - t_i$ (s)	Reliability
317-U1352A-							
4H	APCT-3	32.7	10.33	8	66	58	Poor
317-U1352B-							
6H	APCT-3	55.7	11.10	47	167	120	Poor
10H	APCT-3	93.7	12.57	50	775	725	Good
15H	APCT-3	141.2	14.84	71	678	607	Good
20H	APCT-3	179.7	16.31	81	763	678	Good
38X	SET	313.2	22.69	77	867	790	Good

Notes: Times t_i and t_f are the initial and final times of the interval, respectively, picked to estimate asymptotic temperature for each data set. Estimated temperatures are considered reliable when the picked interval, $t_f - t_i$, is >300 s. APCT-3 = third-generation advanced piston corer temperature tool, SET = Sediment Temperature tool. APCT-3 measurement depth is the bottom of the cored interval. SET measurement depth is the bottom of the last cored interval plus 1 m, the approximate distance the temperature sensor advances beneath the bit.

Table T28. Thermal conductivity data, Site U1352. (See table notes.)

Hole	Measurement (*N*)		Depth CSF-A (m)		Lab-measured thermal conductivity† (harmonic mean/range; W/[m·K])	
	Good*	Total	Good*	Total	Sediment	Rock
317-						
U1352A	13	32	7.9–42.1	0.2–42.1	1.305/0.849–1.696	—
U1352B	214	443	0.7–792.9	0.7–821.7		
U1352C	149	155	575.1–1920.6	575.1–1920.6	1.180 and 1.487‡	2.360/1.572–3.440

Notes: * = thermal conductivity data were discarded when (1) contact between the probe and sediment was poor, (2) thermal conductivity was close to that of water (0.6 W/[m·K]) because of sediment dilution during coring, or (3) measurements were taken in caved-in layers such as shell hash. † = good measurements. ‡ = measurements were taken with needle probe for Cores 317-U1352C-6R and 18R.

Table T29. Cumulative depth adjustments, Site U1352.

Core	Cumulative depth adjustment (m)
317-U1352D-	
1H	0
2H	2.34
3H	2.34
4H	2.34
5H	2.34
6H	2.34
7H	2.34
8H	3.02
9H	3.02
10H	3.02
11H	10.50
12H	18.13
13H	21.30
14H	21.30
317-U1352B-	
1H	1.28
2H	1.28
3H	1.28
4H	1.28
5H	1.28
6H	1.28
7H	1.28
8H	1.74
9H	1.74
10H through 94X	3.47